

High Order Discontinuous Galerkin Methods for the Simulation of Multiscale Problems

A thesis accepted by the Faculty
of Aerospace Engineering and Geodesy of the University of Stuttgart
in partial fulfillment of the requirements for the degree of
Doctor of Engineering Sciences (Dr.-Ing.)

by

Andrea D. Beck

born in Trier

Main referee: Prof. Dr. Claus-Dieter Munz
Co referee: Prof. Dr. Rupert Klein
Date of defence: February 25, 2015

Institute of Aerodynamics and Gas Dynamics
University of Stuttgart

2015

Für Arno, Christina, Helga und Peter.

Preface

This thesis was developed during my work as an academic employee at the Institute of Aerodynamics and Gas Dynamics (IAG) of the University of Stuttgart.

I wish to thank my doctoral advisor, Prof. Dr. Claus-Dieter Munz, for his guidance and support during the last five years. In particular, I am grateful for his open and approachable leadership style, which makes the Numerics Research Group both successful and a great place to work as well. Furthermore, I would like to thank Prof. Dr. Gregor Gassner for our joint work and all the fruitful discussions. Many thanks also to my co-referee Prof. Dr. Rupert Klein, whose interesting comments both during the “MetStröm” project and my defence have always challenged me to consider new aspects of my research.

A big thank you also goes to all my colleagues at the institute, especially to all past and present members of the Numerics Research Group. In particular, I would like to thank Dr. Andreas Birkefeld and Dr. Christoph Altmann for their support and mentoring during my initial time here. Also, a special thank you goes to Dr. Florian Hindenlang and Thomas Bolemann, with whom I had many fruitful and interesting discussions and who both impressed me with their work ethics and teamwork. Moreover, I would like to thank Hannes Frank and David Flad for sharing their enthusiasm and ideas with me – and their sense of humor.

This work was supported by the Deutsche Forschungsgemeinschaft, through the Schwerpunktprogramm 1276 “MetStröm”. I am very grateful for this support, and also for the opportunity to work with colleagues from different scientific disciplines.

Last but certainly not least I would like to thank my family, Arno, Christina, Helga and Peter for their unwavering support.

Stuttgart, May 1, 2015

Andrea Beck

Contents

Preface	v
Contents	vii
Symbols and Abbreviations	xi
Kurzfassung	xv
Abstract	xvii
1. Introduction	1
1.1. Multiscale Problems: Simulation Strategies	3
1.2. Multiscale Problems: Modeling	4
1.3. Multiscale Problems: Numerics	5
1.4. Objective	6
1.5. Outline	7
2. Turbulence Simulation	9
2.1. Turbulence	9
2.1.1. Phenomenology of Turbulent Flows	9
2.1.2. Governing Equations	19
2.2. A Model Turbulence Problem: The Taylor-Green Vortex	23
2.3. Numerical Simulation Strategies for Multiscale Flows	26
2.3.1. DNS	26
2.3.2. RANS	27
2.3.3. Large Eddy Simulation	27
2.4. Aspects of Large Eddy Simulation	31
2.4.1. General Formalism	31
2.4.2. The “Perfect” LES model	39
2.4.3. Modeling Strategies	47

3. Numerics for Scale-Resolving Simulations	55
3.1. The Points per Wavelength Paradigm	55
3.2. Global Spectral Methods	63
3.2.1. A Pseudo-spectral Code for the Compressible Navier-Stokes Equations	68
3.3. Spectral Element Methods	71
3.3.1. Discontinuous Galerkin Methods	72
3.3.2. Discontinuous Galerkin Spectral Element Collocation Method	73
3.4. Efficiency of DGSEM for Scale-Resolving Simulations	82
3.4.1. Operation Count	82
3.4.2. Parallel Performance	84
3.4.3. Comparison with Other Codes	85
3.5. DNS with DG Methods	89
4. Numerics for Under-Resolved Simulations	97
4.1. Challenges	97
4.1.1. Accuracy for Under-Resolved Problems	99
4.1.2. Stability for Under-Resolved Problems	102
4.2. Aliasing Errors	105
4.2.1. Source and Effect	105
4.2.2. De-Aliasing Strategies	114
4.3. Stable Simulation of Under-Resolved Turbulent Flows	120
4.3.1. Taylor-Green Vortex	120
4.3.2. Flow over a Cylinder at $Re_D = 3900$	133
4.4. Interaction of Subgrid Scale Model and Discretization	139
4.4.1. DNS and LES Setup	141
4.4.2. Stability and Accuracy Investigations	142
4.4.3. Discussion	149
4.5. Flux Functions in Under-resolved Flows	151
4.5.1. Flux Choices	152
4.5.2. Influence of the Numerical Fluxes	154
4.6. LES with DG Methods	160
4.6.1. State of the Art	160
4.6.2. Perspectives for High Order LES	161
5. Conclusion and Prospects	163
5.1. Future Work	166
A. Initial Conditions for Homogeneous Isotropic Turbulence	169

B. Flow over a Cylinder at $Re_D = 3900$ - Extended Results	171
C. Taylor-Green Vortex - Extended Results	179
C.1. Taylor-Green Vortex at $Re=800$, $N=7$	179
C.2. Taylor-Green Vortex at $Re=1600$, $N=7$	181
C.3. Results of the 1st International Workshop on High Order Methods	182
D. Central Finite Differences of Arbitrary Order	187
E. Derivation of the Vorticity Equation	189
Bibliography	191
List of Tables	211
List of Figures	213
Lebenslauf	223

Symbols and Abbreviations

Symbols

C_s	Smagorinsky model constant
$E, E(k)$	Kinetic Energy (at scale associated with wave number k)
I	Imaginary unit, $I = \sqrt{-1}$
k, \vec{k}	Wavenumber, wavenumber vector
L	Large(st) scale / macroscale
M	Polynomial degree of the ansatz for the fluxes in DG
N	Polynomial degree of the ansatz for the solution in DG
N_{Grid}	Number of 1D grid points
n_{PPW}	Number of grid points / DOF required to accurately resolve a scale of size η
T_W	Wall clock time
Δ	Filter width
ϵ	Dissipation rate of kinetic energy
η	Small(est) scale, Kolmogorov microscale
ν	Kinematic viscosity

Abbreviations

1D, 2D, 3D	one, two, three dimensions / -dimensional
ALDM	Approximate Local Deconvolution Method
BR1	First Method of Bassi and Rebay for the viscous fluxes
BR2	Second Method of Bassi and Rebay for the viscous fluxes
cFD	Compact Finite Difference method / discretization
CPR	Correction Procedure via Reconstruction
CPU-h	Computing Time in core hours
DG	Discontinuous Galerkin
DGSEM	Discontinuous Galerkin Spectral Element Method
DES	Detached Eddy Simulation
DNS	Direct Numerical Simulation
DOF	Degree(s) of Freedom
DRP	Dispersion-Relation-Preserving
FCT	Flux Correction Transport
FD	Finite Difference method / discretization
FE	Finite Element method / discretization
FFT	Fast Fourier Transform
FV	Finite Volume method / discretization
HIT	Homogeneous Isotropic Turbulence
HLRS	High Performance Computing Center Stuttgart
HPC	High Performance Computing
iLES	LES with implicit closure
IP	Interior Penalty Method
JSC	Jülich Supercomputing Centre
LDG	Local DG
LAD	Local Adaptive De-aliasing
LES	Large Eddy Simulation
LF	Lax-Friedrichs flux function
LLF	Rusanov or Local Lax-Friedrichs flux function
Ma	Mach number
MILES	Monotonically Integrated Large Eddy Simulation
MPI	Message-Passing-Interface (Parallelization)
NSE	Navier-Stokes equations

ODE	Ordinary Differential Equation
PDE	Partial Differential Equation
PDG	Projection Discontinuous Galerkin
Pr	Prandtl number
PID	Performance Index
PPM	Piecewise Parabolic Method
PPW	Points Per Wavelength
PS	Pseudo-spectral method
RANS	Reynolds-Averaged Navier-Stokes equations
Re	Reynolds number
RK(n)	nth-order Runge Kutta
Roe	Roe's approximate Riemann solver
SGS	Subgrid Scale
SVV	Spectral Vanishing Viscosity
TGV	Taylor-Green vortex
TKE	Turbulent Kinetic Energy
TVD/B	Total Variation Diminishing / Bounded
URANS	Unsteady Reynolds-Averaged Navier-Stokes equations
VLES	Very Large Eddy Simulation
VMS	Variational Multiscale Method
WALE	Wall-Adapted Local Eddy-Viscosity Model
WENO	Weighted Essentially Non-Oscillatory
WU	Work Unit(s)

Kurzfassung

Diese Arbeit stellt einen Beitrag zur effizienten, stabilen und genauen numerischen Simulation von hydrodynamischen nicht-linearen Multiskalenproblemen mit räumlichen Diskretisierungsverfahren hoher Ordnung dar. Aufgrund der großen Bandbreite an räumlichen und zeitlichen Skalen erfordern diese Art von Problemen nicht nur hochgenaue und effiziente numerische Verfahren, sondern auch deren angepaßte Umsetzung auf Höchstleistungsrechnern. Trotz der Weiterentwicklungen auf dem Gebiet der Hardware und Algorithmen bleibt eine vollständige Auflösung aller Skalen typischerweise unerreichbar. Daher muss eine approximative Lösung mit deutlich verringerter Zahl an Unbekannten gesucht werden, die aber in den wesentlichen Größen mit der Lösung des Ursprungsproblems übereinstimmt. Diese Lösung läßt sich aus der Formulierung eines reduzierten Multiskalenproblems berechnen, ergänzt durch einen Modellierungsansatz für die nicht-aufgelösten Skalen und deren Rückwirkung auf die nieder-dimensionale Lösung. Dieser Ansatz ist nur dann zielführend, wenn die Grobstruktur der Lösung sich durch die reduzierten Unbekannten gut approximieren läßt und wenn der nicht-aufgelöste Teil der Skalen universelles Verhalten zeigt, dass sich generell modellieren läßt.

Turbulente Fluidströmungen erfüllen typischerweise diese Voraussetzungen und sind somit ein Beispiel für diese Art von Multiskalenproblemen. In dieser Arbeit werden zwei Verfahren für die Lösung der kompressiblen Navier-Stokes Gleichungen vorgestellt: Ein eigenentwickelter Fourier Pseudo-Spektral-Löser, und ein mitentwickelter Simulationscode basierend auf der Discontinuous Galerkin Spectral Element Method (DGSEM). Beide Diskretisierungsverfahren sind aufgrund ihres spektralen Charakters sehr gut zur Lösung von Multiskalenproblemen geeignet, da sie sehr geringe Approximationsfehler über einen weiten Skalenbereich aufweisen und somit einen hohen Lösungsqualität pro investiertem Freiheitsgrad besitzen. Da DGSEM auf der Variationsformulierung der Evolutionsgleichungen beruht, läßt sich das Rechengbiet element-basiert diskretisieren, was wiederum zur sehr guten Parallelisierbarkeit von DGSEM beiträgt und die Generierung von flexiblen, unstrukturierten Rechengittern erlaubt. Aufgrund dieser Eigenschaften eignet sich daher dieses Verfahren sehr gut für die Direkte Numerische Simulation (DNS) von Turbulenz und macht es – wie in dieser Arbeit gezeigt – im Vergleich zu anderen Diskretisierungsverfahren zumindest gleichwertig und oft überlegen. Die positiven Approximationseigenschaften von DGSEM lassen sich auch auf unter-

aufgelöste Probleme im Rahmen einer Large Eddy Simulation (LES) übertragen, bei denen eine reduzierte Problemformulierung gelöst wird. Je nach Diskretisierung der nicht-linearen Terme in den Erhaltungsgleichungen entsteht dabei jedoch ein selbstverstärkender Fehler, der zu einer Instabilität des Verfahrens führen kann. Die Ursachen und die Auswirkungen dieses sogenannten Aliasing-Fehlers werden in dieser Arbeit untersucht. Es werden Strategien zu seiner Vermeidung oder Kontrolle vorgestellt und in den Simulationscode implementiert. Ein Vergleich dieser Ansätze zeigt, dass nur durch exakte Integration der nicht-linearen Terme die ursprünglichen Verfahrenseigenschaften, die diese Diskretisierung für Multiskalenprobleme effizient machen, erhalten werden können. Mit Hilfe dieser Strategie kann gezeigt werden, dass DGSEM Verfahren hoher Ordnung im Vergleich zu anderen LES-Formulierungen basierend auf Verfahren niedriger Ordnung pro eingesetztem Freiheitsgrad eine höhere Genauigkeit für turbulente Strömungen bei mittleren Reynoldszahlen liefern.

Die Erweiterung auf Probleme mit höheren Reynolds bringt die Notwendigkeit einer Modellierung des steigenden Abbruchfehlers mit sich. Dazu werden zwei Strategien vorgestellt: Im Rahmen einer impliziten LES-Schließung lassen sich die numerischen Flußfunktionen an den Zellgrenzen anpassen, so dass ihre Dissipationsterme als Feinstrukturmodell dienen. Wird im Rahmen einer expliziten Schließung ein zusätzlicher dissipativer Modellterm in die Gleichungen implementiert, so stellt sich die Frage, ob der explizite De-Aliasing-Mechanismus weiter notwendig bleibt, oder ob diese Aufgabe vom Schließungsmodell mit übernommen werden kann. Zur Beantwortung dieser Frage werden die Untersuchungen zum De-Aliasing, kombiniert mit einem expliziten Feinstrukturmodell, wiederholt, und die Interaktion von Diskretisierung und Modell bewertet. Es zeigt sich, dass nur durch vollständiges polynomiales De-Aliasing eine Entkopplung von Modell und Numerik und damit eine hohe Lösungsqualität erreicht werden kann.

Basierend auf den Ergebnissen dieser Arbeit konnte damit eine konsistente Strategie für die stabile und genaue Simulation von turbulenten Strömungen in voll-aufgelösten und unter-aufgelösten Situationen mit DGSEM Verfahren hoher Ordnung etabliert werden. In der Zukunft sollten basierend auf dem spektralen Charakter von DGSEM und dem damit verbundenen hohen Auflösungsvermögen pro Element implizite und explizite LES-Schließungen entwickelt werden.

Abstract

This work provides a contribution to the accurate, stable and efficient numerical simulation of hydrodynamic non-linear multiscale problems with high order discretizations. Due to their wide range of spatial and temporal scale, these types of problems demand not only highly accurate and efficient numerical discretization schemes, but also careful code design with regards to supercomputing architectures. Still, as a rule, even for the most sophisticated algorithms and hardware, a full resolution of all occurring scales remains infeasible. Thus, an approximate solution with drastically reduced number of degrees of freedom is sought, which retains the most important characteristics of the full solution. This solution is obtained by solving a truncated multiscale problem, supplemented by a suitable modeling strategy for the omitted scales and their interaction with the truncated solution. This approach is only meaningful if the resolvable scales determine the mean solution features accurately, and if the non-resolved scales show some form of universality behavior, which allows the derivation of meaningful models.

Hydrodynamic turbulence is one example of these types of problems. In this work, two frameworks for the numerical solution of the compressible Navier-Stokes equations are presented: A self-developed Fourier pseudo-spectral solver, and a co-developed framework based on the Discontinuous Galerkin Spectral Element Method (DGSEM). Both discretization schemes are highly efficient for the resolution of multiscale problems as they – due to their spectral character – exhibit very low approximation errors over a wide range of scales, and thus return a very high resolution capability per invested degree of freedom. Since DGSEM is based on the variational form of the governing equations, it allows an element-based discretization of the computational domain, which in turn leads to superior parallelization and the possibility for flexible, unstructured meshes. These features make it attractive for the full resolution of turbulence in a Direct Numerical Simulation (DNS) approach and – as demonstrated in this work – highly competitive when compared to other discretization strategies.

These favorable discretization properties carry over into the under-resolved situation (Large Eddy Simulation, LES), where a lower-dimensional version of the problem is solved numerically. However, depending on the discretization of the scale-producing mechanism, its truncation can introduce a self-feeding error into the solution, that can lead to a global instability. The source and effects of these aliasing errors are investigated in this work. Strategies for countering or avoiding it are presented, and the code frame-

work is extended accordingly. These strategies are compared and evaluated, showing that only the exact quadrature of the non-linear terms recovers the favorable approximation properties and thus the efficiency of the spectral approach. With this discretization strategy, it is shown that high order DGSEM can outperform established, lower-order LES formulations in terms of accuracy per invested degree of freedom for challenging test cases at moderate Reynolds number turbulence.

Extension to higher Reynolds numbers necessitates the introduction of some form of closure for the un-resolved scales, due to the increase in the truncation error. Aspects of two modeling approaches are discussed: An implicit modeling strategy for DGSEM can be based on the modification of the dissipation introduced by the inter-cell fluxes. The addition of an explicit modeling term which provides a subgrid dissipation mechanism raises the question whether de-aliasing remains essential in that situation. The de-aliasing strategy is revisited, and its interactions with an explicit closure model are examined. It is shown that only through a proper de-aliasing mechanism, the superior scale-resolving capabilities of the scheme can be recovered, and that a decoupling of explicit model and numerics is imperative.

Through these investigations, a consistent strategy for stable and accurate DNS and LES of turbulent flows with high order DGSEM has been established. As an outlook, further research strategies into LES modeling should take full advantage of the spectral character of DGSEM, and the associated scale range resolved within each element can be exploited in both an implicit as well as explicit closure approach.

1. Introduction

The overwhelming majority of all processes in nature and science involve interacting mechanisms on multiple spatial, temporal or frequency scales [2, 3, 61]. While the term scale defies a strict definition, it is usually associated with an observable feature of the problem that shows a wide range of variation in a characteristic quantity. Often, these variations span orders of magnitude in all associated dimensions, giving the problem its chaotic appearance, when regarded from the “macroscale” level. The macroscale is usually defined as the largest occurring or observable scale of the problem, while the smallest features are commonly referred to as “microscales”. Depending on the physical processes and the scale separation involved, the macro- and microscale regimes may be ruled by different governing sets of equations, but even when the same mathematical description of the underlying problem remains valid across all scales, a different set of effects may dominate across the considered scale bandwidth.

Figure 1.1 shows an example of a multiscale problem of geophysical fluid dynamics: Two temperature bubbles interact due to buoyancy forces in a stratified medium, forming a range of temporal and spatial scales.

What almost all of the multiscale problems have in common and what makes them challenging from an analytical and numerical point of view, besides the fact that the involved scales can differ in size by many orders of magnitude, are three issues: i) interactions between scales occur across the full spectrum, ii) these interactions are typically non-linear and iii) the mutual importance of physical effects and associated boundary conditions is a function of the position within the scale spectrum. Fluid turbulence is a classical example of this behavior. In fact, the development of one of its most famous statements follows along the thoughts delineated by i) to iii): In deriving relations for the scales of turbulent flows, Kolmogorov made use of conjectures (called the “Kolmogorov’s similarity hypotheses” [116, 117]) which touched on these aspects of multiscale problems: By assuming a balance of large scale non-linear energy production and small scale linear dissipation, a dominance of viscous actions and a trend towards universality at the small scales and dimensional analysis he arrived at the well-known Kolmogorov’s $k^{-5/3}$ law (actually first published by Obukhov [150]), which gives a relationship for the universal shape of the kinetic energy spectrum in the inertial subrange region:

$$E(k) \sim \epsilon^{2/3} k^{-5/3}, \quad (1.1)$$

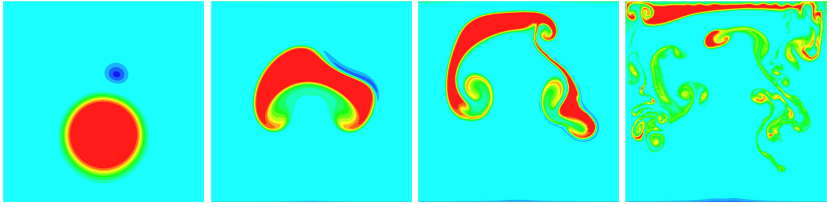


Figure 1.1.: Temporal evolution (from left to right) of two temperature bubbles in a stably stratified medium. Shown are isocontours of temperature difference $\Delta\theta = \theta - \theta_{background}$.

where $E(k)$ denotes the kinetic energy at wave number k , and ϵ is the rate of kinetic energy dissipation. Another illuminating result of his work is an estimate for the ratio of the largest and smallest length scales L and η in turbulence:

$$\frac{L}{\eta} \sim \left(\frac{VL}{\nu} \right)^{3/4} = Re^{3/4}, \quad (1.2)$$

where V denotes the large scale velocity, ν the kinematic viscosity and Re the associated Reynolds number. This relation can also be interpreted as an estimate for the information content (or the number of degrees of freedom, DOF) of the problem. An extension to three dimensions shows that the total number of spatial information bits B_{total} in a turbulent flow scales as

$$B_{total} \sim Re^{9/4}, \quad (1.3)$$

without taking temporal scales into account. This estimate demonstrates the overwhelming complexity and information density of this multiscale problem and raises an important question: How can these types of problems be analyzed, when the complex nonlinearities restrict analytical treatment to only very simplified “toy problems”, and when the sheer amount of degrees of freedom makes an experimental and numerical investigation infeasible?

Interestingly, the same ideas that led Kolmogorov through his derivation process, can help to answer this question: The scale separation itself and with it the separation of dominant effects and boundary condition influence can be exploited to devise suitable strategies for tackling multiscale problems.

1.1. Multiscale Problems: Simulation Strategies

While we are mainly interested in multiscale problems occurring in turbulent fluid flow in this work, the general principles outlined in this section can be transferred to other types as well: For the numerical simulation of multiscale problems, two general strategies exist. Either a laboratory-type experiment with well-defined initial and boundary conditions for a single representative scale or a very limited bandwidth of scales can be conducted, which allows the detailed observation of the local processes and interactions, or the mean (temporal and spatial) effects at the large scales can be observed, while neglecting or approximating (modeling) small scale effects. The first approach usually aims at understanding the basic building blocks (i.e. the physical mechanisms) on the small scale level, taking advantage of their universality and decoupling from large scale boundary conditions and deriving suitable models for their effects (e.g. [193]). The second approach is motivated by the observation that the mean statistics of the flow are often mainly governed by large scale effects, which are strongly dependent on the boundary conditions of the flow. Since the small scales are more universal, there is a chance that finding suitable models for their interaction with the large, anisotropic scales is feasible [168].

Although these approaches might seem very different, they are complementary in their exploitation of the universality and of the dominance of different physical effects at opposite ends of the scale range.

While the idea of devising models on the small scale level and coupling them to large scale dynamics is attractive, a major issue is the loss of universality of the building block, either through a singular event or through insufficient scale separation. Insufficient scale separation can occur for two reasons: i) The problem itself does not support this approach, i.e. there is no scale range with universal physical behavior, or no dominating physical effect can be identified. In that case, if no suitable model can be defined, the only remaining strategy would be to restrict any analysis to problems with low dimensionality. ii) An induced insufficient scale separation can occur when the small scale model is applied in a scale region that does not support the underlying universality assumption. One example of an event that violates the universality assumption in turbulent flows is the phenomenon of backscattering, where the main direction of non-linear interaction is not from the anisotropic large scales to the universal small scales, but reversed [156]. In such a case, the small scale dynamics result in the generation of large scale features. This directly contradicts the model assumptions, and can render this building block approach obsolete.

In summary, the main questions that arise when devising strategies for multiscale problems are: Is there universality or at least a dominating effect at a given scale level? Can we model this regime, and how do we couple building blocks at different scale levels?

Where do we have to give up this building block model? And how can singular, non-typical events be treated?

In the end, the current state of the art can be summed up in a practical paradigm: resolve as much as possible of the scales which are non-universal or lead to singular behavior, and model everything assumed to be universal or strongly dominated by well-understood physical processes. In fluid dynamics, this approach is commonly referred to as the Large Eddy Simulation (LES) method. It should be noted that it consists of at least two important subtasks: The accurate numerical simulation of the non-universal scales and the modeling of the small scale effects.

1.2. Multiscale Problems: Modeling

The aim of the modeling approach is to reduce the complexity of the multiscale problem to a point where it becomes tractable by numerical simulation. Ideally, this should be achieved by modeling the small scale dynamics in such a way that the large scale properties remain unaltered. Issues shared by all modeling methods arise from the general question of modeling physical systems. The identification of “model-able” regimes with a universal character has been discussed above. The inclusion of singular events that break this universality like backscattering requires special treatment, for example through a stochastic approach [64, 137, 138]. Another important aspect is to ensure that the model fulfills the transformation invariances and symmetries of the governing equations as well as realizability constraints [187], and regulates itself in well-resolved scenarios.

Two main approaches exist in the development of these models: i) “Building block” models are derived either from an analysis of the continuous dynamics or from numerically obtained correlations of high-resolution, small scale simulations. These models are usually based purely on physical and mathematical reasoning and are independent from the numerical strategies for the large scale computations. This approach results in additional terms or equations describing the model which then complements the original problem formulation. It is called explicit modeling or “explicit LES”. ii) Altering the discretization properties of the large scale simulation schemes in such a way that the discretization itself performs the regularization of the problem is referred to as “implicit LES”. An important drawback of this strategy is the dependence of the modeling terms on the type of the discretization and additionally on the local resolution, which makes an a priori evaluation of these models very difficult. Explicit models, on the other hand, while based on physical reasoning, rely on error-free resolution of the large scales. This exactness can usually not be guaranteed, thereby resulting in an unwanted interaction of model and numerical errors.

1.3. Multiscale Problems: Numerics

As discussed above, small scale modeling and large scale numerical simulation are two interacting fields. Either, this interaction is sought and exploited in an implicit modeling approach, or it is to be minimized for explicit small scale models. In both cases, the selection and design of the numerical scheme for the large scale simulation plays a crucial role.

The most basic issue that arises when solving multiscale problems numerically is that of finite digital precision and rounding errors. Since the scales involved can span many orders of magnitude, the representation of these scales can lead to conditioning problems. In addition, non-linear problems exhibit a high sensitivity to slight changes in initial and boundary conditions (or run-time round-off errors), which can affect the instantaneous realization of the turbulent flow, but not its statistics [181]. While the effects of finite precision are indeed a concern, the range of physical scales present is usually restricted by the computational cost of the simulation and does not exploit the full digital resolution available. Therefore, typically also a scale separation between the smallest resolved scales and the round-off errors exists, which prevents these errors from dominating the numerical solution.

An estimate for the range of scales occurring in a problem has already been given in Equation (1.2). Assuming that the spatial discretization scheme requires n_{PPW} grid points or degrees of freedom per wavelength (PPW) resolve the smallest length scale η , the total number of grid points N_{3D} in three dimensions can be estimated as [176]

$$N_{3D} = \left(\frac{L}{\eta/n_{PPW}} \right)^3 \sim n_{PPW}^3 Re^{9/4}. \quad (1.4)$$

A refined analysis even found a more stringent requirement of $N_{3D} \sim n_{PPW}^3 Re^{37/14}$ [44]. Considering not only the spatial degrees of freedom, but also the fact that the characteristic time scale of the dissipation scales is directly proportional to η , the total computational cost in terms of spatial and temporal degrees of freedom N_{total} becomes

$$N_{total} \sim n_{PPW}^4 Re^3. \quad (1.5)$$

This relationship highlights two important issues: i) The computational effort of resolving all scales can quickly become unbearable and ii) the scale-resolving capabilities of the discretization dramatically influence the overall cost, i.e. the total effort is a function of both the physics (through Re) and of the numerical capabilities (through n_{PPW}). When resolving only a fraction of the scales in a LES approach, the demands stemming from the physics can be lowered to $N_{3D} \sim Re^{9/5}$ [42] or $N_{3D} \sim Re^{13/7}$ [44] for wall-resolved LES, making the influence of the numerics on the total simulation cost

even stronger. Thus, a fundamental demand for efficient numerical simulation of all or a subset of the scales of turbulent motion can be formulated as: The number of degrees of freedom or grid points required to accurately resolve the smallest occurring relevant scale must be minimized.

In addition to efficiency, which is directly related to the behavior of the approximation errors of a given discretization, stability of the simulation is also an issue of concern. Stability can always become an issue when physical processes are not correctly represented in a discrete setting, leading to a violation of associated symmetries (e.g. the skew-symmetry of the convective term), constitutive equations (e.g. positivity of density and pressure) or governing laws (e.g. inconsistent LES closure). When resolving all scales of the multiscale problem adequately, stability becomes purely a matter of numerics (if the underlying continuous problem is well-posed and stable), i.e. any instabilities are due to inappropriate numerical methods and can be treated as such. When resolving only a partial range of scales of the continuous problem and modeling the rest in a LES setting, overall stability has three contributors: The discretization and the model, as well as their complex interactions. The question which of these two should provide the stability is an open issue of research, some LES methods rely on the model, e.g. [142, 158], others on the scheme itself, e.g. [6, 94, 180].

Directly related to the question of stability is the control over the interaction of model and discretization errors. Model errors include the incorrect prediction of physical behavior (a “non-perfect” model) as well as the representation of the model in a discrete setting. Discretization errors result in an inaccurate resolution of the resolved scales, and therefore in imperfect “input parameters” for the model itself. For implicit LES, where the discretization itself generates the modeling terms, scale-resolving efficiency, stability and model behavior are completely interdependent.

1.4. Objective

The objective of this work is to provide a contribution to the accurate, efficient and stable numerical simulation of turbulent flows, in particular in under-resolved situations. As discussed before, the efficiency of a discretization in terms of invested degrees of freedom can become a limiting factor in the simulation of multiscale problems. We demonstrate the effectiveness of high order Discontinuous Galerkin discretizations for both simulation strategies outlined above: For high resolution, large scale DNS on a “building block” level as well as for under-resolved simulations combined with a modeling approach. In the latter case, we focus on the approximation properties over the full scale range and the treatment of non-linear terms, which both influence the stabil-

ity of the discretization operator. We present and evaluate de-aliasing options and show that the favorable scale-resolving capabilities of the schemes can only be recover through exact integration of the non-linear terms. For moderate Reynolds number flows, we compare de-aliased high order Discontinuous Galerkin schemes without additional closure models against low order formulations, both with explicit and implicit LES models, and show the increased accuracy in terms of invested degrees of freedom for our approach. In addition, we present two strategies for the extension to higher Reynolds number flows, where the effects of the truncation error become more pronounced: An implicit modeling through the surface flux functions, and the inclusion of an explicit LES closure model. For this second strategy, we investigate the interaction of the discretization choice of the non-linear term, the approximation properties of the scheme and the model, and we conclude that polynomial de-aliasing is essential, not only from a stability point of view, but also to exploit the accuracy of the high order discretization and to develop and evaluate explicit closure models. Finally, we propose a strategy for extending the capabilities of current DG LES methods, both for explicit and implicit modeling approaches, based on our findings.

1.5. Outline

In this work, we will present and discuss numerical schemes for the approximation of fully resolved and under-resolved multiscale problems, focusing on the example of hydrodynamic turbulence as described by the Navier-Stokes equations. We will briefly discuss the features of turbulence that make it a challenging problem from both a numerical and a fluid mechanics standpoint in Section 2.1, followed the description of a canonical test case in Section 2.2 and by a discussion of numerical strategies for its simulation in Section 2.3. Focusing on a Large Eddy Simulation strategy, we will derive a general formalism for the classification of the different LES approaches in Section 2.4, and discuss the perfect and actual closure strategies.

In Chapter 3, we focus on numerical schemes for efficient resolution of multiscale problems. The importance of the “points per wavelength” concept will be demonstrated in detail in Section 3.1, followed by the discussion of two families of methods suitable for scale-resolving numerics: The global spectral methods in Section 3.2 and the spectral element methods in Section 3.3. We will present in detail two representative schemes belonging to each category, and the associated computational frameworks developed in this work. In particular, we will focus on the details and properties of the Discontinuous Galerkin Spectral Element method and its efficiency for scale-resolving computations in Section 3.4, followed by examples of scale-resolving simulations with this framework in

Section 3.5.

Extending the discussion from well-resolved to under-resolved problems in Chapter 4, we will focus on the additional numerical and modeling challenges that arise in these situations in Sections 4.1 and 4.2. The discretization of the scale-producing term requires special attention, as it can cause instabilities. Different countering strategies for under-resolved flows will be discussed and compared in Section 4.3. In Section 4.4, we investigate the interaction of numerics and explicit modeling, and highlight the importance of neutrally stable numerics for LES. Finally, we briefly demonstrate the influence of the flux functions in a LES setting in Section 4.5 and discuss perspectives and state of the art for LES with high order methods in Section 4.6. We conclude with a summary and an outlook on research strategies in Section 5.

2. Turbulence Simulation

In this chapter, we briefly describe the most prominent features of turbulent flows and the general numerical solution strategies, with a special focus on aspects of Large Eddy Simulations.

2.1. Turbulence

Turbulence is a state of fluid motion characterized by non-linear interactions over a wide range of scales. It is the results of an instability mechanism of a steady base flow that amplifies successive instability modes and finally leads to turbulence [67]. The onset of this transition process and the resulting range of turbulent scales is governed by the Reynolds number $Re = \frac{VL}{\nu}$ of the flow (see Equation(1.2)), a similarity parameter relating the non-linear convective effects and the linear diffusive actions. An exact, all-encompassing definition of turbulence is difficult to state due to the many aspects it would have to include, and thus, the question “what is turbulence ?” is usually answered by listing its most important features.

2.1.1. Phenomenology of Turbulent Flows

Following the discussion presented in [57,167,192] and in lieu of a definition, turbulence is characterized by the following features:

- **Non-linearity and scale range**

Turbulence is characterized by a wide range of spatial and temporal scales, usually associated with coherent structures called “eddies” with a characteristic length (or wave number as its inverse) and a turn-over frequency. The largest scales or eddies are constrained by the boundary conditions and mean flow conditions and are thus non-universal and anisotropic, while the smallest scales become (with increasing Reynolds number) isotropic and universal. The kinetic energy is extracted from the mean flow and fed into smaller eddies, which in turn interact with each other and the mean flow. While these interactions form scales across the whole scale range, the majority of the resulting transfer of kinetic energy is “downwards” (called forward scatter), i.e. produces higher wave number eddies [166]. The viscosity of the fluid is the limiting agent for this scale generation, as the dissipative

2. Turbulence Simulation

effects on regions of high curvature (i.e. small, high-frequency eddies of sizes on the order of η) overcome the scale production mechanisms.

The non-linearity of the convective term in the governing equation of fluid flow is responsible for the generation of this scale cascade. Non-linearity implies an interaction of different scales, i.e. a strong coupling of the degrees of freedom of the system. While linear systems may also possess an arbitrary high number of degrees of freedom, these are not coupled and thus do not interact.

The simplest model of non-linear interaction is described by the viscous Burgers' equation for a scalar $u = u(x, t) \in \mathbb{R}$, given by

$$\frac{\partial u}{\partial t} + \frac{1}{2} \frac{\partial u^2}{\partial x} - \frac{1}{Re} \frac{\partial^2 u}{\partial x^2} = f(x, t), \quad (2.1)$$

with $u = u(x, t)$, $x \in [0, 2\pi]$, $t \in [0, \infty^+)$.

Here, $Re = \frac{1}{\nu}$ is the Reynolds number based on the kinematic viscosity $\nu > 0$ and f a forcing term. Equation (2.1) contains a quadratic non-linearity in the convective term and a linear viscous term, which also arise in the incompressible Navier-Stokes equations (plus the pressure contribution). Therefore, Burgers' equation often serves as a model for the full Navier-Stokes system, as its forced version with special $f(x, t) \neq 0$ can exhibit chaotic behavior resembling certain aspects of fully three-dimensional turbulence [79, 139, 145].

Considering an initial solution at time t_0 to Equation (2.1) of the form $u(x, t_0) = \hat{u} \sin(kx)$ with an initial amplitude \hat{u} and a single wave number k , the total flux at $t = t_0$ becomes

$$\begin{aligned} \left. \frac{\partial u}{\partial t} \right|_{t=t_0} &= -u \left. \frac{\partial u}{\partial x} \right|_{t=t_0} + \frac{1}{Re} \left. \frac{\partial^2 u}{\partial x^2} \right|_{t=t_0} \\ &= -\frac{1}{2} \hat{u}^2 k \sin(2kx) - \frac{\hat{u} k^2}{Re} \sin(kx). \end{aligned} \quad (2.2)$$

This simple model equation shows that the initial flux will introduce a term with wave number $2k$ into the time evolution of the solution, i.e. higher wave numbers will be generated through this term. This is the root of the scale producing mechanism that generates the energy cascade. The second term on the right hand side of Equation (2.2), stemming from the viscous flux, does not introduce additional higher frequency waves, but dampens the initial wave. Note that the magnitude of the damping is a function of k^2 , i.e. high wave numbers will be affected more

strongly by this term. In general, Equation (2.2) shows that an initial state containing wave numbers k_1 and k_2 will produce – through the quadratic non-linearity – waves with $2k_1$, $2k_2$ and $k_1 + k_2$, which will interact over time and thus successively generate waves over the full wave number range, until their production is balanced by viscous effects. The relation of k to Re determines which effect dominates in the current situation. For $k \ll Re$, the second term on the right hand side of Equation (2.2) will become negligible, and the flux will be governed by the inviscid contributions. In the other extreme $k \gg Re$, the dissipative flux will dominate. Thus, this simple scalar model equation demonstrates the basic mechanism of scale production and destruction in the cascade.

Another important aspect of turbulence and the non-linear terms can be derived from Equation (2.1). By defining the kinetic energy $E(t)$ of the solution $u(x, t)$ as

$$E(t) = \frac{1}{2} \int_0^{2\pi} u(x, t)^2 dx, \quad (2.3)$$

an evolution equation for this energy can be derived from the unforced viscous Burgers' equation by multiplication with u and integration over the spatial domain $x \in [0, 2\pi]$:

$$\begin{aligned} 0 &= \int_0^{2\pi} \left(u \frac{\partial u}{\partial t} + \frac{1}{2} u \frac{\partial u^2}{\partial x} - \nu u \frac{\partial^2 u}{\partial x^2} \right) dx \\ &= \int_0^{2\pi} \left(\frac{1}{2} \frac{\partial u^2}{\partial t} + \frac{1}{3} \frac{\partial u^3}{\partial x} - \nu \left(\frac{\partial}{\partial x} \left(u \frac{\partial u}{\partial x} \right) - \frac{\partial u}{\partial x} \frac{\partial u}{\partial x} \right) \right) dx \\ &= \frac{dE}{dt} + \frac{1}{3} u^3 \Big|_0^{2\pi} - \frac{1}{2} \nu \frac{\partial u^2}{\partial x} \Big|_0^{2\pi} + \nu \int_0^{2\pi} \frac{\partial u}{\partial x} \frac{\partial u}{\partial x} dx \\ &\Leftrightarrow \frac{dE}{dt} = F_{bc} \Big|_0^{2\pi} - \nu \int_0^{2\pi} \frac{\partial u}{\partial x} \frac{\partial u}{\partial x} dx, \end{aligned} \quad (2.4)$$

where we have collected the boundary fluxes in F_{bc} . It is important to note that the non-linear term does not have a volume contribution to the kinetic energy, only a flux across the domain boundaries, while the viscous term contributes through a surface flux as well as a volume term. If we consider F_{bc} to be zero (for example for a periodic problem), the only contributing factor to the kinetic energy balance would be the viscous term, i.e. the kinetic energy would decrease with the rate prescribed by the viscosity ν and the integral over the product of the velocity gradients. Therefore, the non-linear term is only responsible for the distribution of kinetic energy across the scales, but it is conservative, while the linear diffusion term does not cause scale interaction, but serves as a sink for the kinetic

2. Turbulence Simulation

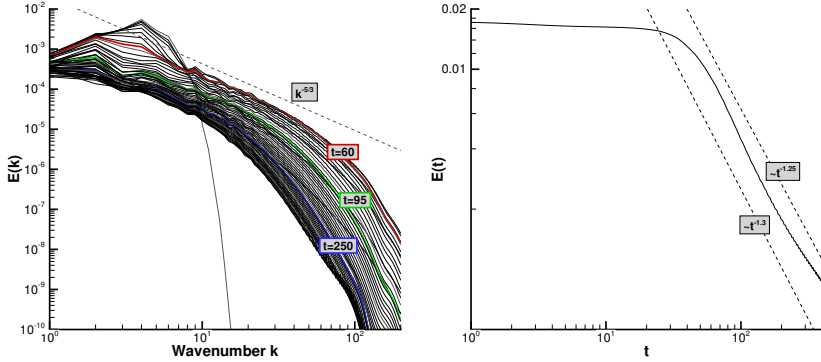


Figure 2.1.: Decaying homogeneous isotropic turbulence. Computations with pseudo-spectral code *Spex* described in Section 3.2.1.

Left: Temporal evolution of the spectrum of kinetic energy $E(k)$. Dashed line denotes Kolmogorov's $k^{-5/3}$ law.

Right: Temporal evolution of total kinetic energy E . Dashed lines denote decay laws published by [53] and [102].

energy. These two effects found in the Burgers' model equation are also present in the full Navier-Stokes equations. Their balance (expressed through the flow Reynolds number) determines the magnitude of the scale cascade, i.e. the scales at which the viscous effects overcome the scale production mechanism. Figure 2.1 *left* depicts the spectrum of kinetic energy of decaying isotropic turbulence of the three-dimensional Navier-Stokes equations. While the scaling laws are different from those for Burgers' equation, the region dominated by inertial forces (following Kolmogorov's $k^{-5/3}$ law in the so-called inertial subrange) and the dissipation range with its rapid energy decay are clearly visible.

It should be noted that while non-linearity is essential for the production of turbulence, it is not sufficient. Non-linear interaction may lead to multiscale phenomena that show organized, large scale behavior, for example the shocks forming in the unforced Burgers' equations or the solitons of the Korteweg-de Vries equations [197, 205].

- **Spatio-temporal irregularity and loss of predictability**

The scale production and dissipation mechanisms highlighted by the Burgers' equation can be translated directly to the three-dimensional Navier-Stokes equations. However, due to the three-dimensionality and the long-mode pressure coupling, the resulting structures are a lot more intricate and complex. Turbulent fields appear – although they are still solutions to a set of deterministic equations – highly irregular and chaotic. It is important to note that this randomness is *not* dependent on randomized forcing or boundary conditions, as opposed to the Burgers' equation, which only produces chaotic solutions under stochastic forcing. Instead, hydrodynamic turbulence (and the Navier-Stokes system) possess an intrinsic “self-stochastization” property [197], in which chaotic motions can occur from smooth initial and boundary conditions. The root of this behavior is the extreme sensitivity to minuscule changes in the current state or the boundary conditions, a feature also observed in experiments [72].

Equation (2.5) describes a simple system of ordinary, non-linear differential equations for a spatial position $\vec{x}(t) = [x(t), y(t), z(t)]$, originally proposed by Lorenz as a model for particle movement in atmospheric convection [132]:

$$\begin{aligned}\frac{dx}{dt} &= a(y - x) \\ \frac{dy}{dt} &= x(b - z) - y \\ \frac{dz}{dt} &= xy - c.\end{aligned}\tag{2.5}$$

Depending on the choice of the scalars $(a, b, c) \in \mathbb{R}^+$, its numerical solution exhibits a highly irregular, chaotic behavior. Figure 2.2 shows the solution trajectories of Equation (2.5) for two slightly different initial starting points and the temporal development of their x -components. Up to about $t = 40$, both solutions are indistinguishable, but deviate strongly after this time. The x -component plot clearly shows the chaotic behavior. In the solution space visualizations, the trajectories begin to deviate, although their general, long term behavior is stable and governed by a structure called the “Lorenz attractor”. The circular markers in Figure 2.2 *top* denote the position in the solution space after the same time t_{end} for both initial conditions. Although the distance between both starting positions was minimal, their current state differs greatly, visualizing the high sensitivity of the system to small deviations.

These properties of the Lorenz system have made it a model problem for deterministic non-linear equations that show inherent chaotic behavior. Its behavior as outlined above can be translated to the turbulence described by the Navier-Stokes

2. Turbulence Simulation

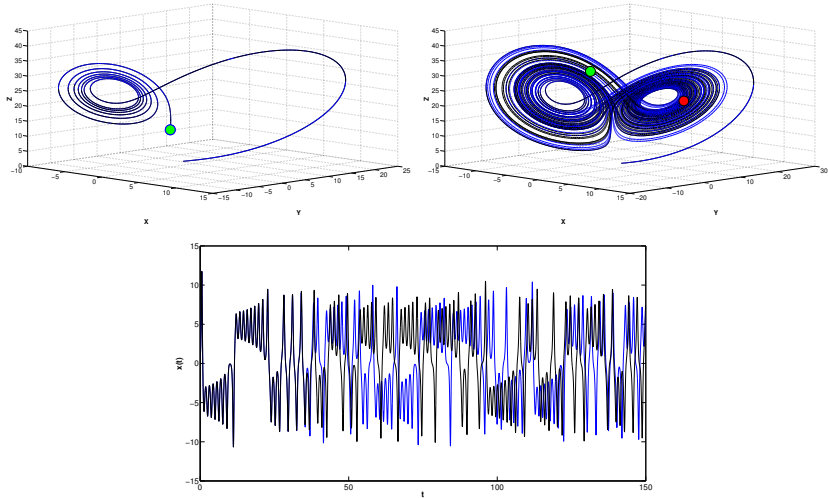


Figure 2.2.: Solution of the Lorenz System (Equation (2.5)) with $a = 3$, $b = 25$, $c = 1$. Blue lines: initial condition $\vec{x}_0 = [1, 1, 2]$; Black lines: initial condition $\vec{x}_0 = [1.00001, 1, 2]$. *Top:* Solution trajectories up to $t_{end} = 10$ (left) and $t_{end} = 90$ (right). Green and red markers show the particle position of blue and black trajectories at t_{end} . *Bottom:* Temporal evolution of x -components of particle positions.

equations: When subjected to slight changes in the initial and boundary conditions, large deviations in the resulting local solution can occur. However, the long term, mean solution is governed by so-called “structurally stable attractors” [90], which are insensitive to these small deviations. This combination of predictability and unpredictability results in the fact that while single realizations of turbulence (both numerical and experimental) can differ significantly in their local, small scale behavior, their statistical properties remain constant against slight perturbations. Turbulence therefore remains statistically stable on the large scales (which allows the prediction of integral quantities like drag and lift), but becomes unpredictable and chaotic on the small scales.

- **Three-dimensionality and vorticity**

Turbulence is characterized by regions of highly three-dimensional, coherent structures undergoing rotational motion. The concept of vorticity as the curl of the velocity gradient $\vec{\omega} \equiv \nabla \times \vec{u}$ is used to quantify and visualize these structures. Vorticity is defined as the vector aligned with the local axis of fluid rotation, with the sign determined by the local right hand system. The length of the vector corresponds directly to the strength of the vortex, i.e. to the radial velocity gradient. Within a turbulent field, regions of high vorticity can be observed and the overall initial vorticity is not conserved, i.e. three-dimensional turbulence contains a mechanism of producing vorticity. This mechanism can be identified by taking the curl of the momentum equation of the incompressible Navier-Stokes equations (full derivation in Appendix E):

$$\nabla \times \left(\frac{\partial \vec{u}}{\partial t} + (\vec{u} \cdot \nabla) \vec{u} = -\frac{\nabla p}{\rho} + \nu \nabla^2 \vec{u} \right), \quad (2.6)$$

which leads to an evolution equation for the vorticity:

$$\frac{D\vec{\omega}}{Dt} = \frac{\partial \vec{\omega}}{\partial t} + (\vec{u} \cdot \nabla) \vec{\omega} = (\vec{\omega} \cdot \nabla) \vec{u} + \nu \nabla^2 \vec{\omega}. \quad (2.7)$$

Equation (2.7) shows that from the non-linear term of the momentum equation, the term $(\vec{\omega} \cdot \nabla) \vec{u}$ on the right hand side evolves, which acts as a source term for vorticity if a velocity shear exists. This term is usually referred to as “vortex stretching”, where the actual stretching is due to the aligned component and a turning or bending of the vortex is due to the cross components, e.g. for the first component of $\vec{\omega}$

$$\frac{D\omega_1}{Dt} = \underbrace{\omega_1 \frac{\partial u_1}{\partial x_1}}_{\text{Stretching}} + \underbrace{\omega_2 \frac{\partial u_1}{\partial x_2} + \omega_3 \frac{\partial u_1}{\partial x_3}}_{\text{Turning}} + \underbrace{\nu \left(\frac{\partial^2 \omega_1}{\partial x_1^2} + \frac{\partial^2 \omega_1}{\partial x_2^2} + \frac{\partial^2 \omega_1}{\partial x_3^2} \right)}_{\text{Diffusion}}. \quad (2.8)$$

For the vortex stretching mechanism to be non-zero, two conditions must be met: i) a velocity shear in the flow must exist, and ii) the flow must be three-dimensional, i.e. the vorticity vector must not be perpendicular to the plane of shear. This is always the case in two-dimensional flows, and thus, a production mechanism for vorticity is absent in these flows. Due to the absence of this mechanism, the term “two-dimensional turbulence” is often disputed, as this flow lacks the basic mechanism of generating vorticity (without external forcing) [121]. In fact, in two dimensions, only two vortex interactions occur:

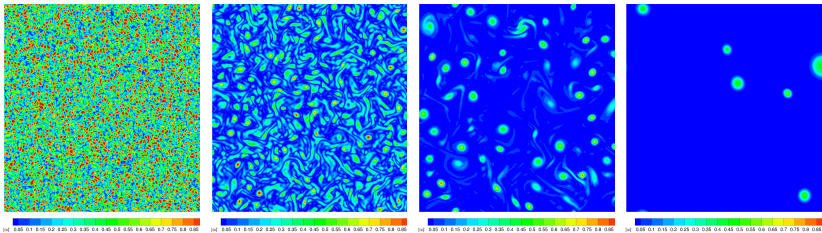


Figure 2.3.: Vortex interactions in two dimensions, shown are contours of vorticity magnitude. From left to right: initial random vorticity field at $t = 0$, resulting fields at $t = 100, 500, 10000$.

The creation of a dipole or the merging of two vortices into a single vortical structure at a larger scale. This behavior leads to the so-called “inverse cascade” of two-dimensional turbulence, where kinetic energy is transferred to larger structures instead of smaller structures as in three-dimensional turbulence. Since this upward transfer always occurs when the rotational axes of two vortices are parallel (or have parallel components), this effect is also present in three-dimensional turbulence, where the alignment of the vortices loses directionality and anisotropy of the large scale boundary conditions and becomes chaotic at the small scales. This interaction with its upward energy transfer is the physical cause of the backscattering effect. It should be noted that even in three-dimensional flows with a preferred directional alignment, e.g. due to external forces like gravity, a quasi-two-dimensional turbulence with dominating upward transfer can develop [178, 195].

Figure 2.3 demonstrates the vortex interactions in two dimensions that lead to the generation of large scale structures. Starting from an initial field with random velocity fluctuations about a mean, the backscattering mechanism continuously merges the small scale structures into successively larger vortices.

Returning to a discussion about the vortex stretching mechanism that increases vorticity locally in three dimensions (Equation (2.8)), each vortical structure can be assigned an angular momentum, defined as $\frac{1}{2}\Theta\vec{\omega}$, where the Θ is the (scalar or tensor) moment of inertia associated with the mass of fluid contributing to the vortex. In an inviscid flow, there are no viscous torques acting as retarding moments,

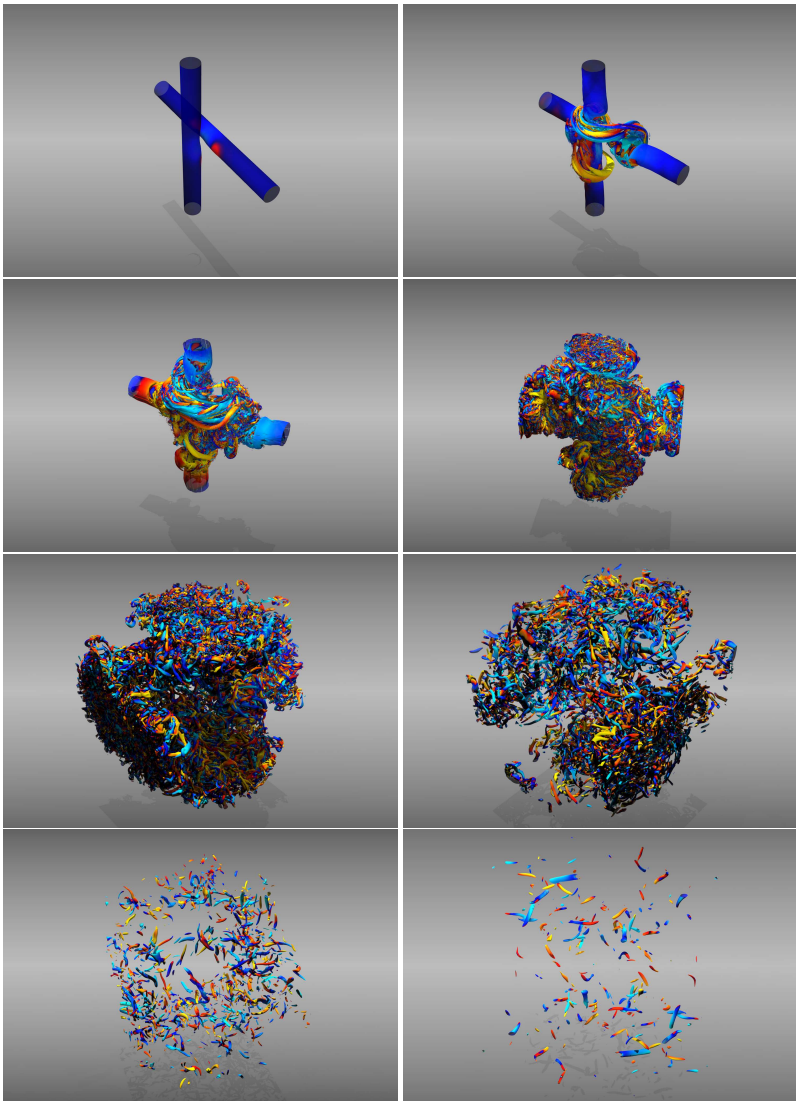


Figure 2.4.: Interaction of two mono-scale vortices: Development of vortical structures and scale cascade. Shown are $\lambda_2 = -0.001$ isocontours, colored by normalized helicity. Temporal evolution from upper left to lower right.

so the angular momentum is conserved according to

$$\begin{aligned} \frac{D\Theta \vec{\omega}}{Dt} &= 0 \\ \Leftrightarrow \Theta \frac{D\vec{\omega}}{Dt} &= -\vec{\omega} \frac{D\Theta}{Dt}. \end{aligned} \tag{2.9}$$

As $\frac{D\vec{\omega}}{Dt}$ increases through the vortex stretching mechanism in Equation (2.7), it must be balanced by a decrease in the moment of inertia on the right hand side of Equation (2.9), thus, higher vorticity results in a lower moment of inertia. For a fully incompressible flow, a decrease in the moment of inertia can only be accomplished by a thinning of the vortex tube, along with a lengthening along its axis to conserve the volume. Thus, the conservation of rotational momentum causes the elongation and thinning of the structures undergoing the stretching mechanism, and so explains the generation of small scale, high frequencies vortices. This process is self-amplifying, and is only stopped when the small scale structures succumb to the dissipation due to their self-induced high strain rates.

Figure 2.4 visualizes these three-dimensional vortex interaction mechanisms and the development of a full scale cascade from two large scale structures.

- **High diffusion and dissipation**

Turbulent flows are both highly diffusive and dissipative. Due to their chaotic small scale motion, interchange of momentum, energy and passively transported objects is highly enhanced. This leads to a perceived increase in “turbulent viscosity” and “turbulent diffusivity” which can be orders of magnitude stronger than their molecular counterparts. However, these “turbulent” terms are not (like the molecular viscosity and diffusivity) properties of the fluid, but of the local turbulence statistics of the flow. The resulting increase in strain due to the non-linear interaction leads to a rapid dissipation of kinetic energy into heat, and thus turbulent flows require a form of energy input (large scale gradients, buoyancy, forcing) to sustain themselves. This transformation of energy from an ordered (large scale, kinetic) to an unordered (chaotic, thermal) state causes the highly enhanced losses encountered in turbulent flows, e.g. over bluff bodies or in internal flows.

- **Non-locality**

Quoting Tsinober [197], non-locality is “probably one of the main reasons the problem of turbulence is so difficult.” The term “non-locality” refers to two issues: i) The non-locality of the pressure field with respect to the velocity field. In the incompressible limit, the pressure equation $\frac{\partial^2 p}{\partial x_i^2} = -\frac{\partial u_i}{\partial x_j} \frac{\partial u_j}{\partial x_i}$ becomes elliptic,

i.e. the pressure becomes non-locally dependent on the velocity field in the whole domain. It is this elliptic nature of the pressure, called the pressure-velocity coupling, that is associated with long-range forces and thus the non-locality in time that differentiates the Burgers' equation model turbulence from the Navier-Stokes turbulence. ii) By the same argument, the velocity field at each space point is defined by the global vorticity field, i.e. the large scales (represented by the velocity) and their associated small scales (the vorticity) are strongly coupled. This coupling is *bidirectional* in its non-locality [197], i.e. the backward reaction of the small onto the large scales also occurs in a non-local manner.

2.1.2. Governing Equations

In the following section, the governing equations of motion for both compressible and incompressible fluids are collected.

2.1.2.1. Compressible Navier-Stokes Equations

The temporal and spatial evolution of a viscous, compressible fluid is governed by the conservation statements for mass, momentum and energy. In conservative form this set of partial differential equations (PDE) for a Newtonian fluid is given by

$$\begin{aligned} \frac{\partial \rho}{\partial t} + \frac{\partial (\rho u_j)}{\partial x_j} &= 0, \\ \frac{\partial (\rho u_i)}{\partial t} + \frac{\partial (\rho u_i u_j + p \delta_{ij})}{\partial x_j} &= \frac{\partial \sigma_{ij}}{\partial x_j}, \\ \frac{\partial (\rho e)}{\partial t} + \frac{\partial [(\rho e + p) u_j]}{\partial x_j} &= -\frac{\partial q_j}{\partial x_j} + \frac{\partial (\sigma_{ij} u_i)}{\partial x_j}. \end{aligned} \quad (2.10)$$

Here, the Einstein summation convention applies, δ_{ij} denotes the Kronecker delta function and $i, j = 1, 2, 3$. The conservative variables of mass, momentum and energy are $U = [\rho, \rho u_1, \rho u_2, \rho u_3, \rho e]$, where ρ denotes the density, u_i the i -th component of the velocity vector and the total energy ρe is given by

$$\rho e = \rho \left(\frac{1}{2} u_i u_i + c_v T \right). \quad (2.11)$$

Herein, c_v constitutes the specific heat at constant volume and T the temperature. Using the equation of a perfect gas, this defines the pressure p and the adiabatic exponent γ as

$$p = \rho RT, \quad \gamma = \frac{c_p}{c_v}, \quad (2.12)$$

2. Turbulence Simulation

with $R = c_p - c_v$ as the specific gas constant computed from c_v and the specific heat at constant pressure c_p . The viscous stress tensor σ_{ij} is a function of the viscosity μ (which itself is dependent on temperature) and the velocity vector

$$\sigma_{ij} = \mu(T)S_{ij}, \quad (2.13)$$

where the rate of strain tensor is given by

$$S_{ij} = \frac{\partial u_i}{\partial x_j} + \frac{\partial u_j}{\partial x_i} - \lambda \delta_{ij} \frac{\partial u_k}{\partial x_k}. \quad (2.14)$$

The bulk viscosity coefficient λ is commonly chosen to be $\frac{2}{3}$, which removes the trace from S_{ij} . The remaining unknown in Equation (2.10) is the definition of the heat flux vector q_j as

$$q_j = -k \frac{\partial T}{\partial x_j}, \quad \text{with } k = \frac{c_p \mu}{Pr}, \quad (2.15)$$

where Pr denotes the Prandtl number of the fluid. In compact form, Equation (2.10) can be recast as

$$\frac{\partial U}{\partial t} + \nabla \cdot F^c(U) = \nabla \cdot F^v(U, \nabla U), \quad (2.16)$$

where F^c denotes the matrix containing the three Euler flux vectors from the left hand side of Equation (2.10) and F^v the matrix containing the viscous contributions from the right hand side.

2.1.2.2. Incompressible Navier-Stokes Equations

For a fluid of constant density, Equation (2.10) reduces to

$$\begin{aligned} \frac{\partial u_i}{\partial x_i} &= 0, \\ \frac{\partial u_i}{\partial t} + \frac{\partial (u_i u_j)}{\partial x_j} + \frac{1}{\rho} \frac{\partial p}{\partial x_i} &= \frac{\mu}{\rho} \frac{\partial^2 u_i}{\partial x_j^2}, \end{aligned} \quad (2.17)$$

with the associated Poisson equation for pressure derived by taking the divergence of the momentum equation and inserting the continuity condition

$$\frac{\partial^2 p}{\partial x_i^2} = -\frac{\partial u_i}{\partial x_j} \frac{\partial u_j}{\partial x_i} = -\frac{\partial}{\partial x_j} \left(\frac{\partial u_i u_j}{\partial x_i} \right). \quad (2.18)$$

By taking the scalar product of the momentum equation in Equation (2.17), taking advantage of the continuity condition and integrating over a periodic domain Ω , the evolution equation for the contained kinetic energy $E(t) = \frac{1}{2}u_i u_i$ can be derived as

$$\frac{dE(t)}{dt} + 2 \frac{\mu}{\rho} \frac{1}{\Omega} \int_{\Omega} \frac{\partial u_i}{\partial x_j} \frac{\partial u_i}{\partial x_j} dx = 0. \quad (2.19)$$

Note that the non-linear term does not contribute to the energy budget, as it just shifts the kinetic energy between scales. Instead, the only mechanism governing the evolution of the kinetic energy is the viscous dissipation.

2.1.2.3. Incompressible Navier-Stokes Equations in Spectral Space

Most of the computational and theoretical research on the basic turbulence dynamics focuses on the abstraction of incompressible, homogeneous, isotropic turbulence in periodic domains [16, 155]. For these situations, a spectral description of turbulence is highly appropriate, as it allows the examination of turbulent properties as a function of wave number and of the resulting interactions, and as it forms the basis of the most common numerical schemes in basic turbulence research.

For a periodic velocity field in a cubic domain $\vec{x} \in [0, L]^3$, with L “large” compared to largest length scale in turbulence, each component of the velocity can be represented by a three-dimensional Fourier series as

$$u_i(\vec{x}, t) = \sum_{\vec{k}} \hat{u}_i(\vec{k}, t) e^{I\vec{k} \cdot \vec{x}}, \quad (2.20)$$

where I denotes the imaginary unit and the summation occurs over all wave vectors \vec{k} . We drop the temporal dependency in the following for clarity. Defining the Fourier transform as

$$\mathbb{F}_{\vec{k}}\{f(\vec{x})\} = \frac{1}{L^3} \int_0^L \int_0^L \int_0^L f(\vec{x}) e^{-I\vec{k} \cdot \vec{x}} dx^3, \quad (2.21)$$

the expansion coefficients thus become

$$\hat{u}_i(\vec{k}) = \mathbb{F}_{\vec{k}}\{u_i(\vec{x})\} = \frac{1}{L^3} \int_0^L \int_0^L \int_0^L u_i(\vec{x}) e^{-I\vec{k} \cdot \vec{x}} dx^3. \quad (2.22)$$

Transforming the continuity condition of Equation (2.17) yields

$$\mathbb{F}_{\vec{k}} \left\{ \frac{\partial u_i}{\partial x_i} \right\} = I k_i \hat{u}_i = I \vec{k} \cdot \vec{\hat{u}} = 0, \quad (2.23)$$

2. Turbulence Simulation

indicating that both vectors are orthogonal in wave space. Applying the transform term by term to the momentum equation in Equation (2.17) results in:

$$\begin{aligned}
 \mathbb{F}_{\vec{k}} \left\{ \frac{\partial u_i}{\partial t} \right\} &= \frac{\partial \hat{u}_i}{\partial t}, \\
 \mathbb{F}_{\vec{k}} \left\{ \frac{\mu}{\rho} \frac{\partial^2 u_i}{\partial x_j^2} \right\} &= -\frac{\mu}{\rho} k^2 \hat{u}_i, \\
 \mathbb{F}_{\vec{k}} \left\{ \frac{1}{\rho} \frac{\partial p}{\partial x_i} \right\} &= I \frac{k_i}{\rho} \hat{p}, \\
 \mathbb{F}_{\vec{k}} \left\{ \frac{\partial (u_i u_j)}{\partial x_j} \right\} &= \hat{G}_i(\vec{k}, t),
 \end{aligned} \tag{2.24}$$

with $k^2 = \vec{k} \cdot \vec{k}$. Following Pope [167], the pressure term cancels with $-\hat{G}^{\parallel}$, the component of \hat{G} in the direction of the wave vector. The remaining perpendicular component can be expressed as:

$$\begin{aligned}
 \hat{G}_j^\perp(\vec{k}, t) &= \mathbb{F}_{\vec{k}} \left\{ \frac{\partial (u_j u_k)}{\partial x_k} \right\} = I k_k \mathbb{F}_{\vec{k}} \{ u_j u_k \} \\
 &= I k_k \mathbb{F}_{\vec{k}} \left\{ \left(\sum_{\vec{k}'} \hat{u}_j(\vec{k}') e^{I \vec{k}' \cdot \vec{x}} \right) \left(\sum_{\vec{k}''} \hat{u}_k(\vec{k}'') e^{I \vec{k}'' \cdot \vec{x}} \right) \right\} \\
 &= I k_k \sum_{\vec{k}'} \sum_{\vec{k}''} \hat{u}_j(\vec{k}') \hat{u}_k(\vec{k}'') \mathbb{F}_{\vec{k}} \left\{ e^{I(\vec{k}' + \vec{k}'') \cdot \vec{x}} \right\} \\
 &= I k_k \sum_{\vec{k}'} \sum_{\vec{k}''} \hat{u}_j(\vec{k}') \hat{u}_k(\vec{k}'') \delta_{\vec{k}, \vec{k}' + \vec{k}''} \\
 &= I k_k \sum_{\vec{k}'} \hat{u}_j(\vec{k}') \hat{u}_k(\vec{k} - \vec{k}').
 \end{aligned} \tag{2.25}$$

Combining Equations (2.24) and (2.25) results in the spectral evolution equation for the modal coefficients of one component of the velocity field in wave space

$$\left(\frac{\partial}{\partial t} + \frac{\mu}{\rho} k^2 \right) \hat{u}_j(\vec{k}, t) = -I P_{jk}(\vec{k}) k_l \underbrace{\sum_{\vec{k}'} \hat{u}_j(\vec{k}', t) \hat{u}_k(\vec{k} - \vec{k}', t)}_{T_j(\vec{k}, t)}, \tag{2.26}$$

with the operator P that projects onto the plane orthogonal to \vec{k} as

$$P_{jk}(\vec{k}) = \delta_{jk} - \frac{k_j k_k}{k^2}, \tag{2.27}$$

and $T_j(\vec{k}, t)$ called the non-linear transfer operator. Equation (2.26) thus describes the incompressible Navier-Stokes equations in spectral space. The terms on the left hand side only contain modal content at wave vector \vec{k} , i.e. the temporal derivative and the viscous terms do not couple different scales. This coupling is introduced by the non-linear term on the right hand side, as discussed in Section 2.1.1. It contains velocity modes at wave vectors \vec{k}' and \vec{k}'' with $\vec{k}' + \vec{k}'' = \vec{k}$, i.e. only a subset of the total occurring wave vectors [30]. The triads formed by the three interacting wave vectors are separated into local and non-local interactions, depending on their relative location in spectral space [63]. In physical space, local interactions are those among structures of comparable length scale, while non-local contributions stem from the interactions of different-sized eddies.

The evolution equation for the kinetic energy of a wave vector $E(\vec{k}, t)$ can be derived from Equation (2.26) by multiplication with the complex conjugate $\hat{u}_j^*(\vec{k}, t)$ and $\frac{1}{2}$, leading to

$$\left(\frac{d}{dt} + 2\frac{\mu}{\rho}k^2 \right) E(\vec{k}, t) = \hat{T}^*(\vec{k}, t), \quad (2.28)$$

with the modified transfer term \hat{T}^* . When summing over all wave modes \vec{k} , the sum $\sum_{\vec{k}} \hat{T}^*$ is equal to zero, i.e. this term does not contribute to the overall balance of kinetic energy. Thus, the change of the total kinetic energy is only governed by the viscous dissipation, while the non-linear term governs its distributing among the modes (see Sections 2.1.1 and 2.1.2.2).

2.2. A Model Turbulence Problem: The Taylor-Green Vortex

The three-dimensional, viscous Taylor-Green vortex flow (TGV) is a classical example of periodic, decaying turbulence. It has been analyzed extensively both theoretically and numerically to understand transition and turbulence and to evaluate numerical schemes. Its inviscid version is conjectured to develop a vorticity singularity in finite time, but the theoretical and numerical evidence were deemed inconclusive [183]. We describe its features here briefly, as it will be used as a benchmark problem in later chapters.

Originally proposed by [190] as a mechanism of producing a scale cascade for the incompressible Navier-Stokes equations, the kinetic energy of the TGV is initially contained in 8 Fourier modes on the wavenumber shell with radius $\sqrt{3}$. Starting from these laminar initial conditions, the ordered large scale structures interact, break down and undergo transition into a turbulent field with a wide range of temporal and spatial vortical scales. Beyond a Reynolds number of $Re_{crit} \approx 1000$, a turbulent kinetic energy spectrum with the expected $k^{-\frac{5}{3}}$ slope in the inertial subrange develops and a nearly

2. Turbulence Simulation

isotropic velocity field is found beyond $t = 7s$ [73]. Following Brachet [29], the velocity and length scales of this problem are of order one, so the associated Reynolds number is defined as $Re = \frac{1}{\nu}$, with ν being the kinematic viscosity. The dissipation rate of kinetic energy peaks at around $t = 9s$, independent of the Reynolds number (for $Re > Re_{crit}$). Since no kinetic energy production at the large scales exists due to the absence of a mean shear or forcing term, the vortical structures finally decay and the energy cascade subsides.

The initial flow conditions in a triple periodic box of length 2π are given by

$$\begin{aligned}
 \rho &= \rho_0 = 1, \\
 u_1 &= V_0 \sin(x_1) \cos(x_2) \cos(x_3), \\
 u_2 &= -V_0 \cos(x_1) \sin(x_2) \cos(x_3), \\
 u_3 &= 0, \\
 p &= p_0 + \frac{\rho_0 V_0^2}{16} (\cos(2x_1) + \cos(2x_2)) (\cos(2x_3) + 2), \quad (2.29)
 \end{aligned}$$

where ρ, u_i with $i = 1 \dots 3$ and p denote the density, the components of the velocity vector and the pressure, respectively and the velocity scale V_0 typically set to 1. The relationship for pressure is obtained from the solenoidal velocity field by solving Equation (2.18). Fig. 2.5 shows the development of this flow at $Re = 5000$ from an initial mono-scale state to a full multiscale problem with final dissipative decay. As noted by [29], the initial development of the flow is governed by near-inviscid roll-up and stretching of the anisotropic large scale vortical structures. At about $t = 3s$, an onset of instability is observed, which leads to the successive breakdown of the coherent structures. This breakdown is complete after about $t = 7s$, when the velocity field becomes nearly isotropic. Due to lack of large scale kinetic energy production, the flow decays self-similarly for $t \rightarrow \infty$.

Figure 2.6 *left* depicts the spectrum of the kinetic energy after the transitional phase. The spectrum clearly shows the multiscale nature of this flow as well as the characteristic inertial subrange region connecting the large and small scales. The plot in Figure 2.6 *right* emphasizes the non-stationary behavior of this flow by depicting the evolution of the kinetic energy dissipation through the development of the scale cascade, from the laminar initial state through the transition to turbulence and the final viscous decay. The total kinetic energy and the associated energy dissipation rate are given by

$$k := \frac{1}{16\pi^3} \int_0^{2\pi} \int_0^{2\pi} \int_0^{2\pi} \vec{v} \cdot \vec{u} \, d\vec{u}, \quad \epsilon := \frac{2\nu}{8\pi^3} \int_0^{2\pi} \int_0^{2\pi} \int_0^{2\pi} \vec{\nabla} \vec{u} : \vec{\nabla} \vec{u} \, d\vec{x}. \quad (2.30)$$

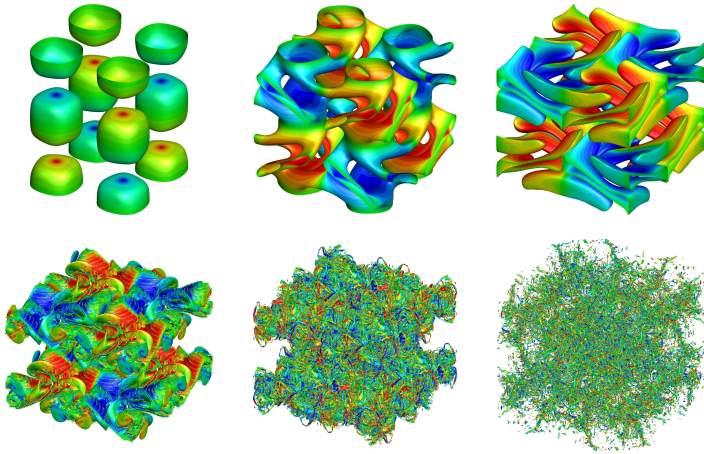


Figure 2.5.: Temporal evolution of the Taylor-Green vortex, from upper left to lower right at time $t = 0.4s, 1.4s, 2.7s, 5.9s, 8.9s$ and $15.5s$ Shown are contours of vorticity, colored by relative helicity.

Due to its easily reproducible initial and boundary conditions yet complex physical behavior, the Taylor-Green vortex flow is a prototypical case the study of turbulence. It is a widely used benchmark for both DNS and LES simulations (see e.g. [28, 60, 69, 73]). Orszag [154] sums up the rationale for the prominence of the TGV in the numerical community:

“In addition to the fundamental fluid dynamical interest in the development of the Taylor-Green vortex, the flow is a most convenient one on which to debug and perform tests of sophisticated three-dimensional numerical hydrodynamics simulation codes.”

2. Turbulence Simulation

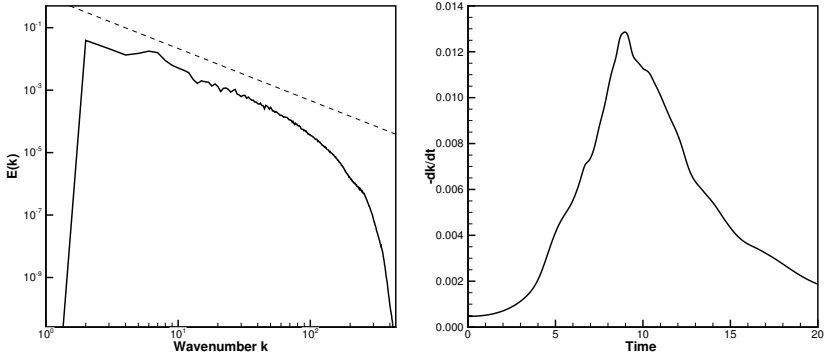


Figure 2.6.: Integral quantities of the Taylor-Green vortex flow.

Left: Spectrum of kinetic energy for $Re = 5000$ at $t = 9.0$, dashed line: $k^{-5/3}$ slope.

Right: Temporal evolution of the rate of kinetic energy dissipation for $Re = 1600$.

2.3. Numerical Simulation Strategies for Multiscale Flows

Due to the complexities of the multiscale nature outlined in Section 2.1, the simulation of turbulent flows poses some unique challenges, not only from a numerical, but even from a conceptual standpoint. In this section, we briefly give an overview of the classical strategies and continue with a deeper discussion of LES in Section 2.4.

2.3.1. DNS

The Direct Numerical Simulation (DNS) aims at finding an exact solution to the full incompressible or compressible Navier-Stokes equations in physical or spectral space (Equations (2.10), (2.17), (2.26)). An often overlooked implicit premise of this approach is the validity of the continuum assumption at the smallest scale level, where large local Knudsen numbers can occur [88]. However, this assumption is often made, and conclusive evidence to the contrary is still lacking.

By design, in DNS, no modeling error is introduced, however, approximation errors and the sensitivity to perturbations discussed in Section 2.1.1 may influence the solution. Clear advantages of a DNS strategy are the availability of the full spatial and temporal

information of the solution, while the numerical costs restrict its application to flows of low complexity. The major advantage from a simulation perspective is the (approximate) independence from the underlying numerical scheme, i.e. if the resolution requirements dictated by the physics (the Reynolds number) and the numerics (the requirements to resolve the smallest occurring scales) are met, the choice of the numerical discretization becomes arbitrary. Thus, from a numerical standpoint, a DNS is driven by the search for the most efficient and accurate numerical solvers.

2.3.2. RANS

Whereas DNS resolves all the scales of turbulent motion, the RANS (Reynolds-Averaged Navier Stokes) approach is situated at the opposite end of the resolution spectrum. This approach abandons the attempt to resolve the scales of motion, but assumes the motion to be random about a mean and thus adopt a statistical treatment. Reynolds [173] decomposed the flow field into a mean Φ_i and fluctuating component ϕ'_i of a variable ϕ_i as

$$\begin{aligned}\Phi_i &= \lim_{T \rightarrow \infty} \frac{1}{T} \int_0^T \phi_i(t) dt, \\ \phi'_i &= \phi_i - \Phi_i,\end{aligned}\tag{2.31}$$

which is valid as long as a wide scale separation between the averaging period T and the time scale of the variation of the mean exists. Applying this averaging operation to the incompressible Navier-Stokes equations yields their RANS formulation (details and derivation found e.g. in [204]):

$$\begin{aligned}\frac{\partial U_i}{\partial x_i} &= 0 \\ \frac{\partial U_i}{\partial t} + U_j \frac{\partial U_i}{\partial x_j} + \frac{1}{\rho} \frac{\partial P}{\partial x_i} &= \frac{1}{\rho} (\overline{\sigma_{ij}} - \rho \overline{u'_i u'_j}),\end{aligned}\tag{2.32}$$

where capital letters denote the mean component and the overline denotes the explicit application of the averaging operation in Equation (2.31). $\overline{\sigma_{ij}}$ thus denotes the stress tensor of the mean flow quantities, and $\overline{u'_i u'_j}$ the unclosed Reynolds turbulent stresses. Finding a suitable closure, i.e. a model, for this term is the main challenge of the RANS approach.

2.3.3. Large Eddy Simulation

The idea of filtering (or averaging) the high amount of information contained in a multiscale flow to reduce complexity and thus make it computationally tractable can be

2. Turbulence Simulation

translated from the temporal domain (RANS) to the spatial domain (LES). Formally, the LES formulation the Navier-Stokes equations can be derived by applying a spatial filter operator to the equations, leading to an evolution equation for the filtered quantities with an additional unclosed (subgrid) term. Details will be given in Section 2.4. The rationale for solving the spatially filtered equations instead of the full equations is three-pronged:

1. **Computational necessity:** As noted in Section 1.3, the space-time scale resolution of the numerical solution of turbulence must be at least as fine as the continuous problem, i.e. the smallest dynamically active scale must be resolved with the appropriate numerical accuracy. Since this becomes arbitrarily costly, such a DNS resolution remains restricted to low Reynolds numbers [105]. In LES, either an explicitly or implicitly enforced filter width Δ is introduced, which fixes the smallest occurring scale and thus gives direct control over the computational costs.
2. **Structural stability of the filtered solution:** The concept of a solution trajectory and an attractor in phase space has been introduced in Section 2.1.1, where single realizations of a solution are highly sensitive to small scale perturbations, but the general structure of the solution is invariant to them. While this is generally true for the turbulence of the Navier-Stokes equations, it can be shown that the truncated (or filtered) Navier-Stokes equations have attractors that are comparable in their large scale structural layout to those of the continuous Navier-Stokes system [191]. In other words, the DNS solution in phase space and the LES solution in the corresponding truncated space share a number of properties. How large this overlap is depends strongly on the filter width Δ , the subgrid modeling and the numerical realization of the LES approach. This commonality between the two solutions and their attractors is the reason why the average and higher moment properties LES solutions are often in good agreement with their DNS counterparts, and thus, a numerical simulation based on the filtered equations can give meaningful predictions [182].
3. **Universality of the model region:** The scale separation through filtering introduces a need for the incorporation of the subgrid effects back into the filtered formulation. A modeling approach for these small scale properties depends on the assumption of universality of these scales, i.e. their independence from large scale boundary conditions. While this small scale “memory loss” and approach to isotropy is supported by the behavior of homogeneous, isotropic, laboratory-type experiments [16], it immediately loses validity in the presence of boundary layers, where the imposed boundary conditions influence the full range of scales. An

additional underlying assumption for the classical modeling approach is the cascade of kinetic energy, in which the energy content of the scales decreases rapidly with increasing wave number. Thus, only a very small percentage of large scale structures carry the overall dynamics of the flow and thus need to be resolved for a good approximation to the full solution.

Figure 2.7 depicts a model spectrum based on Kolmogorov's understanding of the turbulence cascade. While this view is only strictly valid for homogeneous, isotropic turbulence, it is often applied qualitatively to other high Reynolds number situations as well, where the isotropy of the small scales due to their large separation from the boundary conditions is assumed. Loosely, the wave number range covered by the turbulent scales of motion can be separated into three regions:

- I) The large scale region, where the scales are of a size typically determined by the boundary conditions. These scales introduce kinetic energy into the scale cascade and act as a low-frequency feeding of the system, typically through a mean shear or large scale vortical motion. Dissipative effects are negligible in this range. As these scales are strongly anisotropic and non-universal, they need to be resolved accurately in a LES approach.
- II) In the inertial subrange, the spectrum of the kinetic energy is solely dependent on the dissipation rate ϵ at the small scales (a function of the Reynolds number) and the local wave radius k , following Kolmogorov's law [116, 117]:

$$E(k) \sim \epsilon^{\frac{2}{3}} k^{-\frac{5}{3}}. \quad (2.33)$$

In this region, the dissipation time scale is much larger than the time scale of vortex interaction, and thus, energy is only transferred between scales, but not dissipated. It should be noted that the redistribution is on average down-scale, but backscatter exists. Equation (2.33) stresses that the dynamics of the inertial subrange are not dependent on the large scale feeding mechanism or the boundary conditions, but universal. Thus, for LES, the modeling approach requires the resolution of scales into the inertial subrange, where non-universal effects subside.

- III) With increasing wavenumber, the viscous effects overcome the vortex interactions, thereby imposing a lower limit on the smallest occurring scale η . The high frequency fluctuations lead to isotropy and independence from boundary conditions in this dissipation region. It is important to note that the scale separation between regions I) and III) increases with the Reynolds number according to Equation (1.2), and thus the assumption of isotropic,

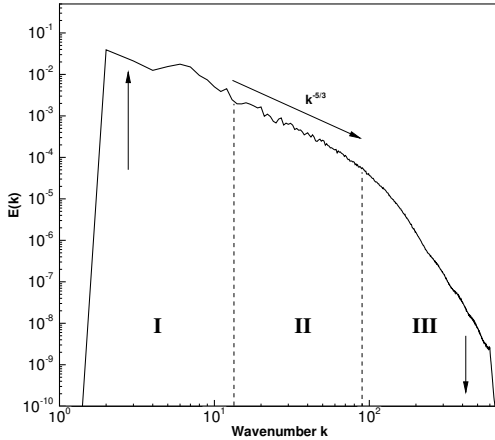


Figure 2.7.: Spectrum of kinetic energy of isotropic homogeneous turbulence (Taylor-Green Vortex at $Re = 5000, t = 11s$). I: Anisotropic large scale energy production, II: Inertial subrange, III: Small scale isotropic dissipation range.

universal small scales amenable to modeling becomes more valid as well. Therefore, two features of the dissipation region support the modeling approach of the unresolved scales: a) Their (approximate) independence from large scale anisotropies and b) their dominant, viscous action, which turns organized, directed kinetic energy into isotropic, chaotic internal energy. One counterexample of this general picture occurs in reacting flows, where molecular mixing and reaction kinetics occur within this region, and thus render it non-isotropic and non-universal [140].

In summary, the rationale behind LES combines the need for reduced computational cost with physical properties that support a resolution of anisotropic large scale structures and the modeling of universal small scale features.

It should be noted that while LES can result in a significant reduction in complexity, the range of anisotropic scales can still make it very challenging in terms of computa-

tional effort. Various alternative, but related methods like URANS (unsteady RANS) and VLES (Very Large Eddy Simulations) as well hybrids like DES (Detached Eddy Simulation) exist, which all aim at further reducing the computational costs. An overview is given in for example in [177].

2.4. Aspects of Large Eddy Simulation

In the previous section, we have given a brief introduction into the rationale behind LES. In the following section, we will provide further details on the method and on some of its important aspects. More general overviews and detailed discussion can be found in e.g. [81, 90, 127, 177].

2.4.1. General Formalism

As stated above, the basis of the LES approach is to solve the conservation equations governing the multiscale problem in a suitably filtered form, with reduced spatial and temporal degrees of freedom. In the following section, we will derive the LES formulation and its different subversions in an abstract manner.

Generally, we can formulate any multiscale problem as

$$P(u) = 0, \tag{2.34}$$

where u is the (full) solution to the multiscale problem and $P(\cdot)$ is the operator, e.g. the Navier-Stokes operator. Equation (2.34) can thus represent any of the conservation laws described in Section 2.1.2, with u representing the vector of conserved variables. Each LES method is by definition a reduction in degrees of freedom of the solution, so the first step is to find a lower-dimensional representation of u in terms of limited degrees of freedom. When thus discretizing this multiscale problem, we first approximate the solution u (by choosing a computational grid or by limiting the number of degrees of freedom)

$$u \approx \bar{u}. \tag{2.35}$$

In this first step, a representation of the solution on the computational grid with reduced number of degrees of freedom is sought. Naturally, this automatically results in a truncation error, which describes the differences between the full and reduced-dimension solution $\epsilon_{trunc} = u - \bar{u}$. This operation (denoted by the bar) can be interpreted and implemented either as a projection or more generally as a filter step. The filter type and the filter resolution depends on the choice of the grid and on the choice of how to represent the approximation, e.g. in terms of local or global polynomials or discrete point

2. Turbulence Simulation

values. While the solution is now represented on the grid, the operator itself is naturally also subject to a discretization:

$$P(\cdot) \approx P_h(\cdot), \quad (2.36)$$

which depends strongly on the numerical method (e.g. finite difference (FD), finite volume (FV), finite element (FE)) and the numerical model parameters (e.g. order of the method, stencil choice, numerical flux function). In turn, the approximation of the operator usually introduces an error, which will manifest itself in an approximate, filtered solution \bar{u}_h . Thus, in practice, in an LES, one solves the problem

$$P_h(\bar{u}_h) = 0, \quad (2.37)$$

instead of the multiscale problem (2.34). The natural question to ask is how good the solution \bar{u}_h approximates that of the multiscale problem. This question can be formulated in two different ways:

1. How good does \bar{u}_h approximate u ?
2. How good does \bar{u}_h approximate \bar{u} ?

While both questions are valid, they focus on different aspects of the solution of Equation (2.37). Of course one is typically interested in the answer to question one, i.e. how the simulation result \bar{u}_h including all assumptions and approximations compares to the solution u of the continuous problem. However, as we are dealing with multiscale problems and with their severely under-resolved discretizations, the comparison of u with \bar{u}_h might be unfair due to the large truncation error caused by the inherent grid induced filtering. As stated above, the first step in a discretization $u \approx \bar{u}$ causes a truncation error, which significantly reduces the number of scales represented on the grid. Therefore, it is reasonable to ask how the numerical approximation \bar{u}_h compares to the truncation of the multiscale solution \bar{u} on the same grid, i.e. question two. It should be noted here that the initial selection of a grid (or of the number of degrees of freedom one can afford to compute) thus plays a primary role in what to expect from an LES and that even an error-free numerical discretization cannot reproduce the continuous solution with limited degrees of freedom - at least not in all quantities of interest.

To further discuss question two and to derive the general LES strategies in terms of filtering and modeling approaches, it is possible to introduce a general problem formulation for the filtered solution \bar{u} by (analytically) filtering the whole multiscale problem itself. This is considered the traditional approach to the derivation of the LES formulation [177]. Starting from the continuous multiscale problem in Equation (2.34) again,

we define a mathematical filtering operation with a general filter by $\widetilde{(\cdot)}$ and arrive at

$$\begin{aligned} \widetilde{P(u)} &= 0, \\ P(\widetilde{u}) &= \underbrace{P(\widetilde{u}) - \widetilde{P(u)}}_{:=S}. \end{aligned} \quad (2.38)$$

It should be noted that this filtering process is at the root of each LES formulation, regardless whether it is executed explicitly or implicitly. It is this step that reduces the number of degrees of freedom of the problem and yields a mathematical description of the reduced multiscale problem. A general expression for this one-dimensional spatial filter operation is given by

$$\widetilde{u}(x) = \frac{1}{\Delta} \int_{-\infty}^{+\infty} G\left(\frac{x-\xi}{\Delta}\right) u(x) d\xi, \quad (2.39)$$

where the convolution kernel G is defined by the filter used, and is associated with the filter width Δ . Multidimensional filtering can be achieved in a tensor-product dimension-by-dimension manner. To separate this filter from the filter introduced by the computational grid introduced in Equation (2.35), we indicate this explicit filtering process by $\widetilde{(\cdot)}$. Compared to the original multiscale problem (2.34), the filtered problem (or the LES formulation) contains the additional term

$$S := P(\widetilde{u}) - \widetilde{P(u)}, \quad (2.40)$$

which describes exactly the effect of subfilter scales on the filtered solution \widetilde{u} . Note that the solution in terms of \widetilde{u} requires the modification of the original problem by the addition of the source term S . It is this term, or more precisely the effects of this term, that are the cause and target for a subgrid multiscale model such as e.g. turbulence models. The complexity of the modeling task arises from the fact that the term S depends on the full multiscale solution u via the term $\widetilde{P(u)}$ and thus cannot be determined solely by the filtered solution \widetilde{u} . In other words, while the reduction of the complexity of the problem seems to have been achieved by replacing $\widetilde{P(u)}$ with $P(\widetilde{u})$, the generated source term re-introduces the dependence on the full solution u again. The question of why such an approach is then beneficial at all lies in the basic assumptions of LES described in Section 2.3.3: By choosing a sufficiently wide filter that filters out only the universal scales and retains the anisotropic scales in the resolved solution \widetilde{u} , the resulting source term S becomes universal and mainly dissipative in nature, which allows its replacement by suitable models.

In fluid dynamics, the dependence of the source term on the solution itself is often referred to as the *closure problem* (of turbulence), as an exact closure of this unknown term

2. Turbulence Simulation

is impossible without access to the full solution u . Three basic strategies exist for the closure and filtering strategies of these multiscale problems. To incorporate the effects of a closure formulation into the general formalism, we introduce a suitable model for the subgrid source terms into Equation (2.34):

$$P(u) + M(u) = 0, \quad (2.41)$$

where we have formally added the operator $M(u)$ to denote any type of model as a function of the fully resolved u . In particular, to recover the original multiscale problem Equation 2.34, $M(u) = 0$ must hold, i.e. in a fully resolved setting, the effect of the model must be zero. We introduce this term here to show how the model term appears in the further derivation of the LES formulation.

We now repeat the formal filtering of the whole problem to derive an expression for the filtered solution \tilde{u} :

$$\begin{aligned} \widetilde{P(u)} + \widetilde{M(u)} &= 0, \\ \widetilde{P(u)} + P(\tilde{u}) - P(\tilde{u}) + \widetilde{M(u)} + M(\tilde{u}) - M(\tilde{u}) &= 0. \end{aligned} \quad (2.42)$$

Rearranging yields the LES formulation for Equation (2.41) as

$$\begin{aligned} P(\tilde{u}) + M(\tilde{u}) &= S, \\ S &= -\widetilde{P(u)} + P(\tilde{u}) - \widetilde{M(u)} + M(\tilde{u}). \end{aligned} \quad (2.43)$$

The source term S re-appears as an additional term that incorporates the effects of the subfilter solution u onto the filtered part \tilde{u} . In comparison with the source term in Equation (2.40), a model contribution $M(\tilde{u})$ occurs, which is generally non-zero, even for a consistently defined model.

Following the discussion leading to Equation (2.37), the representation of Equation (2.41) in a numerical scheme is of the form

$$P_h(\widetilde{\tilde{u}_n}) + M_h(\widetilde{\tilde{u}_n}) = 0, \quad (2.44)$$

where the solution \tilde{u} is first filtered by an explicit filter $\tilde{\cdot}$ defined in Equation (2.39). As discussed above, the introduction of a numerical grid generates an additional filter $\widetilde{\cdot}$, acting on the analytically filtered solution. This discretization filter function inherits its properties from the choice of the discretization, and can represent a FD, FV, FE or any other type of consistent discretization strategy. As an example, the FV discretization can be interpreted as a box filter in physical space, where the filter width is given by the cell size and the convolution reduces to an averaging operation.

The numerical scheme itself then introduces an approximation error in the representation of the operators P and M , i.e. the double-filtered solution $\widetilde{\widetilde{u}}$ is advanced in time by inexact operators P_h and M_h , which in turn leads to an approximate solution $\widetilde{\widetilde{u}}_h$, the final result of any computed LES solution.

To put Equation (2.44) into the context of the LES-formulation of the filtered problem in Equation (2.43), we can manipulate Equation (2.44) by addition and subtraction of suitable terms:

$$\begin{aligned}
 P_h(\widetilde{\widetilde{u}}_h) + M_h(\widetilde{\widetilde{u}}_h) &= 0 \Leftrightarrow \\
 P(\widetilde{\widetilde{u}}_h) + M(\widetilde{\widetilde{u}}_h) &= P(\widetilde{\widetilde{u}}_h) + M(\widetilde{\widetilde{u}}_h) - P_h(\widetilde{\widetilde{u}}_h) - M_h(\widetilde{\widetilde{u}}_h) \Leftrightarrow \\
 P(\widetilde{\widetilde{u}}_h) + M(\widetilde{\widetilde{u}}_h) &= P(\widetilde{\widetilde{u}}_h) + M(\widetilde{\widetilde{u}}_h) - P_h(\widetilde{\widetilde{u}}_h) - M_h(\widetilde{\widetilde{u}}_h) \\
 &\quad - \widetilde{P}(u) - \widetilde{M}(u) + \widetilde{P}(u) + \widetilde{M}(u).
 \end{aligned} \tag{2.45}$$

Rearranging the last expression in Equation (2.45) according to the terms in Equation (2.43) yields

$$\begin{aligned}
 P(\widetilde{\widetilde{u}}_h) + M(\widetilde{\widetilde{u}}_h) &= S, \\
 S &= -\widetilde{P}(u) + \widetilde{P}(\widetilde{\widetilde{u}}_h) - \widetilde{M}(u) + \widetilde{M}(\widetilde{\widetilde{u}}_h) \underbrace{- P_h(\widetilde{\widetilde{u}}_h) - M_h(\widetilde{\widetilde{u}}_h) + \widetilde{P}(u) + \widetilde{M}(u)}_{\stackrel{!}{=} 0}.
 \end{aligned} \tag{2.46}$$

Comparing this expression with the LES-formulation in Equation (2.43), i.e. comparing the analytically filtered continuous LES formulation with the actual discretized version, we note that we recover the LES equation in terms of $\widetilde{\widetilde{u}}_h$ if the last four terms on the right hand side cancel out. In that case, Equation (2.46) and Equation (2.43) (repeated here for clarity) read as:

$$\begin{aligned}
 P(\widetilde{\widetilde{u}}) + M(\widetilde{\widetilde{u}}) &= -\widetilde{P}(u) + P(\widetilde{\widetilde{u}}) - \widetilde{M}(u) + M(\widetilde{\widetilde{u}}), \\
 P(\widetilde{\widetilde{u}}_h) + M(\widetilde{\widetilde{u}}_h) &= -\widetilde{P}(u) + P(\widetilde{\widetilde{u}}_h) - \widetilde{M}(u) + M(\widetilde{\widetilde{u}}_h).
 \end{aligned} \tag{2.47}$$

Thus, the discretized and grid-filtered solution reverts to the true solution of the underlying LES problem, i.e.

$$\widetilde{\widetilde{u}}_h = \widetilde{\widetilde{u}}. \tag{2.48}$$

This is however only exact if the marked terms in Equation (2.46) cancel out. A closer look at this general error term reveals that it contains some interesting features. In particular, it allows a distinction between the three different LES strategies in terms of filtering and modeling that exist. To describe these strategies, we start by rewriting this term as

$$\boxed{\widetilde{P}(u) - P_h(\widetilde{u}_h) = M_h(\widetilde{u}_h)}, \quad (2.49)$$

where we have left off the term $\widetilde{M}(u)$, as by initial definition, for a consistent model, $M(u)$ is zero. It should however be noted that a number of commonly used models, among them the classical Smagorinsky model, indeed violate this condition [186]. From this equation, we can now recover the features of the different LES strategies.

2.4.1.1. Implicit Filter and Implicit Modeling

A natural choice is to choose the filter of the multiscale problem $\widetilde{(\cdot)}$ identical to the filter induced by the computational grid $\overline{(\cdot)}$, i.e. *not* to perform an explicit filtering step in addition to the discretization. This is referred to as *implicit filtering*, as this is implicitly part of the discretization process as discussed above. Thus, the discretization combines the effect of these two filter operations into a single one. Consequently, all filters in the error formulation Equation (2.49) are represented by the single filter function $\overline{(\cdot)}$. In addition, a choice is made to introduce no explicit modeling term M , so we can drop the terms relating to the modeling. This reduces Equation (2.49) to

$$\boxed{P(\overline{u}) - P_h(\overline{u}_h) = 0}, \quad (2.50)$$

and analogously the solution equation (Equation (2.48)) to

$$\overline{u}_h = \overline{u}. \quad (2.51)$$

Thus, the requirement for this type of LES (and the source of its error) is to construct a discretization (consisting of both the implicit filtering/projection $\overline{(\cdot)}$ and the discretization properties of P_h) that models the effect of the subgrid scales $\overline{P(u)}$, i.e. the modeling is achieved by tuning the numerical properties and therefore the approximation errors. One feature of this LES strategy is that for $h \rightarrow 0$, both the discretization error in terms of h and the filter width go to zero (not necessarily at the same rate), so that the filtering and the operator can be commuted and the original LES formulation converges to the unfiltered original multiscale problem (Equation (2.34)), and thus

$$\lim_{h \rightarrow 0} \overline{u}_h = u. \quad (2.52)$$

This means that the solution of this approach converges to the DNS solution of the unfiltered problem, which takes full advantage of the available degrees of freedom but makes the establishment of grid convergence in a LES resolution regime impossible, as the underlying problem is defined by the grid itself.

Thus, the modeling approach in this strategy consists of constructing the numerical method in such a way that it models the effect of the subgrid scales. As this modeling approach is implicitly given by the numerical approximation, this strategy is referred to as *implicit filtering with implicit modeling of the subgrid scales*. While the formulation for this strategy was directly derived from the error Equation (2.49), an alternative route is to approach directly from the general multiscale formulation, again noting the implicit filtering and the omission of the model (Equation (2.43)):

$$P(\bar{u}) = P(\bar{u}) - \overline{P(u)}. \quad (2.53)$$

Comparing with the discretized multiscale problem (2.37) gives

$$\begin{aligned} P(\bar{u}) &= P(\bar{u}) - \overline{P(u)}, \\ P(\bar{u}_h) &= P(\bar{u}_h) - P_h(\bar{u}_h), \end{aligned} \quad (2.54)$$

which again results in the conclusion that the term $\overline{P(u)} - P_h(\bar{u}_h)$ has to vanish for $\bar{u}_h = \bar{u}$, as shown above.

2.4.1.2. Implicit Filter and Explicit Modeling

It should be noted that the implicit modeling approach burdens the discretization scheme with two tasks: Being suitable for the correct representation of the resolved parts of the scales, and having a meaningful approximation error for modeling of subgrid terms. If these two tasks are to be separated, an explicit modeling term M can be introduced. Then, Equation (2.49) reduces to

$$\boxed{P(\bar{u}) - P_h(\bar{u}_h) = M_h(\bar{u}_h)}. \quad (2.55)$$

From this expression, it is clear that the discretization and the modeling now together have to balance the subgrid term $\overline{P(u)}$, i.e. that there is a strong interaction of numerics and model. This can be seen by considering an error-free discretization, i.e. the discrete operators are equal to the continuous ones. Thus, dropping the subscript h results in

$$\overline{P(u)} - P(\bar{u}) = M(\bar{u}), \quad (2.56)$$

which highlights the fact that only for this idealized case, the model and the scheme would indeed be independent from each other. This interaction of explicit model and

numerics can be troublesome, as the derivation of explicit closures is usually done independent from any numerical scheme, i.e. for an “ideal” discretization. In practical LES, the resolution of the underlying problem is by definition coarse, and if the model does not perfectly smooth it on the given grid, interactions of numerics and model become unavoidable.

Another interesting aspect of this approach is that grid refinement (and thus a vanishing filter) does not necessarily lead to the DNS result, as the effect of the model for the full solution u comes into play:

$$P(u) - P(u) = M(u) \quad (2.57)$$

If the model is chosen in such a way that $M(u) \neq 0$, i.e. if the model also acts in fully resolved regions, then a refined discretization $h \rightarrow 0$ will not lead to the DNS solution. Instead, a source term of the form $M(u)$ will pollute the original problem. One example of such a model that does not return zero contributions in the fully resolved case but introduces unwanted dissipation is the classical Smagorinsky model [186]. This should be kept in mind, as the most commonly used form of “engineering LES” is indeed an implicitly filtered approach with the classical Smagorinsky model.

2.4.1.3. Explicit Filtering with Explicit SGS Model

For this most general case, an explicit filter step is used for scale separation, and the influence of the subgrid terms is closed again via an explicit modeling term. Thus, the error term remains as derived in Equation (2.49):

$$\boxed{\widetilde{P(u)} - P_h(\widetilde{u_h}) = M_h(\widetilde{u_h})}, \quad (2.58)$$

In this case, if the discretization parameter is driven to a value well below the grid cut-off scale $h \ll \Delta$, the error term becomes

$$\widetilde{P(u)} - P(\widetilde{u}) = M(\widetilde{u}), \quad (2.59)$$

which is exactly the source term S in Equation (2.42). Thus, for $h \ll \Delta$, the solution does not converge to the DNS solution u but to the explicitly filtered solution \widetilde{u} . This is the major advantage of explicit filtering, as the decoupling of the model and the numerical scheme (no dependence on the grid filter or the discretization remains in Equation (2.59)!) allows an independent development and evaluation of both.

In the next section, we will demonstrate this strategy and show the closure with a “perfect” LES model.

2.4.2. The “Perfect” LES model

In a “perfect” LES model, by definition, the model term $M(\tilde{u})$ based on the filtered scales perfectly matches the difference between the filtered operator and the operator applied to the filtered solution, i.e. Equation (2.59). The existence of such a model would thus lead to the “perfect” LES solution. Clearly, no general model that fulfills these properties exists. However, an a posteriori generation of such a model from the full space-time information of a DNS is possible by defining a suitable filter. By analyzing this perfect closure, both the physics of scale dynamics and the coupling and interaction of the exact model and the discretization can be investigated [58, 146]. In this section, we will derive the perfect model equation based on the concepts from Section 2.4.1 and show that by explicit filtering, the solution becomes independent of the discretization.

2.4.2.1. Problem Formulation

The one-dimensional viscous Burgers’ equation (Equation (2.1)) serves again as a simplified model for the non-linear wave interactions and small scale dissipation that characterize turbulent flows. The equation includes all the relevant terms for scale production and removal and reads in advection form as

$$u_t + u u_x - \nu u_{xx} = 0. \quad (2.60)$$

In the following, we will refer to Equation (2.60) as the “ u ”- or DNS-problem. Following the explicit filtering approach to generate a perfect source term independent from numerics, we define the filtered solution as (assuming that the temporal differentiation and the filtering commute)

$$\tilde{u}(x, t) = \int_{-\infty}^{\infty} G(x, y, \Delta) u(y, t) dy, \quad (2.61)$$

where $G(x, y, \Delta)$ is the filter kernel and Δ a general filter width. Applying this operator to (2.60) yields the filtered Burgers’ equation

$$\tilde{u}_t + \widetilde{u u_x} - \nu \widetilde{u_{xx}} = 0. \quad (2.62)$$

However, this formulation does not lend itself to a straight forward discretization due to the non-linear term $\widetilde{u u_x}$, as its evaluation would entail knowledge of the unfiltered quantity $u u_x$ (corresponding to $\widetilde{P(u)}$ in Equation (2.59)). Since only filtered quantities

2. Turbulence Simulation

are available (those in terms of \tilde{u}), we derive the standard LES formulation by rewriting Equation (2.62) as

$$\tilde{u}_t + \tilde{u} \tilde{u}_x - \nu \tilde{u}_{xx} = S(x, t), \quad (2.63)$$

with

$$S(x, t) = (\tilde{u} \tilde{u}_x - \widetilde{u u_x}) - \nu (\tilde{u}_{xx} - \widetilde{u_{xx}}), \quad (2.64)$$

where we did not assume commutation of spatial differentiation and filtering. The source term $S(x, t)$ represents the effect of the subgrid scales $u' := u(x, t) - \tilde{u}(x, t)$ onto the filtered solution \tilde{u} . It is this expression that cannot be computed exactly during a coarse grid simulation and hence has to be closed by an appropriate model. Note that this source term exactly matches the formal definition in Equation (2.38).

2.4.2.2. The Perfect Closure

With the assumption that an exact solution to Equation (2.60) exists, the source term in Equation (2.64) can be evaluated exactly for a given filter definition. This requires of course the availability of the full temporal and spatial solution u . Assuming that such a source is available, we can define the following new problem for $v(x, t)$ (henceforth called the “ v -problem”) as

$$v_t + v v_x - \nu v_{xx} = S(x, t). \quad (2.65)$$

The v -problem shares the same structure as the original LES formulation in Equation (2.63), so for an exact solution of the v -problem (Equation (2.65)), the solution v is identical to the filtered solution of the u -problem (Equation (2.60)):

$$v(x, t) \equiv \tilde{u}(x, t). \quad (2.66)$$

Importantly, a full resolution of the v -problem requires significantly less effort (depending only on the filter width, i.e. the number of scales in v) than the solution of the u -problem, as v is smoother than u due to the inherent regularization through filtering. In this sense, the source term (2.64) constitutes the perfect closure, as the exact solution of the associated v -problem leads to the exact reproduction of the large-scale solution \tilde{u} . In particular, the only parameter in the definition of the source term is the selection of a suitable filter, i.e. no assumptions about the numerical scheme have to be made.

2.4.2.3. LES with Perfect Model

To demonstrate this approach and its advantages, we apply it to the viscous Burgers’ equation with sinusoidal initial and periodic boundary conditions:

$$u(x, 0) = \sin(2\pi x) + 0.5 \text{ for } x \in [0, 1] \text{ and } \nu = 0.003, \quad (2.67)$$

where the exact solution of this problem develops a range of at most K scales (wavenumbers) limited by the viscosity ν . Note that the resulting single shock is not “turbulent”, but it is a suitable model problem with a scale range produced by non-linear interactions and viscous small scale dissipation. For the filter definition, we choose the most natural formulation: a sharp spectral cut-off filter with a cut-off wavenumber $K_c \ll K$, such that waves with wavenumber $k > K_c$ are considered unresolved scales. Thus \tilde{u} (and consequently v) are bandwidth-limited to K_c frequencies. From the source term definition in Equation (2.64), it is also obvious that the maximum range of scales of S is $2K_c$ due to the non-linear term $\tilde{u}\tilde{u}_x$. Consequently, a resolution of at most at most $2K_c$ is required to solve the v -problem exactly, in contrast to K scales for the unfiltered u -problem. This “saving potential” in terms of required degrees of freedom for an exact computation of $\tilde{u} = v$ is

$$\frac{2K_c}{K}, \quad \text{with } K_c \ll K, \quad (2.68)$$

which is one of the three main rationales for the Large Eddy Simulation approach denoted in Section 2.3.3.

Following the method outlined later in Section 3.2, a pseudo-spectral Fourier-based one-dimensional DNS solver without de-aliasing with a 5-stage 4th order Runge Kutta time integrator is used to generate the “exact” DNS solution of the u -problem. The total number of grid points was chosen as $N_u = 1024$, resulting in a resolvable scale band up to $K = 512$ due to the Nyquist criterion. For an end time of $t = 0.25$, this resulted in 7865 time steps based on the advective time step criterion and also ensuring a DNS resolution in time. Figure 2.8 shows the DNS solution u and the filtered solution \tilde{u} at $t = 0.25$. For the spectral filter, a cutoff wavenumber of $K_c = 16$ was chosen. The right part of the figure shows the corresponding energy spectra at time $t = 0.25$, revealing that the DNS resolves all scales down to machine precision and the position of the cut-off within the self-similar scale range.

The corresponding source term is computed from the DNS solution for each Runge-Kutta stage and stored as a space-time matrix of the source $S = S(x, t)$ for the definition the v -problem. Figure 2.9 shows the energy spectra of this source for different times t , confirming the observation that the source consists of at most $2K_c = 32$ waves as required by the filter definition. As a side note, the temporal development of the source term is consistent with the development of the shock structure, as it shows the injection of energy into the higher modes and the near equi-distribution among these modes. With this source term available, the v -problem is now completely defined. Since it is thus independent from the original problem, it can be solved by any discretization.

In a first step, we re-use the same pseudo-spectral framework. Since the source contains 32 modes, $N_v = 64$ grid points are needed for the pseudo-spectral method to correctly represent the source. To focus on the spatial aspects only, we choose the same time step

2. Turbulence Simulation

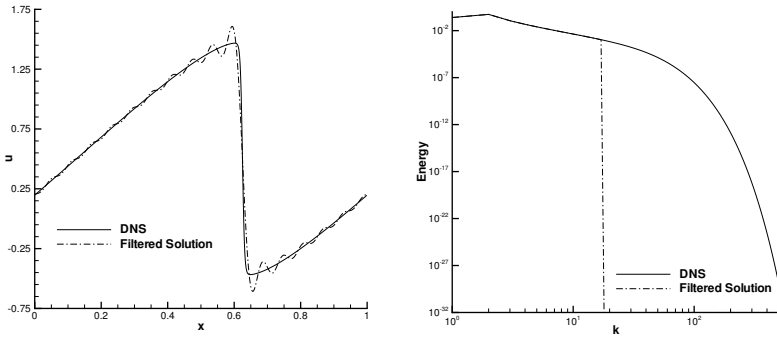


Figure 2.8.: Moving shock solution of the viscous Burgers' equation.
Left: DNS and filtered solution at $t = 0.25$. *Right:* Corresponding energy spectra.

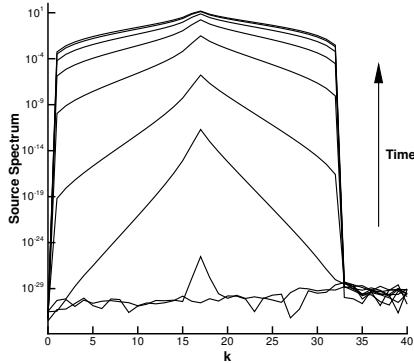


Figure 2.9.: Temporal evolution of the energy spectrum of the source $S(x, t)$.

size for the discretization of the v -problem as for the DNS of the u -problem. This is of course not a general necessity, as the space-time information could easily be interpolated onto the time grid of the v -problem. For the spatial discretization of the v -problem with grid points $N_v < N_u$, the source term is spectrally projected onto the grid with N_v

points.

Table 2.1 shows the convergence of the solution of the v -problem towards the filtered DNS solution \tilde{u} . As expected, the L_∞ -norm of the difference of v and \tilde{u} reaches machine zero (with some roundoff errors) when $N_v \geq 64$, confirming that the exact solution of the v -problem is equal to the filtered DNS solution of the u -problem. Figure 2.10 shows a zoomed-in plot of the different approximate v solutions and Figure 2.11 shows the exact solution of the v -problem with $N_v = 64$ at $t = 0.25$. Thus, these findings corroborate the claim that large scale simulations with suitable model can (theoretically) be both accurate and stable at a fraction of the computational costs.

N_v	32	48	60	64	72
L_∞	2.82E-1	1.94E-2	1.30E-3	1.03E-14	1.62E-14

Table 2.1.: L_∞ -errors with respect to \tilde{u} for different resolutions N_v of the v -problem at time $t = 0.25$ with the pseudo-spectral method.

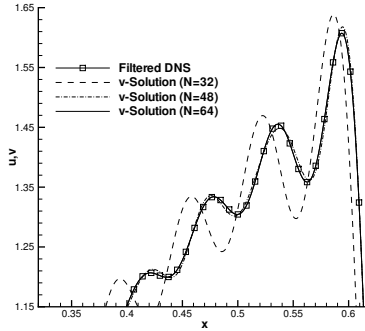


Figure 2.10.: Comparison of different approximate solutions to the v -problem at time $t = 0.25$.

It is worth noting that a computation of the u -problem with only $N_u = 64$ grid points and without any source term, as plotted in Figure 2.12, results in an erroneous solution which is even unstable due to the aliasing errors for this coarse resolution, furthermore

2. Turbulence Simulation

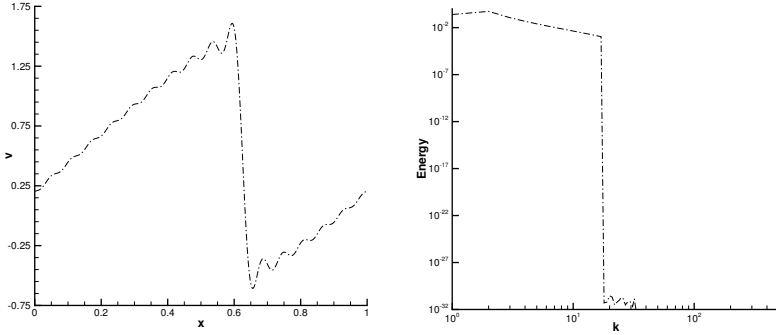


Figure 2.11.: Solution of the v -problem with the pseudo-spectral method.
Left: Solution v computed with $N_v = 64$ grid points at $t = 0.25$.
Right: Corresponding energy spectrum.

confirming the regularizing effect of the model (source) term.

N_v	64	96	128	256
L_∞ FD $\mathcal{O}2$	5.92E-1	1.66E-1	7.85E-2	1.56E-2
EOC	-	3.1	2.6	2.3
L_∞ FD $\mathcal{O}4$	4.05E-1	3.58E-2	4.00E-3	2.41E-4
EOC	-	6.0	7.6	4.0

Table 2.2.: L_∞ -errors with respect to \tilde{u} for different resolutions N_v of the v -problem at time $t = 0.25$ with the FD method.

In a second step we take advantage of the fact that the v -problem is an independent PDE, and thus we are free to select a discretization strategy of our choice to find the solution, a great advantage of explicit filtering which decouples the problem formulation (and thus modeling) from the numerics. To demonstrate this, we discretize the v -problem by central FD schemes of second and fourth order. Table 2.2 shows the results of h -convergence for these simulations. We compute the L_∞ norm of the difference of the FD approximation v_{FD} and the filtered DNS solution \tilde{u} . The results clearly indicate

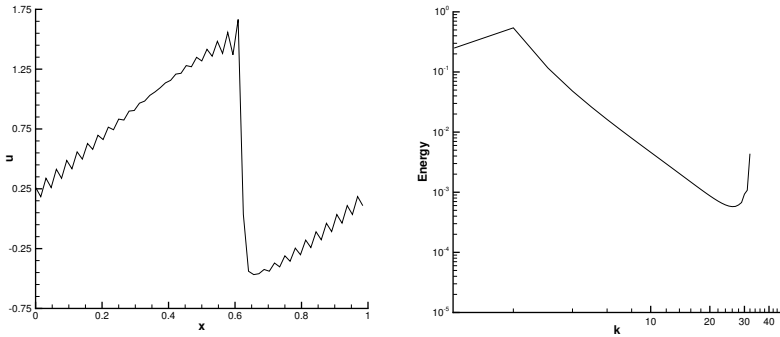


Figure 2.12.: Coarse solution of the u -problem with $N_u = 64$.

Left: Coarse solution u at $t = 0.25$.

Right: Plot of the corresponding energy spectrum.

that the design order of convergence is achieved. Thus we have a convergence towards the solution of the v -problem, which means a grid convergence towards the coarse scale (LES) solution. Furthermore, we can observe that the high order approximation is more efficient in resolving the v -problem, yielding an overall better accuracy on the same grid. Compared to the global method in Table 2.1, the FD approximations give a much larger error for the same number of degrees of freedom, i.e. the faithful resolution of the scales in the filtered problem requires considerably more degrees of freedom for low order than for high order methods.

For completeness, Figure 2.13 shows the results of the fourth order FD solution with 128 grid points and the corresponding spectrum. Note that for this resolution, the Nyquist wave number is 64, while the agreement between the DNS and FD spectra diverge at about $k = 18$. Also, we note that coarsely resolved simulations based on central finite difference scheme without the source terms are prone to aliasing and yield oscillatory and even unstable solutions in these cases, again showing the regularization through the source term.

Thus, the numerical solution of the regularized v -problem can be achieved by any suitable discretization method. The numerical solution will converge to the exact solution of the underlying v -problem for a sufficiently high resolution, keeping in mind that different numerical formulations can differ greatly in terms of approximation quality and thus number of degrees of freedom for an essentially fully resolved DNS of this v -problem.

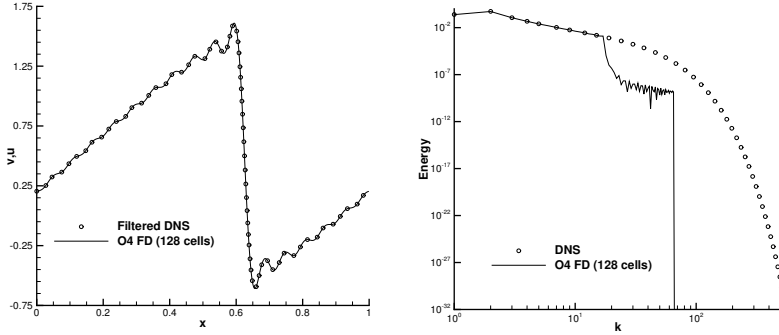


Figure 2.13.: Solution of the v -problem with the FD $\mathcal{O}4$ method.

Left: Solution v_{FD} computed with $N_v = 128$ grid points at $t = 0.25$ and comparison to the DNS results.

Right: Corresponding energy spectra.

This gives a strong indication that high order schemes are well suited for this approach, since they provide higher efficiency per DOF (or a lower number n_{PPW}) for resolved approximations of smooth problems.

Regarding the applicability of this approach to actual turbulence modeling, it is obvious that the exactness of the source term representation is crucial for the potential of success of the method. Since an exact computation of the source term is practically infeasible in almost all cases (and would defy the concept of a LES by relying on the solution of the DNS), the approximation of the source term by a suitable closure model is essential.

In this section, we have demonstrated the most formal LES concept based on inducing an external scale separation by filtering, i.e. regularizing the underlying problem independent from the discretization choice. This approach clearly decouples the numerical properties and the model definition, thereby allowing an independent choice of both: Modeling can be based on physical considerations, while numerics can focus on efficient scale resolution. Since high order discretizations are particularly efficient at the latter, they are highly attractive baseline schemes for this type of LES.

2.4.3. Modeling Strategies

In this section, we will briefly describe typical closure models applicable to the three formal LES approaches outlined in Section 2.4.1.

2.4.3.1. Implicit Models: MILES

One of the first purely implicit LES methodologies (both the filtering and modeling is implicit, see Equation (2.50)) is the so-called MILES (Monotonically Integrated Large Eddy Simulation) approach by Boris et al. [25], with a more recent update given in Grinstein et al. [93]. The base of this method are so-called monotone discretizations, mainly developed for capturing strong compressibility effects (shocks) in a monotone way. A prominent candidate is the flux correction transport (FCT) method developed by Boris and Book [94]. In this method, a high order low dissipation approximation is combined via a non-linear switch with a first order monotone flux in such a way that for well resolved cases, the low dissipation flux with its low numerical damping is used, while in under-resolved cases, the monotone flux becomes dominant to ensure numerical diffusion, guaranteeing an overall monotone approximation. Other monotone methods, such as TVD FV methods or the PPM method are also used in this context [82]. By applying such algorithms primarily designed for capturing shocks to under-resolved turbulence computations, it was found that the non-linear dissipation mechanism inherent in the FCT method provides a form of subgrid scale viscosity. In this case, the leading error term of the discretization acts like a subgrid scale model. For an overview of applications we refer to [25, 93]. It is interesting to note that MILES is often used based on Euler equations only, without the explicit viscous terms of the Navier-Stokes equations. Investigations show that such a MILES computation converges towards a high Reynolds number flow for sufficiently fine grids. This is not surprising, as in the limit of $Re \rightarrow \infty$, the actual form of the dissipation operator becomes less important. Due to the implicit nature of the filtering and the FV character, such algorithms can be directly applied in complex geometries. Investigations show that for sufficient fine grids (i.e. guaranteeing a sufficient resolution of the large scales) MILES results compare well to reference data. The fundamental disadvantage of the MILES approach lies in the origin of the monotonicity of the method, i.e. the limiter. A limiter relates the grid to the evolution of the represented solution and is thus strongly dependent on the grid topology. In this sense, the implicit filtering is a disadvantage, as the filter shape and width is not known and may vary throughout the grid, causing different subgrid dissipations independent from the solution. Furthermore, this methodology does not satisfy the Galilean invariance as a consequence. In summary, such an implicit LES type approach relying on the leading error term as a subgrid scale model with non-linear limiter based dissipation can never

be expected to mimic the missing subgrid scales accurately, but numerical experiments show that large scale motion can be simulated with reasonable accuracy.

2.4.3.2. Implicit Models: ALDM

The Approximate Local Deconvolution Method (ALDM) was introduced by Hickel [97] as a form of implicit LES for incompressible flows. Again, the idea is to use the numerical error terms as a replacement for an explicitly added LES model. Based on a FV discretization, the filter is implicitly given by the grid via the spatial averaging. Deconvolution refers to the inverse of a convolution filter and is thought of as a recovery of small scales from the large scales. Hickel differentiates between a “hard” and “soft” deconvolution, where the first describes the inversion of the filter into the unrepresented scales (obviously, this problem is ill-posed), and the soft deconvolution refers to the recovery of the represented, but not (well) resolved scales. While the soft deconvolution is feasible, it cannot account for the lack of the non-represented dissipation by pure deconvolution alone, but requires an additional dissipative mechanism. Still, this approach allows a certain useful methodology to construct LES models, e.g. Adams et al. [188]. In ALDM, deconvolution is based on a non-linear reconstruction similar to the WENO (Weighted Essentially Non-Oscillatory) philosophy applied to shock capturing. In the first step of the reconstruction process, several different biased stencils are constructed. For each of the reconstruction polynomials, a measure for the oscillations is computed. In the WENO method, the different reconstruction polynomials are combined according to the oscillation indicators in such a way that the smoothest polynomial gets the highest weight. These reconstruction polynomials are used to determine input values for suitable numerical flux functions which typically have a dissipative nature. As an implicit LES approach, the ALDM method tries to control the discretization error term by introducing several free parameters into the numerical flux function as well as into the local WENO type reconstructions. These parameters control the numerical discretization to a certain extent and are used to tune the behavior of the method for under-resolved turbulence simulations. For this, a canonical turbulent benchmark problem, namely the homogeneous isotropic turbulence (HIT) test case, is used. With an optimization approach based on a genetic algorithm, the free discretization parameters are tuned in such a way that the dissipation spectrum for the HIT simulation fits the theory for high Reynolds numbers. ALDM offers basically the same advantages and disadvantages as the MILES approach. A difference to MILES is the introduction of the free parameters which can be used to tune the method. Originally, the ALDM method was developed for incompressible flow. However with this tuning approach, a new parameter set was derived for compressible flows [98]. On the one hand, the free parameters are an advantage as they allow the adaptation of the method to new physics, on the other hand it is obviously a drawback that

the performance of the method relies this heavy on auxiliary parameters. For instance when parts of the flow problem are nearly incompressible and other compressible, the set of parameters is difficult to choose. However, results from literature show that this methodology compares favorable to a lot of standard explicit closures, e.g. [97].

2.4.3.3. Explicit LES Closures

Most of the explicit subgrid scale (SGS) model approaches can be combined with either explicit filtering of the flow variables or an implicit filtering approach. As already discussed in the sections above, explicit filtering has a major impact on the performance of the LES model and is thus not computationally efficient. The advantage of implicit filtering is the lower computational effort as no additional filter operation is needed and in theory all grid resolved scales (up to Nyquist) are used to represent the flow field. It is important to note that with implicit filtering, the subgrid scale model parameters and coefficients must be tuned depending on the actual used discretization and may even depend on the grid topology. An approach based on explicit filtering is obviously free of all those limitations as long as the explicit filter width is large enough in comparison to the grid scale.

2.4.3.4. Explicit Model: Smagorinsky-Lilly

The Smagorinsky-Lilly model is the earliest and most commonly used SGS models based on the eddy viscosity approach. It was developed and expanded by Smagorinsky and Lilly [186], and used by Deardorff in the first published LES [59]. It assumes the instantaneous equilibrium of energy production at the large scales and its dissipation at the small scales and gives a simple relation for the turbulent viscosity:

$$\nu_t = (C_s \Delta)^2 |\bar{S}|, \quad (2.69)$$

where C_s is a tunable model constant, Δ the filter width and \bar{S} the large scale strain rate tensor. The theoretical value for homogeneous isotropic turbulence was found to be $C_s = 0.18$, but it has to be adjusted to the flow conditions and the numerical scheme used. Due to the equilibrium assumption, the model performs poorly outside of isotropic regions, especially in wall-near regions, where a modification by van Driest [68] is added to account for the changing length scale. By construction, the model is always dissipative, even in well resolved and laminar regions and thus allows no backscatter. Due to its simplicity and early availability, this model has been widely used in many flow situations (see e.g. [23]), even when its largest drawback - the inconsistency for well-resolved regions - can play a significant role in the flow physics. Figure 2.14 depicts the influence of the model on a DNS of laminar flow. Clearly, the model fails to regulate itself in

this situation, producing additional dissipation (as a function of its model constant) that falsifies the solution.

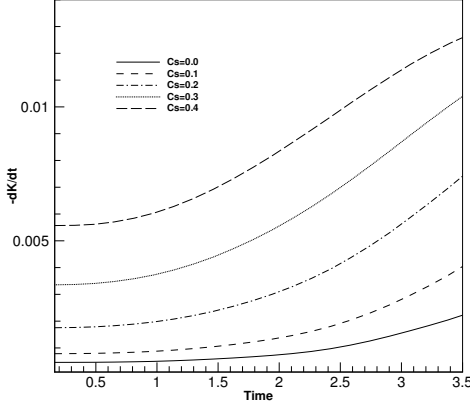


Figure 2.14.: Smagorinsky model for laminar flow. Kinetic energy dissipation rate over time as a function of the model constant C_s .

2.4.3.5. Explicit Model: Dynamic Smagorinsky

The shortcomings of the Smagorinsky model with its a priori fixing of the model constant led to an improved version by Germano et al. [89], the so-called Dynamic Smagorinsky model. The idea is to determine the model parameter C_s continuously during the computation from the smallest resolved scales. This is achieved by applying a (computational) test filter that is wider than the grid filter-width. The “Germano identity” relates the resolved turbulent stresses L_{ij} to the filtered subgrid and sub-testfilter stresses $\widehat{\tau}_{ij}$ and T_{ij} by

$$L_{ij} = T_{ij} - \widehat{\tau}_{ij} \quad (2.70)$$

For both stresses, an eddy viscosity model is assumed, where ν_t is approximated as in the Smagorinsky model (Equation. (2.69)). However, due to the similarity assumption, the models for both stresses share the same model constant C_s . Thus, in combination with

relationship (2.70), this model constant can then be determined for each time and position in space from a comparison of the subgrid and sub-testfilter stresses. This approach is self-contained and thus parameter-free, and is self-adjusting to the flow situation. It allows backscattering and requires no additional wall treatment, while remaining relatively computationally efficient. It has been applied in a wide area of applications [55], however, due to the possibility of negative values of C_s , numerical stability problems can occur [91].

2.4.3.6. Explicit Model: Spectral Vanishing Viscosity

The concept of Spectral Vanishing Viscosity (SVV) was originally introduced by Tadmor [189] to stabilize Fourier-Galerkin discretizations of the shock solution occurring in an inviscid Burgers' equation. The basic idea is to add a spectral viscosity term (given by an amplitude and a specific kernel function) with maximum amplitude at the highest wave number, but vanishing amplitude for low wave numbers. This regularization retains spectral accuracy and satisfies the entropy condition, leading to the occurrence of the correct weak solution. The application of this concept is particularly easy in a global Fourier-based setting, where the modal solution representation can be modified directly. Karamanos and Karniadakis [109] were the first to extend this concept to spectral/hp element methods, where they used polynomial filtering to establish the scale separation. Depending on the filter kernel, the numerical application of the method is relatively cheap compared to more elaborate modeling. SVV can be viewed as a cross between monotone methods like TVD and an exponentially accurate, but unstable spectral discretization [112]. It has been applied successfully to a number of turbulent flows, from channels to bluff body flows [160]. One drawback of the methods remains the choice of the filter kernel, which can significantly influence the solution [115].

2.4.3.7. Explicit Model: Scale Similarity

Scale similarity models were first introduced by Bardina et al. [10], and are based on the assumption that the subgrid stresses close to the cut-off can be extrapolated from the resolved scales near the cut-off. These "largest subgrid scales" can be determined from the subgrid scales $u_i' = u_i - \overline{u_i}$ by filtering as

$$\overline{u_i'} = \overline{u_i} - \overline{\overline{u_i}}, \quad (2.71)$$

so that the subgrid stress tensor τ_{ij} is then closed as

$$\tau_{ij} = \overline{\overline{u_i u_j}} - \overline{\overline{u_i}} \overline{\overline{u_j}} \quad (2.72)$$

Since this modeling relies on the self-similarity assumption in the inertial subrange, it is often not dissipative enough, so that it is generally combined with a more dissipative model like the Smagorinsky model [1]. While the scale-similarity is often used in research with very good results and outperforms the Dynamic Smagorinsky model when coupled with a suitable eddy viscosity model, its relatively high computational cost (the cut-off must lie in the inertial subrange) and the additional filtering make it less numerically efficient.

2.4.3.8. Explicit Model: Interscale Transfer

The interscale transfer model is based on the same principles as the the scale similarity model, but remedies its shortcomings in terms of low overall dissipation [5]. It is based on the idea of balancing the small scale production terms that lead to a build-up of energy near the cut off wavenumber. Three wavenumber bands are identified by progressive filtering of the velocity field u :

$$\begin{aligned} R_1 : u_i^1 &= \widehat{u}_i, \\ R_2 : u_i^2 &= \overline{u}_i - \widehat{u}_i, \\ R_3 : u_i^3 &= u_i - \overline{u}_i, \end{aligned} \tag{2.73}$$

where R_3 denotes the unresolved scales in LES. Given these bands, the quadratic non-linear term can be decomposed into its contributions

$$\frac{\partial u_i u_j}{\partial x_j} = \frac{\partial}{\partial x_j} \sum_m \left(\sum_p u_i^p \sum_q u_j^q \right)^m, \tag{2.74}$$

where the superscripts p and q represent the bands in wavenumber space and m denotes the region affected by the non-linear interaction, not an exponent. Based on physical considerations and DNS data, a model consisting of terms from Equation (2.74) is constructed, that balances the energy transfer to R_2 (R_3 itself is absent) and prevents a buildup. Due to the scale separation idea, this model is a natural candidate for spectral methods. It has been applied successfully in a Fourier pseudo-spectral solver applied to channel flows.

2.4.3.9. Explicit Mode: WALE

The wall-adapted local eddy-viscosity model (WALE) by Nicoud and Ducros [147] is an algebraic model similar to the Smagorinsky model with modifications such that the SGS viscosity is strongly reduced in wall-bounded laminar flows and vanishes towards

the viscous sublayer in turbulent boundary layers. It is therefore capable of producing the laminar to turbulent transition and furthermore recovers the correct wall-asymptotic y^3 -variation of the SGS viscosity and needs no wall damping functions. In the WALE model, the eddy viscosity is modeled as

$$\mu_t = \rho L_s^2 \frac{S_{ij}^d S_{ij}^d}{(S_{ij}^d S_{ij}^d)^{5/2} + (S_{ij}^d S_{ij}^d)^{5/4}}, \quad (2.75)$$

with L_s given by

$$L_s = \min(\kappa d, C_s \Delta), \quad (2.76)$$

where κ is the von Karman constant and d the wall distance. The tensor S_{ij}^d is defined as

$$S_{ij}^d = \frac{1}{2}(\bar{g}_{ij}^2 + \bar{g}_{ji}^2) - \frac{1}{3}\delta_{kk}\bar{g}_{ij}^2, \quad (2.77)$$

where

$$\bar{g}_{ij} = \frac{\partial \bar{u}_i}{\partial x_j}. \quad (2.78)$$

The constant C_w must be tuned for the considered example.

3. Numerics for Scale-Resolving Simulations

From the discussion in Chapters 1 and 2, it has become obvious that the numerical simulation of multiscale flows poses two inter-connected challenges for the discretization: First, the large scale bandwidth requires an accurate resolution of as many waves as possible, while second, the necessary modeling of the subgrid terms demands low (in the case of explicit modeling) or controllable (in the case of implicit modeling) approximation errors. Both requirements are closely connected, as accuracy over the resolved wave range is a direct consequence of the approximation errors, and these errors vanish for consistent discretization in well-resolved situations.

In this section, we will focus on aspects of the spatial discretization for DNS-like resolutions, i.e. this implies the assumption that the underlying solution is smooth and that all dynamically active scales are fully resolved. Due to the higher dimensionality of space and the direct coupling of the smallest resolvable spatial structure to its temporal scale, the resolution requirements in space are the main contributor to the computational cost in terms of degrees of freedom. Also when following the common method-of-lines approach, the resulting semi-discretized (in space) formulation is linear in time, so none of the complexities and increased resolution requirements of the non-linear spatial operator come into play. Thus, the spatial discretization is the determining factor for scale-resolving numerics.

It should be noted that generally, each LES also contains regions and wave number ranges that are well-resolved, so the items discussed below for a DNS situation also transfer to the LES setting.

3.1. The Points per Wavelength Paradigm

As has been discussed in Section 1.1, the number of grid points n_{PPW} required to accurately resolve the smallest occurring scale of a problem has a dominant effect on required number of DOF and thus on the computational cost. Therefore, minimizing n_{PPW} is of prime importance for scale-resolving schemes for all types of multiscale problems. In general, when approximating the spatial operator of differential or the associated integral conservation laws of the form shown in Section 2.1.2, the main complexity (besides the treatment of non-linearities) and source of error is the approximation of derivatives (or the equivalent fluxes over control volume boundaries), which in turn is immediately

related to the approximation of the solution itself. Two distinct concepts exist that directly determine the magnitude of n_{PPW} : A global representation of the solution and the derivatives, or a local one. The notion of globality here refers to the way in which spatial information is processed to evaluate the solution and its derivatives: a global method involves all the degrees of freedom in the domain, e.g. through a global ansatz function, while a local method is based on a subset of these degrees of freedom, where these subsets are then coupled in some appropriate way.

Figure 3.1 depicts this concept by showing the information stencils for three different families of discretization schemes. Without loss of generality, a regular grid is used to highlight the differences. The first of the plots depicts a global (pseudo-spectral) method. Here, the solution is approximated by an ansatz that is global itself, i.e. all the available degrees of freedom contribute to the approximation at each node in the domain. Furthermore, the solution representation and the discretization of the derivative are unique within the domain, i.e. the approximation errors of the derivatives are isotropic with respect to space. Note that a truncation error of the solution may still exist, its form is dependent on the choice of determination of the expansion coefficients. The derivative is then approximated as the derivative of the global ansatz. For derivatives of smooth functions, the associated error in the L_2 norm with N_{Grid} denoting the number of spatial degrees of freedom can be estimated as [164]

$$\|e_{spectral}\|_2 \sim \mathcal{O}\left(\frac{1}{N_{Grid}}\right)^{N_{Grid}} \quad (3.1)$$

If the grid is refined by increasing N_{Grid} , both the grid spacing *and* the order of the error change, thus, the error decreases faster than any finite power of N_{Grid} , leading to “infinite order” or spectral convergence. Thus, the incorporation of all available information leads to the most efficient approximation in terms of invested DOF.

The second subplot in Figure 3.1 shows a discretization based on the FD method. Here, the solution and the derivatives are approximated by locally defined polynomials. The size of the local stencil and the associated weights determine the approximation error as a function of grid spacing as

$$\|e_{FD}\|_2 \sim \mathcal{O}\left(\frac{1}{N_{Grid}}\right)^p, \quad (3.2)$$

where the order p is solely dependent on the choice of the derivative approximation. Thus, since p is fixed, increasing the number of degrees of freedom through N_{Grid} still results in lower error, but the convergence rate is now finite and given by p (so-called geometric convergence). In other words, the behavior of the discretization itself (its accuracy) is no longer governed by the choice of the global N_{Grid} , but by the choice of

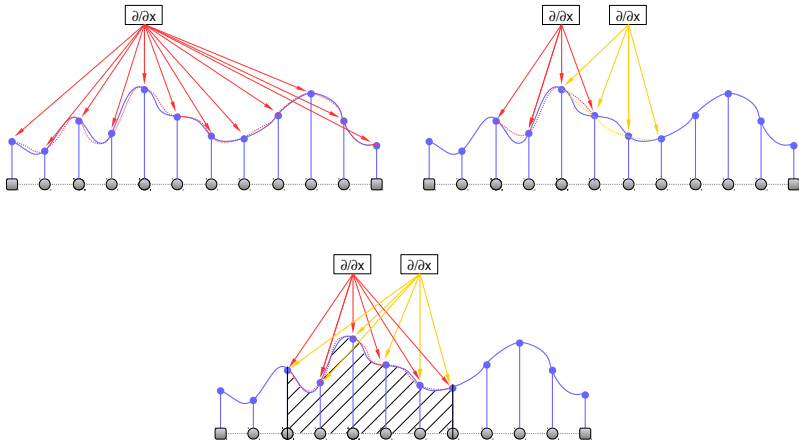


Figure 3.1.: Global vs. local approximation of spatial derivatives. The regular grid is denoted by circles, the boundary points by squares. Blue lines denote the solution, red and yellow lines the approximate solution based on the stencil indicated by the arrows. Vertical black lines indicate a subcell.

p . Note that while the differentiation operator itself is usually chosen as fixed (for inner points), i.e. isotropic, the representation of the derivative is not unique within the domain.

The final subplot represents a subdomain- or element-based discretization type, e.g. continuous or discontinuous FE methods. The spatial domain is divided into non-overlapping elements. Within each of these elements, a polynomial ansatz for the solution and the derivatives is constructed. Depending on the details of the method, these ansatz functions can be low order functions like the hat function, often called “classical” FE, or higher order polynomials, often applied in a tensor product manner in higher dimensions, which leads to the name “spectral FE”. Besides the choice of the basis, another distinguishing feature is the choice of the coupling of the subdomains. In continuous FE, the coupling occurs by enforced C^0 continuity at the subdomain interfaces, i.e. the solution representation is unique there. For discontinuous formulation, the degrees of freedom are purely element-local, i.e. they are double-valued at the boundaries. The coupling is then usually

3. Numerics for Scale-Resolving Simulations

done by a penalty term added to the strong form of the equation, e.g. [62] or a numerical flux function for the surface contributions resulting from a weak formulation e.g. [100]. Within each element, the solution representation is unique, but the discretization of the differential operator (its associated stencil and weights) depends on the location within the domain, i.e. it is generally a one-side biased approximation. For this type of discretization, the global order of accuracy is determined by the choice of the local basis functions. When refining the mesh, h -convergence for a fixed polynomial degree p can be shown. Increasing the local degree of the ansatz p is akin to a N_{Grid} -refinement in global spectral methods and thus leads to spectral convergence, if the coupling is done in a consistent manner.

Of the three different discretization concepts depicted in Figure 3.1, the global approximation incorporates all the available information into the construction of the operators, and thus introduces the lowest approximation error and the smallest number n_{PPW} . The FE and FD methods limit the size of the information stencil by introducing subdomains or incorporating only certain DOF in the local approximation, which results in a higher n_{PPW} .

$\delta \backslash N$	1	2	3	4	5	6	7	8	9	10	cFD O6
0.01	9.61	7.60	6.53	5.91	5.49	5.20	4.98	4.80	4.67	4.55	4.22
0.001	15.98	10.86	8.65	7.48	6.75	6.24	5.88	5.60	5.37	5.19	5.76
0.0001	25.62	15.25	11.35	9.38	8.22	7.43	6.87	6.45	6.13	5.86	7.93
0.00001	41.63	21.26	14.80	11.68	9.89	8.76	7.96	7.37	6.94	6.57	10.92

Table 3.1.: $n_{PPW_{min}}(N, \delta)$ for the Gauss DGSEM and the 6th order compact FD for a given dispersion error δ and the degree N of the local polynomial ansatz. Reproduced with permission from [85].

Figure 3.2 and Table 3.1 examine the dispersion error relations for the scalar one-dimensional transport equation

$$\begin{aligned}
 u_t + a u_x &= 0, \\
 u(x, t) &= e^{i(kx - \omega t)},
 \end{aligned}
 \tag{3.3}$$

with a constant transport velocity a and $\omega = ka$. The equation is discretized by a Discontinuous Galerkin Spectral Element Collocation Method (DGSEM) as a representative of the FE-type methods, a central finite difference scheme and a pseudo-spectral method (as a representative of global methods). For the global method, the dispersion relation remains exact, i.e. no phase error is introduced up to the Nyquist frequency

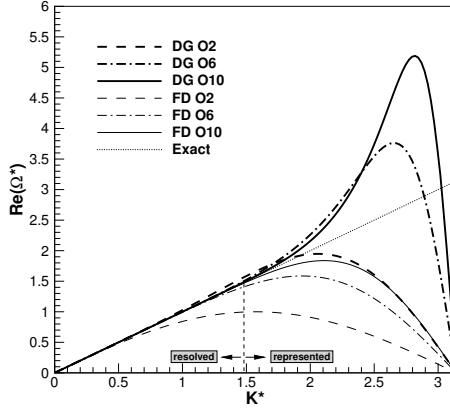


Figure 3.2.: Dispersion relation for the linear transport Equation (3.3) of DGSEM with Gauss nodes, central finite differences and global spectral (exact) scheme. $K^* = \frac{K}{N+1}$ is the normalized wavenumber and $\Omega^* = \frac{\Omega}{N+1}$ is the corresponding modified normalized numerical mode (eigenvalue). For FD, $K^* = K$ and $\Omega^* = \Omega$.

of the grid [76]. This would correspond to a requirement of $n_{PPW_{min}} = 2$, regardless of the number of grid points (or expansion coefficients $N + 1$) in Table 3.1. For the non-global FD and DGSEM methods, $n_{PPW_{min}}$ (for a given dispersion error δ) is clearly a function of the underlying degree N of the local approximation. For both methods, the deviation from the exact dispersion relation moves to higher frequencies and thus results in a reduced numerical cost in terms of n_{PPW} . Note that the overshoot for DGSEM in the marginally resolved region is characteristic of one-sided approximations, due to the element-local approximation of the differentiation operator which leads to a bias towards the cell boundaries. Both Figure 3.2 and Table 3.1 thus support the conclusion that higher order approximations which incorporate more information become more “global” in their approximation character and thus lead to a more efficient approximation for smooth problems in terms of n_{PPW} . This concept of efficiency of the approximation cannot only be expressed in terms of points per wavelength required to resolve the smallest scale, but – in a measure more relevant to practical applications

3. Numerics for Scale-Resolving Simulations

– in the effective usage of the available degrees of freedom. When planning a numerical simulation, the most prominent limiting factor in terms of memory, wall clock time and pre- and post-processing capabilities is the total number of degrees of freedom of the simulation. With each choice of this number comes a theoretically distinguishable range of scales, determined by the associated Nyquist number. Depending on the discretization, only a fraction of these represented scales can be resolved, which – for a non-global method – is only a function of the local approximation order (polynomial degree, stencil size). In Figure 3.3, R defines the ratio of the scales recovered up to a chosen dispersion error $\delta = e_i$ by a central FD discretization of arbitrary order p to the theoretical limit (achievable with global spectral methods). The dispersion relations for these discretiza-

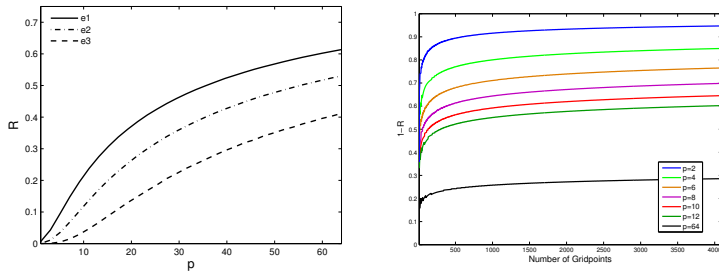


Figure 3.3.: *Left:* Ratio R of resolved scales (limit determined by phase error e_i) to available scales on a $N_{Grid} = 1024$ grid, $e_{i=1,2,3} \in \{0.1, 0.01, 0.001\}$, p : order of central FD discretization
Right: Percentage of modes lost to dispersion error $1 - R$ as a function of p for increasing number of grid points.

tions are given analytically, for details see Appendix D. The left plot of Figure 3.3 depicts the ratio R on a grid with $N_{Grid} = 1024$ nodes for three dispersion errors. Naturally, for the largest dispersion error, the ratio of recoverable modes is highest. Increasing p for a fixed N_{Grid} here corresponds to extending the associated stencil, so a larger p (although large stencils beyond $p \geq 10$ would be impractical) corresponds to a higher ratio of recovered modes. Note that in the region $p \leq 10$, the large slope of R indicates that here the gain from using higher order polynomials is most pronounced. The right subplot of Figure 3.3 shows the percentage of lost modes $1 - R$ (lost to the dispersion error, i.e. not contributing to the resolution) for a fixed error, but a changing grid size N_{Grid} , again as a function of p . While for all p , the amount of lost modes increases linearly with

N_{Grid} (for large N_{Grid}), the general level differs greatly with p . Most importantly, the fraction of resolvable modes only increases through p -refinement, while it deteriorates through h -refinement. Thus, in terms of practical applications where the total number of degrees of freedom is the determining factor, the choice of the discretization directly corresponds to the ratio of recoverable information from these DOF, i.e. the recovered scales per invested DOF dramatically increase for higher order approximations. Note that for a global spectral method with perfect dispersion behavior, $1 - R$ would be 0, regardless of N_{Grid} .

While the discussion in the last paragraph is not directly transferable to other discretization types, it exemplifies the superiority of high order approximations for the resolution of multiscale problems, both in terms of accuracy and computational efficiency. It should be noted that the term computational efficiency has been used rather loosely here to refer to the number of required degrees of freedom to resolve a wave length, but not to the *cost* associated with the numerical algorithm for providing the approximation. In fact, the cost of evaluation a high order discretization is significantly larger in terms of operation count as that of a low order discretization, mainly due to the fact that more operations on the contributing DOF are necessary. These operations however typically scale as a fixed power of N . For example, a matrix-matrix multiplication of two square matrices of size $N \times N$ requires N multiplications and $N - 1$ additions for each of the N^2 entries, leading to $N^2(2N - 1)$ total operations. From Equation (3.1), the error of a global method scales spectrally as $(\frac{1}{N})^N$, so the gain in accuracy can outweigh the operation cost. Clearly, operation count is by far not the only factor determining the numerical efficiency of a practical implementation of any method, but it gives an indication that global or high order methods can be efficient, even in terms of wall-clock times.

Figure 3.4 supports this claim by showing the temporal evolution of the dissipation rate of the Taylor-Green vortex flow (Section 2.2) for different choices of approximation order N for a DGSEM scheme, compared to a DNS solution. Details of DGSEM will be discussed later in Section 3.3.2, the important aspect here is that they allow an arbitrary combination of number of elements and local polynomial ansatz degree N , so that the total number of DOF can be kept constant while changing the underlying discretization. The required wall clock time is indicated. All computations were run with the same DOF load per core to minimize the influence of parallelization. The $\mathcal{O}(2)$ scheme with 64^3 DOF ($N = 1, 32$ Cells) has a very low wall clock time, but is overly dissipative and misrepresents the physics. In other words, the very high n_{PPW} requirement (or the very small resolved wavenumber band) of this scheme is too limiting to capture the essential physics for the given total number of DOF. On the other hand, the $\mathcal{O}(16)$ scheme with 64^3 DOF ($N = 15, 4$ Cells) requires significantly more CPU time for the same number

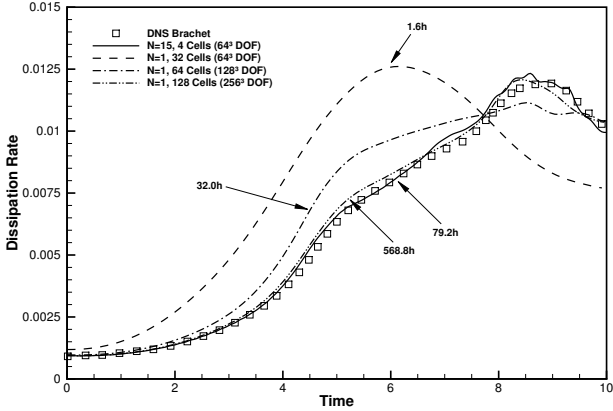


Figure 3.4.: Dissipation rate $-\frac{dk}{dt}$ of the kinetic energy of the Taylor-Green Vortex at $Re = 800$. Results for the DNS data taken from Brachet [29]. The required wall-clock time for each computation is indicated in $[h]$.

of DOF (also suffering from the stringent time step restriction), but resolves most of the relevant scales and is in very good quantitative agreement with the DNS result with 384^3 DOF. Increasing the number of elements for the $\mathcal{O}(2)$ scheme results in convergence towards the DNS result, but the associated increase in wall clock time to achieve comparable accuracy as the $\mathcal{O}(16)$ scheme makes this approach highly ineffective, rendering it about 7 times slower than the high order computation. Note that the required number of degrees of freedom for this result increases from 64^3 to 256^3 , which corresponds to a factor of 4 in one dimension. This fits well with the n_{PPW} criteria for low and high order DGSEM listed in Table 3.1, assuming an asymptotic extension to higher N . In a companion plot, figure 3.5 compares the spectra of kinetic energy for the TGV at $t = 9s$. Again, the total amount of DOF is limited to 64^3 . A DNS solution serves as a reference. Although each computation has nominally the same spatial resolution, the computed spectra show a clear convergence towards the DNS result for increasing N . This is in accordance with the lower PPW requirement of high order discretizations, thereby demonstrating the better scale resolving capabilities per DOF for high order methods.

In this section, we have demonstrated the importance of an efficient numerical discretiza-

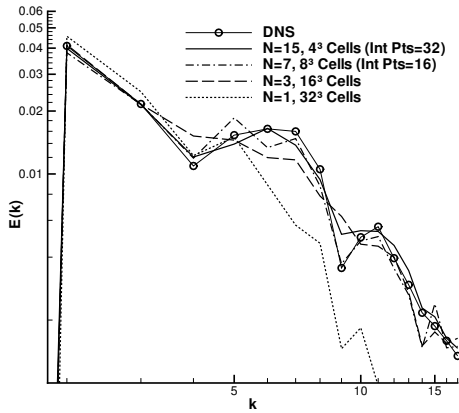


Figure 3.5.: Taylor-Green Vortex at $Re = 1600$. Comparison of the spectra of kinetic energy for $N = 1$, $N = 3$, de-aliased $N = 7$ and de-aliased $N = 15$ solution. All discretizations with a total of 64^3 DOF, except DNS.

tion, expressed in terms of points per wavelength n_{PPW} , for the resolution of multiscale problems. Due to their spectral error behavior, global methods are superior in this aspect, but due to their limitations not always flexible enough for practical applications. FE-type methods or spectral element-type methods with a local high order solution representation are thus the best alternative for efficient scale-resolving numerics. In the next two Sections 3.2 and 3.3, we will discuss these two approaches in detail.

3.2. Global Spectral Methods

Due to their spectral accuracy as outlined above, approximations to partial differential equations based on a global methods can be highly attractive for specific equations and problems, in particular smooth periodic problems that support the concept of global basis functions. These approaches all share the property that they approximate the solution by a linear combination of orthogonal trial functions which form a complete basis of global,

smooth functions:

$$u(x) \approx u_h(x) = \sum_{k=0}^N \hat{u}_k \phi_k(x), \quad x_0 \leq x \leq x_1, \quad (3.4)$$

with u_h being the approximation to the function u in terms of the expansion coefficients \hat{u}_k and the trial or basis functions $\phi_k(x)$, defined on the whole domain.

The choice of this ansatz is determined by the nature of the problem and the boundedness of the domain; for periodic problems, Fourier trigonometric polynomials are the most popular. For non-periodic but bounded problems, Chebyshev or Legendre polynomials are often the method of choice, while rational Chebyshev functions have also been used [164]. The choice of the basis is reflected in the first part of the name commonly given to the method, e.g. ‘‘Chebyshev-Galerkin Method’’.

The second part of the denomination is determined by the choice of the test function or the method to determine the expansion coefficients \hat{u}_k in Equation (3.4):

- **Galerkin Methods:**

Galerkin methods are the most common representative of a projection approach, where the residual $R(x) = u - u_h$ projected onto a set of test functions ψ_k chosen identical to the trial functions ϕ_k is forced to vanish, i.e. the first $(N + 1)$ terms of the spectral representation of $R(x)$ are zero:

$$(R, \psi_i) = \int_{x_0}^{x_1} \left(u - \sum_{k=0}^N \hat{u}_k \phi_k(x) \right) \psi_i dx = 0, \quad \psi_i = \phi_i, \quad i = 0, \dots, N. \quad (3.5)$$

One interpretation of this approach is the ‘‘error distribution principle’’, which denotes the fact that the first non-zero contribution to the residual error can be driven to arbitrary high modes by increasing N [164]. Since the Fourier and Chebyshev coefficients decrease exponentially fast (and the residual is assumed to be smooth), the error over the whole domain rapidly decreases with N . The more common denomination for Equation (3.5) is the variational or weak formulation, as the residuum is to be minimized in an integral (or weak) sense.

By choosing the same number of basis functions (determining the number of expansion coefficients) and test functions (determining the number of available equations), the expansion coefficients \hat{u}_k can be determined from Equation (3.5) by exploiting the orthogonality properties of the basis as

Continuous Fourier Coefficients:
$$\hat{u}_k = \frac{1}{a} \int_{x_0}^{x_1} u \psi_k dx, \quad a \in \mathbb{R}, \quad k = 0, \dots, N. \quad (3.6)$$

The earliest application of spectral Galerkin methods to the solution of PDEs was reported by Silberman in 1954 [184]. While their accuracy and stability made them attractive, the extensive cost associated with the evaluation of non-linear terms reduced their efficiency compared to FD methods [104]. Using again the inviscid Burgers' equation (Equation (2.1)) with periodic boundary conditions in a domain $x \in [-\pi, \pi]$ as an example, a set of Fourier polynomials $\{\phi_k(x) = e^{Ikx}, k \in [0, \dots, N]\}$ as basis and the ansatz $u(x) = \sum_{k=0}^N u_k e^{Ikx}$ with associated continuous orthogonality property

$$\int_{-\pi}^{\pi} \phi_k \phi_l^* dx = \int_{-\pi}^{\pi} e^{Ikx} e^{-Ilx} dx = 2\pi \delta_{kl}, \quad (3.7)$$

inserting the ansatz term by term into the inviscid Burgers' equation yields:

$$\begin{aligned} \frac{\partial u}{\partial t} &= \frac{\partial}{\partial t} \sum_{k=0}^N \hat{u}_k e^{Ikx}, \\ \frac{1}{2} \frac{\partial u^2}{\partial x} &= \frac{1}{2} \frac{\partial}{\partial x} \left(\sum_{k=0}^N \hat{u}_k e^{Ikx} \sum_{l=0}^N \hat{u}_l e^{Ilx} \right) \\ &= \frac{1}{2} \sum_{k=0}^N \sum_{l=0}^N I(k+l) \hat{u}_k \hat{u}_l e^{I(k+l)x}, \\ \Rightarrow \frac{\partial}{\partial t} \sum_{k=0}^N \hat{u}_k e^{Ikx} + \frac{1}{2} \sum_{k=0}^N \sum_{l=0}^N I(k+l) \hat{u}_k \hat{u}_l e^{I(k+l)x} &= 0. \end{aligned} \quad (3.8)$$

Projecting Equation (3.8) onto Fourier modes $0 \leq m \leq N$ and taking again advantage of the orthogonality property (Equation (3.7)) results in an expression for the temporal evolution of the modal expansion coefficients \hat{u}_m

$$\begin{aligned} 2\pi \frac{\partial \hat{u}_m}{\partial t} &= \frac{1}{2} \int_{-\pi}^{\pi} \sum_{k=0}^N \sum_{l=0}^N I(k+l) \hat{u}_k \hat{u}_l e^{I(k+l)x} e^{-Imx} dx \Leftrightarrow \\ \frac{\partial \hat{u}_m}{\partial t} &= \frac{1}{2} \sum_{k=0}^N \sum_{l=m-k}^N I(k+l) \hat{u}_k \hat{u}_l \Leftrightarrow \\ \frac{\partial \hat{u}_m}{\partial t} &= \frac{1}{2} \sum_{l+k=m}^N I(k+l) \hat{u}_k \hat{u}_l. \end{aligned} \quad (3.9)$$

Equation (3.9) shows that the non-linear term results in the double sum $\sum \hat{u}_k \hat{u}_l$ (also called convolution sum), which introduces an operation count that scales as $\mathcal{O}(N^2)$. For high N , this becomes prohibitively expensive, and puts the global Galerkin methods at a clear disadvantage when compared to for example FD with $\mathcal{O}(N)$ operations for the non-linear term. This led to the development of collocation or pseudo-spectral methods, primarily by Orszag [152].

- **Collocation Methods:**

In collocation or pseudo-spectral methods, the test function ψ becomes the Dirac delta function, i.e. the residual $R(x)$ does not vanish in an integral, but in a pointwise sense at the so-called N collocation points $x_j = \frac{2\pi j}{N}$. The associated *discrete* orthogonality property derived from the continuous expression (Equation (3.7)) by numerical integration with the trapezoidal rule [27] becomes

$$\phi_k^T \phi_l = \sum_{j=0}^{N-1} e^{I x_j (k-l)} = \begin{cases} N & \text{if } k-l = mN, m = 0, \pm 1, \pm 2, \dots \\ 0 & \text{otherwise.} \end{cases} \quad (3.10)$$

The general idea of the pseudo-spectral approach is to compute all non-linear terms in a collocative manner in physical space, but all derivatives in spectral or modal space. Returning to the inviscid Burger's equation as an example again, the coefficients of the interpolating Fourier polynomial of the solution $u(x)$ are determined by

$$\begin{aligned} \text{Discrete Fourier coefficients: } \tilde{u}_k &= \frac{1}{aN} \sum_{j=0}^{N-1} u(x_j) e^{-I k x_j}, \\ k &= -\frac{N}{2}, \dots, \frac{N}{2} - 1, \end{aligned} \quad (3.11)$$

with the associated interpolating polynomial given by

$$\text{Spectral Interpolant: } I_N(u(x)) = \sum_{k=-N/2}^{N/2-1} \tilde{u}_k e^{I k x}, \quad I_N(u(x_j)) = u(x_j). \quad (3.12)$$

Here, I_N indicates the interpolation and the tilde denotes that the coefficients are determined by a numerical approximation of the integral in Equation (3.6), not the exact integral. Depending on the form of the convective term of the Burgers' equation (advection form $u \frac{\partial u}{\partial x}$ vs. conservative form $\frac{1}{2} \frac{\partial u^2}{\partial x}$), the order in which

the non-linear terms are evaluated differs, but the basic principle remains the same. For the conservative form, the spatial derivative of its spectral interpolant at the collocation node x_j becomes

$$\begin{aligned} \frac{\partial u^2(x_j)}{\partial x} &= \frac{\partial}{\partial x} I_N (u(x_j)^2) = \sum_{k=-N/2}^{N/2-1} Ik\tilde{v}_k e^{Ikx_j}, \\ \tilde{v}_k &= \frac{1}{aN} \sum_{j=0}^{N-1} u^2(x_j) e^{-Ikx_j}. \end{aligned} \quad (3.13)$$

For the advection form of the non-linear term, this reduces to

$$\begin{aligned} u(x_j) \frac{\partial u(x_j)}{\partial x} &= I_n \left(u(x_j) \frac{\partial}{\partial x} u(x_j) \right) = u(x_j) I_N \frac{\partial}{\partial x} u(x_j) \\ &= u(x_j) \sum_{k=-N/2}^{N/2-1} Ik\tilde{u}_k e^{Ikx_j} \end{aligned} \quad (3.14)$$

Thus, for both forms, the differentiation is achieved in a spectral manner, but the evaluation of the non-linear term is done in a collocative manner on the physical grid. This exploitation of the duality of the physical and spectral representation gave the method the name *pseudospectral*. The drawback of this last step is the introduction of aliasing errors, first noted in [165] (but not labeled as such) and remedied by filtering the upper half of the modes, which was refined by Orszag to the 2/3-rule [153]. The origin of this error stems from the difference between the convolution and following projection (Equation (3.9)) and the collocation approach for the non-linear term. Returning to Equation (3.11), the inverse discrete transform to obtain the nodal values at location x_j from the discrete Fourier coefficients of two arbitrary functions b and c is given by

$$b(x_j) = \sum_{m=-N/2}^{N/2-1} \tilde{b}_m e^{Imx_j}, \quad c(x_j) = \sum_{n=-N/2}^{N/2-1} \tilde{c}_n e^{Inx_j}, \quad j = 0, 1, \dots, N-1. \quad (3.15)$$

Collocation of the product of these two functions is given by

$$d(x_j) = b(x_j)c(x_j) = \sum_{m=-N/2}^{N/2-1} \sum_{n=-N/2}^{N/2-1} \tilde{b}_m \tilde{c}_n e^{I(m+n)x_j}, \quad j = 0, 1, \dots, N-1. \quad (3.16)$$

Note that this step already introduces the aliasing error, as the range of occurring modes is doubled (through $m+n$), while the number of available expansion coefficients remains N , as the spatial grid only supports N modes. This can be shown by examining the modal content of $c(x)$. The modal expansion coefficients \tilde{c}_k are again given by

$$\tilde{d}_k = \frac{1}{aN} \sum_{j=0}^{N-1} d(x_j) e^{-I k x_j}, k = -N/2, \dots, N/2 - 1. \quad (3.17)$$

Inserting Equation (3.16) into (3.17) and taking advantage of the discrete orthogonality property (Equation (3.10)) leads to

$$\tilde{d}_k = \underbrace{\sum_{m+n=k} \tilde{b}_m \tilde{c}_n}_{\text{Convolution sum}} + \underbrace{\sum_{m+n=k \pm N} \tilde{b}_m \tilde{c}_n}_{\text{Aliasing error}} \quad (3.18)$$

The resulting modes \tilde{d}_k contain two contributions: the convolution sum, resulting from the exact projection of the non-linear term (see Equation (3.9)) and an additional aliasing error.

The summations occurring in Equations (3.11) (the forward discrete fast Fourier transform, FFT) and Equations (3.13) and (3.14) (the backward discrete Fourier transform) can be computed in operations on the order of $\mathcal{O}(N \log(N))$ [54], as opposed to $\mathcal{O}(N^2)$ for the Galerkin method or a direct differentiation via a spectral differentiation matrix. For large N , this reduction in computational cost becomes immense, and it is what makes the pseudo-spectral methods the method of choice for the direct simulation of isotropic, periodic turbulent flows, see e.g. [56, 66, 106–108, 123].

3.2.1. A Pseudo-spectral Code for the Compressible Navier-Stokes Equations

As an example of global spectral methods, a Fourier based pseudo-spectral code for the three-dimensional compressible Navier-Stokes equations in conservation form named *Spex* was developed within this work. It represents the solution (i.e. the conservative variables) at regular interpolation points in a cubic domain. All flux terms are evaluated by collocation on the physical grid, and then transferred to wave space via a highly efficient implementation of the discrete Fourier transform [78]. All spatial derivatives are then computed in wave space, and a backward transform bring them onto the physical grid. The parallelization is achieved by a two-dimensional domain composition which

gives better parallel scaling on $\mathcal{O}(10^3)$ cores than the traditional one-dimensional decomposition. Following the method of lines, once the spatial operator has been evaluated at a time t , the resulting system of ordinary differential equations is advanced in time by an explicit time step with a standard fourth order, five stage Runge-Kutta method [34]. De-aliasing is achieved by a cut-off filter in spectral space according to [152], that removes the inaccurate modes in Equation (3.17). The code was validated by the method of manufactured solution [174] and by comparison with a validated pseudo-spectral code for the incompressible Navier-Stokes equations developed at the Université Catholique de Louvain (UCL) [37]. Figure 3.6 shows the spatial convergence over grid spacing h , measured against an exact solution enforced by an appropriate source term. The spectral behavior of the spatial error is clearly visible at $h \approx 0.8$. Decreasing h further results in two separate regions with distinct scaling as $\sim h^4$ and $\sim h^8$, respectively. These slopes can be attributed to the fact the temporal approximation error dominates over the spatial one once the region of spectral error decay is reached. As the advection time step scales linearly with h and a fourth order temporal scheme was used, a slope of $\sim h^4$ develops. Once the viscous time step restriction which imposes a scaling of $\Delta t \sim h^2$ dominates, the resulting error scales as $\sim h^8$.

Figure 3.7 compares the results for the spectrum of kinetic energy for the Taylor-Green

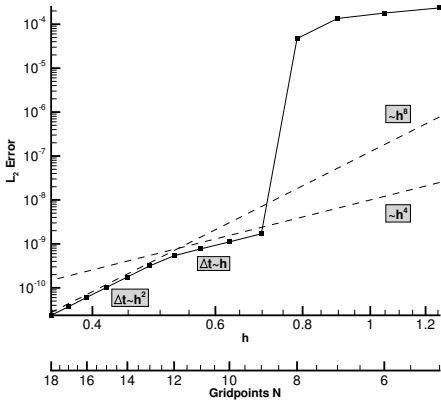


Figure 3.6.: L_2 error of density over grid spacing h for the pseudo-spectral code *Spex*, obtained with the method of manufactured solutions.

3. Numerics for Scale-Resolving Simulations

vortex flow for *Spex*, the incompressible pseudo-spectral code developed at UCL and the DGSEM framework *Flexi* (see Section 3.3.2). The agreement between the DG results and *Spex* is nearly perfect, while a slight deviation exists with regards to the *Louvain* code. This can be attributed to two reasons: i) The kinetic energy spectra provided by the *Louvain* code has been smoothed in a preprocessing step, while the others have not, ii) although the computations with the compressible codes (*Spex* and *Flexi*) were run at a low Mach number of $Ma = 0.1$, slight compressibility effects exist in the solution. The *Spex* code and associated post-processing framework is mainly used to provide high resolution reference results for comparison with DGSEM methods, see e.g. Figures 2.1 and 2.3.

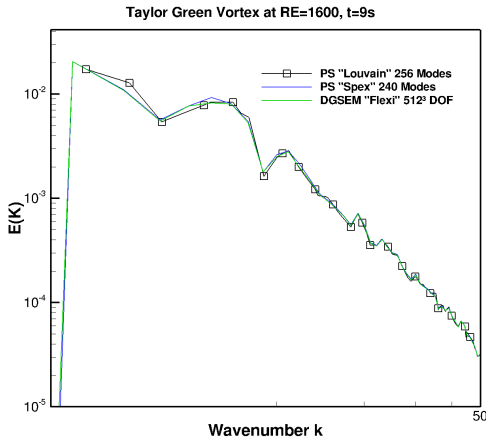


Figure 3.7.: Spectrum of kinetic energy for the Taylor-Green vortex at $Re = 1600$ and $t = 9s$. Comparison of pseudo-spectral codes *Spex* and *Louvain* and DGSEM code *Flexi*.

3.3. Spectral Element Methods

Spectral element methods are essentially Galerkin methods with a basis of high order orthogonal polynomials of Legendre or Lagrange type, applied locally to a subset of the whole computational domain. For this approach, the computational domain of interest is first subdivided into non-overlapping elements or cells. For each of these elements, a solution representation in terms of a locally defined basis with compact support is sought. Patera [161] was the first to propose these methods as a combination of the advantages of global spectral methods and classical FE methods: The accuracy in terms of a low n_{PPW} requirement and spectral convergence for smooth problems in combination with the flexibility of an element based approach with non-periodic basis functions, allowing a flexible domain discretization, non-periodic boundary conditions and efficient domain decomposition strategies for parallelization. The information interchange between the non-overlapping elements can be achieved by incorporating the coupling directly into the local bases, i.e. by keeping the solution at the interfaces unique through C^0 continuous basis functions (continuous spectral elements) or introducing double-valued degrees of freedom at the interface (discontinuous spectral element or spectral penalty schemes). Some appropriate penalization of the jump term, either for the weak or the strong formulation of the variational problem, then enforces the coupling of neighboring cells, e.g. [62, 100].

Due to the well-known stability problems continuous FE formulations share with other centered approximation for the convection terms in FV and FD methods [92], a number of remedies to recover stability exists, which generally include some form of parameter-dependent upwinding and thereby introduce numerical diffusion. Common formulations include the streamline-upwind Petrov Galerkin [32] and Galerkin Least-Squares [103] approach, which differ in terms of the element-based weighting function. While these methods have been applied with success to both incompressible and compressible problems [124, 194], the stabilization introduces additional terms that decrease computational efficiency and free non-unique parameters that require tuning [39].

As opposed to continuous formulations, discontinuous approximations show better stability for advection-dominated problems. This is due to the inherent upwinding in their local stencil (see discussion in Section 3.1), which adds numerical diffusion for stability, and to the jump occurring at the interfaces in under-resolved situations, which allows a “weak decoupling” of the local approximations – the solution is allowed to be non-unique, and coupling is only achieved weakly through a penalty term with associated additional diffusion. This idea of introducing a non-unique solution that absorbs an under-resolved approximation into a jump term is at the heart of the FV method, which has superior stability properties for advection dominated problems and – depending on the specific formulation – can guarantee stable solutions. Due to this inherent stability

for problems with strong gradients for continuous FE, we will focus on a discontinuous discretization in the following section as an example of spectral element methods.

3.3.1. Discontinuous Galerkin Methods

Discontinuous Galerkin (DG) methods are a hybrid of high order FE methods and FV methods, which gives them a number of favorable properties for scale-resolving simulations:

- Spectral accuracy for smooth problems when increasing the degree of the local ansatz (p-refinement), which results in low n_{PPW} requirements
- The possibility to use arbitrarily shaped, unstructured grids to mesh non-trivial geometries
- Local grid refinement in regions of interest (h-refinement)
- Stability for hyperbolic problems with discontinuities
- Local conservation for each element
- Weak imposition of the boundary conditions
- Efficient parallelization due to minimal coupling to neighbor cells
- Orthogonal hierarchical bases which resolve a wave range within an element, which can be exploited in multiscale modeling

DG methods have a relatively recent history. They were introduced by Reed and Hill [171] in 1973 for linear advection problems of neutron transport on triangular meshes (the name “Discontinuous Galerkin” is not mentioned in their original paper) and analyzed by Lesaint and Raviart in 1974 [126]. Applications of the methods and widespread use lay dormant for another two decades until Cockburn and Shu extended this approach in a series of publications to non-linear conservation laws [45–48] such as e.g. the compressible gas dynamics. Bassi and Rebay were the first to introduce a mixed finite element type approach for the discontinuous Galerkin discretization of viscous flow problems [12] and extended the DG method to the compressible Navier-Stokes equations [14]. Importantly, they also remarked on the need for consistent high-order boundary discretization to achieve high order accuracy in curved domains [13]. These efforts were accompanied by a number of researchers focusing on alternative approximations for the viscous fluxes [8, 9, 86, 131, 162], shock capturing [11, 38, 114], spatial and temporal adaptation options [87, 113] and extension to problems beyond gas dynamics, e.g.

solid mechanics [129], magneto-hydrodynamics [201] and biological systems [206]. It is worth noting that even before Reed and Hill in 1973, Nitsche [148] proposed a non-conforming finite element method for elliptic problems which is nowadays referred to as the symmetric interior penalty DG method [7], also available for the compressible Navier-Stokes equations [71, 95].

As discussed in Section 3.2, the variational formulation of the problem is the basis for the spectral approximation in a (sub)domain. Beyond the type of subdomains in multi-dimensions, various choices for the specifics of the DG method exist that each lead to a different formulation. Among these (spatial) choices are the basis functions with associated quadratures (e.g. Lagrange or Legendre-type polynomials), the approximation space spanned by these functions in multi-dimensions (a tensor-product approach or a full order basis), the weak or strong DG-formulation, the discretization choices for the inviscid and viscous surface fluxes and the treatment of non-linearities. The temporal integration introduces another level of possible choices.

Among these different variants, the Discontinuous Galerkin Spectral Element Collocation Method [120] combined with an explicit time integration scheme has shown to be highly effective and competitive for scale-resolving simulations (see also Section 3.4). Details of this method will be discussed in the following section.

3.3.2. Discontinuous Galerkin Spectral Element Collocation Method

In this section, we derive details of the Discontinuous Galerkin Spectral Element Collocation Method for a system of hyperbolic-parabolic conservation equations, following Kopriva [120] and Hindenlang et al. [100]. We use the compressible Navier-Stokes equations in physical space \mathbb{R}^3 (Equation (2.16)) as an example

$$\begin{aligned} \frac{\partial U}{\partial t} + \frac{\partial}{\partial x} F^c(U) + \frac{\partial}{\partial y} G^c(U) + \frac{\partial}{\partial z} H^c(U) \\ - \frac{\partial}{\partial x} F^v(U, \nabla_x U) - \frac{\partial}{\partial y} G^v(U, \nabla_x U) - \frac{\partial}{\partial z} H^v(U, \nabla_x U) = 0 \end{aligned} \quad (3.19)$$

with the vector of conserved variables U , the associated inviscid and viscous physical fluxes $\{F^c, G^c, H^c\}$ and $\{F^v, G^v, H^v\}$ and the divergence operator defined in physical space as $\nabla_x = (\partial_x \ \partial_y \ \partial_z)^T$. Introducing the flux vectors $\vec{F}^c = (F^c, G^c, H^c)^T$ and $\vec{F}^v = (F^v, G^v, H^v)^T$ and their combination $\vec{F} = \vec{F}^c - \vec{F}^v$, a compact way of writing Equation (3.19) becomes

$$\begin{aligned} \frac{\partial U}{\partial t} + \nabla_x \cdot \vec{F}^c(U) - \nabla_x \cdot \vec{F}^v(U, \nabla_x U) = 0, \\ \frac{\partial U}{\partial t} + \nabla_x \cdot \vec{F}(U, \nabla_x U) = 0. \end{aligned} \quad (3.20)$$

Together with suitable initial and boundary conditions, Equation (3.20) describes a system of conservation equation of hyperbolic-parabolic type, that can be now be discretized by the DGSEM method.

3.3.2.1. Spatial Discretization

In order to solve this system of equations, a discretization of the computational domain consisting of non-overlapping elements is defined. In the DGSEM method, the type of elements is restricted to hexahedral cells which support a tensor product basis. The elements can be connected in a fully unstructured way. Conformity of the element faces is not required by the method itself, but is assumed for the following derivation.

Each element in the physical domain is mapped to a unit reference element $E \in [-1, 1]^3$ with coordinates $(\xi^1, \xi^2, \xi^3)^T$. The associated mapping function $\vec{x}(\vec{\xi})$ from reference to physical space is approximated as a polynomial itself and is then used to calculate the Jacobian $J(\vec{\xi}) = \det(\frac{\partial \vec{x}}{\partial \vec{\xi}})$. Clearly, for the mapping to be defined and invertible, $J(\vec{\xi})$ has to be positive everywhere, which can be challenging for non-linear mappings of curved elements [99].

The resulting element-based mapping is then used to transform Equation (3.20) to reference space

$$U_t + \frac{1}{J(\vec{\xi})} \nabla_{\vec{\xi}} \cdot \vec{\mathcal{F}}(U, \nabla_x U) = U_t + \frac{1}{J(\vec{\xi})} \nabla_{\vec{\xi}} \cdot (\vec{\mathcal{G}}(U) - \vec{\mathcal{H}}(U, \nabla_x U)) = 0, \quad (3.21)$$

where $J(\vec{\xi}) := \vec{a}_1 \cdot (\vec{a}_2 \times \vec{a}_3)$ is again the Jacobian of the mapping $\vec{x}(\vec{\xi})$, calculated from the covariant basis vectors $\vec{a}_l := \frac{\partial \vec{x}}{\partial \xi^l}$. The covariant transformed fluxes are given by

$$\mathcal{F}^l := J \vec{a}^l \cdot \vec{F}, \quad l = 1, 2, 3, \quad (3.22)$$

with the metric terms

$$J \vec{a}^l := \vec{a}_k \times \vec{a}_m \quad (l, k, m) \text{ cyclic}. \quad (3.23)$$

The way the metric terms are discretized and implemented is important for the properties of the resulting method. We refer to Kopriva [119] for a discussion on how this choice ensures the so-called free-stream preserving property. In Equation (3.21), the divergence operator in reference space is defined as $\nabla_{\vec{\xi}} = (\partial_{\xi^1} \quad \partial_{\xi^2} \quad \partial_{\xi^3})^T$, and the terms $\vec{\mathcal{G}}(U)$ and $\vec{\mathcal{H}}(U, \nabla_x U)$ are the Euler and viscous contributions to the transformed fluxes $\vec{\mathcal{F}}(U, \nabla_x U)$.

Since the equation for each element is now defined in a common reference frame, we

can choose a polynomial solution approximation in the same space, which facilitates the evaluation of many element-local operators in a pre-processing step. In DGSEM, the solution vector within each element is approximated by a tensor product of 1-D Lagrange polynomials ℓ^N of degree N

$$U(\vec{\xi}, t) \approx \sum_{i,j,k=0}^N \hat{U}_{ijk}(t) \psi_{ijk}^N(\vec{\xi}), \quad \psi_{ijk}^N(\vec{\xi}) = \ell_i^N(\xi^1) \ell_j^N(\xi^2) \ell_k^N(\xi^3), \quad (3.24)$$

where $\hat{U}_{ijk}(t)$ are time dependent nodal degrees of freedom and $\ell_i^N(\xi)$ denotes the standard Lagrange polynomial of degree N defined by a nodal set $\{\xi_i\}_{i=0}^N \subset [-1; 1]$. Following Kopriva [120], the $N + 1$ Gauss-Legendre quadrature points $\{\xi_i\}_{i=0}^N$ are chosen as interpolation nodes. Another possible choice would be Gauss-Lobatto-Legendre points, leading to a slightly less efficient and accurate scheme due to inexact integration of the mass matrix [118]. Note that due to the Lagrange property of the basis functions, we have

$$\ell_j^N(\xi_i) = \delta_{ij}, \quad i, j = 0, \dots, N, \quad (3.25)$$

where δ_{ij} denotes the Kronecker delta function as above. This property of the basis functions, together with the double function of the interpolation nodes as integration points, makes the DGSEM variant the most efficient DG implementation.

Analogously to the solution vector U , the discrete transformed flux $\vec{\mathcal{F}}$ reads as

$$\mathcal{F}^l(\vec{\xi}) \approx \sum_{i,j,k=0}^M \hat{\mathcal{F}}_{ijk}^l \psi_{ijk}^M(\vec{\xi}), \quad l = 1, 2, 3 \quad (3.26)$$

$$\hat{\mathcal{F}}_{ijk}^l = \mathcal{G}^l(U) - \mathcal{H}^l(U, \vec{\nabla}_x U) |_{\vec{\xi}_{ijk}} \quad (3.27)$$

with $\psi_{ijk}^M(\vec{\xi}) = \ell_i^M(\xi^1) \ell_j^M(\xi^2) \ell_k^M(\xi^3)$. Note that the nodal fluxes are evaluated on $M + 1$ Gauss-Legendre quadrature points, with $M \geq N$. This implementation allows for polynomial de-aliasing of the non-linear flux terms [111]. The choice of M depends on the non-linearity of the flux for under-resolved calculations, more information on this topic is given in Section 4.2. For the classical DGSEM, $M = N$ is chosen, which leads to a collocation of solution and fluxes on the same nodes.

Now that the domain discretization and the solution and flux approximations are in place, we can derive the variational formulation of the problem and from it the DGSEM scheme. We start by multiplying Equation (3.21) by a test function $\phi(\vec{\xi})$ (taken from the

same space as the basis functions) and integrating over the reference element E to arrive at the variational formulation in reference space

$$\int_E \left(JU_t + \nabla_\xi \cdot \vec{\mathcal{F}}(U, \nabla_x U) \right) \phi(\vec{\xi}) d\vec{\xi} = 0. \quad (3.28)$$

Using a spatial integration by parts to remove the differentiability requirement from the flux term and noting that the solution is discontinuous across element interfaces yields the weak formulation

$$\int_E JU_t \phi d\vec{\xi} + \oint_{\partial E} \underbrace{(\mathcal{G}_n^* - \mathcal{H}_n^*)}_{\mathcal{F}_n^*} \phi ds - \int_E \vec{\mathcal{F}}(U, \nabla_x U) \cdot \nabla_\xi \phi d\vec{\xi} = 0, \quad (3.29)$$

where \mathcal{G}_n^* denotes the surface normal numerical flux function for the inviscid terms, given by $\mathcal{G}_n^* := \mathcal{G}_n^*(U^+, U^-)$ and superscripts \pm denote the values at the grid cell interface from the neighbor and the local grid cell, respectively. For the inviscid numerical flux, several well-known flux functions derived for FV formulations are possible, which ensure consistency and uniqueness of the numerical flux. Within the DG community, the most commonly applied flux functions are Godunov's method, the local Lax-Friedrichs or Rusanov flux and Roe's approximate Riemann solver. For details on those Riemann solvers we refer to the textbook by Toro [196] and to Section 4.5. The choice of \mathcal{H}_n^* will be postponed to Section 3.3.2.3.

3.3.2.2. Strong Form

Equation (3.29) is the so-called weak DG formulation, since the original conservation equation appears in a weak sense, as the flux divergence has been shifted to the test function in the volume integral. To recover the strong form, this volume contribution is integrated in parts again

$$- \int_E \vec{\mathcal{F}}(U, \nabla_x U) \cdot \nabla_\xi \phi d\vec{\xi} = \int_E \nabla_\xi \cdot \vec{\mathcal{F}}(U, \nabla_x U) \phi d\vec{\xi} - \oint_{\partial E} \mathcal{F}_n^i \phi ds, \quad (3.30)$$

where \mathcal{F}_n^i denotes the normal component of the flux $\vec{\mathcal{F}}$ evaluated at the inner element boundary, i.e. based on element-local information only to achieve analytical consistency. Re-inserting Equation (3.30) into the weak formulation (Equation (3.29)) and collecting terms yields the strong form

$$\int_E \left(JU_t + \nabla_\xi \cdot \vec{\mathcal{F}}(U, \nabla_x U) \right) \phi d\vec{\xi} + \oint_{\partial E} \left(\mathcal{F}_n^* - \mathcal{F}_n^i \right) \phi ds = 0. \quad (3.31)$$

The first integral in Equation (3.31) is just the Galerkin projection of the original equation, and the second term can be interpreted as a penalty term, that relaxes the orthogonality constraint on the projection of the residual. In this sense, the DG formulation in strong form can be interpreted as a spectral penalty method, where the local approximations are coupled by an appropriate diffusion term that penalizes the jump at the cell interface, i.e. in some sense the under-resolution of the problem [96]. Since for continuous FE, the solution is C^0 continuous at the interfaces, this penalty term is always zero and the stabilization mechanism is missing, which overburdens the global ansatz for advection dominated problems and leads to stability issues, as discussed in the introduction of Section 3.3. In this sense, the discontinuity of the ansatz for DGSEM leads to a more local approximation, as the weak coupling to neighbors through penalty terms can at least partially absorb de-stabilization effects of under-resolution.

It should be noted that while Equations (3.31) and (3.29) are analytically equivalent, differences can arise through implementation choices. In this work, the weak form is used exclusively.

3.3.2.3. Second Order Derivatives

Returning to Equation (3.29), the last missing term to be defined is \mathcal{H}_n^* . This term denotes the numerical flux function for the viscous term, resulting from the viscous flux $\vec{\mathcal{H}}$ in Equation (3.21). Through this viscous flux, Equation (3.29) depends on the solution gradient in physical space $\nabla_x U$. Thus, an approximation of the solution gradient is necessary to define \mathcal{H}_n^* . The treatment of the gradient terms in the context of DG approximations was first tackled by Bassi and Rebay [12, 15], who introduced a mixed finite element approximation. They showed that a local evaluation of the gradient leads to instabilities, and that some form of “lifted” gradient, containing information from both adjacent elements, is needed.

To derive the mixed formulation, the system of governing equations is rewritten as a corresponding system of first order equations with an auxiliary variable \vec{S} as an approximation of the lifted gradients

$$\begin{aligned} \vec{S} - \nabla_x U &= 0, \\ U_t + \nabla_x \cdot \vec{F}(U, \vec{S}) &= 0. \end{aligned} \tag{3.32}$$

3. Numerics for Scale-Resolving Simulations

Applying the discretization steps outlined above to the auxiliary equation leads to

$$\begin{aligned}
 c = 1, \dots, 5 : \quad & \int_E J \vec{s}_c \phi \, d\vec{\xi} + \oint_{\partial E} \vec{u}_{c,n}^* \phi \, ds - \int_E u_c \cdot \nabla_\xi \phi \, d\vec{\xi} = 0, \\
 & \int_E JU_t \phi \, d\vec{\xi} + \oint_{\partial E} (\mathcal{G}_n^* - \mathcal{H}_n^*) \phi \, ds - \int_E \vec{\mathcal{F}}(U, \vec{S}) \cdot \nabla_\xi \phi \, d\vec{\xi} = 0,
 \end{aligned} \tag{3.33}$$

with the component u_c of the state vector U and its lifting operator \vec{s}_c . The numerical flux of the auxiliary equation is $\vec{u}_{c,n}^*$, and $\mathcal{H}_n^* = \mathcal{H}_n^*(U^+, U^-, \vec{S}^+, \vec{S}^-)$ denotes the numerical flux function for the viscous terms. Following [12], we choose

$$\begin{aligned}
 c = 1, \dots, 5 : \quad & \vec{u}_{c,n}^* = (\alpha_{visc} u_c^+ + (1 - \alpha_{visc}) u_c^-) \vec{n}, \\
 & \mathcal{H}_n^* = \left(\alpha_{visc} \mathcal{H}_n(U^+, \vec{S}^+) + (1 - \alpha_{visc}) \mathcal{H}_n(U^-, \vec{S}^-) \right),
 \end{aligned} \tag{3.34}$$

with \vec{n} denoting the outward pointing surface normal. For a parameter of $\alpha_{visc} = \frac{1}{2}$, this treatment of the viscous fluxes is usually labeled BR1 (first method of Bassi and Rebay [12]) and is known to be formally unstable for purely elliptic problems. However, for advection dominated problems, the inviscid numerical flux function is helping in stabilizing the overall operator and no issues have been observed in any of our computations.

3.3.2.4. Boundary Conditions

Due to the weak coupling of the elements through fluxes in DG methods, it is an obvious idea to enforce the boundary conditions in the same manner, even for the Dirichlet type. Instead of prescribing a state U at the boundary, an appropriate right hand side state U^+ (akin to a ghost cell state) is used to compute the resulting boundary flux. The rationale for this approach is to ensure consistency in the approximation of the solution and the boundary conditions, i.e. to use the same discretization operators for both and thus avoid stability issues [17]. Collis [51] investigated the effect of weakly versus strongly imposed Dirichlet conditions for the case of an under-resolved one-dimensional stationary boundary layer problem and turbulent channel flows. He found that the solution quality measured in the L_2 and H_1 error norms is greatly enhanced when using a weak application of the boundary conditions, while the L_∞ norm slightly favors the strong form, as this norm reacts directly to the error directly at the boundary, where an exact fulfillment cannot be guaranteed in a weak formulation, but is enforced when using the strong imposition.

We follow this approach, and we enforce the boundary conditions for Equation (3.33) weakly through the prescription of the boundary fluxes $\vec{u}_{c,n}^*$, \mathcal{G}_n^* and \mathcal{H}_n^* . While Collis reported improvements using weakly enforced wall boundary conditions, we also have noted positive effects at freestream and outflow boundaries: reflections stemming from outgoing acoustic waves are rarely encountered, and are often negligible. Even in aeroacoustic computations, where an unpolluted instantaneous pressure field is highly important, this treatment was found to be sufficient when using Roe's approximate Riemann solver which computes the surface flux according to the local flow characteristics [75].

3.3.2.5. The DGSEM Operator

Equation (3.33) describes the general analytical, semi-discretized form of the DG method of a hyperbolic-parabolic system of equation with the second order derivatives treated by the first method of Bassi & Rebay and an arbitrary Euler flux function. A full, very detailed derivation of the DGSEM operator from Equation (3.33) is given by Hindenlang et al. in [100], here, just some of the details are repeated to highlight the efficiency of DGSEM.

As noted in Equations (3.24) and (3.26), the solution and the flux are represented by tensor products of one-dimensional Lagrange interpolating polynomials, associated with either one-dimensional Legendre-Gauss or Legendre-Gauss-Lobatto quadrature points. The Lagrange property of the basis functions on these nodes makes the evaluation of the basis at these points and thus of the solution and fluxes trivial, as only one nodal degree of freedom gives a contribution. The evaluation of the inner products is then achieved by the corresponding quadrature rule, which reverts to a sequence of three one-dimensional sums along a reference coordinate line, which reduces the number of operations from $\mathcal{O}(N+1)^6$ for a standard DG formulation to $\mathcal{O}(N+1)^4$ for DGSEM.

We demonstrate this concept by applying the DGSEM formulation to the first volume integral, containing the time derivative of the degrees of freedom, from Equation (3.29). First, we insert the ansatz for the solution (Equation (3.24)) into the semi-discrete form and choose the test function ϕ from the space of Lagrange polynomials of degree N as ψ_{ijk}^N with associated $N+1$ Legendre-Gauss nodes $\{\xi_i\}_{i=0}^N$

$$\int_E J(\vec{\xi}) U_t \phi d\vec{\xi} = \int_E J(\vec{\xi}) \left(\frac{\partial}{\partial t} \sum_{r,s,t=0}^N \hat{U}_{rst}(t) \psi_{rst}^N(\vec{\xi}) \right) \psi_{ijk}^N d\vec{\xi}. \quad (3.36)$$

3. Numerics for Scale-Resolving Simulations

The integral over the reference space is now split into the coordinate directions and then replaced by Legendre-Gauss quadrature with associated weights ω :

$$\begin{aligned}
 \int_E J(\vec{\xi}) U_t \phi d\vec{\xi} &= \int_{-1}^1 \int_{-1}^1 \int_{-1}^1 J(\vec{\xi}) \left(\frac{\partial}{\partial t} \sum_{r,s,t=0}^N \hat{U}_{rst}(t) \psi_{rst}^N(\vec{\xi}) \right) \psi_{ijk}^N(\vec{\xi}) d\xi^1 d\xi^2 d\xi^3 \\
 &= \sum_{\alpha,\beta,\gamma=0}^N J(\vec{\xi}_{\alpha\beta\gamma}) \left(\frac{\partial}{\partial t} \sum_{r,s,t=0}^N \hat{U}_{rst}(t) \underbrace{\ell_r^N(\xi_\alpha^1)}_{=\delta_{r\alpha}} \underbrace{\ell_s^N(\xi_\beta^2)}_{=\delta_{s\beta}} \underbrace{\ell_t^N(\xi_\gamma^3)}_{=\delta_{t\gamma}} \right) \psi_{ijk}^N(\vec{\xi}_{\alpha\beta\gamma}) \omega_\alpha \omega_\beta \omega_\gamma \\
 &= \sum_{\alpha,\beta,\gamma=0}^N J(\vec{\xi}_{\alpha\beta\gamma}) \frac{\partial}{\partial t} \hat{U}_{\alpha\beta\gamma}(t) \underbrace{\ell_i^N(\xi_\alpha^1)}_{=\delta_{i\alpha}} \underbrace{\ell_j^N(\xi_\beta^2)}_{=\delta_{j\beta}} \underbrace{\ell_k^N(\xi_\gamma^3)}_{=\delta_{k\gamma}} \omega_\alpha \omega_\beta \omega_\gamma \\
 &= \underbrace{J(\vec{\xi}_{ijk}) \omega_i \omega_j \omega_k}_{pre-compute} \frac{\partial}{\partial t} \hat{U}_{ijk} .
 \end{aligned} \tag{3.37}$$

Note that the Kronecker delta functions indicate the occurrence of the Lagrange property and thus reduce the associated summation to a single evaluation. Also, the Jacobian of the mapping is treated in a collocation way in this approach, i.e. it is not integrated exactly if the mapping is beyond bi-linear. In this case, an additional error akin to mass-lumping for Gauss-Lobatto integration of the mass matrix is introduced.

From an efficiency point of view, Equation (3.37) demonstrates how the three-dimensional integrals reduce to point-wise evaluations in DGSEM. For each of the $(N + 1)^3$ DOF \hat{U}_{ijk} per element, just a single multiplication with a pre-computed term is necessary, due to the “folding” of the three-dimensional integral based on the tensor-product structure and the collocation of interpolation and integration nodes.

For the surface and flux volume integrals in Equation (3.29), a similar reduction in operations can be shown, where the volume integral retains an operation count of $(N + 1)$ multiplications per DOF, as the occurrence of the derivatives of the basis functions does not support the Lagrange property. Further details and a full discretization of the operator can be found in [100]. Following the discussion therein, pre-computed one-dimensional operators can be defined. For the volume integral, the differentiation matrix and the

weighted differentiation operator read

$$D_{ij} = \left. \frac{d\ell_j(\xi)}{d\xi} \right|_{\xi=\xi_i}, \quad (3.38)$$

$$\hat{D}_{ij} = -D_{ji} \frac{\omega_i}{\omega_j}, \quad i, j = 0, \dots, N.$$

The weighted basis functions are given accordingly by

$$\hat{\ell}_i = \frac{\ell_i}{\omega_j}, \quad i, j = 0, \dots, N, \quad (3.39)$$

and \hat{s} is the surface element, relating the physical to the reference surface. With these definitions, the semi-discrete form of the DGSEM operator for the weak form becomes

$$-J_{ijk} \left(\hat{U}_{ijk} \right)_t = \left(\sum_{\alpha=0}^N \hat{D}_{i\alpha} \hat{\mathcal{F}}_{\alpha j k}^1 \right) + \left([\mathcal{F}^* \hat{s}]_{jk}^{+\xi^1} \hat{\ell}_i(+1) + [\mathcal{F}^* \hat{s}]_{jk}^{-\xi^1} \hat{\ell}_i(-1) \right) +$$

$$\left(\sum_{\beta=0}^N \hat{D}_{j\beta} \hat{\mathcal{F}}_{i\beta k}^2 \right) + \left([\mathcal{F}^* \hat{s}]_{ik}^{+\xi^2} \hat{\ell}_j(+1) + [\mathcal{F}^* \hat{s}]_{ik}^{-\xi^2} \hat{\ell}_j(-1) \right) +$$

$$\left(\sum_{\gamma=0}^N \hat{D}_{k\gamma} \hat{\mathcal{F}}_{ij\gamma}^3 \right) + \left([\mathcal{F}^* \hat{s}]_{ij}^{+\xi^3} \hat{\ell}_k(+1) + [\mathcal{F}^* \hat{s}]_{ij}^{-\xi^3} \hat{\ell}_k(-1) \right). \quad (3.40)$$

Thus, for DGSEM, the three-dimensional operator essentially collapses to a sequence of three consecutive one-dimensional operators, which is responsible for the dramatically decrease in operation count for DGSEM. The volume integral reduces to an evaluation along a line (effort($N + 1$)), and all other operations are point-wise. Thus, especially for high N , the volume integral is the determining factor in terms of operation count.

3.3.2.6. Temporal Discretization

Both Equations (3.40) and (3.29) describe how to discretize the spatial operator, leaving the temporal dimension continuous. These semi-discrete forms can be advanced in time by any suitable method. Since the DGSEM operator itself is very local in the sense that it only communicates with the direct neighbors through the surface fluxes (and not across corners) and the local operations are very dense, it is suitable for an explicit time integration. Also, multiscale problems, particularly in fully resolved situations, are governed by the temporal scale of their smallest structures, and an implicit treatment

3. Numerics for Scale-Resolving Simulations

with large time steps can lead to the introduction of a sizable approximation error. Thus, we choose to treat the time dimension explicitly by a fourth order accurate, five stage Runge-Kutta method of Carpenter and Kennedy [34]. The time step for advection for DG is of the form

$$\Delta t_{max}^{adv} \sim \frac{1}{\lambda_{max}^{adv}} \frac{\Delta x}{2N+1}, \quad (3.41)$$

with Δx as the grid spacing and λ_{max}^{adv} the maximum eigenvalue of the flux Jacobian matrix for advection, and the viscous time step is given by

$$\Delta t_{max}^{diff} \sim \frac{1}{\lambda_{max}^{diff}} \left(\frac{\Delta x}{2N+1} \right)^2, \quad (3.42)$$

where λ_{max}^{diff} the maximum eigenvalue of the diffusion matrix [50]. This strong dependence on the polynomial degree N is due to the overshoot in the dispersion relation at high wave numbers, and is one of the drawbacks of DG [40].

3.4. Efficiency of DGSEM for Scale-Resolving Simulations

As discussed in Chapter 1, efficient numerics are mandatory for scale resolving simulations. In the previous sections, efficiency has been defined in terms of points per wavelength required by a given numerical discretization to accurately reproduce a scale of a given size. In Section 3.1, we discussed the importance of spectral accuracy and high order approximations with spectral character in terms of reducing the n_{PPW} requirement and taking advantage of the invested DOF. In Sections 3.2 and 3.3, global spectral schemes and spectral element schemes, in particular the DGSEM variant, were introduced. DG methods offer the potential for high order accuracy and spectral convergence in smooth regions. From the discussion in Section 3.1 and an investigation of the dissipation and dispersion relations for DGSEM in [85], the factor n_{PPW} in Equation (1.5) for a global spectral method is 2, while it lies between 4 and 7 for a high order DGSEM scheme. Lower order schemes such as second order FV schemes or classic FE schemes typically require at least 15 to 20 PPW for a comparable accuracy [43, 128]. Thus, in terms of pure resolution requirement, high order DGSEM can be considered an efficient method, since it combines a low n_{PPW} requirement with geometric flexibility.

3.4.1. Operation Count

While this estimate in terms of DOF is useful to gauge the limits of each method, it is not a suitable measure for overall code performance or wall clock time. In particular, the

operation count per degree of freedom for all spatial discretization schemes scales with some power of the size of their local (or global) stencil, i.e. a global spectral method also scales “globally” with the number of degrees of freedom, while a low order FD method will scale with its local stencil size.

For example, for a one-dimensional linear first order transport equation discretized on a grid with N_{grid} nodes, the best scaling for a global method is given by a pseudo-spectral approach, which reduces the operation count for one evaluation of the spatial operator from $\sim N_{grid}^2$ to $\sim N_{grid} \log(N_{grid})$ (due to the FFT). For a standard first order FD discretization, the stencil size is 2, i.e. 2 operations are required per grid point, leading to an operation count of $\sim 2 N_{grid}$. Table 3.2 summarizes the estimates for the operation count for different discretizations of a one-dimensional domain with N_{grid} DOF and approximation order p . Note that for DGSEM, the operation count per element is $p + 1$, plus an additional evaluation of a surface flux. The number of elements in DGSEM is estimated as total DOF divided by DOF in a single element. This estimate does not take the doubling of the interface nodes into account, but the general scaling remains the same. With these simplifications, it can be seen that the DGSEM method scales similarly to a FD method, and as discussed in Section 3.3.2.5, this extends to multi-dimensions due to the dimension-by-dimension outline of DGSEM. Of particular importance is the fact that when the total number of DOF remains fixed, the operation count is only weakly dependent on p , which makes high order DGSEM with the n_{lowPPW} particularly attractive for scale-resolving simulations. Clearly, counting operations is a very crude measure of performance, due to a number of reasons: a) Different operation types require different amount of clock cycles on a CPU, b) memory access and caching effects can dominate the operation speed depending on the size of the operator, c) hardware architectures differ in terms of execution speed for specific operations beyond multiplication and d) parallelization efficiency can completely change the picture. Nonetheless, the operation count indicates whether a discretization is theoretically able to be efficient

<i>Discretization</i>	<i>Operation Count</i>
Pseudo-spectral	$\approx N_{grid} \log(N_{grid})$
FD $\mathcal{O}(p)$	$\approx N_{grid} (p + 1)$
DGSEM $\mathcal{O}(p)$	$\approx N_{elems} (p + 1) + N_{elems}, \quad N_{elems} \approx N_{grid}/(p + 1)$

Table 3.2.: Estimated operation count for one-dimensional spatial operators for different discretizations.

when compared to others, thus, it poses some form of upper limit on performance on an ideal computing system.

3.4.2. Parallel Performance

In the previous sections, we have shown that DGSEM has two properties that are favorable for efficient multiscale numerics: a) spectral accuracy for a high wave number resolution per invested DOF and b) an operation count that is comparable to FD schemes, the simplest and least costly discretization choice in terms of operations. However, an efficient parallelization and implementation of the code along with optimizations specific to the hardware architecture is as important for large scale simulations as the scheme properties themselves.

On massively parallel systems, any operation imbalance will cause a bottleneck. Thus, load balancing (in terms of work per core, but also in terms of communication vs. computing) is essential. The DGSEM operator has two favorable properties that support efficient parallelization: a) The operator itself is very local, and elements communicate only with their direct neighbors, i.e. the waiting time and the communication connections to other cores are minimal. b) The volume integral is a purely local operation, that does not require neighbor information. It can be used to hide the communication latency by creating temporal buffers through a non-blocking communication. The dimension-by-dimension structure of this operator allows the design of buffer sizes that “fit” the communication bandwidth. In addition, our MPI parallelization does not introduce additional operations (besides the data transfer), for example the surface fluxes will only be computed by one of the neighboring cores and then send to the partner (with this operation also being equally distributed between the two processors sharing a face). More details on parallelization, scaling, load balancing and domain decomposition for DGSEM can be found in [4,99]. Two of the most important results concerning the parallel performance of DGSEM are repeated here, as they pertain directly to the efficiency of high order DGSEM for scale-resolving simulations: a) As shown in [99], the computing time to update a single DOF (i.e. the evaluation of the spatial operator) remains nearly constant over increasing polynomial degree N . Thus, for our DGSEM implementation, a “high order” DOF is not substantially more expensive than a “low order” DOF. This means that for the same number of degrees of freedom, the low and high order DGSEM schemes will take similar CPU times (neglecting the time step restriction), with the high order discretization offering much improved spatial resolution. b) Weak scaling is near optimal [4], allowing simulations with many DOF (on the order of hundreds of millions), while strong scaling (which allows manageable wall times for large scale problems) can become super-linear due to caching effects. Figure 3.8 shows strong scaling results on the BlueGene Q at JSC with a speed-up from 32, 678 to 262, 144 ranks (down to 8 ele-

ments with $N = 7$ per core) of 116%, as the decrease in core load allows the caching of the local data and thus reduces memory bandwidth issues.

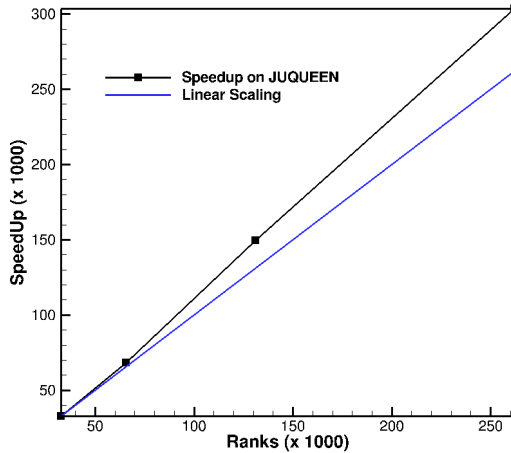


Figure 3.8.: Strong scaling of DGSEM on BlueGene Q “JuQueen” at JSC. 128^3 elements, $N = 7$ up to 262, 144 ranks (131, 072 cores with $2\times$ hyperthreading). Results from the Porting and Scaling Workshop, 2013.

3.4.3. Comparison with Other Codes

At the “1st International Workshop on High Order Methods in CFD, 2012” a comparison of various high order schemes from different contributors for a scale-resolving simulation of the Taylor-Green Vortex problem at $Re = 1600$ (see Section 2.2) was conducted. Details on the problem definition and on the errors measures for comparison are published in [200]. The result from this workshop have been reproduced here with permission.

Table 3.3 lists the participants of the workshop and the computational methods. Note that all computations were conducted with DNS schemes, i.e. without additional LES modeling. The contributions included DGSEM, other DG methods (modal, nodal, Recovery-DG, CPR-DG), FD and DRP-FD (dispersion-error minimized FD) and 3rd and 4th or-

3. Numerics for Scale-Resolving Simulations

Color in Fig. 3.9	Affiliation	Authors	Method
Red	University of Stuttgart	Beck	DGSEM,RK5
Dark Blue	Cenaero Carton,	Hillewaert	DG/IP,RK4
Green	ONERA	Chapelier et al.	DG/BR2, RK4
Light Blue	NASA Glenn	Debonis	FD,RK4
Light Blue	NASA Glenn	Debonis	DRP,RK4
Purple	Iowa State University	Wang et al.	DG-CPR, RK4
Black	ONERA	Le Gouez	FV/Recon, RK3
Yellow	University of Michigan	Varadan et al.	DG/RDG, RK4

Table 3.3.: Contributors and scheme details for the 1st International High Order Workshop, test case 3.5, see Figure 3.9.

der reconstructed FV formulations. The computational effort was judged by comparing against a benchmark tool on each employed architecture, however, some doubts about the inter-comparability remain. Figure 3.9 compares the error (computed against a reference solution with 512^3 DOF of a pseudo-spectral solver) over invested DOF (top) and over computational time in Work Units (WU) (bottom). Starting with the top plot, a few general trends discussed in Section 3.1 can be observed here in practice: The order of the discretization and the discretization choices themselves strongly influence the accuracy and efficiency. For a given accuracy, the higher order formulations are located towards the left of the plot, indicating a lower requirement in DOF, consistent with their lower n_{FPW} demands. Also, DG formulations can return comparable or better accuracy per invested DOF than FD or FV schemes for this problem. In terms of minimizing the error, high order DGSEM ($\mathcal{O}(8)$ and $\mathcal{O}(10)$) outperforms the other implementations. Note that the DGSEM $\mathcal{O}(16)$ results likely suffer from aliasing issues, which explains their somewhat reduced accuracy. Thus, in terms of invested DOF, DGSEM with $N \geq 4$ is very favorable.

The bottom plot in Figure 3.9 repeats the comparison, but in terms of computational effort instead of invested DOF. This essentially scales the left plot by the Work Unit per degree of freedom, i.e. by a measure of computational efficiency of the scheme. In general, the DG formulations lose compared to the FD schemes for reasons discussed in Section 3.3.2.5, and they move towards higher Work Units, requiring one to two orders of magnitude more computational effort than FD. Only the DGSEM formulation is capable of competing with FD in terms of accuracy per cost, and it marks the lower limit in terms of WU for all DG variants. Note that the DGSEM results are between a factor

of 1.1 and 1.2 more expensive than the FD computations, but this is made up by a considerable gain in accuracy. Another interesting issue is the fact that the DGSEM results are almost on a vertical line in this plot, indicating very little difference in WU for the different order approximations, making high order discretizations as cheap as low order ones. A number of factors contribute to this behavior: a) The overall number of DOF for all DGSEM cases was constant, i.e. the number of elements was adjusted accordingly. b) Just counting operations according to Table 3.2, the number of operations should be similar in all cases, even in three dimensions. c) The excellent strong scaling performance of the code, as all computations were performed on 4096 cores, i.e. a constant load per core of 4096 DOF, which is close to the optimum region where performance is near independent from polynomial degree. Note that changing the polynomial degree will result in a shift between communication and computation time, which can - in conjunction with the grid spacing - make up for the time step penalty of high order DGSEM.

In summary, these results indicate that the DGSEM method constitutes the most effective DG implementation, and that it can offer comparable accuracy and computational efficiency to high order FD methods, while retaining the advantage of fully unstructured meshing.

3. Numerics for Scale-Resolving Simulations

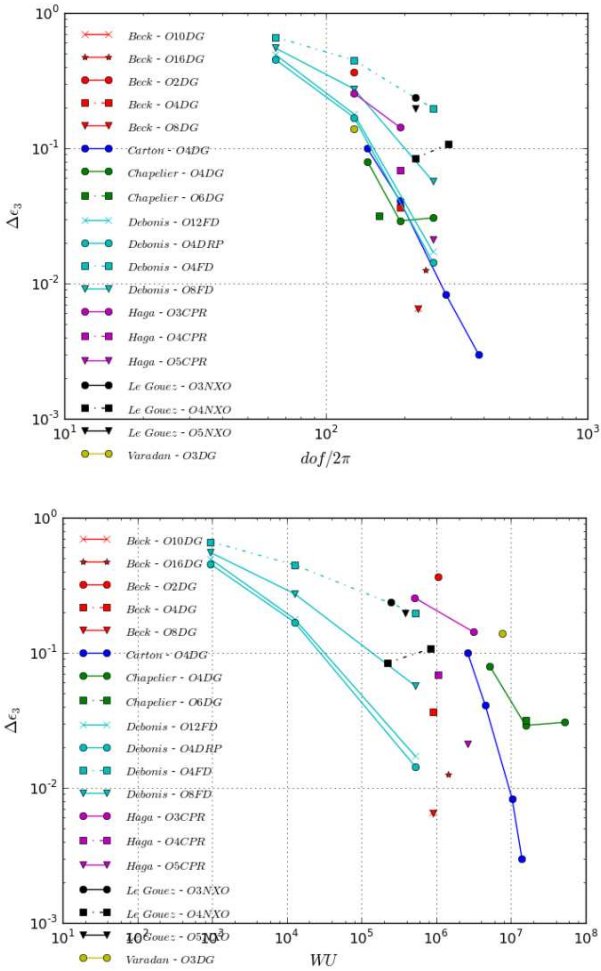


Figure 3.9.: Code comparison for DNS of Taylor-Green Vortex at $Re = 1600$.

Top: Error in computed vs. reference dissipation rate over DOF.

Bottom: Error in computed vs. reference dissipation rate over Work Units (CPU time).

Results from the 1st International Workshop on High Order Methods in CFD, 2012, with permission from Koen Hillewaert (Cenaero) and from [200]. For legend refer to Table 3.3.

3.5. DNS with DG Methods

Despite the favorable approximation properties and computational efficiency discussed in the previous sections, the number of scale-resolving simulations with DG methods published in literature is still remarkably low. This can be attributed to a number of reasons: a) The relative newness of the Discontinuous Galerkin method and its extension to system of evolution equations compared to more established methods that have been adopted for industrial applications and research, b) the focus on incompressible turbulence in basic research, where continuous spectral element methods are the established codes, c) the perceived increased complexity of DG compared to FD and d) the sharp time step restriction. Another issue that is hindering the widespread use of high order methods in basic and industrial research is the generation of high order meshes for complex, curved geometries, which has up-to-date not been solved in a satisfactory manner [99, 101].

Collis in 2002 was the first to use a high order DG method ($p = 6$) for the DNS of a weakly compressible turbulent channel flows at a low Reynolds number, with about 13 mio DOF for his finest mesh [51]. More recently, Wei et al. [202] extended this investigations from sub- to supersonic channel flow and moderate Reynolds number, using an over-integrated 10th order DG scheme with a total of 4.3 mio DOF and found satisfactory agreement with previously published results. Carton de Wiart et al. investigated fourth order DG methods for DNS of the Taylor-Green Vortex with 384^3 DOF and showed convergence towards a pseudo-spectral reference solution. They also reported a DNS with 10 mio DOF of a transitional flow over an SD7003 airfoil [35]. Recently in 2014, Renac et al. evaluated DNS with a modal DG scheme for the Taylor-Green Vortex and a channel flow, as well as a two-dimensional dipole interaction with a wall [41]. They used approximation order up to 8, and at most 56 mio DOF.

In the following, we will briefly outline some exemplary DNS computations with our DGSEM framework. It should be noted that the simulation code itself is just one building of the framework. Single block structured meshes with volume curving can be generated from analytical functions by a stand-alone preprocessor, while for general, multi-block structured or unstructured meshes, existing grid generators are used. Due to the necessity of high order curvature information which is usually not supplied by the meshing software, curved mappings have to be generated in a preprocessing step. Several strategies exist, a detailed overview is given in [99]. In addition to mesh format transformation and curving, the preprocessor strings all elements along a space-filling curve, which results in a one-dimensional list structure, in which elements that are close in physical space are also close in terms of list position. This approach allows efficient parallel read-in and ad-hoc domain decomposition. Within the simulation code, the same sorting is used to write the results simultaneously in a single file, as each process “knows” its location

within the complete list and can fill its slot without conflicts.

The post-processing of large scale data is achieved by a collection of specific tools, all of which share a common code basis for general tasks and use the same data structure as the code itself. Visualization of surface and volume data is achieved by super-sampling the DG polynomials on equidistant grids, derived quantities like λ_2 can be computed within the polynomial space and then visualized as well. A standalone parallelized three-dimensional FFT tool exists to compute volume spectra. On meshes with at least one structured dimension, spatial averaging based on the high order accurate quadrature can be performed. All post-processing tools write data readable standard visualization software (Tecplot¹, Paraview²). A special output format and Python-scripted tool chain connects the post-processing output to professional rendering software like *blender*³ for high quality visualizations.

For the evaluation of turbulent statistics, a time-averaging of conserved and derived quantities is implemented. The averaging of fluctuation products (like Reynolds stresses) follows from

$$\begin{aligned}
 \overline{uv} &= \frac{1}{\Delta t} \int_t^{t+\Delta t} uv \, dt \\
 &= \frac{1}{\Delta t} \int_t^{t+\Delta t} (\bar{u} + u')(\bar{v} + v') \, dt \\
 &= \overline{\bar{u}\bar{v}} + \overline{\bar{u}v'} + \overline{\bar{v}u'} + \overline{u'v'} \\
 &= \overline{\bar{u}\bar{v}} + \overline{u'v'} \\
 \rightarrow \overline{u'v'} &= \overline{uv} - \overline{\bar{u}\bar{v}}
 \end{aligned} \tag{3.43}$$

where both relations are computed and stored during runtime and assembled in post-processing. All time averaging is done in independent time slices which can later be used to perform the averaging over user-specific time intervals. Additionally, record points or probes can be specified a priori, which record the time series of prescribed quantities for spectral analysis. They are located in the mesh in a pre-processing step and stored along the space filling curve together with their pre-evaluated local basis functions for efficient evaluation during the actual computation.

To facilitate comparisons between different computing architectures and to measure the performance of our code, we compute the performance index PID for each computation as

$$\text{PID} := \frac{T_{CPU}}{n_{DOF} \times n_{\Delta t}} [s], \tag{3.44}$$

¹www.tecplot.com

²<http://www.paraview.org/>

³www.blender.org

where $n_{\Delta t}$ denotes the number of explicit time steps and the total CPU time T_{CPU} is computed as the number of computing cores n_{cores} times the simulation wall clock time T_W . The number of spatial degrees of freedom per state vector component n_{DOF} is given by the product of the number of grid cells n_{cells} and the collocation points per element $(N + 1)^3$. While the absolute value of the PID is strongly dependent on the computing systems, its relative changes within a single system allow us to find the optimal configuration in terms of processor load for a given system. Where meaningful, also informations about the wall time per characteristic time unit is given, as for turbulent simulations with statistics gathering, the length of the averaging period is the determining factor in overall computational cost. The relevant computational data for all cases presented below is gathered in Table 3.4. Denoted are details about the spatial discretization, the number of DOF per conservative variable, the computing cores and a characteristic time step Δt divided by a reference time unit T^* (which is 1 for both vortex test cases). Also the wall time per characteristic time unit T_W/T^* , the number of time steps, the overall wall clock time and the computing architectures are listed.

Case	N	no. DOF	no. cells	cores	$\overline{\Delta t}/T^*$	PID [μs]	T_W/T^*	no. time steps	T_W
Sphere	4	$2.6 \cdot 10^6$	21, 128	4, 096	$1.5 \cdot 10^{-4}$	22.0	90s	$1.9 \cdot 10^6$	7.5h
Vortex	7	$57 \cdot 10^6$	110, 592	6, 912	$3.8 \cdot 10^{-3}$	11.4	-	$2.1 \cdot 10^5$	1.9h
TGV	11	$216 \cdot 10^6$	125, 000	125, 000	$6.9 \cdot 10^{-5}$	72.3	-	$1.8 \cdot 10^5$	7h
Cylinder	7	$164 \cdot 10^6$	319, 488	4, 992	$4.7 \cdot 10^{-4}$	17.1	1.9h	$1.5 \cdot 10^6$	460h

Table 3.4.: Computational cost for DNS simulations with DGSEM. All computations were run on the “Hermit” Cray XE6 at HLRS, except the TGV case, which was run on the “Jugene” BlueGene P at JSC.

Among others, the following large-scale DNS simulations of turbulent flow problems were conducted, demonstrating the suitability and performance of the full tool chain for demanding multiscale simulations.

- Sphere at $Re = 1000$: A weakly compressible flow at Mach number $Ma = 0.3$ and moderate Reynolds number based on the diameter $Re = 1000$ was computed. Further details can be found in [100]. The cylindrical domain consists of about 20, 000 hexahedral elements, which are curved on the geometry surface. The polynomial degree was chosen to be $N = 4$, leading to about 2.5 mio DOF for this computation. The simulation was run on the Cray XE6 cluster “Hermit” on 4096 cores, with the computational effort for one characteristic time unit $T^* = D/u_\infty$ of 100 CPU-h, corresponding to a wall clock time per characteristic time unit of

1.5 minutes. Note that for this low load of only about 600 DOF per core, the PID is not optimal.

- **Vortex Cascade:** As discussed in Section 2.1.1, vortex interaction is the mechanism that produces a turbulent cascade. In this simulation, two large scale, stationary isentropic vortices of equal strength interact in a periodic domain of size $[20 \times 20 \times 20]$. The Mach number based on the average initial vortex velocity is set to $M = 0.1$, while the Reynolds number based on the same velocity scale and the initial vortex diameter ($D = 2$) is $Re = 1000$. The domain is discretized by 48^3 cubic elements with 8^3 inner points per cell, leading to $56 \cdot 10^6$ DOF total. We have computed this flow on 6,912 cores on the Cray XE6, leading to a DOF per core load of about 8,000. The total wall clock time in this configuration for 800 time units was 6,800s.

Figure 3.11 *right* shows the development of the spectrum of kinetic energy $E(k)$ over time, and a visualization of λ_2 isocontours of the flow field is depicted in the left subplot.

- **Taylor-Green Vortex at $Re = 5000$:** A DNS of the TGV described in Section 2.2 at a high Reynolds number of $Re = 5000$ was computed to establish a reference DNS. Two discretizations were chosen, one leading to 384^3 DOF, and the second one with 600^3 , resulting in 210 mio DOF per conservative variable. This is up to date the largest reported computation with a DG method in literature. Figure 3.12 depicts a visualization of the vortical structures and the spectra of kinetic energy at the time of maximum dissipation. The cut-off frequencies for both resolutions and Kolmogorov's scaling is also indicated. Note that a clear inertial subrange can be observed, and also that even for 600^3 DOF, the resolution in the dissipation region at high wave numbers is not yet fully converged.

Table 3.4 lists the computational details for the case with 50^3 elements and $N = 11 \cdot 125k$ cores were used on the Bluegene P "Jugene" at JSC. Due to the high resolution, the explicit time step is very small, but the problem remained dominated by the advective time step. Because of the lower clock speed of the Jugene and the different architecture, the PID on this machine is generally worse than on the Cray system, however, this is partially due to the file I/O, which is not consistent on this number of cores. Nonetheless, due to excellent scaling of the framework, the full simulation was completed in about 7 hours, thereby demonstrating its potential for massively parallel multiscale simulations.

- **Cylinder at $Re_D = 3900$:** This flow is a classical test case for LES and DNS. It was computed at a Reynolds number based on the diameter D of $Re_D = 3900$ and a Mach number $Ma = 0.1$. At the given flow conditions, the boundary layer

remains laminar until the separation point, where the shear layer is shed periodically. The ensuing transition to turbulence occurs very close to the geometry in the shear layer, and interacts with the resulting reverse flow region. We have simulated this flow on a grid with 319,488 elements, spanning a circular domain of radius $R = 100D$ and $\Delta z = 8D$, with elements of degree $N = 7$, leading to 164 mio DOF. The characteristic time is given by $T^* = D/u_\infty$, and the characteristic shedding time is $T_{Str} \approx 5T^*$. Statistics were gathered over 50 shedding cycles. Figure 3.13 shows a visualization of the flow features in the cylinder wake. Due to limitations on the computing system at that time, the number of cores for this simulation was restricted to 4992, which resulted in a deterioration of the PID and very long wall clock times per shedding cycle.

In summary, we have presented in this chapter a highly efficient numerical scheme for scale-resolving simulations and have demonstrated the capabilities of the whole framework, from pre-processing to visualization, to handle massively parallel large-scale simulations.

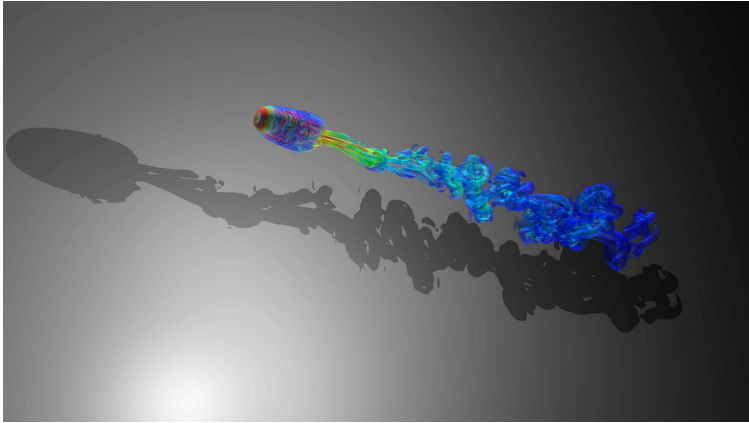


Figure 3.10.: Flow over a sphere at $Re = 1000$ and $Ma = 0.3$. The computation was run the Cray XE6 “Hermit” at HLRS on 4096 cores. The picture shows the laminar separation, the vortex street and the transition in the wake ($\lambda_2 = -0.01$ criterion, colored by vorticity magnitude). Computation by F. Hindenlang [100].

3. Numerics for Scale-Resolving Simulations

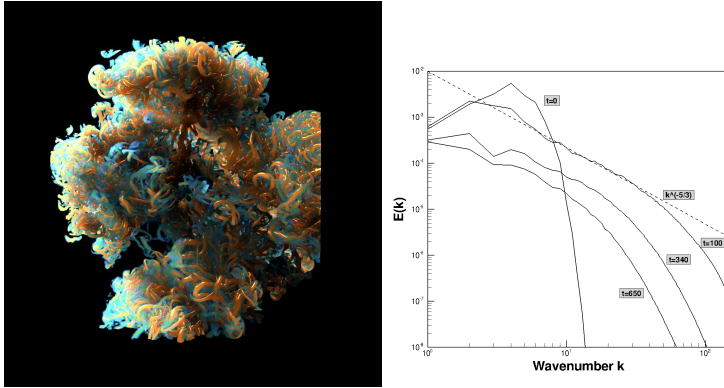


Figure 3.11.: Vortex Cascade at $Re = 1000$. *Left:* λ_2 isocontours, colored by helicity. *Right:* Temporal development of energy spectrum.

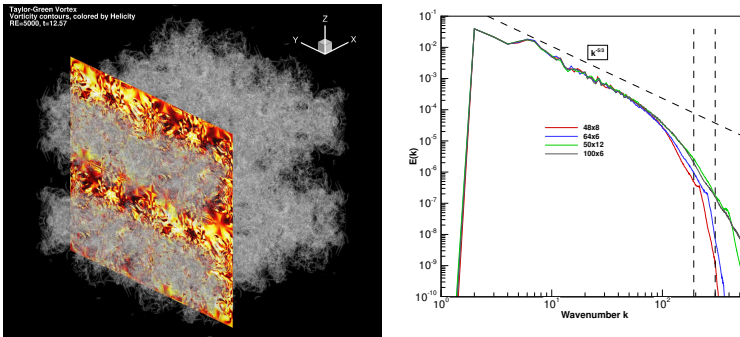


Figure 3.12.: Taylor-Green Vortex at $Re = 5000$. Computation with 384^3 and 600^3 DOF on 125,000 cores on BlueGene P (“Jugene”) at JSC. *Left:* Isocontours of vorticity magnitude, colored by helicity. *Right:* Spectrum of kinetic energy for 384^3 and 600^3 DOF, corresponding cut-off wavenumbers denoted by dashed lines.

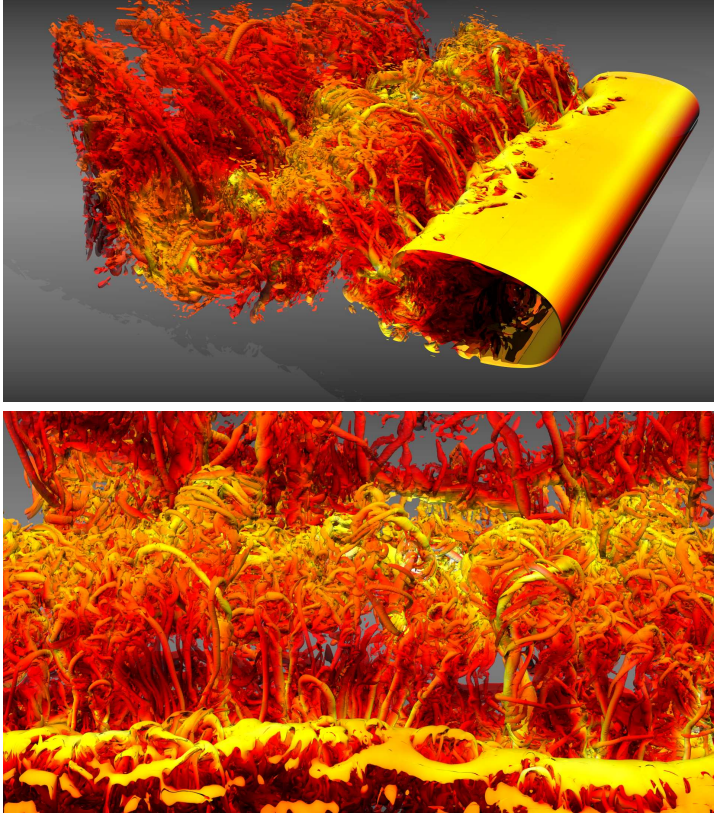


Figure 3.13.: Flow over a circular cylinder at $Ma = 0.1$, $Re = 3900$. Computation with 164 mio DOF on 4, 992 cores on Cray XE6 “Hermit” at HLRS. $\lambda_2 = -0.001$ criterion, colored by vorticity magnitude.
Top: side view. *Bottom:* Top view of near wake.

4. Numerics for Under-Resolved Simulations

In Chapter 3, we have presented a numerical scheme optimally suited for scale-resolving simulations. It provides high geometrical flexibility due to unstructured meshes, as well as excellent computational efficiency on High Performance Computing (HPC) platforms. Due to its spectral character, the “solution quality per invested DOF” is very high compared to other discretizations, which results in fast convergence for well-resolved problems.

As highlighted in Chapter 1, the full resolution of all scales in a multiscale problem remains only feasible for a limited set of moderately complex flows. The limits of the simulation envelope can easily be overstepped by a mere doubling of the Reynolds number. This is a different interpretation of the “curse of dimensionality” concept, as for three-dimensional, time-dependent problems, the scales and therefore the resolution requirements are coupled across all dimensions. Thus, full scale-resolving simulations are the exception, while marginally or under-resolved simulations remain the rule. This in turn opens two issues, both of which have been discussed in Sections 2.3 and 2.4: i) A conceptual approach to limit the number of scales or to regularize the problem becomes necessary. ii) If a perfect regularization is not possible and the closure is imperfect, the solution of the regularized problem becomes dependent on the discretization of the regularizing mechanism, of an explicit or implicit closure and of the equations themselves. In this chapter, we will focus on the LES approach to reduce the complexity of the problem, and we will discuss some of the aspects of numerics and modeling that become significant in under-resolved situations. We will discuss a strategy for LES with DGSEM, and present results for high order LES simulations of turbulent flows.

4.1. Challenges

In this section, we will briefly outline the challenges that arise in under-resolved situations as opposed to well-resolved problems discussed in Chapter 3. As discussed before, the fundamental challenge when simulating multiscale problems comes from the inherent under-resolution of the physical quantities. Thus, only a fraction of the occurring scales can be resolved and computed with sufficient accuracy. If we assume that the problem supports some form of scale structure, which can be distinguished and classified into waves or scales, we can denote the maximum number of physically occurring

4. Numerics for Under-Resolved Simulations

scales by K . In other words, the problem exhibits a range of scales of width K . Typically, only $m \ll K$ scales can be resolved due to the computational limits

$$\sum_{j=1}^K a_j(\vec{x}, t) \approx \sum_{j=1}^m \tilde{a}_j(\vec{x}, t). \quad (4.1)$$

When discretizing this problem, the approximation steps introduce several sources of error: The first one stems from the truncation itself

$$\epsilon_{trunc} = \sum_{j=m+1}^K a_j(\vec{x}, t), \quad (4.2)$$

which is due to the under-resolution of the problem and depends on two factors: i) the ratio of m/K and ii) the significance of scales beyond m for the solution. The importance of the high wavenumber scales depends on the physical problem, and the ratio m/K is determined by the amount of available computing resources, the time allotted for the computation and the efficiency of the discretization in terms of n_{PPW} . By defining the resolution of the computational grid via either the number of grid cells and/or the value of the local polynomial degree, the maximum representable wavenumber on this computational grid is limited by Nyquist's theorem: A wave can only be detected by a sign change, i.e. at least two points per wavelength are required to distinguish a signal. Thus, for a given computational grid with total resolution $(N_x \times N_y \times N_z)$, the upper bound on representable wavenumbers is given the Nyquist criterion per dimension as $N_x/2$, $N_y/2$ and $N_z/2$. This requirement of 2 PPW comes solely from information theory, the only discretization that can resolve waves accurately up to this limit are spectral Fourier methods, as discussed before, while other methods will incur a higher truncation error. Still, $N_x/2$, $N_y/2$ and $N_z/2$ is a valuable estimate, as it represents the theoretical limit of representable information on a given grid. One important aspect of the truncation error is that it is determined by the local resolution and that it thus limits the approximation quality a priori. Once the initial projection onto the available grid is completed, the discretization then interacts with the truncated solution. This interaction then introduces another source of error, namely the approximative determination of the grid-resolved scales $\tilde{a}_j(\vec{x}, t)$ via discretization operators, i.e. the error

$$\epsilon_{discj} = |\tilde{a}_j(\vec{x}, t) - a_j(\vec{x}, t)|, \text{ for } j = 1, \dots, m. \quad (4.3)$$

Note that for a non-linear problem, these discretization errors interact across the scales and will eventually influence all resolved scales $1, \dots, m$, even if ϵ_{discj} of a scale j is zero initially. Therefore, control and minimization of the numerical discretization error of the overall framework is the key to an efficient and reliable simulation. This includes

both the phase and the amplitude information (dispersion and dissipation error). Due to these errors, only those parts of the solution which are resolved by $n > n_{PPW}$ points per wavelength can be considered as accurately resolved, where n_{PPW} denotes again the theoretical limit depending on the discretization methods, as discussed in Section 3.1. It should be reiterated that the error relations can only be determined for linear problems and are then used as an estimate for the non-linear multiscale simulation. In Section 3.4, typical values from 4 up to 7 for n_{PPW} for efficient discretizations like high order polynomial based methods were discussed, while low order approximations with inherent upwinding can become prohibitively inefficient with $n_{PPW} \geq 25$. However, due to the under-resolution, even when using appropriate numerical methods with non-excessive dispersion and dissipation errors, there is always a range of scales in the approximate solution that is resolved with less than the optimal points per wavelength and is thus affected by numerical errors. As opposed to the discussion in Chapter 3, the fundamental difference between well-resolved and marginally resolved situations is the fact that the discretization is not only acting in the wavenumber region where its errors are minimal or zero, but across the whole range of scales represented on the grid. Thus, in terms of discretization accuracy, one should distinguish between resolved scales that carry no considerable discretization error and the represented scales, which are afflicted by errors. In Figure 3.2, the approximate range (determined by an arbitrary dispersion error bound) of those two scale bands has been indicated.

In addition to the errors occurring on the represented scales, the fundamental issue of non-linear multiscale problems like turbulence is that due to the interaction of the different scales, i.e. the influence of all scales onto each other, the temporal evolution of the approximative coefficients $\tilde{a}_j(\vec{x}, t)$ depends on the missing smaller scales, i.e. the truncation error from Equation (4.2) describing the subgrid scales. The effect of these scales not represented on the grid may have a significant influence on the represented and resolved scales. Thus, an effective numerical discretization must be augmented by a mechanism that models the physical effect of those missing subgrid scales for an accurate solution of the multiscale problem.

The complexity of the multiscale problem stems from the fact that these three sources of uncertainty (truncation, discretization and model) cannot be separated and even interact with each other. Therefore, all aspects of a numerical model have to be taken into account to judge its accuracy and efficiency.

4.1.1. Accuracy for Under-Resolved Problems

Numerical discretizations are typically constructed to minimize the approximation errors across the resolved scales, while keeping the formal design order of accuracy (an exception would be DRP FD schemes, that aim at extending the boundary between re-

solved and represented scales by sacrificing optimal convergence). In other words, they are commonly designed and analyzed for $h \rightarrow 0$, i.e. for a vanishing grid spacing and perfect resolution. The often used classification of discretizations based on their formal order of convergence is a statement about the behavior of the leading error term of the approximation as $h \rightarrow 0$, i.e. this concept is only meaningful when considering 'small' h . In fact, for 'large' h , a non-monotone error behavior is often observed, which only asymptotically returns to the design order when the grid is refined. A silent assumption, often not clearly stated in the high order CFD community, is that one needs sufficient smoothness of the underlying problem for high order discretizations to be efficient. For a multiscale problem, the underlying solution is smooth at the fine scale level, but can often only be coarsely resolved due to the large range of occurring spatial and temporal scales. This has the consequence of artificial roughness being induced by insufficient grid resolution. With respect to the discretization parameter, this entails that h is 'large' and thus the theoretical error behavior considerations for $h \rightarrow 0$ are not valid and not useful to judge the accuracy of high order methods. Statements about the superiority of these methods thus cannot simply be translated to the under-resolved case, which is the common case in practical fluid flow simulations and furthermore the rule in multiscale simulations.

Thus, a 'non-small' h is exactly the situation that occurs in a LES type approach to simulate multiscale problems. The only exception to this situation would occur in an explicitly filtered LES with a perfect subgrid closure, as shown in Section 2.4.2. If both the filtering operation (also a form of discretization with associated error) and the closure were perfect in a sense that they would regularize the problem and keep the range of scales bounded, then the associated grid spacing h_{disc} could be chosen independent from the filter width Δ , and h_{disc} and thereby the associated discretization error could be chosen arbitrarily small. However, the two basic assumptions in this idea (perfect filter and closure) cannot be met, unless in specifically constructed test cases, which are impractical for general use. Thus, in a typical LES setting, the problem is always under-resolved and the discretization is applied not only in the regime $h \rightarrow 0$ (it is of course for well-resolved parts of the problem). It is important to note that in those situations, the numerical discretization behaves drastically different to the resolved case and even unpredictably due to the non-linear nature of the underlying problem. In short, we can state that for 'large' discretization parameters h , the error of the approximation is 'large'. The exact definition of 'large' is difficult and strongly depends on the actual underlying problem, but error convergence in agreement with the design order of the scheme cannot be expected.

A better measure for the accuracy of the numerical discretization is not its behavior for small h , but rather its behavior when approximating solutions with a wide range of scales. Analysis methods for non-linear problems are still in their infancy and the only

possibility up to this point is to investigate their behavior for linear problems. In spite of this limitation, it is worth noting that this is still an important analysis, since one basically measures the accuracy of the derivative operator, which is also used to approximate the more complex non-linear problems.

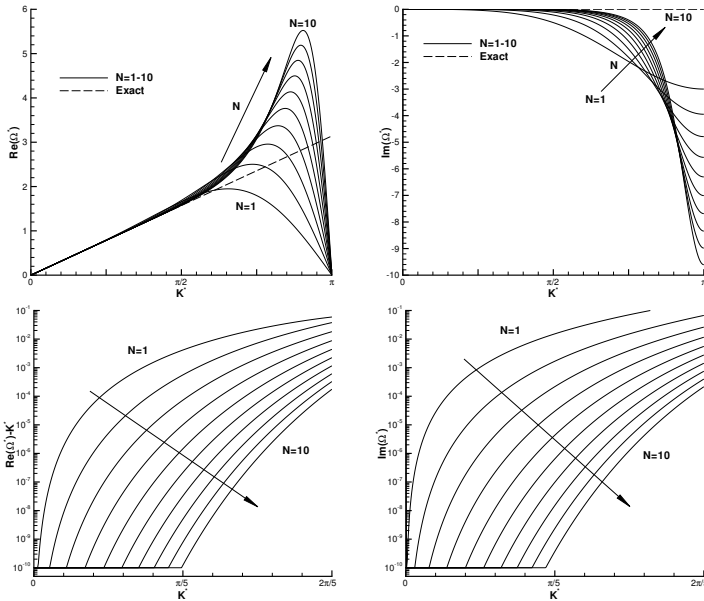


Figure 4.1.: Dispersion (*left*) and dissipation error (*right*) for DGSEM with Gauss nodes. $K^* = \frac{K}{N+1}$ is the normalized wavenumber and $\Omega^* = \frac{\Omega}{N+1}$ is the corresponding modified normalized numerical mode (eigenvalue). Bottom row: logarithmic plot with zoom on low wavenumber region. Note that the error is cut off at 10^{-10} to avoid numerical noise. Plots with permission from [85].

Figure 4.1 shows the dispersion and dissipation properties of DGSEM for varying polynomial degree N . Together with Figure 3.2 and Table 3.1, they show two essential issues: Firstly, for increasing N , the boundary between resolved and represented scales is pushed to higher wavenumbers, making higher order schemes more accurate over a

wider scale range. Secondly, as the resolution per scale decreases, the associated errors become significant, until at $K^* = \pi$, the wave is no longer represented by the approximation. This is in agreement with Nyquist's theorem which states that at least two points per wavelength are necessary to capture a wave. The reasons for the overshoot in the dispersion error, which give DG schemes their restricting explicit time step limit, have already been discussed before. For the dissipation error, the behavior towards large N moves towards a spectral cut-off filter. Since the strong form of DGSEM (Equation (3.31)) can be interpreted as a penalized spectral scheme, this behavior is not surprising, as with increasing N , the relative importance of the penalty dissipation is reduced, and the scheme becomes essentially a global spectral scheme in character.

Obviously, in a LES setting, all wavenumbers up to the Nyquist number will be part of the solution. Furthermore, the scales close to the grid cut-off will not be energetically small as in well-resolved situations, but contain significant dynamics. Thus, in such a situation, due to the relatively coarse grid, large errors in the discretization often cannot be avoided. When using the implicit filtering with implicit modeling approach for LES, it is important to note that these discretization errors are tuned in such a way that they replace the subgrid scale effects. In this sense, those discretization errors are in principle not a problem for this approach, since they are actively taken into account in the LES approach. On the other hand, the purely explicit filter and explicit modeling approach is not negatively impacted by this either, as in this case, the filter width is chosen larger than the grid resolution. Due to the explicit filtering of the solution, one actively ensures that only well resolved solution components are represented by the numerical approximation. In this case, the computation of the derivatives of the filtered solution components has small errors. However, when using the mixed approach, implicit filtering with explicit modeling, the solution has components with wavenumbers down to the Nyquist limit. The derivative operator working in this wavenumber range will then be inaccurate. In this case, the mixed approach with implicit filtering and explicit modeling has to deal with an interaction of the explicit turbulence model and the inherent numerical discretization errors. Due to the non-linearity of the underlying problem, this interaction is hard to predict and to quantify and can be either positive or negative on the overall fidelity of the approach. Hence, the mixed approach – although the most commonly used approach in LES – is the least suitable LES approach, except if one tunes the subgrid scale model depending on the actual discretization used.

4.1.2. Stability for Under-Resolved Problems

Stability of a discretization or numerical simulation is influenced by a number of factors, and the term “stability” is used in many different contexts, i.e. stability of an interpolation with respect to the nodes, temporal integration stability with respect to the time

step, stable boundary conditions, etc. While all those issues also have to be captured in under-resolved situations, a somewhat special stability issue becomes more prevalent for high order methods. We will discuss it here briefly and give more details in Section 4.2. An important issue not captured by the linear analysis is the influence of the approximation of non-linear terms, e.g. the convective terms in the Navier-Stokes equations. As discussed in Section 2.1.1 and in the discussion about Equation (2.2), the convective term drives the scale cascade and couples the interaction across the whole wavenumber range. It effectively sums the wavenumbers of two interacting scales, thereby introducing higher components. For the Burgers' or incompressible Navier-Stokes equations, the non-linearity is quadratic, i.e. a scale just at the grid Nyquist wavenumber N_{Nyq} will produce a scale at $2 N_{Nyq}$, thereby leaving the range of representable scales. For the compressible Navier-Stokes equations, where the Euler fluxes are cubic, this situation becomes worse. By definition, when introducing a cut-off through a LES resolution, this cut-off will almost always be located in the range where the non-linear term is dominant (inertial subrange). This scale truncation of the term introduces an additional source of error (besides the truncation itself), as the higher wavenumbers that are created contain information that must be evaluated correctly when solving the underlying equation. Correct evaluation of the represented scales then implies exact evaluation of these subgrid terms, which is contradictory to the definition of the subgrid itself, i.e. a grid with N_{Nyq} as a cut-off is not capable of resolving scales at $2 N_{Nyq}$. Still, these higher wavenumber components must be incorporated into the evaluation of the non-linear terms on the existing grid. The most basic – and mathematically problematic – way of doing that is by *aliasing* the higher frequencies onto the representable grid scales. However, while this is numerically efficient, it can lead to an unstable operator and thus to a guaranteed unstable solution. How this problem of aliasing is solved determines greatly the stability of high order methods in under-resolved situations, more details will follow in Section 4.2. The issue of aliasing instabilities could also be resolved by an explicitly filtered LES approach. In this case, the size of the smallest occurring scales and thus the smallest aliasing wavenumber can be decoupled from the spatial resolution, which is chosen sufficiently fine such that all sub-filter scales and their non-linear interactions are well-resolved. However, although such an explicit filtering approach is very beneficial on paper, the additional work associated with the proper resolution of the smallest eddies comes with a high computational cost. Another reason that explicitly filtered LES is less prevalent than its implicit counterpart is the additional mathematical and numerical complexity introduced through the explicit filter operator, in addition to some open issues such as the commutation properties of the filter at boundary conditions and the filter isotropy on non-regular grids. For those reasons, practical applications of explicitly filtered LES are relatively scarce [26, 133]. Therefore, we will focus on implicitly filtered LES, where the discretization itself acts as a filter via the projection of the solution onto

the computational approximation space in every time step.

Besides the issues stemming from improper discretization of non-linear terms, another source of instability comes from the truncation error itself. Since in LES, the cut-off is typically chosen far away from the dissipation region, the solution lacks a regularization mechanism to account for the missing scales or their effects. Also, the lack of represented scales blocks the scale cascade, as not all partners for the triadic interaction are represented on the grid, leading to errors introduced into the large scales [63]. Therefore, if these effects are not modeled properly, instabilities may occur from “insufficient” physics representation. The mechanisms by which this problem manifests itself are typically strong gradients and oscillations in the velocity field, i.e. the velocity field appears “rough”. For incompressible formulations, this can lead to convergence problems for the elliptic pressure solver, but the underlying equations are usually not violated. For compressible solvers, this situation is quite different, as strong oscillations will quickly shift energy from internal to kinetic energy (the total energy is the conserved variable), causing violations of the constitutive equations, i.e. typically the gas law. Therefore, instabilities introduced by truncation are caused by a non-perfect closure, not by numerical approximations. Thus, a fundamental problem with under-resolved approximations of turbulence is that at least two de-stabilizing mechanisms exist. Therefore, the turbulence modeling aspect has to be extended by these stability issues: In a non-optimal LES approach, the role of the turbulence model is often first to stabilize the computation and not to model the physical effect of missing scales. Especially when using the mixed LES approach, i.e. implicit filter and explicit model, one deals with solution components at Nyquist’s limit and hence with possible aliasing issues. For the purely explicit filtering and explicit modeling approach aliasing issues can be circumvented when the explicit filter width is large enough compared to the actual grid size. In the implicit filtering and implicit modeling approach, the issue of aliasing and stability is actively incorporated into the discretization and accounted for by tuning the discretization errors to act as the turbulence model. It is worth pointing out that there are discretizations and formulations which are aliasing free. Most prominent is the case of the incompressible Navier-Stokes equations, which can be formulated in the so called skew-symmetric form. Discretizations based on this skew-symmetric form retain the kinetic energy balance and are hence free of stability issues [144]. For the compressible Euler equations, such energy-bounded forms are a current topic of research [83, 172].

In summary, three issues arise in under-resolved discretizations. First, the accuracy of a discretization strongly depends on the resolution of each scale and deteriorates with increasing wavenumber. Methods with good dispersion and dissipation behavior over a large range of scales are favorable for this task, whereas the property ‘formal order of convergence’ is in such cases irrelevant due to the discretization parameter h being large

and not asymptotically small. Second, operating near Nyquist's limit opens the door to aliasing related issues which can even affect the stability of the overall discretization. The impact of this non-linear stability is different for the three different LES approaches and must be taken into account individually. Lastly, modeling of the truncation error or its effects must regularize the problem and prevent a violation of the conservation laws, which could render the truncated problem unstable due.

4.2. Aliasing Errors

The term aliasing is often defined as “misrepresentation of high frequency content (beyond the grid cut-off) as lower frequencies”. This is a rather general description, which de-emphasizes the most important aspect of aliasing in terms of multiscale problems like turbulence – its self-feeding mechanism. Aliasing occurs when a physical non-linear mechanism is wrongfully represented on a lower-dimensional grid, i.e. aliasing is the violation of some (physical) governing law by numerical inaccuracy. It is obvious that for fully resolved simulations, where the grid resolution is sufficient to resolve all scales and their occurring interactions, aliasing is not an issue. For under-resolved simulations where the modal content in the higher modes is not negligible, these aliasing errors accumulate energy in the high modes, and eventually lead to an instability of the scheme. In particular, if the higher modes become excited and more energetic through aliasing, they will in turn generate additional high energy aliasing errors. Or, in terms of turbulent scales, when energy is pushed into the scale range near grid cut-off, the cascade to smaller scales (i.e. the feeding of the aliasing mechanism) will be enhanced. Thus, aliasing is directly related to the under-resolution of a multiscale problem, and thereby to the LES approach. Also, the non-linearity of the physical process is important, as it leads to a growth of the aliasing error and finally to the blow-up. In this section, we will give details about the origin and effect of aliasing and on numerical strategies countering it.

4.2.1. Source and Effect

4.2.1.1. Conservation of Kinetic Energy

As stated above, aliasing by misrepresentation of the non-linear term can violate the flow physics. In Section 2.1.2.3, we discussed that the non-linear term in spectral space, when summed over all wavenumbers, cancels out, and does not contribute to the kinetic energy equation (see also Equation (2.19)). We also demonstrated in Equation (3.18) how a misrepresentation (rather: an under-representation) of non-linear products in a collocative manner can introduce an error term into the representation that acts on the

high wavenumbers. We will repeat this discussion here briefly with a very simple model for the continuous incompressible Navier-Stokes equations.

Starting from the Equation (2.17), we take the scalar product of the momentum equation for u_i with u_i itself, just focusing on the non-linear term:

$$u_i \cdot \left(\frac{\partial u_i u_j}{\partial x_j} \right) = \frac{1}{2} \frac{\partial u_i u_j u_i}{\partial x_j} + \frac{1}{2} u_i u_i \frac{\partial u_j}{\partial x_j}. \quad (4.4)$$

Since the divergence condition $u_{i,i} = 0$ holds, the continuous non-linear term thus conserves kinetic energy and only modifies it through fluxes across the domain boundaries. We now assume some error of the form $k(u_i)$, with $k \in \mathbb{R}$, in the continuous term (as a simplistic model for an error introduced by the differential operator acting on the non-linearity), this error modifies the representation of $u_i u_j$ to $\approx u_i u_j k(u_i)$. Then, the contribution of the convective term becomes

$$u_i \cdot \left(\frac{\partial u_i u_j k}{\partial x_j} \right) = \frac{1}{2} \frac{\partial u_i u_j u_i k}{\partial x_j} + \frac{1}{2} u_i u_i k \frac{\partial u_j}{\partial x_j} + \frac{1}{2} u_i u_j u_i \frac{\partial k}{\partial x_j}, \quad (4.5)$$

where the first two terms on the right hand side again do not change the kinetic energy budget, but a third term that is generally non-zero and has an unknown sign appears. This term thus acts as a source (or sink) for the kinetic energy, thereby violating the kinetic energy budget.

While this simple demonstration was based on the continuous equation, the same mechanism (the misrepresentation of the non-linear term) can be introduced through the discretization of this term. Figure 4.2 depicts the influence of the aliasing error on the flow physics for the Taylor-Green vortex. Focusing on the left subplot first, the evolution of the mean temperature (as a measure of internal energy and normalized by the initial value) and the kinetic energy dissipation rate are shown. Since the discretization conserves the total energy and all boundary conditions are periodic, the energy just changes its form between internal and kinetic energy. The black curves denote a discretization which allows aliasing errors, while the red curve is an aliasing-free solution. More details on the de-aliasing procedure are given in Section 4.2.2. Note that the transfer of kinetic to internal energy is enhanced for the aliasing-influenced solution, resulting in a higher final mean temperature. This is the effect of the increased dissipation rate, which in turn results from the excitation of the higher wavenumbers through aliasing. The aliasing errors transfer kinetic energy into the upper third (for an essentially incompressible flow) of the polynomial modes, thereby enhancing vorticity on these scales, which is then attacked by both physical and numerical dissipation. Therefore, although the aliasing energy is initially injected into the kinetic energy cascade, it eventually results in higher dissipative losses, if numerical and resolved dissipation are strong enough to keep the simulation stable. The right plot in Figure 4.2 shows the temporal evolution of

maximum of the vorticity within the domain. Clearly, the aliasing-influenced vorticity shows more pronounced peaks, resulting from the aliasing energy injected into the high wavenumber modes. As discussed above, this increase in small scale activity results in higher energy dissipation. Thus, these plots indicate that aliasing errors indeed act as a source term within in the kinetic energy equation, locally increasing gradients and high wavenumber energies, which – if kept bounded – induce a more rapid transfer to internal energy.

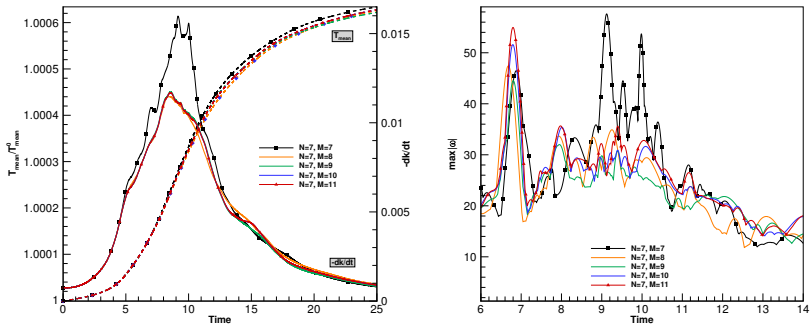


Figure 4.2.: Taylor-Green Vortex at $Re = 1000$. Effect of aliasing on flow physics.
Left: Mean temperature and kinetic energy dissipation rate over time.
Right: Maximum vorticity over time.

4.2.1.2. Discretization of the Non-Linear Term

In Section 3.2, we introduced the concept of inexact evaluation of non-linear products through collocation for the pseudo-spectral methods. The same error is introduced into a DG method when the inner products of non-linear terms are not evaluated exactly, i.e. when the underlying projection onto the test functions becomes inexact. It should be noted that in DGSEM, where the interpolation and integration are collocated on the same nodes, both operations introduce this form of error, as the Gauss quadrature relies on the interpolation of the integrand. We will now discuss how the aliasing error occurs in DGSEM, depending on the discretization choice of the non-linear term.

4. Numerics for Under-Resolved Simulations

In Section 3.3.2, we introduced the transformed flux function in Equation (3.26) as

$$\mathcal{F}^l(\vec{\xi}) \approx \sum_{i,j,k=0}^M \hat{\mathcal{F}}_{ijk}^l \psi_{ijk}^M(\vec{\xi}), \quad l = 1, 2, 3, \quad (4.6)$$

$$\hat{\mathcal{F}}_{ijk}^l = \mathcal{G}(U) - \mathcal{H}(U, \vec{\nabla}_x U) |_{\vec{\xi}_{ijk}}, \quad (4.7)$$

where the non-linearity of the advection part of the flux $\mathcal{F}^l(U)$ is either quadratic for incompressible flows or cubic in a compressible setting with respect to the primitive variables. When evaluating the compressible flux in terms of conserved variables, it even becomes a rational function. Note that in Equation (3.26), we have chosen an ansatz of degree M for the fluxes, which is independent from the ansatz of degree N for the solution itself. Since \mathcal{F}^l is a non-linear product of the solution U and therefore may have a larger wavenumber range than the solution, a collocation of \mathcal{F}^l on $(N+1)^3$ solution points $\vec{\xi}_{ijk}$, which in our implementation double as integration nodes, would introduce an error in the interpolant (Equation (3.26)) and subsequently in the associated integration, the volume contribution of Equation (3.29):

$$\begin{aligned} \int_E \mathcal{F}^l \frac{\partial}{\partial \xi^l} \phi(\vec{\xi}) d\vec{\xi} &\approx \int_E \sum_{i,j,k=0}^M \hat{\mathcal{F}}_{ijk}^l \psi_{ijk}^M(\vec{\xi}) \frac{\partial}{\partial \xi^l} \phi(\vec{\xi}) d\vec{\xi} \\ &\approx \sum_{p,q,r=0}^M \sum_{i,j,k=0}^M \hat{\mathcal{F}}_{ijk}^l \psi_{ijk}^M(\vec{\xi}_{pqr}^M) \frac{\partial}{\partial \xi^l} \phi(\vec{\xi}) \Big|_{\vec{\xi}=\vec{\xi}_{pqr}} \omega_p^M \omega_q^M \omega_r^M \\ &= \sum_{p,q,r=0}^M \hat{\mathcal{F}}_{pqr}^l \frac{\partial}{\partial \xi^l} \phi(\vec{\xi}) \Big|_{\vec{\xi}=\vec{\xi}_{pqr}} \omega_p^M \omega_q^M \omega_r^M, \end{aligned} \quad (4.8)$$

where we have introduced the approximation of the integral through a tensor product of one-dimensional Gauss quadratures with $(M+1)^3$ associated nodes ($\vec{\xi}_{pqr}^M$) and weights ($\omega_p^M, \omega_q^M, \omega_r^M$). Since \mathcal{F}^l is at most a polynomial of degree $3N$ for compressible flows, there exist values of M for which the quadrature of the right hand side of Equation (4.8) becomes exact. From the exactness of the quadrature rule, M is found to be $2N$ for cubic and $\frac{3}{2}N$ for quadratic non-linear integrands. Consequently, an inexact integration of these terms, i.e. an insufficient choice of M , results in an approximation error of the non-linear fluxes: the aliasing error discussed in Section 4.2.1.1.

4.2.1.3. Operator Spectrum

We now turn to an investigation of the effect of this inexact integration on the stability of the DG operator itself, as shown in [19]. To highlight the effects of the choice of M , we consider the following linear transport model problem with non-constant advection velocity in a periodic domain

$$u_t + (a(x) u)_x = 0, \quad x \in [-1; 1]. \quad (4.9)$$

By choosing the advection speed $a = a(x) > 0$, we can simulate aliasing and can investigate its effect on the operator spectrum for different number of integration points $M + 1$. While it might seem that the linear transport Equation (4.9) is too simplistic to serve as a model for aliasing effects in the full Navier-Stokes equation, it should be noted that Equation (4.9) can be interpreted as a linearization of Burgers' equation about a given "turbulent" state $u_0(x) = a(x)$. Since the scale-producing mechanism of Burgers' equation is similar to that of the Navier-Stokes equations, we can control the non-linearity in the convective term and thereby the aliasing effects.

For a single grid cell $[-1; 1]$, periodic boundary conditions and an upwind flux at the element edges, the DGSEM formulation (3.40) in matrix-vector notation reduces to [85]

$$\underline{M} \frac{\partial \underline{u}}{\partial t} + \underline{S} \underline{a} \underline{u}^- + \underline{V} \underline{a} \underline{u} = 0, \quad (4.10)$$

where $\underline{u} := (u_0(t), \dots, u_N(t))^T$ is the vector of nodal DOF, $\underline{a} \underline{u}$ is the collocation vector of \underline{u} and \underline{a} , and $()^-$ indicates an evaluation from the (periodic) neighbor. The matrices are given by

$$\begin{aligned} M_{ij} &= \delta_{ij} \omega_i, \\ S_{ij} &= -\ell_i(-1) \ell_j(1), \\ V_{ij} &= \ell_i(1) \ell_j(1) - D_{ji} \omega_j, \end{aligned} \quad (4.11)$$

with D_{ji} , ℓ_i and ω_i as defined in Section 3.3.2.5. Inverting the diagonal mass matrix and collecting terms, this can be written as a linear dynamical system for fixed $a(x)$ as

$$\underline{u}_t = \underline{\underline{A}}^M \underline{u}, \quad (4.12)$$

where $\underline{\underline{A}}$ is the spatial operator containing the surface and volume fluxes integrated with a specific Legendre Gauss integration rule M (and thus $M + 1$ integration nodes and integration precision $2M + 1$). Note that for this linear system, the solution \underline{u} remains stable if all eigenvalues of the operator matrix have zero or negative real parts. We now take a look at different choices of $a(x)$ and M , and the associated eigenvalue spectra.

Constant Advection Velocity

For this simplest case, we choose the advection speed $a = 1 = \text{constant}$. Thus, if the solution u is a polynomial of degree N , the flux function is also a polynomial of degree N . Then, $N + 1$ Gauss points with integration precision $2N + 1$ are more than sufficient to integrate the flux exactly. The corresponding spectrum of the DG operator for $N = 15$ is plotted in Figure 4.3. As expected, the linear flux can be treated exactly with $N + 1$ points and thus the spectrum does not change when increasing the number of integration points to 26. The maximum of the real parts of the eigenvalues is 0, confirming the stability of the DGSEM operator for this linear advection velocity.

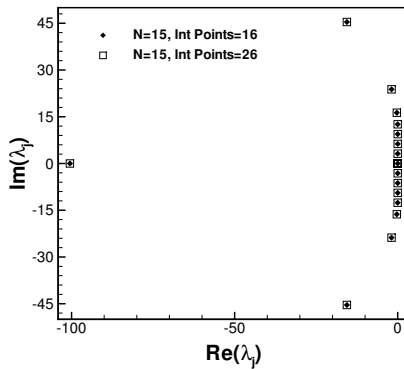


Figure 4.3.: Operator spectrum for constant advection speed and $N = 15$ with either $M + 1 = 16$ or 26 integration points, respectively. The maximum of the real parts of the eigenvalues is 0.

Polynomial Advection Velocity

We now select a polynomial advection speed, as this can still be integrated exactly with polynomial-based integration rules. We choose

$$a(x) = 1 + (1 - x^2)^{15}, \quad (4.13)$$

a polynomial of degree 30. For the volume inner product, the flux is multiplied by the spatial derivative of the test function (through the matrix \underline{D}), resulting in a total polynomial degree of $N_{tot} = 30 + N + (N - 1) = 2N + 29$. For an exact evaluation,

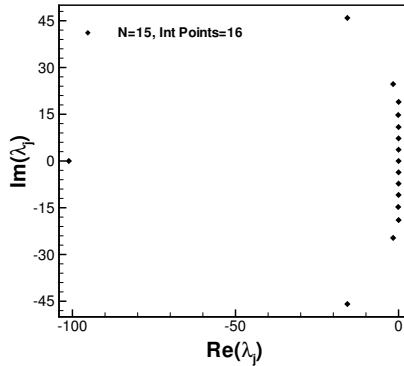


Figure 4.4.: Operator spectrum for polynomial advection speed and $N = 15$ with $M + 1 = 16$ integration points (original DGSEM scheme). The maximum of the real parts of the eigenvalues is 0.016.

$N + 14$ Gauss points are needed. Figure 4.4 shows the spectrum of the resulting DG operator for $N = 15$ and $M + 1 = 16$ integration points. The general shape of the spectrum is similar to the constant case, as the selected polynomial advection speed lies between 1 and 2. Note that this discretization, with a collocation of the flux and the solution on the same grid, is the original form of DGSEM [120]. A closer look at the maximum of the real parts of the eigenvalues reveals that the value is positive and about 0.016, which means that due to the insufficient integration precision, the DG operator has become unstable, and would produce an unbounded solution in time, regardless of the time step. In other words, returning to the discussion in Sections 4.2.1.1 and 4.2.1.2, the inexact treatment of the convective term has resulted in a violation of the governing equation already through a faulty discretization operator.

Since the advection speed is a polynomial, increasing the integration precision M should recover the original stability of the scheme. Figure 4.5 shows the resulting spectrum as a function of M , and Table 4.1 summarizes the maximum of the real parts of the eigenvalues of the associated DGSEM operator. Both the table and the right plot of Figure 4.5 show that by increasing the number of integration points, the real part of the operator eigenvalues move from the unstable region towards the imaginary axis. For $M = 29$ integration points and above, the real parts of the eigenvalues are not positive anymore, resulting in a stable de-aliased approximation.

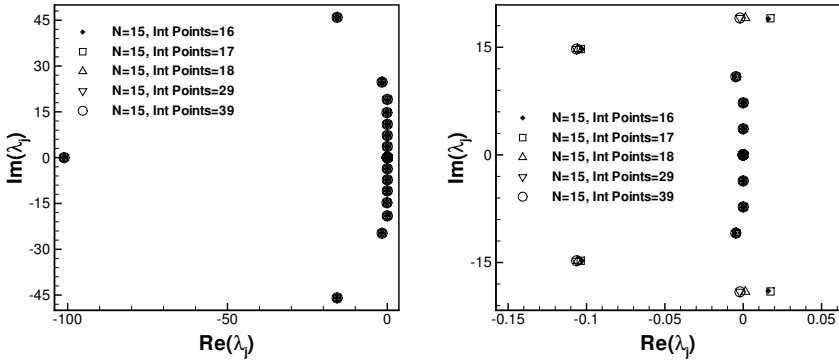


Figure 4.5.: Operator spectrum for polynomial advection speed and $N = 15$ with different number of integration points $M + 1$. The right plot shows a zoomed view of the imaginary axis.

Sinusoidal Advection Velocity

As a final test, we choose two non-polynomial functions

$$a(x) = \frac{1}{2} \left(2 + \sin 2\pi x + \frac{2}{3} \sin 3\pi x \right), \quad (4.14a)$$

$$a(x) = \frac{1}{2} \left(2 + \sum_{j=2}^8 \frac{14}{5j} \sin j\pi x \right), \quad (4.14b)$$

where (4.14b) is just a slight modification of (4.14a) with additional higher frequency terms and a weaker decay of amplitudes. These sinusoidal functions are chosen to re-

Int Points $M + 1$	16	17	18	19	29	39
$\max_j [Re(\lambda_j)]$	$1.6 \cdot 10^{-2}$	$1.7 \cdot 10^{-2}$	$1.4 \cdot 10^{-4}$	$2.6 \cdot 10^{-6}$	0	0

Table 4.1.: Maximum values of the real parts of the eigenvalues of the DGSEM operator ($N = 15$) spectrum with different number of integration points for the polynomial advection velocity.

semble the fluctuating velocity field characteristic of turbulence more closely than the previous test cases.

Due to their non-polynomial nature, it is not possible to integrate the resulting flux function exactly using Gauss-based integration rules. However, by increasing the integration precision to a sufficiently high degree, the integration error can be driven to machine zero and thus becomes negligible. The amount of Gauss points required to achieve this elimination of the error clearly depends on the considered advection speed function, i.e. on its type (polynomial vs. non-polynomial) and on its spectral energy content. The results for advection speed (4.14a) and (4.14b) are shown in Figures 4.6 and 4.7, respectively. The maximum values of the eigenvalue real parts for both functions are shown in Table 4.2.

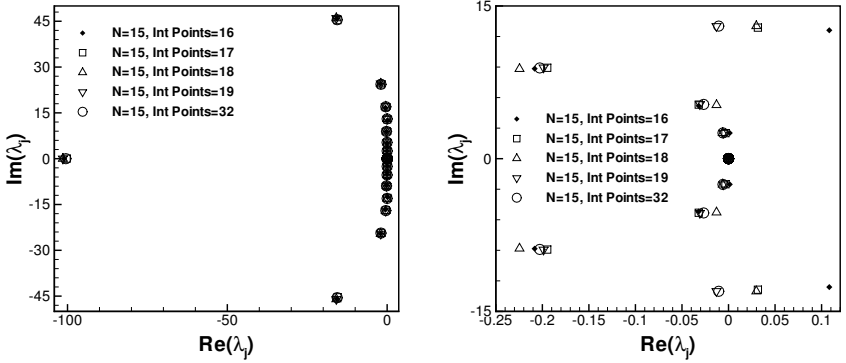


Figure 4.6.: Operator spectrum for sinusoidal advection speed, Equation (4.14a), and $N = 15$ with different number of integration points $M + 1$. The right plot shows a zoomed view of the imaginary axis.

For both sinusoidal functions, the original DGSEM formulation with $M = N$ contains eigenvalues with positive real parts. Increasing the amount of integration points moves these unstable eigenvalues towards the imaginary axis and beyond, thereby recovering stability. For $M \geq 19$ for the lower frequency function and $M \geq 21$ for the higher frequency one, the resulting de-aliased operator is stable with non-positive real parts of the eigenvalues. As expected, the higher frequency advection velocity (4.14b) requires more integration effort to achieve stability.

4. Numerics for Under-Resolved Simulations

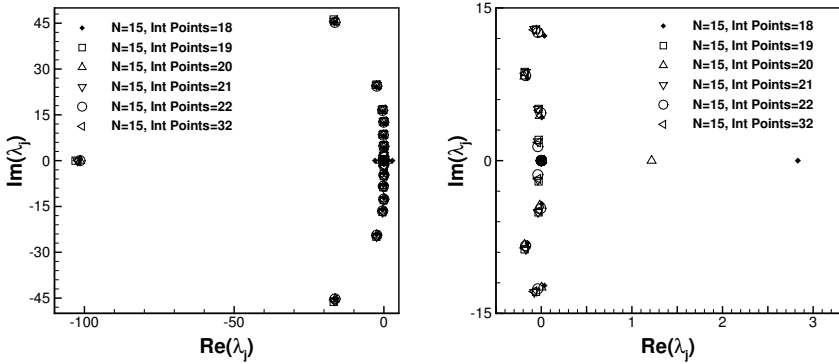


Figure 4.7.: Operator spectrum for sinusoidal advection speed, Equation (4.14b), and $N = 15$ with different number of integration points $M + 1$. The right plot shows a zoomed view of the imaginary axis.

Eqn.	Int Points $M + 1$	16	17	18	19	20	21	22	32
(4.14a)	$\max_j [Re(\lambda_j)]$	$1 \cdot 10^{-1}$	$3 \cdot 10^{-2}$	$3 \cdot 10^{-2}$	0	0	0	0	0
(4.14b)	$\max_j [Re(\lambda_j)]$	4	$4 \cdot 10^{-3}$	2.8	0	1.2	0	0	0

Table 4.2.: Maximum values of the real parts of the eigenvalues of the DG operator ($N = 15$) spectrum with different number of integration points for the sinusoidal advection velocity.

4.2.2. De-Aliasing Strategies

As discussed in Section 4.2.1, the approximation of the flux function is an important discretization choice that determines the stability of the scheme. For the Navier-Stokes equations, the flux function is a non-linear function of the solution and thus in particular not a polynomial of degree N anymore. The inaccurate approximation of the inner products can cause severe aliasing issues for high order methods and influence the solution quality, even if the overall solution remains bounded due to numerical and resolved

dissipation.

In the following, we discuss different strategies for the discretization of the non-linear term to remove aliasing errors and provide a neutrally stable discretization.

4.2.2.1. DGSEM

Starting with the most basic discretization, the DGSEM scheme introduced in Section 3.3.2, we note that this scheme is *not* a properly de-aliased scheme, but just the opposite due to the collocation. It is listed here as a first variant for two reasons: i) It serves as a reference scheme in terms of accuracy, efficiency and stability for the following discussion and ii) for low N , the numerical dissipation of the scheme can provide some robustness against aliasing errors, so that this can be interpreted as an “implicitly de-aliased” version. For this approach however, stability cannot be shown or guaranteed, as the introduced numerical diffusion is dependent on the local resolution and may or may not be sufficient to prevent aliasing accumulation. It should be noted here that the aliasing mechanism is self-sustaining and self-incident: If energy is aliased into the upper modes, these modes will in turn excite a transfer down the cascade to higher (subgrid) modes, which will again be deposited onto the represented scales. Thereby, the energy content in these modes increases constantly. Therefore, if constant energy is supplied to the cascade, the aliasing mechanism will either cause a blow-up due to the continued increase in high frequency content, or it must be bounded by some form of de-aliasing. As shown in Section 3.4, DGSEM is the fastest variant of the DG methods, due to the collocation of the nodal interpolation approximation and the evaluation of the integrals, i.e. the same set of interpolation and integration nodes. By choosing the integration rule in Equation (4.8) as $M = N$, we use the same ansatz for the fluxes as for the solution, reducing the effort in the evaluation of the nodal flux values. Furthermore, the quadrature rules are based on the same nodes, making the evaluation of the integrals highly efficient. The price one pays for this high efficiency is that the approximation of the flux function with polynomial degree $M = N$ is prone to severe aliasing errors. Note that this issue is certainly not exclusive to the DGSEM variant. The choice of $M = N$ for the precision of the quadrature rule is very common in the DG community for both the nodal DG and the modal DG discretizations and hence all of those variants are vulnerable to the same aliasing issues which result from this *under-integration*.

4.2.2.2. Projection DG

As demonstrated in Section 4.2.1.3, inexact integration causes operator instabilities. Thus, a natural remedy for this problem, first discussed by Kirby and Karniadakis [111], is to increase the integration precision according to the non-linearity of the flux func-

tion. Based on the general idea of de-aliasing by exact projection developed by Orszag [153], they showed that de-aliasing for polynomial spectral methods (often called over-integration in this context) is achieved similarly by choosing a sufficient integration precision with respect to the flux function. In other words, the non-linear functions are evaluated with sufficient precision to remove the aliasing ambiguities, i.e. on a finer grid (or with more DOF), and the resulting flux is then incorporated into the spatial operator on the solution grid in a consistent manner, i.e. by projection. The drawback is the increase in the computational complexity through the number of quadrature nodes. For weakly compressible flows at low Mach numbers $Ma \leq 0.1$, the non-linearity of the flux function becomes approximately quadratic, and thus the Gauss quadrature rule demands $M = \frac{3}{2} N$, for higher Mach numbers, M has to be $2N$ for complete de-aliasing (disregarding the fact that the fluxes become rational, when computed from polynomial conservative variables). Another very important aspect when choosing the quadrature rule is that the transformation of the fluxes onto the reference element incorporates the element mapping (through the grid metrics and the Jacobian) into the covariant transformed fluxes (see Equations (3.22) and (3.26)). Thus, the actual flux function to be integrated is no longer solely determined by the complexity of the physical flux, but also by the polynomial mapping. Depending on the degree of the mapping, a higher integration precision might be necessary for exact integration; however, a full investigation of this is still missing. One important distinction should be kept in mind: While insufficient integration of the mapping will introduce an error into the solution, this aliasing error is static in the sense that it does not depend on a temporally evolving field like dynamic solution aliasing: The grid mapping is constant in time, therefore, this error contribution will not self-feed.

Returning to the integration rule as prescribed by the physical fluxes, the choice of M clearly governs the overall computational costs, which is for high N – according to the discussion in Section 3.3.2.5 – mainly a function of the integration effort for the volume integral. Thus, the general behavior observable in actual computations is $\sim \left(\frac{M}{N}\right)^3$, i.e. about 8 in case of $M = 2N$ and about 3.3 in case of $M = \frac{3}{2} N$.

It should be noted that while the values for M derived from the exactness of the quadrature rule result in an exact integration and thus an exact projection of the fluxes, our experience and other published work indicate that a “full” de-aliasing might not always be necessary. Malm et al. [136] showed that for a continuous spectral element method for incompressible flow, a de-aliasing strategy with M^* modes with $N < M^* < \frac{3}{2} N$ can be sufficient, especially when combined with some form of dissipation like SVV. They proposed that only the first aliasing mode has to be integrated exactly, as it is the most energetic one. In our investigations, we found “incomplete” de-aliasing to be sufficient for stabilization of medium Reynolds number flows at moderate spatial resolutions.

In particular, we noted that stability could be regained for these situations by choosing $M^* = N + 1$ or $M^* = N + 2$ [18]. In combination with the numerical dissipation of the scheme, incomplete de-aliasing can thus be sufficient, but does not guarantee stability. It should be remarked (as noted by Kirby and Karniadakis in [111] and shown in Table 4.2), that an increase in M^* does not show a monotone convergence towards stability. Figure 4.2 shows an example of incomplete de-aliasing. Although the DGSEM version ($N = 7, M = 7$) is stable due to the supporting numerical dissipation, de-aliasing with $M = N + 1 = 8$ results in a significant solution change, in particular in the maximum vorticity, indicating that the first aliasing mode is the most important one. Subsequent increase of M only results in minor changes and a convergence of the observed quantities. In the following, unless stated otherwise, we will consider the complete polynomial de-aliasing as given by the nature of the flux function. As in this particular DG discretization the inner products are evaluated exactly (with respect to machine precision), i.e. by projection and not by interpolation, we abbreviate this variant as PDG (projection DG). Other commonly used names are “over-integrated DG” or “polynomial de-aliasing DG”.

- Remark 1: For well-resolved simulations, like DNS of turbulent flows, the difference between the PDG and the DGSEM variants decreases to the point where the DGSEM variant becomes the best choice due to its efficiency. In contrast to the DNS situation in Chapter 3, here we are interested in the behavior of these discretization in a LES type setting where the simulation is by definition under-resolved and the grid size is large, and thus aliasing errors will be important.
- Remark 2: Equation (3.29) highlights another important aspect of the de-aliasing operation: once the inner products are evaluated exactly through sufficient quadrature, the only remaining parameters in the spatial discretization are the viscous and inviscid numerical flux choices \mathcal{H}_n^* and \mathcal{G}_n^* . Thus, through exact integration, the “original” DG scheme and its properties can be recovered and analyzed, without interference from the choices of discretization. Therefore, this formulation is particularly attractive for the evaluation of the DG scheme, the effects of LES subgrid scale models or the choice of the flux functions [20].
- Remark 3: Extension of our DGSEM framework to incorporate this approach is straightforward by using a sharp modal cut-off filter. The calculation is thus performed with a polynomial degree M , i.e. the full spatial operator is evaluated on the fine grid that supports the non-linearity. The approximate solution is then filtered in every Runge-Kutta stage before evaluating the spatial residual using the

filter coefficients

$$\sigma_i := \begin{cases} 1 & \text{if } 0 \leq i \leq N, \\ 0 & \text{if } N + 1 \leq i \leq M, \end{cases} \quad (4.15)$$

which makes certain that only $N + 1$ modes are used for the actual computation, but ensures that the inner products are evaluated with the desired amount of integration points. It is important to note that this exact quadrature does not increase the total number of DOF available for resolving a flow field, but it only removes collocation as a source of error.

- Remark 4: For DGSEM, where solution and fluxes are evaluated on a grid supporting N polynomial modes, an aliasing-influenced flux operator will pollute (in an incompressible situation and in a single operator evaluation) the upper third of the available modes. Opposed to this, for PDG, due to the expansion of the flux on the fine $M + 1$ grid and the subsequent projection back onto the solution grid $N + 1$ through polynomial de-aliasing, the solution modes stay error-free (except for the dissipation and dispersion errors and the effects of the subgrid closure) up to N . Kirby and Karniadakis [111] showed that polynomial de-aliasing is not a purely dissipative mechanism, as the magnitudes of modes either decrease or increase due to the over-integration. Thus, one interpretation of this form of de-aliasing is that it recovers the full solution modes up to N .

4.2.2.3. Filtering

As discussed above, aliasing in a polynomial based approximation typically causes an overestimation of higher polynomial modes, resulting in an oscillatory and even unstable approximation. This high frequency aliasing energy can be removed by dissipative filter techniques that dampen the magnitude of the affected modes. In combination with a collocation discretization like DGSEM, this can result in a stable simulation. One example of such an approach is an exponential based modal filter, e.g. [96]. To construct a modal, hierarchical basis from our nodal representation (Equation (3.25)), we introduce a modal orthogonal Legendre basis $\{\varphi_j(\xi)\}_{j=0}^N$ and compute the Vandermonde matrix \underline{V} associated with our nodal interpolation points $\{\xi_i\}_{i=0}^N$

$$V_{ij} := \varphi_j(\xi_i), \quad i, j = 0, \dots, N, \quad (4.16)$$

which allows us to transform any nodal DOF U to modal DOF \tilde{U} and vice versa

$$U = \underline{\underline{V}} \tilde{U} \quad \tilde{U} = \underline{\underline{V}}^{-1} U. \quad (4.17)$$

A one-dimensional filter matrix, which can again be applied in a tensor product approach, can be pre-computed as

$$\underline{\underline{F}} = \underline{\underline{V}} \underline{\underline{\tilde{F}}} \underline{\underline{V}}^{-1}, \quad (4.18)$$

with the modal filter matrix

$$\tilde{F}_{ij} = \delta_{ij} \sigma_i, \quad i, j = 0, \dots, N, \quad (4.19)$$

and the modal filter coefficients $0 \leq \sigma_i \leq 1$ with

$$\sigma_i := \begin{cases} 1 & \text{if } 0 \leq i \leq N_c - 1, \\ \exp\left(-\alpha \left(\frac{i+1-N_c}{N+1-N_c}\right)^s\right) & \text{if } N_c \leq i \leq N, \end{cases} \quad (4.20)$$

where α , s and N_c are the filter parameters. N_c indicates the number of the unaffected modes, α is typically chosen such that $\exp(-\alpha)$ is machine zero and s is an even number determining the strength of the filter (higher s means weaker filtering in terms of a sharp cut-off), see e.g. the book of Hesthaven and Warburton [96]. Clearly, this modal filter is a purely dissipative mechanism. If applied to a DGSEM formulation, it becomes effective within the modal range up to N , and will reduce the magnitude of the aliasing-afflicted (upper) modes. While this can prevent a blow-up, two disadvantages occur: i) The filter acts on the solution modes up to N , i.e. it affects the scale-resolving capabilities of the scheme and ii) stability and accuracy now depend on the additional filter parameters, which are not known a priori. As opposed to the PDG approach, this method does not prevent the occurrence of aliasing errors, but removes or controls its effects on stability, at the cost of resolution quality. That is, this aliasing countermeasure effectively increases the n_{PPW} requirement of the underlying scheme. The main advantage of this filter approach is its computational efficiency when combined with DGSEM. All operations remain on the N grid, and the additional filtering of the solution per Runge-Kutta stage increases the computational time insignificantly (on the order of 2-3% in our investigations).

Other approaches for removing or avoiding aliasing exist, which are not part of this work. Two should be briefly mentioned here for completeness: A variant of a PDG method labeled “line DG” was introduced in [163]. It takes advantage of the dimension-by-dimension form of the operator and only uses full quadrature precision in the normal direction of the fluxes, i.e. along the associated coordinate line. Persson was able to show stability for transitional flow over an airfoil at $Re = 20,000$ for a two-dimensional computation. Since the basic scale producing mechanism and thus aliasing contributor requires three-dimensionality, stability for realistic turbulence still has to be shown.

A different approach to prevent aliasing is to use split forms of the flux derivative, so

called skew-symmetric forms. Skew-symmetry of the non-linear terms implies the conservation of kinetic energy [185], a property which can be destroyed by aliasing (see Section 4.2.1 and [136]). Thus, constructing skew-symmetric discretizations can lead to kinetic energy stable formulations, which recover the properties of the continuous fluxes on a discrete level [83, 185].

4.3. Stable Simulation of Under-Resolved Turbulent Flows

In this section, we will apply the de-aliasing strategies presented in Section 4.2.2 to turbulent flows and discuss their accuracy, stability and efficiency.

4.3.1. Taylor-Green Vortex

The Taylor-Green Vortex problem has been described in Section 2.2 and it has gained renewed interest as a suitable test model for DNS and LES in the high order community in recent years, e.g. [33, 60, 200]. We use this flow problem to evaluate the polynomial de-aliasing and filtering strategies. The discussion in this section follows closely the publication in [84].

As discussed in Section 4.1, in under-resolved situations, the theoretical approximation order is not a relevant figure of merit, as the grid spacing remains considerably large. However, high order methods may still profit from their improved numerical accuracy, i.e. their lower numerical dispersion and dissipation errors. These benefits come at the price of reduced inherent damping of instabilities like aliasing errors introduced through inexact treatment of non-linearities. Figure 4.8 highlights this dilemma for a LES situation by comparing a DGSEM case for low and high order polynomial degrees, while keeping the overall number of DOF constant. While the low order method fails to resolve the physical structures because of excessive dissipation, the high order method follows the DNS solution closely due to its lower PPW requirement, but succumbs to aliasing instabilities. In the following, we attempt to avoid or remove this instability mechanism and to recover a stable high order method.

4.3.1.1. Computational Setup

All our coarse grid computations presented in this section discretize the computational domain with 4^3 grid cells with polynomial degree $N = 15$, resulting in 64^3 degrees of freedom. The time step of the computation was approximately 7.7×10^{-4} , resulting in about 13,000 time steps for the computation with $t_{end} = 10$. We found that this explicit time step was small enough to essentially remove any temporal integration errors. All computations are performed on the maximum number of processors governed

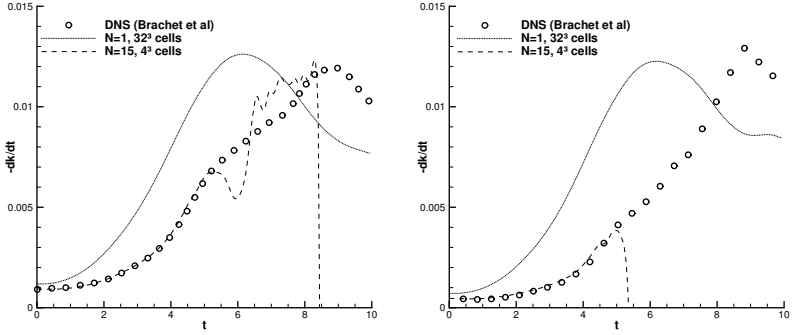


Figure 4.8.: Plot of the kinetic energy dissipation rates of the Taylor-Green Vortex (*Left*: $Re = 800$, *Right*: $Re = 1600$), computed with with 64^3 DOF using either a low order method (2nd order, $N = 1$) or a very high order method (16th order, $N = 15$).

by the MPI parallelization (i.e. 64) on the NEC Nehalem cluster at HLRS. Typical wall clock times for the filtered DGSEM computations were about 10 minutes, and about 1.3 hours for the computations with polynomial de-aliasing. The reference DNS data for the energy spectra was obtained using 384^3 DOF on 512 Nehalem cores. The resolution for the DNS computations is sufficient to achieve grid converged spectra for wavenumbers $k \leq 64$, i.e. twice the coarse grid Nyquist number.

It should be noted that the resolution of 64^3 degrees of freedom was chosen to match the typical resolution for this case published in literature, see e.g. [97]. Especially for the $Re = 800$ case, this is a high spatial resolution, much finer than a typical LES setting would require. Still, those computations are often termed LES. For $Re = 1600$, Figures 4.12 and 4.13 indicate that the resolution is closer to a realistic LES situation.

4.3.1.2. Stabilization via Filtering

As a first stabilization method, we investigate the stabilizing effect of a modal filter described in Section 4.2.2.3 for the TGV flow, that is, we combine a DGSEM approach with $M = N$ with a dissipative mechanism. To examine the effect of the filter type and shape, we choose two significantly different sets of parameters to cover a broad range of filter effects: a strong version of the filter ($\alpha = 36$, $s = 16$, $N_c = 4$) and a weak set

of values ($\alpha = 36$, $s = 32$, $N_c = 4$). Figure 4.9 depicts the transfer functions for the polynomial modes for both filters. While we show only those two example filter settings

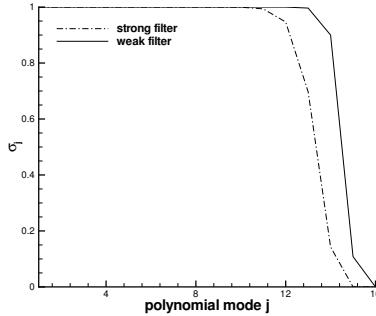


Figure 4.9.: Transfer functions for the weak and strong variant of the modal filters for $N = 15$.

in this work, we found during our investigations that a broad range of filter parameter sets leads to stable computations and comparable results for the presented Reynolds numbers.

Taylor-Green Vortex at $Re = 800$

Figure 4.10 shows the kinetic energy dissipation rate of our computations and the reference data, taken from a DNS from [28]. Whereas the unfiltered computation is only stable up to $t \approx 5$ as noted in Figure 4.8, both filtered computations remain stable for the whole simulation time. Up to $t = 4$, when the laminar flow features are still well-resolved, the difference of the computations are negligible and match the DNS result very closely. Since the polynomial modes affected by the filtering operations are not filled in this well-resolved region, differences for the two filters only appear at a later time, when a considerable scale cascade has been established. Examining the quality of the stabilized computations shows that the strong filter variant introduces too much dissipation, while still following the general trend acceptably. In comparison, the weakly filtered computation almost coincides with the DNS results.

To further investigate the approximation quality for these filter settings, we compute the spectral energy distribution for the TGV at the moment of the maximum dissipation ($t = 9$), Figure 4.11. In agreement with the behavior for the kinetic energy decay rate,

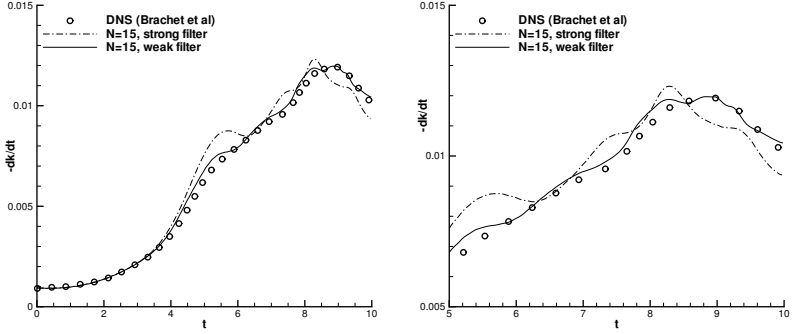


Figure 4.10.: Taylor-Green Vortex at $Re = 800$. Kinetic energy dissipation rate $-\frac{dk}{dt}$ for filter-stabilized $N = 15$ (4^3 grid cells) computation. The right plot is zoomed in on the time range of maximum entrophy production.

the strong filter leads to an inferior approximation of the energy spectrum, even up to the largest scales, thereby indicating a loss in physics due to over-dissipation. In particular, the strong filter removes kinetic energy from the high polynomial modes within each cell, which in turn leads to a blockage of the scale cascade, as described before. This blockage (due to the missing scales near the cut-off) leads to an overestimation of the energy in the low modes. The weak filter variant shows very good spectral agreement, in particular in capturing the low wavenumber range.

The right subplot of Figure 4.11 depicts the contributions to the total kinetic energy dissipation rate. According to Equation (2.19), for a periodic problem, the magnitude of the kinetic energy dissipation rate $-\frac{dk}{dt}$ equals the viscous dissipation action (see also Equation (2.30)). For a DNS situation, these must balance exactly. However, in an under-resolved setting, both terms can differ significantly. They can be computed independently from the solution field, and their difference is an indicator for the amount of numerical dissipation (induced by the approximation error and the filtering). In the right pane of Figure 4.11, the molecular dissipation ϵ created by the resolved scales and the numerical dissipation introduced by the spatial discretization are depicted. Since the strong filter dissipates more resolved scales, the ratio of molecular to numerical dissipation is lower compared to the weak filter, thereby indicating a higher loss of physical information, as also indicated by the wavenumber spectrum on the left.

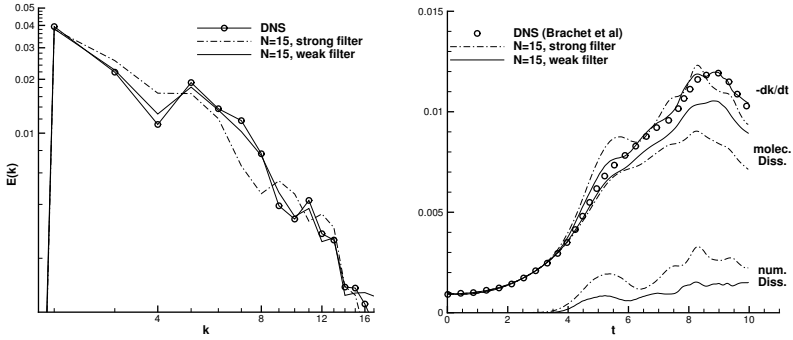


Figure 4.11.: Taylor-Green Vortex at $Re = 800$. *Left:* Kinetic energy spectra at $t = 9$. *Right:* Kinetic energy dissipation rate $-\frac{dk}{dt}$, the resolved (molecular) dissipation rate and the numerical dissipation rate for filter-stabilized $N = 15$ (4^3 grid cells) computation.

Taylor-Green Vortex at $Re = 1600$

By keeping the resolution (64^3 DOF as in the $Re = 800$ case) and the filter parameters fixed but doubling the Reynolds number, we reduce the amount of physical dissipation and thus the inherent stabilization mechanism through kinetic energy drain. At the same time, a higher Reynolds number also entails smaller Kolmogorov scales, thereby increasing the degree of under-resolution of the problem towards a more realistic LES situation. The corresponding results of our filtered coarse resolution computation and the reference data for the kinetic energy dissipation rate are shown in Figure 4.12. The same general observations as for the $Re = 800$ case can also be found for this more difficult flow. Both filters stabilize the computation, and the weak filter in particular gives results very close to the DNS solution. For the strong filter, the general shape of the dissipation rate is still in acceptable agreement, but a shift of the location of the maximum dissipation rate to earlier times is noticeable. This shift can be found when lowering the Reynolds number of the problem [28], indicating that the filter effects now dominate over the resolved dissipation and mimic a more viscous flow. The plot of the energy spectrum in Figure 4.13 supports the observations from the $Re = 800$, with the strong filter results noticeably deteriorating, even for low wavenumbers. The right subplot in Figure 4.13 shows the effect of the increased Reynolds number on both filters. Since the scale range of the turbulent flow has increased but the spatial resolution has remained fixed, the frac-

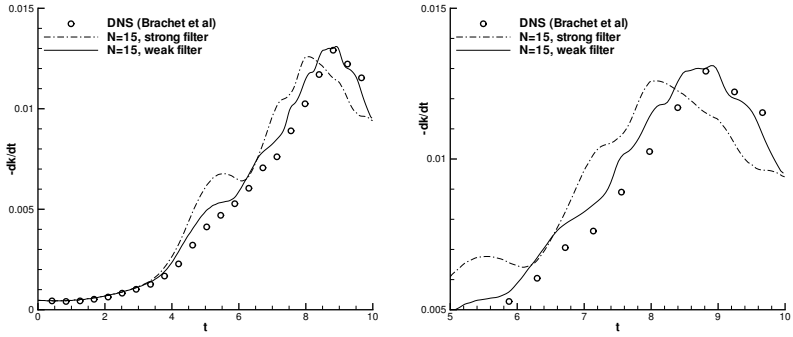


Figure 4.12.: Taylor-Green Vortex at $Re = 1600$. Kinetic energy dissipation rate $-\frac{dk}{dt}$ for filter-stabilized $N = 15$ (4 grid cells) computation. The right plot is zoomed in on the time range of maximum enstrophy production.

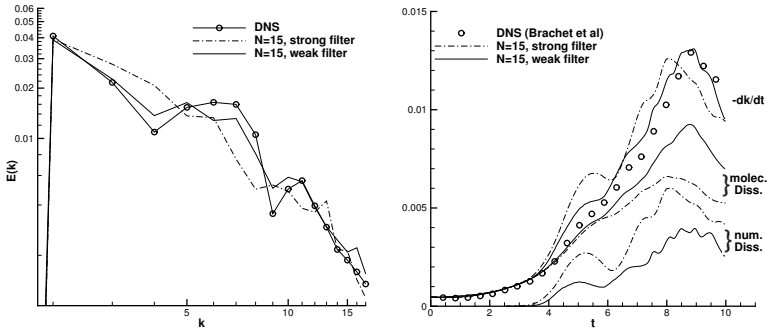


Figure 4.13.: Taylor-Green Vortex at $Re = 1600$. *Left:* Kinetic energy spectra at $t = 9$. *Right:* Kinetic energy dissipation rate $-\frac{dk}{dt}$, the resolved (molecular) dissipation rate and the numerical dissipation rate for filter-stabilized $N = 15$ (4 grid cells) computation.

tion of numerical dissipation to resolved dissipation is higher compared to the $Re = 800$ test case. For the weak filter, a considerable amount of the scales is still resolved, but for the strong filter, the overall dissipation rate is strongly influenced by the amount of the numerical dissipation, which contributes about as much to the overall dissipation rate as the resolved part. Thus, as obvious from the shift in dissipation rate maximum, the structure of the numerical dissipation begins to govern the flow physics. This effect will continue to grow in severity with larger Reynolds numbers and thus the burden on the “physics capturing” capabilities of the numerical dissipation and the filter will increase. We have demonstrated in this section the stabilization of DGSEM via a filtering approach in under-resolved turbulence. Next, we repeat our investigations for the computationally more costly, but parameter-free and numerically more accurate PDG approach.

4.3.1.3. Stabilization via Polynomial De-Aliasing

In this section, we examine the effects of polynomial de-aliasing (PDG formulation) for de-aliasing of high order computations with respect to their approximation accuracy. The advantage of this approach compared to the previous filtering technique lies in the fact that as long as we capture the non-linearity of the flux function, i.e. use a sufficient number of quadrature points for the evaluation of the inner products, the stabilization is parameter-free. Since the TGV is an essentially incompressible problem, a choice of $M = 3/2N$ would be justified, however, to rule out any weak compressibility effects on stability, we choose $M = 29$ and $M = 31$, i.e. the number of corresponding quadrature points becomes 30 and 32.

Taylor-Green Vortex at $Re = 800$

Again, we first investigate the accuracy of this approximation for the test case with the lower Reynolds number. The kinetic energy dissipation rates are plotted alongside the reference data in Figure 4.14. Both de-aliased computations are essentially identical, i.e. no influence of the integration precision is visible, supporting our assumption that compressibility effects are negligible. Both results match the DNS data almost perfectly, except for a slight deviation near the maximum of the dissipation rate, where the small scale action is most prominent. The plot of the spectral energy distribution (Figure 4.15) corroborates this observation. The match between the DNS spectrum and the coarse resolution result with only 64^3 DOF is excellent. The underlying reason for this near perfect spectral agreement between the PDG scheme and the reference data can be deduced from the right pane of Figure 4.15. The de-aliasing mechanism does not introduce dissipation into the polynomial modes up to N like the filtering approach, but instead just removes the aliasing error term from them. Thus, the full modes remain available for the resolution of vortical structures, and the n_{PPW} requirement is *not* altered by the

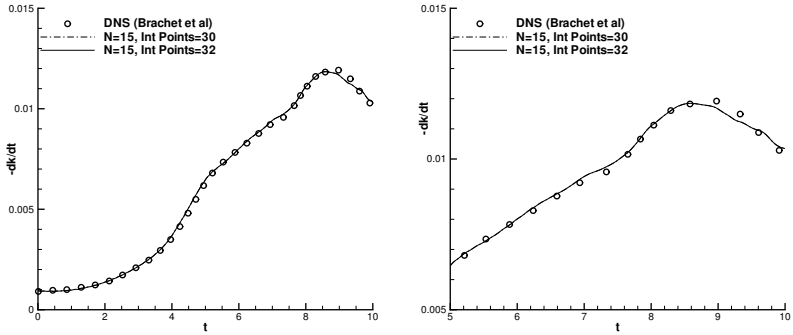


Figure 4.14.: Taylor-Green Vortex at $Re = 800$. Kinetic energy dissipation rate $-\frac{dk}{dt}$ for PDG $N = 15$ (4 grid cells) computation. The right plot is zoomed in on the time range of maximum enstrophy production.

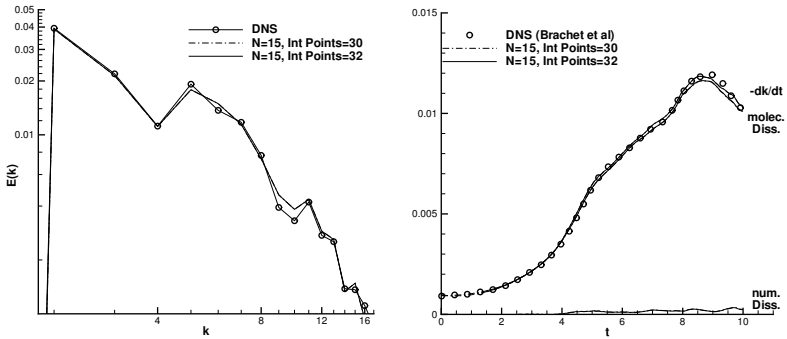


Figure 4.15.: Taylor-Green Vortex at $Re = 800$. *Left:* Kinetic energy spectra at $t = 9$. *Right:* Kinetic energy dissipation rate $-\frac{dk}{dt}$, the resolved (molecular) dissipation rate and the numerical dissipation rate for PDG $N = 15$ (4 grid cells) computation.

de-aliasing procedure. This allows us to take advantage of the full potential of this high order approximation and capture most of the relevant scales possible with only 64^3 DOF. Note that the grid Nyquist wavenumber for 64 DOF per direction is 32. Considering a polynomial approximation, which requires (in the limit) $n_{PPW} = \pi$, and around 4 for a realistic N , up to 16 scales should be resolved with good accuracy by our approach. The energy spectrum on the left shows an almost perfect agreement up to this wavenumber, indicating that the associated scales are nearly perfectly resolved. Since those scales provide a molecular dissipation rate which is already close to the total energy loss, the overall agreement with the DNS is excellent, and the effect of the numerical dissipation is negligible in this case. Thus, this example clearly demonstrates that the polynomial de-aliasing recovers the full resolution capabilities of the scheme and supports a very low PPW requirement.

Taylor-Green Vortex at $Re = 1600$

Following the reasoning from before, we increase the difficulty of the problem by keeping the resolution fixed, but again doubling the Reynolds number. Figure 4.16 shows the energy dissipation rates for these simulations. Again, both simulations with different integration points are basically identical and show very good agreement with the DNS reference data. The higher scale range of this test case is evident, as the maximum of the dissipation rate is underestimated due to lack of small scale representation of the flow by the 64^3 DOF discretization.

Figure 4.17 shows the detailed view of the energy spectrum, which again follows the DNS reference closely for both choices of M . In the right hand plot, the ratio of resolved to numerical dissipation is still substantial, although – as expected – smaller than for the $Re = 800$ case. In comparison with the filtering approach in Figure 4.13 however, the superior accuracy of PDG in terms of resolution capabilities is evident.

Comparison of De-Aliasing Strategies

We now focus on a comparison of the two de-aliasing techniques that have been examined: The simple filtering approach and a more complex polynomial de-aliasing method. Figure 4.18 compares the results of these two high order schemes. In the left plot, we present the total energy decay rate together with the contribution of the numerical dissipation. Although the dissipation rate matches the DNS reference data well for both simulations and shows almost negligible quantitative difference, the numerical dissipation curves reveal the conceptual difference due to the stabilization methods. The purely dissipative nature of the filter, acting on the solution modes N , manifests itself in a higher fraction of numerical dissipation compared to the PDG solution. Thus, poly-

4.3. Stable Simulation of Under-Resolved Turbulent Flows

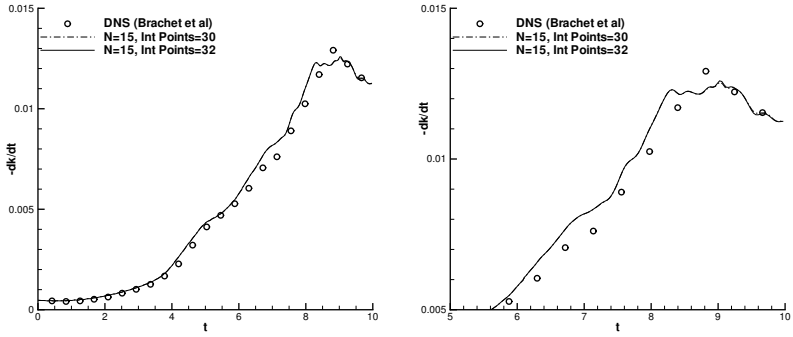


Figure 4.16.: Taylor-Green Vortex at $Re = 1600$. Kinetic energy dissipation rate $-\frac{dk}{dt}$ for PDG $N = 15$ (4^3 grid cells) computation. The right plot is zoomed in on the time range of maximum enstrophy production.

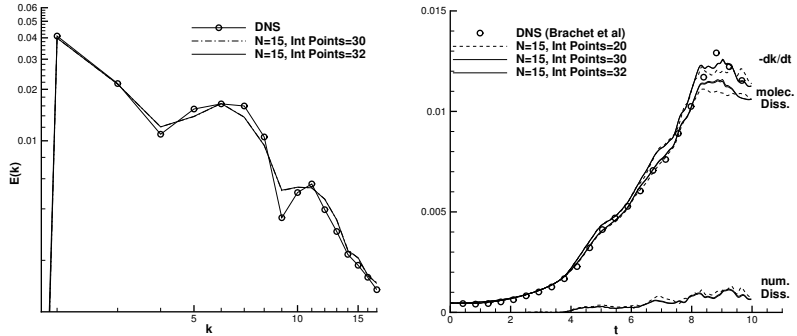


Figure 4.17.: Taylor-Green Vortex at $Re = 1600$. *Left:* Kinetic energy spectra at $t = 9$. *Right:* Kinetic energy dissipation rate $-\frac{dk}{dt}$, the resolved (molecular) dissipation rate and the numerical dissipation rate for PDG $N = 15$ (4^3 grid cells) computation.

4. Numerics for Under-Resolved Simulations

mial de-aliasing captures more of the scales present on the 64^3 DOF grid, which is also confirmed by the right part of the plot where we compare the energy spectra of the two computations.

Figure 4.19 allows for a more qualitative evaluation of the approximation properties of the two approaches. It shows the λ_2 contours of the Taylor-Green Vortex at $Re = 800$ for 4 different discretizations: i) A DNS reference solution with 384^3 DOF that shows no grid influence and smooth contours, indicating a fully resolved field (the lower right), ii) a $\mathcal{O}(2)$ computation with 32^3 elements, resulting in 64^3 (lower left), iii) the solution with the weak filtering from Section 4.3.1.2 (upper left) and iv) the PDG solution from Section 4.3.1.3 (upper right). The difference between the second and 16th order computation is remarkable, clearly, the inherent numerical dissipation of the low order scheme smoothens all but the largest features of the flow field. Both high order results are in very good agreement with the reference DNS, in particular, most of the large scales structures are in very close agreement with the DNS. Note that the PDG solution shows sharper features than the filtered version and is visually slightly closer to the reference; presumably, this is an effect of the filter dissipation that smoothens the gradients, leading to a more “washed-out” impression. In terms of computational efficiency, the superior

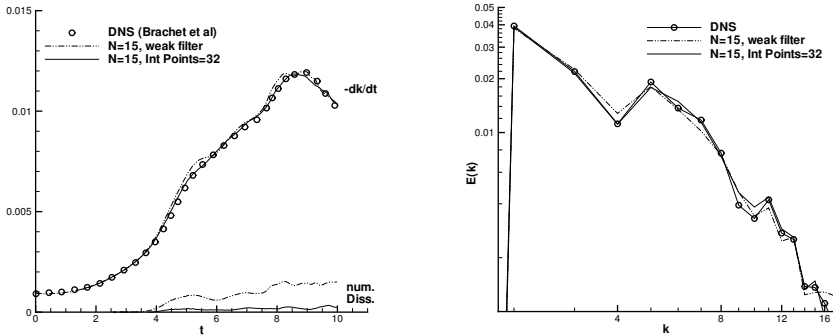


Figure 4.18.: Taylor-Green Vortex at $Re = 800$. Comparison of kinetic energy dissipation and numerical dissipation (*left*) and energy spectra (*right*) for $N = 15$ (4^3 grid cells) computations with stabilization via polynomial de-aliasing vs. filtering.

accuracy of the PDG solution comes at an increase in computational cost. In case of the compressible Navier-Stokes equations, where the number of integration points and

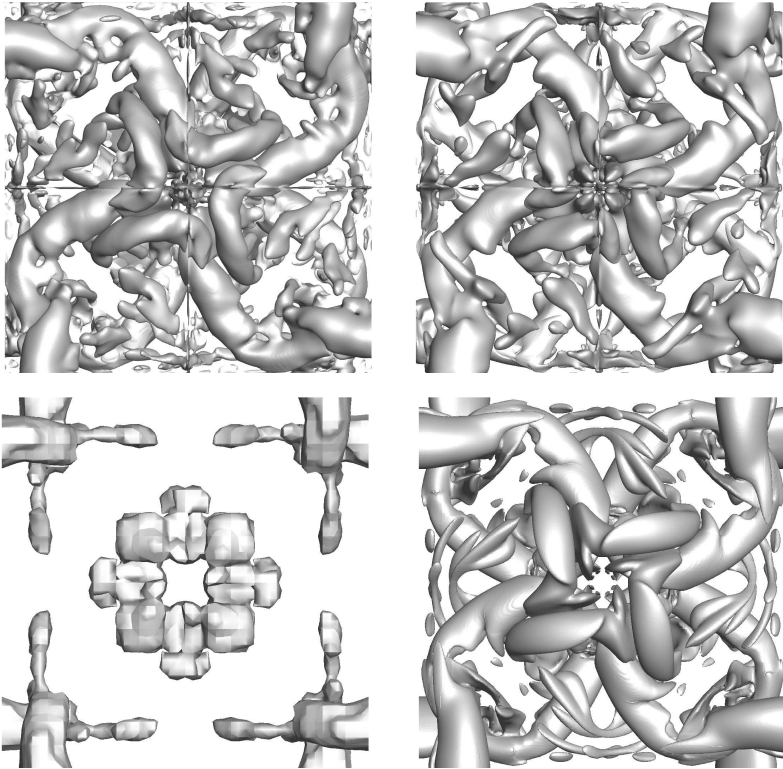


Figure 4.19.: Taylor-Green Vortex ($Re = 800$). Isocontours of $\lambda_2 = -1.5$ at $t = 8.5$. All computations with 64^3 DOF except DNS. From upper left to lower right: i) 16th order filtered computation, ii) 16th order computation with polynomial de-aliasing, iii) 2nd order computation, iv) DNS reference result with 384^3 DOF.

thus the volume operator cost is doubled, the CPU time increases by a factor of eight compared to the filtered computations. On the other hand, the filter depends on a set of parameters, whose optimal values are not known a priori, while the PDG approach is

parameter-free.

It should be noted that both approaches are limited in their extension to higher Reynolds number flows. For the filtered method, as the discrepancy between resolved and subgrid scales increases, the burden on the filter operator rises immensely, shifting its primary function from a de-aliasing mechanism to a subgrid closure. In other words, the filter function should no longer be motivated by the suppressing of aliasing, but by providing physically sound dissipation to account for the subgrid effects. This approach then becomes an LES with an added dissipation mechanism (it is a philosophical question whether the filter is more like an explicit closure model or an implicit modification of the discretization itself). The PDG approach on the other hand does not have a mechanism of introducing dissipation; instead, the inherent approximation errors must act as a subgrid closure. If the Reynolds number is too large and the resolution too low, this energy drain will not be sufficient to suppress oscillations, which will eventually become large enough to violate the physical constraints of the equations. In this way, PDG is akin to implicit LES closure models.

Comparison with LES Methods

Figure 4.20 displays the results of PDG computations with fixed resolution (64^3 DOF) for increasing Reynolds number and compares them with other LES methods. DNS data from Brachet and Fauconnier [28, 73] obtained with 256^3 and 864^3 nodes serves as a benchmark for the quality of the solutions. We compare the PDG results with both an explicit and an implicit LES closure: the standard dynamic Smagorinsky formulation and the ALDM (see Section 2.4.3), both results published by Hickel and based on an at most 4th order FV WENO formulation [97]. Since Hickel used 64^3 DOF for both his LES as we do in our computations, a direct comparison of the quality of the results per invested DOF is possible. It is worth noting that our PDG results are at least comparable with respect to accuracy to more sophisticated state of the art LES results and show a considerably closer agreement for the higher Reynolds numbers. Note that while our result matches the DNS data for $Re = 800$ almost perfectly, the effect of the fixed resolution limit is evident from the $Re = 1600$ and $Re = 3000$ cases, especially in the situation of the dominance of the smallest scales (i.e. maximum of the dissipation rate at $t \approx 9$). The missing effects which cannot be captured on the fixed grid therefore must necessarily be generated with either implicit or explicit subgrid models, if this approach is to be extended to higher Reynolds number regimes.

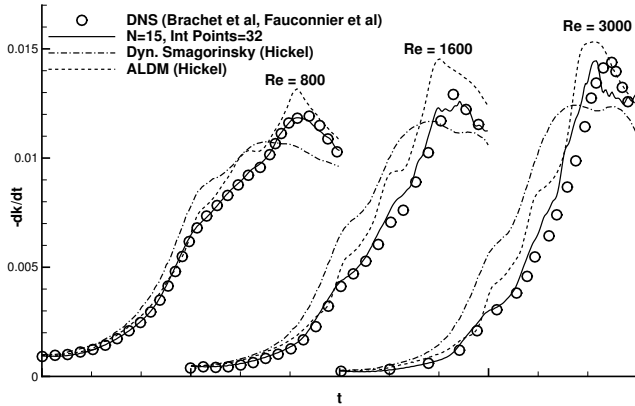


Figure 4.20.: Comparison of LES methods: Kinetic energy dissipation rate for $Re \in \{800, 1600, 3000\}$ for PDG computations with $N = 15$ compared to DNS and LES reference data.

4.3.2. Flow over a Cylinder at $Re_D = 3900$

In Section 4.3.1.3, we have demonstrated that with proper de-aliasing, non-linear stability of DGSEM can be achieved in under-resolved situations. Additionally, exact quadrature of the non-linear terms recovers the scale-resolving capabilities of the high order discretization, and thus makes this approach attractive for multiscale problems. In the following section, we show results from [18], where we applied the PDG strategy with a high order ansatz to the subsonic flow over a circular cylinder at $Re_D = 3900$, a classical benchmark problem for LES.

4.3.2.1. Computational Setup

The subcritical flow over a cylinder with circular cross section at $Re_D = 3900$, where D is the diameter, is a well-established test case for the evaluation of implicit and explicit LES modeling approaches and has been extensively investigated by a large number of researchers [23, 77, 80, 122, 135, 141, 157]. The boundary layer on the upstream face of the geometry remains laminar until it sheds periodically, forming a trailing shear layer. Within this layer, transition to turbulence occurs, which interacts with the turbulent

4. Numerics for Under-Resolved Simulations

back-flow region in the wake of the body. Due to its rather simple geometry, initial and boundary conditions yet complex physics, this flow is very popular among researchers to assess the accuracy of LES methods for incompressible or weakly compressible flows. A considerable spread in literature exists, often attributed to the sensitivity to the spanwise domain extensions [135]. Recent DNS results by Lehmkuhl et al. [125] show the occurrence of very low frequency oscillations within the wake region, which might also contribute to the partially conflicting published results. In terms of LES, the most commonly reported strategy consists of an implicitly filtered approach with an explicitly added classical Smagorinsky model. Although the shortcomings of this model in laminar and transitional flow situations are known, many publications report the results for this type of subgrid scale closure, e.g. [23, 31, 80, 122, 134, 157].

Table 4.3 collects the integral quantities of LES and DNS simulations of this flow from literature.

<i>Author</i>	$C_{P_{Base}}$	Str	C_D	L_r/D	Scheme	LES	DOF
Kravchenko et al. [122]	-0.94	0.210	1.04	1.35	B-Spline SEM	Smag.	1-2 M
Blackburn et al. [23]	-0.93	0.218	1.01	1.63	GL-SEM	Smag.	1.5 M
Meyer et al. [141]	-0.92	0.210	1.05	1.38	FV	ALDM	6.0 M
Fröhlich et al. [80]	-1.03	0.216	1.08	1.09	FV	Smag.	1.4 M
Ouvrard et al. [157]	-0.85	0.218	0.99	1.54	FV/FE	Smag.	1.5 M
Ouvrard et al. [157]	-0.81	0.226	0.93	1.68	FV/FE-VMS	Smag	1.5 M
Franke et al. [77]	-0.85	0.209	0.98	1.64	FV	Yoshizawa	1.2 M
Ma et al. (I) [135]	-0.96	0.203	0.96	1.12	h/p-FEM Fourier spanw.	DNS	24 M
Ma et al. (II) [135]	-0.84	0.219	0.96	1.59	h/p-FEM Fourier spanw.	DNS	12 M
Current: $N = 11$	-1.01	0.206	1.10	1.13	PDG	-	0.7 M
Current: $N = 7$	-0.91	0.208	1.00	1.31	PDG	-	1.6 M

Table 4.3.: Integral quantities and simulation parameters for $Re_D = 3900$ cylinder flow, reproduced from [18]. $C_{P_{Base}}$: pressure coefficient at the downstream position $x = D/2, y = 0$, Str : Strouhal number of the lift coefficient $f_{Lift} D/U_\infty$, C_D : drag coefficient, L_r : length of separation bubble.

Spatial Discretization and Statistics Gathering

While our framework supports fully unstructured hexahedral meshes, we choose to discretize this simple geometry in a structured manner with a fully volume-curved mesh, i.e. the mapping $\vec{x}(\vec{\xi})$ from reference to physical space is a polynomial of arbitrary degree,

which can be chosen to match the polynomial ansatz for the unknown flow variables to ensure a consistent geometry discretization. The physical domain is circular with radius $r = 100D$ in the plane perpendicular to the geometry axis, and extruded along $4D$ in spanwise direction. In axial and tangential direction ($x - y$ plane), we choose an exponential stretching in the radial and a Gaussian stretching in the circumferential direction to cluster the grid points towards the geometry and in the wake.

Referring to the published resolution data collected in Table 4.3 as a reference, we limit

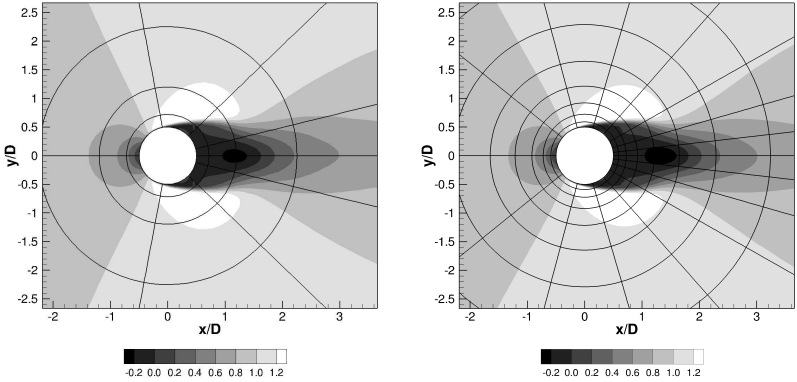


Figure 4.21.: Time- and spanwise-averaged streamwise velocity component and grid. *Left:* $N = 11$ grid with $8 \times 8 \times 6$ elements (circumferential, radial and spanwise), *right:* $N = 7$ grid with $16 \times 16 \times 12$ elements.

the number of degrees of freedom of our computations to a maximum of 1.6 mio. Following our discussion from Section 4.3.1, we choose two high order discretization approaches to take full advantage of their low n_{PPW} requirements: first, an $N = 7$ setup, leading to $(N + 1)^3 = 512$ degrees of freedom per element and a total of 1.57 M DOF on the associated grid. For an exact integration, we choose $M = 11$ in accordance with the integration rule for quadratic non-linear functions, as we set the Mach number $Ma = 0.1$ for an essentially incompressible flow. The second discretization consists of an ansatz of $N = 11$ polynomials with $M = 17$, giving a total of only 0.66 million DOF on the associated grid, far below the number of DOF usually reported for this case. A zoomed-in view of both grids and the resulting time- and spanwise-averaged streamwise velocity distribution is shown in Figure 4.21. We use the local Lax-Friedrichs flux for

the convective fluxes, and Bassi and Rebay's first method BR1 for the viscous contributions. The wall boundary conditions are set to isothermal, with a stagnation temperature of $1.002 T_\infty$. Periodic boundary conditions are applied in the spanwise direction, while the remaining ones are weakly enforced Dirichlet free stream conditions. The collection of the time averaged data was started after the establishment of stable vortex shedding at $100 T^*$, with the convective time unit T^* defined as D/U_∞ (and U_∞ denoting the freestream velocity) and continued for 80 shedding cycles.

4.3.2.2. Results for PDG

Table 4.3 lists the results for the integral flow quantities of the PDG computations. In general, the computed integral quantities agree well with the published data, while the match for the $N = 11$ case is weaker, due to the very low total number of degrees of freedom for this case and the insufficient wall resolution. Still, even for this severely under-resolved situation, the results are in reasonable agreement.

Figure 4.22 gives an impression of the importance of the de-aliasing procedure. The left subplot depicts the instantaneous u -component of the flow velocity. Here, the vortex street is clearly visible. In the middle plot, the value of a resolution indicator is plotted. This indicator evaluates the slope of the norm of the hierarchical modal degrees of freedom of the x -momentum in each cell. Yellow and red colors denote a high energy content in the higher modes, i.e. a likely occurrence of aliasing. This is in agreement with the physics of this flow, as strong non-linearities in the wake drive the scale cascade. Note that this cell-wise indicator does not have a high spatial resolution, as the associated grid cells are large for the high order method. Still, the wake structure can also be found in the indicator values. The last subplot shows the associated aliasing energy of the (incompressible) u^2 -flux. It is computed as the difference between the projection by proper quadrature and collocation. 2-h waves appear as a checkerboard pattern in each cell, indicating the excitation of the highest modes through the aliasing. Also note that the wake structure is clearly visible in the aliasing error. Comparing first order statistics, Figure 4.23 shows the time- and spanwise-averaged streamwise velocities $\langle u \rangle$, normalized by the freestream velocity U_∞ , at different locations downstream of the geometry. We compare the PDG results with experimentally determined values from Parnaudeau et al. [159], and two LES computations: the implicit approach through an ALDM used in conjunction with a low order Finite Volume formulation presented in [141] and a high order B-Spline based Galerkin projection method with explicitly added Smagorinsky model [122]. The evolution of the wake profile is of particular interest, as the mixing and recovery of the velocity deficit is governed by viscous action, and therefore by the combination of resolved and numerical viscosity. A high viscosity generally leads to a fast interchange of momentum through shear and thus to a less pronounced but overall

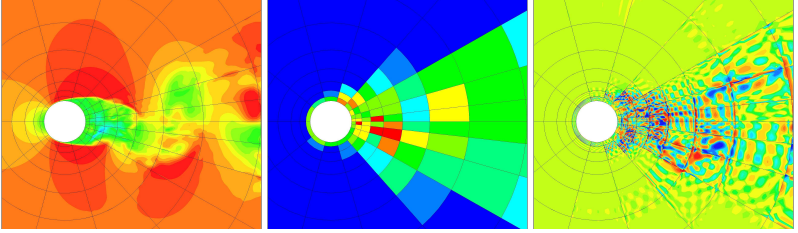


Figure 4.22.: Instantaneous flow field in the cylinder region. *Left:* u -velocity, *middle:* Modal resolution indicator, *right:* Difference between projection and collocation of u^2 .

longer wake.

For the $N = 7$ case, the agreement of the PDG results for the streamwise velocity is very good for all locations in the wake. In particular, a very close agreement with the data from the continuous Galerkin approach can be observed. For the $N = 11$ case, the match with the published data is again very good in the near wake, but deteriorates downstream. Together with the data in Table 4.3 which indicates a higher drag coefficient and reduced length of the separation bubble, this behavior is characteristic of too little dissipation. The notably reduced spatial resolution and the additional reduction in numerical dissipation from an $N = 7$ to an $N = 11$ approximation result in this compact, high drag wake. This motivates the addition of subgrid scale dissipation for higher Reynolds numbers or reduced spatial resolution. More comparisons can be found in [18], combining the results from Table 4.3 and the detailed discussion therein shows that the PDG approach again (as in Section 4.3.1) outperforms classical LES approaches combined with low order schemes at comparable number of DOF.

Table 4.4 summarizes the computational costs in terms of the metrics defined in Section 3.5 and the specific time T^* . Although the PDG approach incurs a penalty on efficiency due to the de-aliasing procedure, the wall clock time per T^* is on the order of minutes, which makes a full LES with extensive statistics gathering possible in very short wall clock times.

In addition to the cylinder flow, computations of a confined periodic hill flow at $Re_h = 2800$ and the transitional flow over a SD7003 airfoil at $Re_c = 60,000$, both established benchmark problems for LES, can also be found in [18]. Also for those cases, our PDG approach achieves equal or better match to experimental and high resolution DNS data

4. Numerics for Under-Resolved Simulations

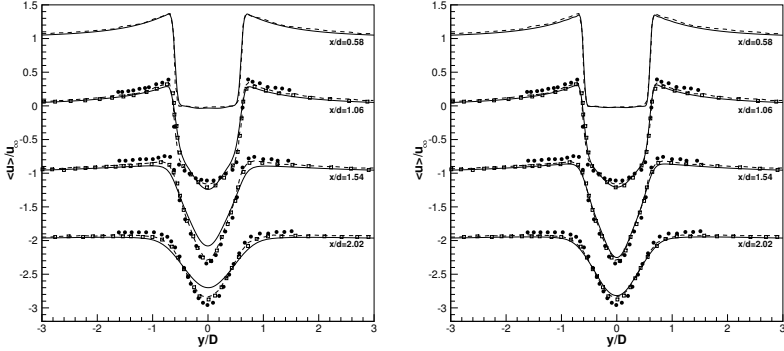


Figure 4.23.: Mean streamwise velocity at different downstream locations in the wake of the circular cylinder flow at $Re_D = 3900$. *Left:* $N = 11$ computation, *Right:* $N = 7$ computation. Solid lines: present DG results, dashed lines: computational LES results from [141], open squares: computational LES results from [122], filled circles: experimental results from [159].

than other (typically low order) implicit and explicit LES results from literature, at the same number of degrees of freedom. It is worth noting that for these two problems, “incomplete” de-aliasing in combination with a moderate degree N was sufficient for stability.

Thus, summarizing Section 4.3, we have shown the accuracy and efficiency, both in terms of invested DOF as well as computing times, of de-aliased DGSEM for under-resolved turbulent flows. Countering or avoiding aliasing effects has been achieved in two ways: an additional computationally cheap filter, that fights the aliasing effects on the solution modes N , thereby increasing the PPW requirement, and a polynomial de-

Case	no. DOF	no. cells	cores	$\overline{\Delta t}/T^*$	PID [μ s]	T_{CPU}/T^* [h]	T_{Wall}/T^* [min]
$N = 7$	1.572 M	3072	3072	$1.3 \cdot 10^{-3}$	13	135	2.9
$N = 11$	0.664 M	384	384	$1.7 \cdot 10^{-3}$	19	105	16.9

Table 4.4.: Computational cost for the cylinder flow computations.

aliasing on a finer quadrature grid that increases computational cost but retains the original scale-resolving capabilities. In terms of accuracy, high order PDG can outperform other LES strategies for moderate Reynolds numbers.

4.4. Interaction of Subgrid Scale Model and Discretization

So far, the numerical strategies presented in Section 4.3, in particular PDG, cannot strictly be classified as either explicit or implicit LES, since neither an explicitly added dissipation is introduced, nor is the discretization error adjusted to account for subgrid effects. Still, the results presented in this section and the comparison with other methods clearly show the potential of this approach for moderate Reynolds numbers. However, as discussed above, the lack of additional dissipation limits the stability of PDG, not in terms of aliasing effects, but in terms of oscillations introduced by the truncation of the full solution. This induced roughness will eventually lead to a violation of the physical constraints, e.g. unphysical flow properties.

Figure 4.24 shows the TGV problem for a fixed spatial resolution of 8^3 elements with $N = 7$ and increasing Reynolds number. All computations, unless stated otherwise, use $M + 1 = 12$ integration points for the non-linear terms, following the assumption of essential incompressibility of this flow. For this PDG discretization, the solution remains stable up to $Re = 3000$, indicating that the scale resolving capabilities of the scheme together with the remaining numerical dissipation are sufficient to regularize the solution. However, examining the solutions for $Re = 2000$ and $Re = 3000$ more closely reveals unphysical oscillations in this integral quantity, which are indicators of the increasing truncation error. For $Re = 4000$, this truncation error becomes large enough to cause a violation of the physical constraints and an unphysical sudden jump in kinetic energy, denoted by the sharp drop of the dissipation rate at around $t = 9$. To rule out compressibility effects in the non-linear terms causing aliasing issues, the computation is repeated with the quadrature rule for cubic non-linearity, but no change in solution is visible, and the crash occurs at the same time. Increasing the integration precision further results in the same behavior. Thus, for this configuration, the PDG computation becomes unstable not due to aliasing, but due to the large truncation error with respect to the missing scales, which causes the solution on the grid to become oscillatory. Adding an explicit subgrid closure (a Smagorinsky model) that introduces a dissipative mechanism stabilizes this solution and allows the stable computation of higher Reynolds number flows.

Thus, in general, an extension of the high order approach – regardless of DGSEM or PDG type – to higher Reynolds number flows will require some form of additional dissipative mechanism, either explicitly or implicitly. We have shown in Section 4.3,

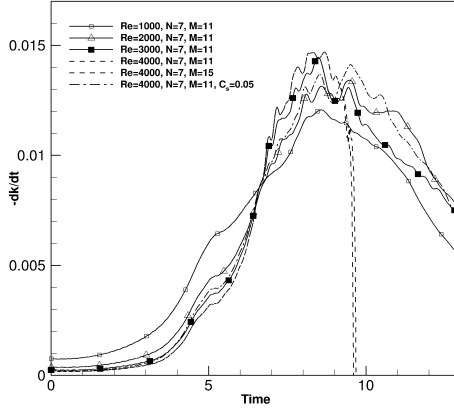


Figure 4.24.: Kinetic energy dissipation rate for the Taylor-Green Vortex with increasing Reynolds number: 8^3 Elements, $N = 7$. $M + 1$ denotes the number of quadrature points for the non-linear fluxes, C_s indicates the Smagorinsky model constant and is 0.0 unless stated otherwise.

that for the under-resolved computations at moderate Reynolds numbers, PDG can provide stable and accurate results, but requires the computationally expensive polynomial de-aliasing. We have also shown that a stabilization by a dissipative filtering is also possible. Since higher Reynolds numbers enforce the need for an additional dissipative mechanism, a valid question is whether explicit de-aliasing remains necessary, or if the closure model itself can also account for this. In this section, we investigate this question by examining the interaction of the discretization scheme, in particular the treatment of the non-linear terms, and a basic closure. We will focus on an explicit closure approach, and use the classical Smagorinsky model due to its prevalence in literature for this case. Thus, our investigations do not aim at explicitly evaluating or optimizing the Smagorinsky model parameter for the given discretization choices, but at demonstrating the general interaction of eddy-viscosity type subgrid closure and the treatment of non-linear terms in a high order DG setting.

Depending on whether the baseline scheme has a de-aliasing mechanism, an explicit

subgrid scale model typically needs to achieve two goals: guaranteeing numerical stability, which is not trivial due to the under-resolution, and at the same time modeling of missing SGS physics. To answer the question posed above, we are investigating two discretization configurations: A de-aliased PDG scheme, which is aliasing-free and thus requires no stabilization from the closure model. Thus, we can run this scheme with or without the model (for moderate Reynolds numbers, as discussed above, as long as the truncation error does not cause instabilities) and the choice of the model parameters is decoupled from the numerics. The second configuration choice is the collocated standard DGSEM, with an added SGS model. In this setting, the closure model has to fulfill the double role of aliasing suppression and physics modeling. When comparing the two approaches in terms of accuracy in a LES setting, we first have to establish the stability of the simulation, and then gauge their accuracy.

As a test case, we have chosen again the cylinder flow described in Section 4.3.2 with slight modifications.

4.4.1. DNS and LES Setup

As discussed in Section 4.3.2.1, a considerable spread exists in the results reported in literature, both for experimental [65, 149, 151, 159] and DNS results [65, 70, 135]. Due to this uncertainty in the reported results and the lack of published reference data for the chosen Mach number of $Ma = 0.3$ (based on the freestream velocity U_∞ and the freestream speed of sound c_∞), we have computed a reference DNS for this case, using our framework presented in Section 3.5.

Figure 4.25 shows a detail of the computational grid for this DNS computation. The unstructured grid consists of 327680 hexahedral elements, spanning a cylindrical computational domain of radius $r_{cyl} = 100 D$ and spanwise extension $\Delta z = 8$. To account for the surface curvature, the geometry is represented through a mapping with $N_{geo} = 4$ within the first cell layer on the cylinder. All other mappings are trilinear. The solution within each element is approximated by a tensor product ansatz of degree $N = 4$, resulting in a total of 40.96 mio degrees of freedom.

The Reynolds and Mach number are set to 3900 and 0.3, respectively, and we enforce periodic boundary conditions on the spanwise domain faces. On the outer domain boundaries, we choose weakly enforced Dirichlet freestream conditions for density $\rho_\infty = 1.0$ and the components of the velocity vector $U_\infty = [1.0, 0, 0]$. The freestream pressure is adjusted to reproduce $Ma = 0.3$. Together with an adiabatic exponent $\gamma = 1.4$, this Mach number yields a stagnation temperature of $1.018 T_\infty$, which we use as a wall temperature for the isothermal cylinder wall boundary condition. The collection of the time-averaged and fluctuating data was started after the establishment of stable vortex shedding at $100 T^*$, with the convective time unit T^* defined as $D/|U_\infty|$ and continued

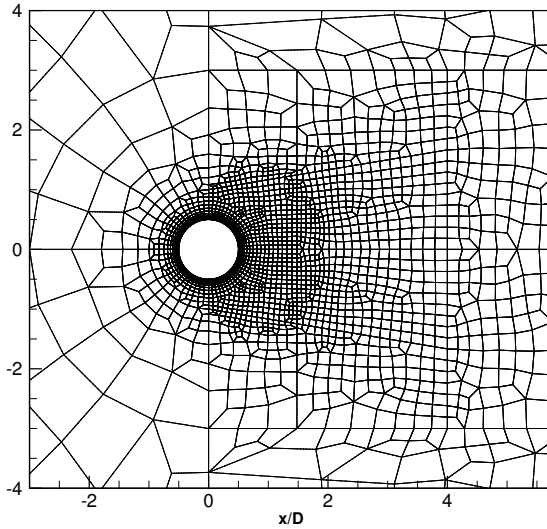


Figure 4.25.: Grid for the DNS computation, detailed view of cylinder vicinity.

for 100 shedding cycles, characterized by the Strouhal period T_{St} .

For reasons of comparability, the setup of the LES computations is identical to that of the DNS described above. In particular, all initial and boundary conditions, averaging periods and physical domain sizes are identical. We choose an upper limit on the number of degrees of freedom of 4.6 mio, and discretize the domain with three consecutively refined grids in a structured, volume-curved manner. Since the total number of DOF is fixed, the coarse mesh corresponds to the highest local ansatz degree N . Figure 4.26 shows the three LES grids and gives mesh details.

4.4.2. Stability and Accuracy Investigations

We will first focus on the stability aspects of PDG and DGSEM, and relegate the closure model to a pure stabilization mechanism. Since the flow under consideration is only weakly compressible at $Ma = 0.3$, the character of the flux function remains quadratic

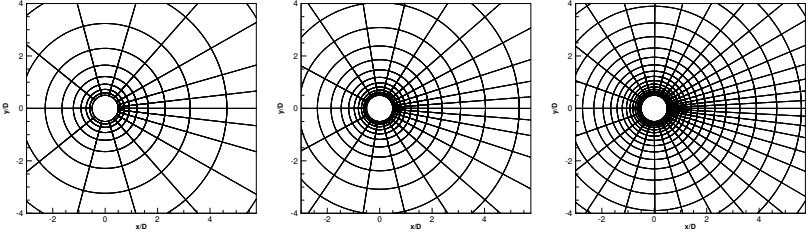


Figure 4.26.: From left to right: Grids I, II and III for the LES computations, detailed view. Grid details: I: $16 \times 16 \times 32$ elements (circumferential, radial and spanwise direction), $N = 7$, II: $22 \times 22 \times 44$, $N = 5$, III: $32 \times 32 \times 64$, $N = 3$.

instead of cubic, and we choose $M = \frac{3}{2}N$ for PDG in all computations. It should be noted that this approximation no longer guarantees complete avoidance of aliasing errors, but we did not encounter any stability issues in our computations. For DGSEM, additional stabilization through the subgrid scale model is needed if the aliasing error cannot be bounded by the numerical dissipation of the scheme. We have chosen the 'minimal' Smagorinsky model constant C_s that resulted in a stable simulation.

Table 4.5 collects the results of our investigations for the three different grids and the associated N . The DGSEM computations (with $M = N$) are denoted by a trailing capital letter following the polynomial degree (e.g. N5-A), while the PDG computations (with $M = \frac{3}{2}N$) are denoted by a trailing numeral. We define a stable simulation as one that does not crash for 100 shedding cycles after the initial transient phase.

A detailed discussion of the results can be found in [21]; here, we just focus on the most important details. As expected, the PDG simulations are stable without an additional viscosity introduced by the closure. The low order DGSEM computation (N3-A) remains stable even for $C_s = 0$, due to inherent high dissipation of the $N = 3$ scheme, while the medium to high order DGSEM formulation require $C_s > 0$. Since the numerical dissipation of DGSEM decreases towards a spectral cut-off behavior with increasing polynomial degree, it is not surprising that the minimal C_s parameter also increases with N for N5-A and N7-A.

Two important trends can be extracted from the data in Table 4.5. First, the match to the DNS reference data improves significantly with increasing N , regardless of the

4. Numerics for Under-Resolved Simulations

<i>Case</i>	C_s^{min}	C_{pBase}	<i>Str</i>	C_D	C_{Lrms}	L_r/D	$\theta_{sep} [^\circ]$	$\theta_{re} [^\circ]$
DNS	-	-0.979	0.204	1.082	0.246	1.160	87.2	116.3
N7-1	0.0	-0.995	0.206	1.085	0.252	1.165	81.8	117.1
N7-A	0.16	-0.919	0.200	1.045	0.164	1.413	87.9	124.8
N5-1	0.0	-0.975	0.208	1.072	0.232	1.217	86.0	117.2
N5-A	0.10	-0.878	0.203	1.016	0.127	1.560	87.6	132.7
N3-1	0.0	-0.847	0.216	0.927	0.106	1.569	90.5	123.4
N3-A	0.0	-0.767	0.236	0.800	0.059	1.655	96.8	128.0

Table 4.5.: Simulation details for the cylinder flow with minimal C_s . C_{pBase} : pressure coefficient at the downstream position $x = D/2, y = 0$, *Str*: Strouhal number of the lift coefficient $f_{Lift} D/U_\infty$, C_D : drag coefficient, C_{Lrms} : RMS value of the lift coefficient, L_r : length of separation bubble, $\theta_{sep}, \theta_{re}$: separation and reattachment location.

choice of PDG or DGSEM. This can be attributed to the general accuracy of high order discretizations in terms of the n_{PPW} requirement, as discussed before. The second important observation supported by this data is a visible shift towards the DNS reference data from DGSEM to PDG, with the N7-1 being in very good agreement with the DNS. All DGSEM results display features of overly dissipative behavior, with case N3-A showing the worst agreement with the DNS data. As noted above, the N3 cases are stable for $C_s^{min} = 0$, however, even here the de-aliasing shows a significant effect on the accuracy of the solution, as all mean values listed in Table 4.5 shift towards the DNS data from DGSEM to PDG. Especially noticeable is the change in the predicted Strouhal frequency, which is governed by the large scale motion. This improvement can be attributed to the increase in accurately represented scales for PDG.

Figure 4.27 depicts the time- and spanwise-averaged streamlines in the wake region. The DNS result is given as a reference, and the subplots contrast the PDG solution (a, c, e) with their DGSEM counterparts (b, d, f). For high N (a, b), the effect of the de-aliasing by subgrid model on the near-wake structure is very pronounced. In particular, N7-1 (a) closely predicts the secondary separation bubble at the downstream face, which is absent for the DGSEM result (N7-A (b)). Also, the length of the back-flow region is significantly overestimated for this case, due to the strong influence of the subgrid viscosity. For the medium N case (c, d), the same behavior, although less pronounced, can be observed. In both cases, the back-flow region is elongated compared to the N7 cases, due to the higher numerical dissipation of the medium N . Although the C_s^{min} required for

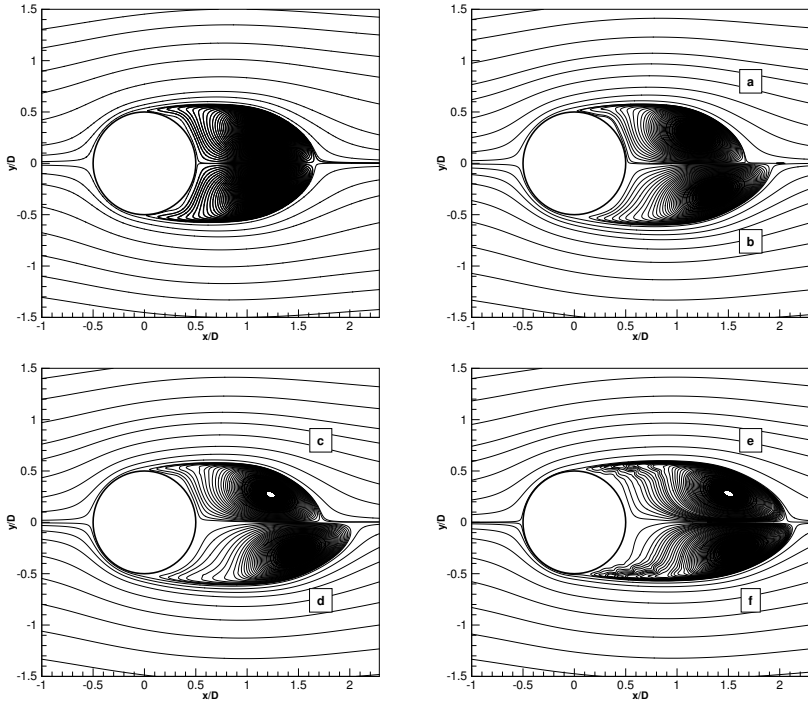


Figure 4.27.: Time- and spanwise-averaged streamlines. Upper left plot: DNS. Rest: a) N7-1, b) N7-A, c) N5-1, d) N5-A, e) N3-1, f) N3-A

stabilization is lower, this increased numerical dissipation and the associated loss in accurately resolved waves results in an overall increased dissipation. For low N (e, f) with $C_s^{min} = 0$, this numerical dissipation is the governing factor on the solution accuracy. Nonetheless, it is interesting to note that the PDG solution (e) shows a better resolution of the region close to the secondary separation bubble and a slightly shorter back-flow region, a result that emphasizes proper de-aliasing even for low order schemes.

Figure 4.28 compares the velocity fluctuations $\langle u'u' \rangle$ at different positions in the wake, which contribute strongly to the turbulent kinetic energy and are thus a measure of the

4. Numerics for Under-Resolved Simulations

quality of the turbulence representation. The general match to the DNS data is greatly improved for PDG, with only N3-1 showing a significant difference to the reference data. For the DGSEM results, the agreement in the near wake region is poor for all cases, as the scale resolution of the scheme is strongly diminished by the aliasing suppression. Further downstream, where the flow physics are less dominated by non-linear small scale effects and more by the mixing through the shear layer gradients, the agreement improves. It is again worth noting that the low order PDG (N3-1) shows a significant improvement over the associated DGSEM results (N3-A). In support of these findings,

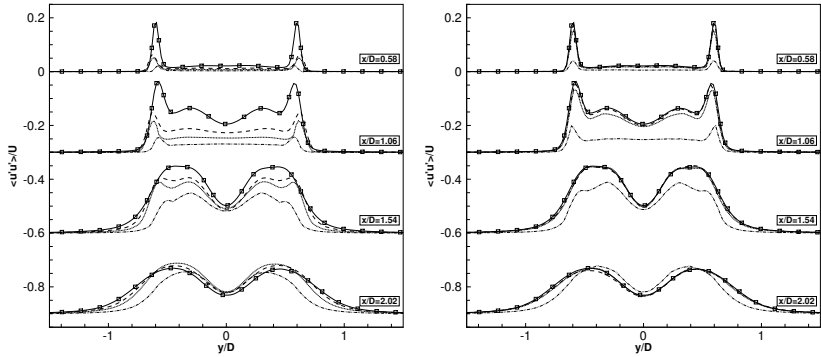


Figure 4.28.: Time- and spanwise averaged velocity fluctuations $\langle u'u' \rangle$ in the cylinder wake. Line with squares: DNS results; *Left:* DGSEM according to Table 4.5. Dashed line: N7-A; dotted line: N5-A; dash-dotted line: N3-A; *right:* PDG according to Table 4.5. Dashed line: N7-1; dotted line: N5-1; dash-dotted line: N3-1.

Figure 4.29 depicts the one-dimensional spectra of the streamwise velocity component, recorded at $x/D = 3.0, y/D = 0.25$ and averaged over 50 equispaced spanwise stations. All frequencies are normalized by the Strouhal frequency of the DNS reference result. The DNS reference spectrum is shown for comparison, the dashed line denotes Kolmogorov's $k^{-5/3}$ law. About 100,000 samples were collected over a dimensionless time interval $TU_\infty/D \approx 500$ (corresponding to about 100 shedding cycles). The

samples were then interpolated on an equidistant temporal grid, using 4th order interpolation, on which a FFT was then conducted. The spectra have been shifted vertically for easier distinction.

As a general observation, the dominant shedding frequency and its first two harmonics

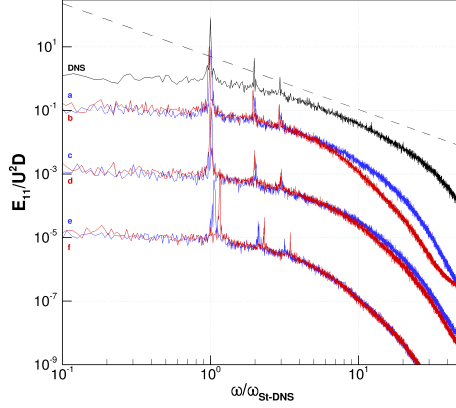


Figure 4.29.: One-dimensional spectra of the streamwise velocity component in the wake at $x/D = 3.0, y/D = 0.25$. All frequencies normalized by the Strouhal frequency of the reference DNS (see Table 4.5). a) N7-1, b) N7-A, c) N5-1, d) N5-A, e) N3-1, f) N3-A; dashed line denotes Kolmogorov's $k^{-5/3}$ law.

are captured in all cases. The associated frequencies are over-predicted for cases N3-1 and N3-A (e, f), which causes the shift to higher frequencies for the chosen normalization. Also, an inertial subrange closely following the $k^{-5/3}$ slope is observable for cases N7-1, N7-A, N5-1 and N5-A (a, b, c, d), with the best agreement to the DNS for N7-1. For N3-1 and N3-A (e, f), the extent of the inertial range is significantly reduced. Most interesting is the influence of PDG versus DGSEM on the high frequency range. For high N (a,b), a significant improvement in scale resolution can be recovered for PDG, as the N7-1 spectrum follows the DNS spectrum more closely up to a significantly higher frequency. Although this trend is also observed for medium N (c, d), the gain is less pronounced, and it is completely covered by noise for low N (e, f). The reason for this

behavior is the interaction of the de-aliasing and the dissipative error of the discretization as a function of N : Following the 3/2 rule, a single evaluation of the non-linear inner product in DGSEM introduces an aliasing error into the upper 1/3 of the polynomial modes. The error of course then interacts non-linearly with the solution and finally manifests itself across all wavenumbers. Therefore, de-aliasing allows the recovery of this 1/3 of the polynomial modes for the accurate representation of the solution. As this upper third is less affected by the approximation errors for high N , the effects of polynomial de-aliasing become more pronounced.

So far, we have only considered results for a minimal C_s , dictated by the aliasing stabilization for DGSEM. In the following, we extend this discussion by choosing the model constant for both PDG and DGSEM to find the best approach for this LES computation. To this end, we have conducted extensive numerical experiments for varying N and C_s , both for PDG and DGSEM. Table B.1 in Appendix B summarizes the details for all computations. While the choice of C_s is arbitrary for PDG, its minimum value for DGSEM is given by the stability discussion above.

Summarizing the results from the investigations and Table B.1, a clear trend can be identified: For high N , increasing the model parameter for both PDG and DGSEM has the same overall effects: A decrease in the base pressure, drag coefficient and lift fluctuations, along with a lengthening of the wake region, all indicative of an increase in viscous actions in the flow. Thus, for both discretization options, any choice of C_s leads to a weaker agreement with the DNS reference. In the PDG case, the basic de-aliased case (N7-1) is already very close to the DNS result due to the moderate Reynolds number and high resolution capabilities of the scheme, and additional viscosity is detrimental. For DGSEM, the lower limit of C_s (N7-A) is already too high from a modeling standpoint, i.e. the suppression of aliasing requires more damping than the truncation error. Thus, the stabilization of the aliasing errors dominates any physically motivated considerations for selecting this model parameter, i.e. the collocative discretization suffers a penalty in terms of accuracy compared to PDG.

For the medium N case, the behavior is very similar to the one described above. It should be noted that the artificial dissipation introduced by the lower degree N becomes more pronounced, resulting in a loss in resolved scales and in turn also in less severe aliasing issues, allowing a wider range of possible model parameters for DGSEM. The optimal C_s for best match with the DNS reference data for DGSEM is not C_s^{min} as for $N = 7$, but slightly higher, although the improvement is not very pronounced (N5-B). Since the loss in scale resolution for the $N = 5$ scheme compared to the $N = 7$ scheme results in a higher truncation error and thus in a stronger cascade blockage (energy cannot be transferred downrange due to lack of small scale interaction partners), a build-up of energy occurs in the large scales, i.e. the large scale energy increase leads to an oscillatory

behavior. For high Reynolds numbers or low resolutions, the numerical dissipation of the scheme may not be sufficient to remove the excess energy. Introducing additional viscosity on these resolved scales can drain this energy and regularize the truncated solution. This interplay of numerical and model dissipation is dependent on the properties of the scheme, the resolution, the model and the flow, which explains why the optimal choice of C_s depends on all of those factors [143]. Thus, although counter-intuitive, a discretization with a stronger artificial dissipation will benefit from a higher value for C_s . In general, according to Table B.1, PDG results show better agreement with the DNS than the DGSEM. It is remarkable that the optimal PDG results for $N = 5$ (N5-1) shows better agreement with the reference data than the DGSEM $N = 7$ (N7-A) solution, indicating again that the excessive damping to counter aliasing essentially negates the scale resolving advantages of the high order discretization.

For the low order cases $N = 3$, the choice of C_s is free, as the numerical dissipation of the low order keeps the aliasing effects bounded. Due to the low scale resolving capabilities and high truncation error, these computations gain from an increase in C_s , with the PDG variants outperforming the DGSEM variants. Even for the same C_s (compare e.g. N3-D and N3-4), the PDG results are in better agreement with the DNS, showing the positive effect of the de-aliasing on the resolved scales.

Figure 4.30 gives a visual impression of the velocity fluctuations $\langle u'u' \rangle$ in the wake region, for the PDG results with and without Smagorinsky model and DGSEM with Smagorinsky model. Shown are the results for the “best” model constant with respect to the DNS, see Table B.1. Note that the PDG results always show better small scale resolution, and that high order discretizations are superior to low order ones. Also, while stabilization of collocation methods with a Smagorinsky closure is possible, the associated loss in accuracy effectively increases the n_{PPW} requirement. This becomes obvious when comparing the $N = 7$ DGSEM (last plot, second row, N7-A) with the $N = 5$ PDG (first plot, third row, N5-1). The PDG solution, although theoretically with a higher n_{PPW} requirement, resolves more scales than its DGSEM counterpart. More details on the results and a fuller discussion can be found in [21].

4.4.3. Discussion

For high Reynolds numbers, some form of dissipative mechanism becomes unavoidable for LES, and the addition of an explicit closure model is the most common approach. For high order methods, the choice of the treatment of the non-linear fluxes plays a major role in solution accuracy and stability and in particular interacts with the closure model. Not only are subgrid scale models evaluated in terms of the flow solution and are thus directly influenced by approximation and aliasing errors, they also act on the same range of resolved scales. Polynomial de-aliasing removes a non-linear source of error that influ-

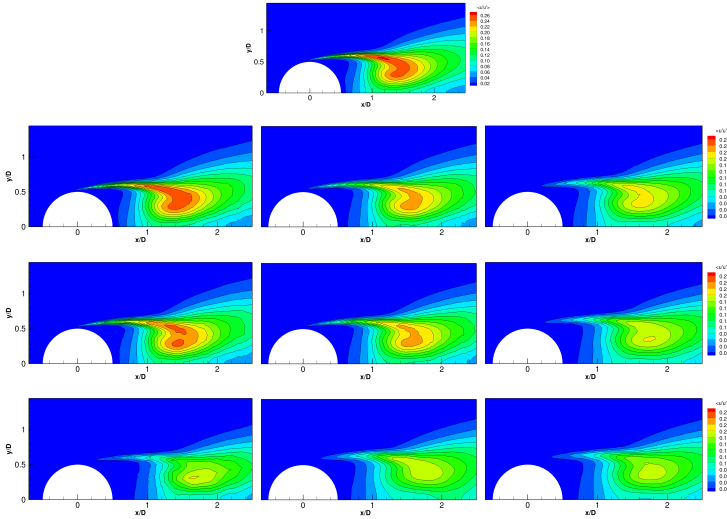


Figure 4.30.: Time- and spanwise-averaged velocity fluctuations $\langle u'u' \rangle$ in the wake region, normalized by U_∞^2 . Top row: DNS reference. First column: PDG results, second column: PDG with Smagorinsky model, last column: DGSEM with Smagorinsky model; second row: N7-1, N7-2, N7-A, third row: N5-1, N5-2, N5-B, fourth row: N3-1, N3-4, N3-D.

ences this interaction, and thus makes a more meaningful evaluation of closure models possible. Particularly for high polynomial degrees with low numerical errors, this approach gives an (approximate) decoupling of numerics and model influences and allows an independent selection of both, hence leading to superior solution accuracy compared to the collocation variant. For LES with low order polynomial degrees, the numerical damping may prevent the aliasing effects from causing stability problems, but their effect on solution accuracy in both “no model” LES and explicit subgrid scale model LES can be pronounced.

Returning to the question posed at the beginning of this section, whether de-aliasing is necessary and beneficial when an explicit dissipation mechanism is needed anyway to counter the truncation error, a three-fold answer can be given:

- i) As summarized above, we have shown the advantages in terms of accuracy for a de-aliased approach. While our investigations cannot be generalized (to other SGS closure strategies), they indicate that the interaction of aliasing and closure can be very strong, non-linear and hard to control a priori, even for low order schemes. Thus, removing the source of instability and error and providing a baseline “neutrally stable” scheme is important.
- ii) Both the development and the evaluation of physically motivated subgrid scale closures require numerical schemes with minimal interaction of approximation errors and the modeling terms. High order DG methods with their inherent low dissipation and dispersion properties are attractive candidates for this approach, however, without de-aliasing, these favorable properties cannot be recovered for efficient LES simulations.
- iii) While the first two answers are strongly in favor of proper de-aliasing, one possible restriction has to be made. The considered test case was at a moderate Reynolds number, and the spatial resolution, while coarse, did capture most of the relevant scales, at least for high N . If the gap between resolution and Kolmogorov scales is increased however, the magnitude of the truncation errors can become larger than the aliasing error, i.e. the necessary dissipation to account for the missing scales can become “large” enough to make de-aliasing by closure attractive, as it comes “for free”. This however depends on the discretization, the resolution and the closure, and has to be investigated further.

4.5. Flux Functions in Under-resolved Flows

While we have focused on a step towards high order DG for LES with explicit modeling in the previous section, we now investigate a discretization aspect that could become important in an implicit LES approach: the choice of the numerical flux functions. For the Discontinuous Galerkin formulation in Equation (3.29), if all inner products are evaluated with the appropriate integration precision (the PDG approach), the discretization itself becomes “analytical” in the sense that it is no longer dependent on the geometrical features of the discretization choices like basis functions, element shapes or node types. The only remaining free parameters are the numerical inviscid and viscous flux functions \mathcal{G}_n^* and \mathcal{H}_n^* . Therefore, their choice determines the consistency, accuracy and stability of the analytical DG method. The task of the flux function is to couple two interfaces with non-unique solutions (and thus non-unique normal fluxes) by determining a suitable unique flux. One method of achieving this is the concept of defining this flux as an (approximate) solution to an initial value problem with constant states (a Riemann problem), an idea developed in the FV method community [196]. While an exact solution to the Riemann problem exists, this so-called Godunov flux function is often too costly to evaluate. Instead, approximations of various degree of physical consistency

exist, leading to a large class of flux functions for the convective and diffusive fluxes.

4.5.1. Flux Choices

4.5.1.1. Inviscid Fluxes

For the DG method, the choice of the flux function for the Euler equations has been investigated by Qui and Qui et al. [169, 170] for smooth and shock-dominated problems. They found that for smooth, well-resolved problems, the flux functions differ only marginally in terms of accuracy and thus the most computationally effective flux is a good candidate. This finding is not surprising, as the number of flux points in a three-dimensional problem scales quadratically with a given reference length of an element, while the volume fluxes scale cubically. Or, considering the strong form of the DG formulation, the influence of the fluxes is just through a surface penalty, which is very small for well-resolved problems. Hence, for higher N and well resolved situations, the influence of the flux functions becomes negligible. Qiu et al. found that for problems with discontinuities, the flux functions with higher physical approximation quality (more waves are considered) clearly outperform more dissipative variants, also a result that can be expected from the experiences of the FV community. Kesserwani et al. [110] also examined these aspects for the dam-break problem of the Shallow Water Equations with similar findings, while Wheatley et al. [203] performed similar numerical experiments with DG for the Magneto-Hydrodynamic (MHD) equations.

The focus of our investigations here is shifted towards the behavior of these flux functions in an under-resolved turbulent setting, which differs significantly from the smooth problems or those with strong, but localized gradients investigated by the researchers mentioned above. In our investigations, we focus on two representatives for the convective fluxes, namely the Local Lax-Friedrichs flux (LLF) and Roe's approximate Riemann-solver. Our choice was governed by the difference in dissipation introduced by these fluxes and their widespread use in the DG community.

Lax-Friedrichs Flux Function

The Lax-Friedrichs (LF) flux and its local variant (LLF or Rusanov flux) are the simplest flux functions, disregarding all but the fastest wave and thus introducing the highest amount of numerical viscosity, see e.g. [196]. Due to its simplicity, robustness and computational efficiency, the LLF is widely used by the DG community. The convective numerical flux in (3.29) is approximated as

$$\mathcal{G}_n^* = - \underbrace{\frac{1}{2} \beta \lambda_{max}^{adv} [U^+ - U^-]}_{\text{Penalty}} + \underbrace{\frac{1}{2} (\vec{\mathcal{G}}_n(U^+) + \vec{\mathcal{G}}_n(U^-))}_{\text{Central flux}}, \quad (4.21)$$

where β is a real number which allows control over the amount of numerical viscosity by penalizing the jump in the solution at the interface (with $\beta = 1$ being the classical LF definition), the superscripts \pm denote the values from the neighbor and local element and λ_{max}^{adv} corresponds to the maximum eigenvalue of the Euler flux matrix as

$$\lambda_{max}^{adv} := \max_{U^+, U^-} (|\vec{v}| + c). \quad (4.22)$$

Here, c denotes the speed of sound waves computed as $c := \sqrt{\kappa RT}$ and \vec{v} is the velocity vector. For the local LF variant considered in this work, the value of λ_{max}^{adv} is computed from the local flow field.

Roe's Approximate Riemann Solver

Another favorite flux function in the DG community (see e.g. [198]) is the approximate Riemann solver due to Roe, see e.g. [196], where the exact Euler flux Jacobian $A = \frac{d\vec{G}}{dU}$ is replaced by a linearization \tilde{A} about an average (Roe) state. The underlying system becomes linear with constant coefficients, i.e. instead of the exact Riemann problem, an approximation is generated, which is then solved exactly. The numerical flux is approximated as

$$\mathcal{G}_n^* = \underbrace{-\frac{1}{2} \beta \sum_{i=1}^m \tilde{\alpha}_i |\tilde{\lambda}_i| \tilde{K}^{(i)}}_{\text{Penalty}} + \underbrace{\frac{1}{2} (\tilde{\mathcal{G}}_n(U^+) + \tilde{\mathcal{G}}_n(U^-))}_{\text{Central flux}}, \quad (4.23)$$

where the $\tilde{\cdot}$ denotes the evaluation at the Roe state, m stands for number of eigenvalues $\lambda_i(U^+, U^-)$ of \tilde{A} , $\tilde{\alpha}_i(U^+, U^-)$ denote the wave strengths and $\tilde{K}^{(i)}(U^+, U^-)$ are the corresponding right eigenvectors. There are two different approaches to finding the intermediate state and from there the wave strengths and eigenvectors which are detailed in [196], in our approach, we use the classical Roe formulation. We have again introduced the parameter β as in Equation (4.21), which allows control over the amount of numerical viscosity.

Note that the structure of both fluxes is similar: a dissipation-free central average of the fluxes, stabilized by a penalty term that introduces some for of numerical diffusion based on the height of the jump and on eigenvalues that describe the strength and direction of information interchange.

4.5.1.2. Viscous Fluxes

For the viscous fluxes, a large choice of formulations exists which, like the convective fluxes, lead to different stability and accuracy properties. An overview of the available

options for the Laplace equation is e.g. given in [9]. The parameter α_{visc} in Equation (3.35) allows a switch between two commonly used variants:

- $\alpha_{visc} = \frac{1}{2}$ leads to the first variant of Bassi and Rebay [12] by using the arithmetic mean for both fluxes. This flux is stable for parabolic problems, while it is known that it becomes unstable for purely elliptic cases.
- $\alpha_{visc} = 0$ or $\alpha_{visc} = 1$ lead to the local DG variant (LDG) by Cockburn and Shu [49].

4.5.2. Influence of the Numerical Fluxes

In this section, we briefly report the influence of the numerical choice of the numerical flux function on the TGV and cylinder computations in a LES setting, as described in Sections 4.3.1 and 4.3.2. As both problems are still advection dominated at the given resolution, we focus on the inviscid fluxes.

4.5.2.1. Taylor-Green Vortex

Following the setup in Section 4.3.1, we have fixed the total number of DOF to 64^3 for all our LES simulations, but have again computed different combinations of grid cells and degree N . This means that for the cases $N = 15$, $N = 7$, $N = 3$ and $N = 1$, we use 4^3 , 8^3 , 16^3 and 32^3 grid cells, respectively. In Figure 4.31, we show the comparison of kinetic energy dissipation rate for the two different convective fluxes described in Section 4.5.1.1. As expected, the polynomial degree has a strong impact on the influence of the flux function on the solution. Although all computations have nominally the same spatial resolution, the difference between the choices is very low for high N and increases subsequently for lower N . Comparing all results from Figure 4.31, we see a clear progression from high order to low order in flux function impact. As the number of cell interfaces increases for a given overall resolution and the approximative strength of the local polynomial ansatz decreases, the influence of the flux function becomes more pronounced. Furthermore, it can be observed that, as expected, the kinetic energy dissipation is lower for the Roe flux function and thus closer to the DNS results. In contrast to the convective fluxes, the impact of the viscous flux function seems negligible in this advection-dominated case. For the low order variants, the numerical dissipation is totally governed by the dissipation mechanism of the Euler fluxes. Only for the case of very high polynomial degree, $N = 15$, where the influence of the Euler flux is low, we observe a measurable impact of the viscous flux choice. But as the results in Figure 4.32 clearly show, the influence on the overall dissipation behavior even in this case remains negligible.

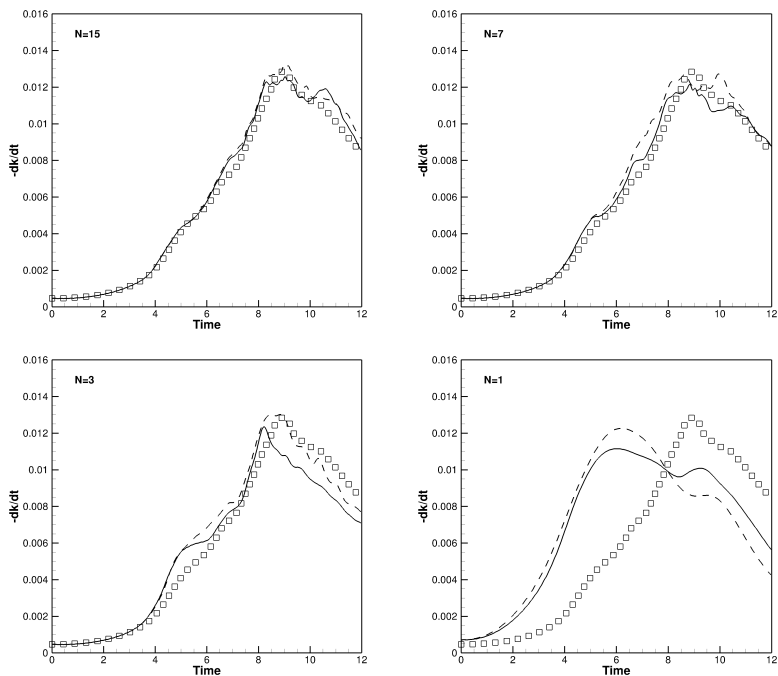


Figure 4.31.: Kinetic energy dissipation rate for the Taylor-Green Vortex at $Re = 1600$: Comparison of convective numerical flux function influence for different polynomial degrees N with same total no. of DOF (64^3). *Square* symbol denotes the reference DNS solution [28], *dashed* line denotes the LLF flux result, the *solid* line denotes the Roe flux result. Plot reproduced from [20].

As expected, in an under-resolved situation, where the inter-cell jump terms become non-negligible, the choice of the flux functions can play a role in solution quality. As long as the spatial resolution in terms of DOF is high enough, for a high order discretization, the scale-resolving capabilities will keep the jumps small, but this mechanism will clearly fail for higher Reynolds number. Thus, modeling the subgrid effects in an implicit LES approach through an appropriate flux function is worth investigating. To demonstrate

4. Numerics for Under-Resolved Simulations

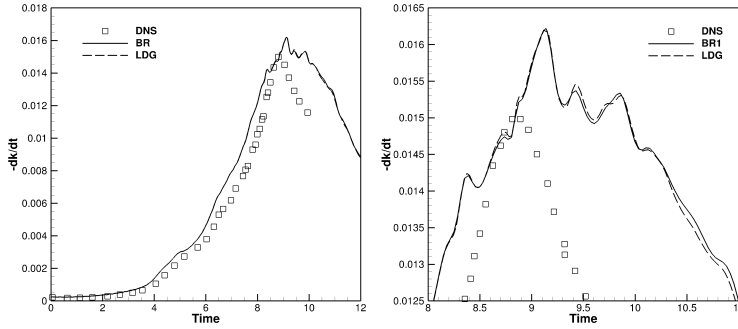


Figure 4.32.: Kinetic energy dissipation rate for the Taylor-Green Vortex at $Re = 3000$: Comparison of LDG flux and BR1 flux with DNS, 4^3 elements, polynomial degree $N = 15$. *Right:* Detailed view. Plot reproduced from [20].

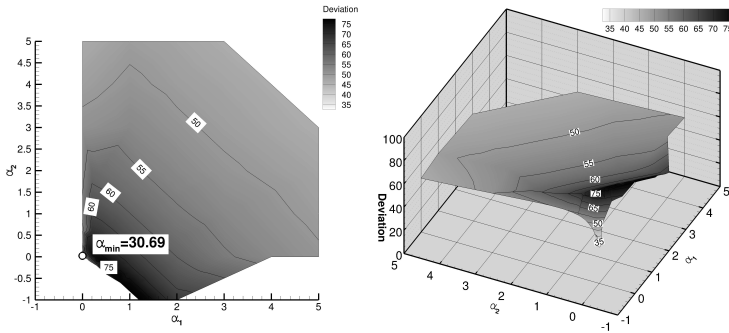


Figure 4.33.: Optimization of the penalty parameters α_1 and α_2 for the kinetic energy dissipation rate. Shown is the L_2 deviation between DNS and LES results as a function of α_1 and α_2 .

the possible benefits and effectiveness of this approach, we have modified the parameter β in Equations (4.21) and (4.23) that penalizes the jump term and thereby regulates

the numerical dissipation. This is a simple ad-hoc version of discretization tuning, but we found a significant increase in solution quality in terms of the energy dissipation rate. Figure 4.34 *left* shows the results for the $Re = 800$ simulation with the classical ($\beta = 1.0$) Roe flux and a modification ($\beta = 0.025$) with lowered dissipation. The overall agreement with the DNS results improves significantly for the modified version, and the physical structure of the dissipation rate reappears in the solution. In the right subplot of Figure 4.34, the modification has been extended to a linear combination of the penalty terms, yielding a combined flux function with free parameters α_1 and α_2 :

$$\mathcal{G}_n^* = -\frac{1}{2} \alpha_1 \lambda_{max}^{adv} [U^+ - U^-] - \frac{1}{2} \alpha_2 \sum_{i=1}^m \tilde{\alpha}_i |\tilde{\lambda}_i| \tilde{K}^{(i)} + \frac{1}{2} \left(\tilde{\mathcal{G}}_n(U^+) + \tilde{\mathcal{G}}_n(U^-) \right). \quad (4.24)$$

Optimization of α_1 and α_2 for various resolution and Reynolds numbers showed a potential of implicit LES modeling through the modification of the penalty dissipation. The kinetic energy dissipation of the DNS served as the target function, and the L_2 error between this reference and the computed dissipation rate was optimized with a gradient based algorithm in parameter space. Figure 4.34 *right* shows the result of such an optimization. While a clear improvement over the standard flux formulations exists, stability issues in the laminar region were encountered. In addition, tuning the flux function for the full range of laminar, transitional, non-decaying and decaying turbulence is not optimal, as it should be conducted for the different physical regimes separately. Thus, while this preliminary study shows the importance of the flux function in under-resolved turbulence and the possibility of implicit modeling through it, the investigations should be repeated with a more efficient optimization algorithm and for homogeneous isotropic decaying turbulence.

4.5.2.2. Cylinder at $Re_D = 3900$

To examine whether the choice of the inviscid flux functions influences the cylinder results from Section 4.3.2 and thereby acts as an implicit LES model, we have repeated the computations for the Roe flux function. Table 4.6 compares the results for the integral values for the originally used LLF and the Roe flux function, and Figure 4.35 compares the pressure coefficient and crossflow velocity in the wake.

While the effects on the integral quantities are small (except for the ratio L_r/D), the wake structure reveals a considerable difference, with the Roe flux being in better agreement with the experimental results. In general, this flux formulation generates a longer wake, indicative of a higher numerical viscosity (see discussion in Section 4.3.2).

4. Numerics for Under-Resolved Simulations

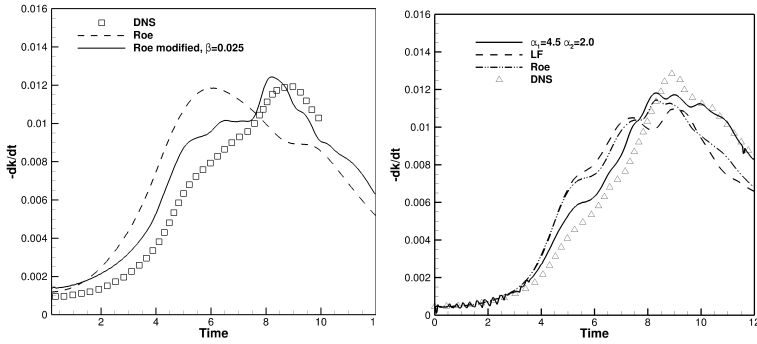


Figure 4.34.: Kinetic energy dissipation rate for the Taylor-Green Vortex: *Left:* $Re = 800$: Comparison of classical Roe flux and modified Roe flux with DNS. *Right:* $Re = 1600$: Comparison of modified combined flux and standard fluxes with DNS.

In this section, we have demonstrated that the choice of the flux functions can play an important role, as the induced dissipation acts as an implicit LES model. Depending on the choice of the polynomial ansatz degree N , the character of DG can be closer to a local, cell-based scheme (a first order DG with $N = 0$ is analytically identical to a first order FV scheme) or a quasi-global, spectral scheme coupled weakly by penalty terms. Thus, in particular for low order DG, the choice of the flux function is important in an under-resolved setting.

We have shown preliminary results for the choice of the inviscid and viscous fluxes and have demonstrated that adjusting the dissipation introduced by the flux function can act as a simple LES closure. In the future, a more thorough analysis of the influence of the flux functions, their behavior in a LES situation and implicit modeling will be necessary.

<i>Case</i>	C_{pBase}	<i>Str</i>	C_D	L_r/D	Scheme	LES	DOF
LLF: $N = 11$	-1.01	0.206	1.10	1.13	PDG	-	0.7 M
Roe: $N = 11$	-1.00	0.212	1.09	1.26	PDG	-	0.7 M
LLF: $N = 7$	-0.91	0.208	1.00	1.31	PDG	-	1.6 M
Roe: $N = 7$	-0.90	0.208	1.02	1.50	PDG	-	1.6 M

Table 4.6.: Integral quantities and simulation parameters for $Re_D = 3900$ cylinder flow, as a function of the Euler flux function. C_{pBase} : pressure coefficient at the downstream position $x = D/2, y = 0$, Str : Strouhal number of the lift coefficient $f_{Lift} D/u_\infty$, C_D : drag coefficient, L_r : length of separation bubble.

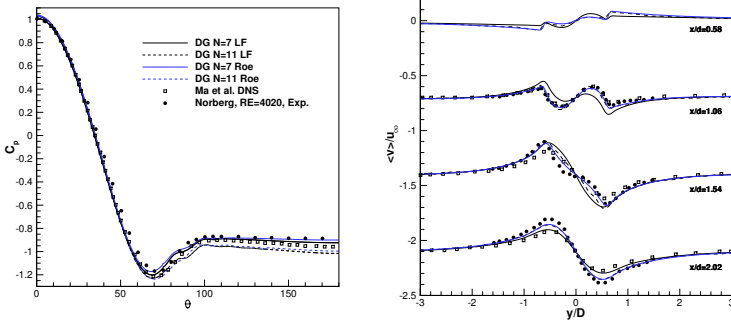


Figure 4.35.: Comparison of Cylinder LES results for Roe and Rusanov-flux for computation described in Section 4.3.2. *Left:* Pressure coefficient along geometry. Filled circles denote experimental data for $Re = 5000$ of Son & Hanratty for vorticity and for $Re = 4020$ of Norberg for pressure coefficient (taken from [141]). Open squares denote DNS results [135]. *Right:* Mean crossflow velocity at different downstream locations in the wake of the circular cylinder flow at $Re_D = 3900, N = 11$ computation. Solid black lines: DGSEM with Rusanov flux. Solid blue lines: DGSEM with Roe flux. Dashed lines: computational LES results from [141]. Open squares: computational LES results from [122]. Filled circles: experimental results from [159].

4.6. LES with DG Methods

In this section, we will briefly summarize the current state of the art regarding LES with DG methods and then outline a more consistent strategy for current application and future research based on our results from the previous sections.

4.6.1. State of the Art

Along with the first DNS with DG, Collis [51] in 2002 was among the first to use DG schemes in a LES setting. He applied a Smagorinsky eddy viscosity model to the small scales via the Variational Multiscale (VMS) method [52]. Sengupta et al. [179] combined the element-wise filtering approach of Blackburn and Schmidt [24] with a DG spectral element method (DGSEM) and performed LES with a dynamic Smagorinsky model. More recently, Uranga et al. [198] used an $N = 3$ DG formulation for the simulation of a transitional flow over a SD7003 airfoil, taking advantage of the numerical dissipation to account for the damping action of the unresolved scales in an implicit LES approach. A similar investigation was carried out by Carton de Wiart and Hillewaert [35]. The accuracy of DG methods for high Reynolds number vortical flows for $N = 3$ was investigated in [36]. For higher orders ($N = 7, \dots, 15$), Gassner and Beck [84] and the discussion in Section 4.3 showed that de-aliased DG schemes applied to under-resolved simulations of isotropic turbulence compare very well with low order FV schemes with explicit or implicit subgrid scale models. In this case, the number of degrees of freedom was chosen as in the FV approach, and no additional dissipation was added explicitly or implicitly to the DG formulation. Instead, the high resolution capabilities of high order discretizations resolve a much larger bandwidth of turbulent scales, thereby allowing the viscous action of the Navier-Stokes operator to remove most of the energy without the need for an additional model. In terms of computational efficiency, it was shown in [200] that high order DG schemes can compete with FD and FV formulations in a LES setting of this flow problem. In [18], this approach was recently extended to transitional and turbulent wall-bounded flows, demonstrating again that for moderate Reynolds numbers and typical LES resolutions, no additional modeling is required, when de-aliased high order DG formulations are used. Also, the importance of de-aliasing and its interaction with an explicit subgrid model was investigated in [21]. Van der Boss et al. [199] conducted a similar analysis for homogeneous isotropic turbulence and found that the numerical dissipation of the scheme and that of an explicit Smagorinsky model interact strongly, and that the optimal model constant strongly depends on the order of the scheme. In particular, they found that an implicit LES approach gave inferior results than one with an added Smagorinsky dissipation, yet, their investigations were limited to low order DG ($N \leq 2$). As discussed in Section 4.4.2, the low order DG discretizations

lack the scale-resolving capabilities of their high order counterparts and need additional dissipation to account for the lack of resolved, dissipative scales.

4.6.2. Perspectives for High Order LES

The current state of the art in LES with DG methods is the use of moderately high approximation orders in an implicit “no model” LES approach for moderate Reynolds numbers. Some publications combining DG with an explicit LES model (typically a version of the standard Smagorinsky model) exist, but the baseline scheme in these investigations is of low to moderate order, thereby not taking advantage of the spectral character of high order DG.

In general, the solution quality of an under-resolved computation is bounded by the available number of degrees of freedom, i.e. the theoretically smallest resolvable scale (Nyquist theorem). The properties of the numerical discretization determine the quality of these degrees of freedom, i.e. the fraction of the complete information represented on this grid. High order discretizations allow the recovery of a significant part of the theoretically available physical information, thereby limiting the “numerical truncation error” (as opposed to the grid or DOF truncation error) compared to low order schemes. The associated reduction in numerical dissipation comes at a cost: De-aliasing becomes necessary not only for stability, but also for accuracy. Since the use of proper polynomial de-aliasing prevents numerical instabilities through wrongfully represented energy, the only issue remaining is the lack of subgrid scales and their associated dissipation, as a direct consequence of under-resolution. Thus a mechanism needs to be present that accounts for the energy transferred to high wavenumbers, or in other words, mimics the dissipation of the unresolved scales, while leaving large scales unaffected. In a classical LES setting, this role is played by the (explicitly added or implicitly introduced) subgrid modeling terms. In high order discretizations, a large bandwidth of scales can be resolved within each cell. These scales can carry a non-negligible physical dissipation, and thereby provide a significant part of the physical regularization through the viscous operator in the Navier-Stokes equations. The remaining numerical dissipation acting near the cut-off wavenumber can effectively serve as a source for the non-resolvable cascaded energy. Thus, a simple principle applies for high order DG for moderate Reynolds numbers and typical LES resolution: The accurate resolution of the dissipative mechanisms is the best available “model”.

Clearly, this approach reaches its limits when the scale range between the smallest physical scale and cut-off scale increases, i.e. when the truncation error becomes larger, or when the small scale physics are no longer dominantly dissipative. In that situation, additional dissipation (or closures modeling other subgrid effects) becomes necessary. For both implicit and explicit modeling approaches, high order DG is particularly well-

sited:

Implicit modeling implies the manipulation of the approximation errors to serve as a subgrid model. In DG, the simplest way to influence the discretization error is through local p -adaptation and through the choice of the flux function. Both mechanisms allow direct control over the numerical dissipation without additional modeling efforts. An interesting approach, directly related to the high wavenumber range resolved within each element, is the implicit LES modeling through controlled, adaptive de-aliasing. As discussed in Section 4.2, the aliasing errors enhance the fluctuation energy in the resolved scales near the cut-off, thereby also enhancing the viscous dissipation through those scales. Since the mechanism is self-feeding, de-aliasing becomes necessary to avoid an excessive build-up for stability. However, to ensure stability, this de-aliasing does not have to become active at every time step. Instead, a locally and temporally adaptive de-aliasing mechanism that relies on intelligent indicators can allow a certain amount of aliasing energy to accumulate and then dissipate, thereby enhancing the overall dissipation and extending the Reynolds number range compared to a “no model” LES.

Still, without an additional explicit source of dissipation or a filtering operation, the implicit strategy outlined above will not be suitable for very high Reynolds numbers. Thus, some form of explicit modeling in combination with high order DG will be necessary. Here again, the high local resolution within a cell can be exploited in three ways: i) The local spectral information content can be used to generate sensitive indicators and analyze the flow field during the computation to select appropriate closures. ii) The very low numerical error makes the combination with explicit models based on physical considerations very attractive, as an (approximate) decoupling of discretization and model becomes feasible. iii) More elaborate models, based not only on the solution and its first order derivatives become meaningful, as the high order discretization provides local spatial derivatives with acceptable accuracy.

In summary, for moderate Reynolds numbers, an implicit LES approach with a de-aliased high order DG discretization is highly accurate and efficient. For higher Reynolds numbers, the most important feature of DG is the local spectral resolution, as it provides nearly error-free numerics and highly accurate information about the local scale cascade, which can be exploited both in an explicit or implicit closure approach.

5. Conclusion and Prospects

Multiscale problems are ubiquitous in nature and science due to the fact that all but the most basic laws of physics contain non-linearities. What makes them difficult to tackle from both an analytical as well as a numerical point of view is not only the resulting large bandwidth of scales, but also the shift in relative importance of the dominating physical effects along the supported scale range. In this work, we have focused on hydrodynamic turbulence as a prominent representative of these types of problems. Although for typical Mach and Reynolds numbers the governing equations remain valid for the whole scale range (other multiscale problems may require different sets of descriptive equations at both ends of their scale range), both their mathematical and physical understanding is still incomplete due to high complexities and sensitivity to boundary and initial conditions. We have started by discussing the prominent features of these flows, with a special focus on two issues that become particularly important when resolving only a truncated subset of the full scales: i) The non-linearities that establish a self-feeding scale cascade in three dimensions and regulate the transfer of energy between the scales and ii) the stability of the large scale solution against deviations, which make the LES methodology meaningful despite the chaotic and highly sensitive small scale behavior.

From this discussion of the physical groundwork, we have outlined the rationale for LES, and derived a general problem description that incorporates the different strategies for filtering and modeling. Next, we have defined what a “perfect” LES would entail: a regularization of the multiscale problem with a significant reduction of its degrees of freedom, combined with an exact closure for the subgrid terms. Both processes can only be approximatively realized for realistic turbulence problems, nonetheless, we have demonstrated that for a simplified problem, this approach leads to the exact solution of the LES problem, independent from the numerical details. These details however become very important in the practical design of discretization schemes for the numerical simulation of these problems, both for fully resolved and under-resolved cases.

For three-dimensional turbulence, the properties of the spatial discretization operator determine strongly the efficiency and accuracy of the numerical solution. In particular, the computational effort for a full resolution of all dynamically active scales is directly proportional (per dimension) to the number of degrees of freedom n_{PPW} required by the discretization to accurately resolve this scale. Thus, minimizing this quantity has a drastic effect on the accuracy and efficiency per invested degree of freedom, and determines

the limit of practically achievable DNS resolutions on HPC systems. We have shown that the magnitude of n_{PPW} is directly related to the domain of dependence of the discretization operators, and that efficiency in terms of the ratio of resolved to represented modes (on a given grid) can only be achieved by methods with a spectral (or high order) character. As an example of global spectral methods, we have discussed Fourier-Galerkin and Fourier-pseudo-spectral methods, and have presented a Fourier-based pseudo-spectral solver for the three-dimensional compressible Navier-Stokes equations developed within this work. Due to the limitations of the global ansatz in terms of geometrical flexibility, the field of application of these methods is limited to basic research on the “building block” level. Discontinuous Galerkin methods combine the idea of incorporating all available information in a domain into the construction of the approximation operators (resulting in spectral error convergence) with the geometrical flexibility of coupling domains weakly through an appropriate penalty term. In addition, by being element-based, these hybrid methods avoid the parallelization bottleneck encountered by global methods.

In this work, we have presented a DGSEM framework for the massively parallel numerical simulation of multiscale problems. We have discussed details of the derivation and implementation, which make this variant of DG highly effective, both in terms of invested degrees of freedom as well as parallel execution speed. We have compared it for a DNS of vortical flows against other codes, and found our implementation to be highly efficient and competitive, clearly distancing other DG methods and challenging FD schemes. In addition, among the DNS cases reported in this work, the computation of the Taylor-Green vortex with 216 mio DOF (per conservative variable) on 125,000 cores is up to date the largest reported DG computation of turbulent flows, both in terms of the number of unknowns as well as number of computing units, thereby demonstrating the capabilities of the full framework for Petascale computing.

Despite the steady increase in computing power, DNS of multiscale flows will remain the exception, while the simulation of truncated flow fields will remain the norm. This truncation (either through a mathematical filter procedure or through the projection onto a finite set of DOF, e.g. the grid) imposes two additional challenges, which we have discussed in detail: i) the truncation operation itself can only in very specific circumstances (e.g. explicit filtering with a commutative filter on a regular, periodic grid) return a consistently regularized truncated problem, and ii) the truncation induces the need for a closure of the unrepresented scales. Since the explicit filtering is numerically very expensive and difficult on non-regular grids, this approach is seldom followed in practice, instead, a grid-filtered implicit LES is the norm. In this situation, the discretization operators act on the grid representation of the full solution of the multiscale problem, i.e. on a “rough” solution containing wavenumbers beyond the resolution capabilities of the discretization. This entails the introduction of approximation errors into the solution,

and as the grid spacing h becomes “large” (with respect to the occurring scales), the concept of “order of error convergence” of a scheme becomes less meaningful. Instead, the dispersion and dissipation properties of a scheme over the full wave range become important. We have discussed these issues and shown that high order DG schemes benefit greatly from their low n_{PPW} requirement, even in under-resolved settings.

Another issue introduced by the truncation onto a limited set of DOF is the occurrence of aliasing errors through the scale-producing terms. We have investigated the source of these errors, both physically and numerically, as well as their effects on accuracy of the solution representation and on the operator stability. Several strategies for avoiding or suppressing these instabilities exist. We have focused on two approaches: i) a polynomial de-aliasing, an idea translated from the Fourier-pseudo-spectral methods to element-based spectral methods, where the non-linearities are evaluated on a sufficiently fine “subgrid” and then accurately projected back onto the computational grid, and ii) a stabilization through a dissipative filtering, that acts directly on the modes represented on the computational grid. We have discussed the implementation of both mechanisms into our framework, and have evaluated them for under-resolved turbulent flows at moderate Reynolds numbers: the Taylor-Green Vortex case and the flow over a circular cylinder at $Re_D = 3900$. In both settings, we have compared against published LES results with approximately the same number of DOF and DNS results. For both cases, we have found that properly de-aliased high order DGSEM without additional LES closure results in better solution accuracy compared to low order methods with implicit or explicit LES modeling. This is due to the superior scale-resolving capabilities of the high order formulations and the moderate Reynolds number. In particular for the Taylor-Green vortex flow, we have shown that while the stabilization through filtering may be effective from a numerical point of view, it destroys the favorable n_{PPW} requirement of high order methods. Thus, our “no model” LES or under-resolved DNS approach based on de-aliased high order DGSEM, is highly attractive for LES at moderate Reynolds numbers.

An extension of this approach to higher Reynolds numbers will necessitate some form of either explicit or implicit LES modeling. As a first step towards this goal, we have investigated the interaction of aliasing errors and a basic explicit SGS model. Since these closure models are essentially dissipative in nature, the question whether an explicit de-aliasing strategy remains necessary or whether the closure can perform both tasks (physical model and aliasing control) opens. We have provided an answer by combining an either aliasing-afflicted or de-aliased discretization with a Smagorinsky model. Our results clearly underline the need for proper de-aliasing to provide a “neutrally stable” discretization, both in terms of solution accuracy as well as subgrid model evaluation.

5.1. Future Work

Based on the results and discussions presented in this work, a number of interesting directions for further research should be explored:

Flux Functions in Under-Resolved Turbulence

In Section 4.5.2, we have briefly touched on the influence of the numerical flux functions (with a focus on the Euler fluxes) for under-resolved turbulence. It is obvious from the strong form of the DG formulation, that for well-resolved situations, the jump at the cell interface and with it the influence of the flux functions diminishes, but if the jump becomes non-negligible, the choice of the flux functions will play a role in solution accuracy. For high order formulations, where the number of volume DOF is much larger than that of the surface nodes, this effect might not be as pronounced as for low order schemes, but still can be significant, depending on the degree of under-resolution. In addition, the choice of Gauss vs. Gauss-Lobatto nodes in combination with the flux functions should also be investigated, as they differ in terms of how the surface flux is incorporated into the volume solution.

With regards to implicit LES modeling, we have shown a very simple ad-hoc modeling approach through the linear combination of penalty terms. This investigation should be extended, combined with other modeling terms and a more efficient optimization framework and repeated for a homogeneous isotropic turbulence and a turbulent boundary layer.

Large Scale Simulations

What makes our DGSEM framework stand out among the other codes for the simulation of multiscale flows are three features: i) As opposed to Fourier spectral or FD methods, fully unstructured meshes are incorporated naturally in this element-based approach, allowing the discretization of complex geometries. ii) Advection-dominated problems like vortical flows do not require additional stabilization like in continuous FE, in addition, the discontinuous approximation space makes efficient parallel scaling easier to achieve. iii) Accuracy can easily be increased through p-adaptation, without losses in numerical efficiency (like for high order FV schemes). Thus, DGSEM is essentially a hybrid, combining the favorable properties from other discretization schemes into a single package. In addition to the scheme itself, it has been shown in Section 3.5 that our complete framework from pre- to post-processing is set up and ready to handle large scale computations at Petascale level. In future work, this framework should be used to push the limits of large scale computations of turbulent flows, both in an industrial setting in complex domains, as well as to establish benchmark computations of compressible turbulence for

basic research on the next generation of supercomputers.

LES Closure for High Order DG

As has been discussed in Section 4.6, the current state of the art for LES with DG methods is either a “no model” implicit LES approach or the incorporation of classical explicit SGS models, both with a baseline scheme of moderate order. While these two approaches have produced acceptable results for moderately complex flows, they both do not exploit the main advantage of a spectral element method: The existence of a solution that contains a significant range of accurately resolved scales within in element. This property can be exploited for both implicit and explicit LES closures strategies:

i) The low approximation errors of high order DG make the combination with an explicit model particularly attractive, as model and numerics can be considered essentially decoupled. Thus, the interaction between the model and the discretization is minimal. This is particularly important for scale-based models, i.e. those derived from physical considerations of the scale cascade (e.g. the Scale Similarity model or Interscale Transfer model discussed in Section 2.4.3), since the numerical representation of the scales close to the grid cut-off retains acceptable accuracy. In addition, high order closure approaches developed within the context of global spectral methods can now directly be transferred to DGSEM [22, 130].

ii) The de-aliasing strategy through exact integration of the non-linear fluxes and its implementation through a modal filtering approach has been discussed in detail in Section 4.2.2. It should be noted that this approach itself should not be considered as an implicit LES closure, as it merely removes a source of error, but does not exploit or manipulate it as a SGS model. Nonetheless, the polynomial de-aliasing procedure gives an idea for a novel SGS closure for high order methods, that is outlined here briefly: From a purely numerical point of view, the expansion of the flux function on a finer grid (with associated quadrature and interpolation points $M > N$) serves as a way of evaluating its non-linearity exactly. From a modeling point of view, this fine grid also serves as a form of subgrid, i.e. an extension of the computational grid beyond N (or the associated Nyquist wavenumber). On this subgrid, the non-linear terms produce fluctuating scales that act as a partner in the triadic interactions and allow the deposition of energy from the larger scales. Due to the truncation error, this energy will accumulate and eventually lead to a crash, if not removed ahead of time. Based on physical considerations, slope indicators can be constructed, that monitor this build up and trigger a de-aliasing step to clear the subgrid scales. This operation can be conducted element-wise. In other words, this locally adaptive de-aliasing mechanism (LAD) exploits the fine integration grid as an energy sink, where it allows the occurrence of subgrid scales in a deconvolution sense. If the deconvolved scales become energetically charged, the energy is

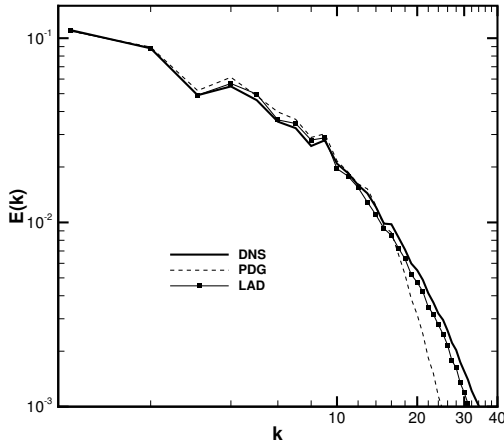


Figure 5.1.: Kinetic energy spectra of HIT at $Re_\lambda = 82$. DNS (solid line) computed with *Spex* on 512^3 nodes. Dashed line denotes PDG result, solid line with markers denotes LAD result, both with 72^3 DOF ($N = 11$). Data taken from [74].

removed by a projection onto the solution grid. Thereby, the de-aliasing procedure can be modified towards an implicit LES closure.

Figure 5.1 shows the potential of this approach for decaying isotropic turbulence. The PDG solution is given for comparison, as it denotes the fixed de-aliasing in every operator evaluation, while the LAD scheme only performs a de-aliasing step when triggered by the indicators. It can be seen that PDG method suffer from a build-up of energy in the low modes, due to the cascade blockage. This blockage is reduced in LAD, resulting in an improvement agreement with the DNS results for all wave numbers. In a related idea, a linear combination of a de-aliased and an aliasing-influenced fluxes could provide a similar energy drain mechanism. Thus, both of these ideas takes full advantage of the spectrality and locality of DGSEM, and should be investigated and improved in future research.

A. Initial Conditions for Homogeneous Isotropic Turbulence

Following Rogallo [175], an initial incompressible velocity field with zero mean and a prescribed energy spectrum for the simulation of homogeneous isotropic turbulence can be generated from the following equations for the Fourier coefficients at wave vector $\vec{k} = (k_1, k_2, k_3)^T$ for the three components of velocity:

$$\begin{aligned}\tilde{u}_1(\vec{k}) &= \frac{\alpha k k_2 + \beta k_1 k_3}{k \sqrt{k_1^2 + k_2^2}}, \\ \tilde{u}_2(\vec{k}) &= \frac{\beta k_2 k_3 - \alpha k k_1}{k \sqrt{k_1^2 + k_2^2}}, \\ \tilde{u}_3(\vec{k}) &= -\frac{\beta(\sqrt{k_1^2 + k_2^2})}{k},\end{aligned}\tag{A.1}$$

where k denotes the magnitude of \vec{k} , α and β are given by Equation (A.2) and the sign error for \tilde{u}_3 in the original publication has been corrected. The incompressibility condition in wave space has been incorporated into the determination of the components in Equation (A.1), and the energy spectrum is prescribed through the magnitude of the random coefficients α and β as

$$\begin{aligned}\alpha &= \left(\frac{E(k)}{4\pi k^2}\right)^{\frac{1}{2}} e^{I\theta_1} \cos \phi \\ \beta &= \left(\frac{E(k)}{4\pi k^2}\right)^{\frac{1}{2}} e^{I\theta_2} \sin \phi,\end{aligned}\tag{A.2}$$

with θ_1, θ_2 and ϕ uniformly distributed random numbers on the interval $(0, 2\pi)$ and $E(k)$ the desired energy spectrum. In our implementation, each coefficient is scaled by the number of wavevectors assigned to its shell, so that the total energy per shell can be described directly. Figure A.1 shows the coefficients α and β for a box spectrum. Note the hollow sphere structure in wave space, and that red colors indicate a higher magnitude, due to the decreasing number of wave vectors on the inner shells. It should

A. Initial Conditions for Homogeneous Isotropic Turbulence

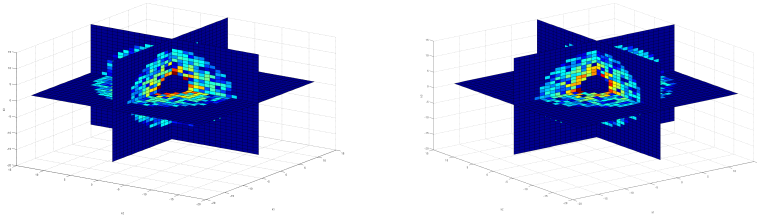


Figure A.1.: Coefficients α (left) and β (right) in wave space for a box spectrum $E(k) = \text{const}$ for $4 \leq k \leq 12$, $E(k) = 0$ otherwise.

be noted that Rogallo's procedure yields a velocity field that isotropic in the x - y plane in physical space, but anisotropic in the y - z plane. Figure A.2 shows the scatter plots of these correlations.

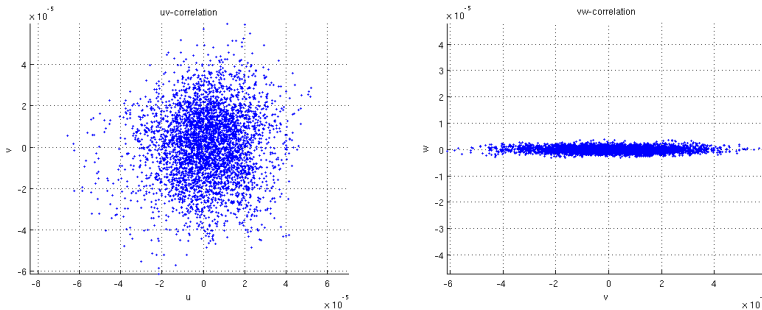


Figure A.2.: Scatter plot of u - v and v - w correlations from Rogallo's procedure (Equations (A.1) and (A.2)).

From Equation (A.1), the resulting modal velocity coefficients can be transferred to physical space with a FFT. The Poisson equation for pressure (Equation (2.18)) can then be solved in a pseudo-spectral manner, where the product $u_i u_j$ is evaluated in a collocation step in physical space, and the differentiation is conducted in spectral space.

B. Flow over a Cylinder at $Re_D = 3900$ - Extended Results

In this appendix, we provide additional results for the investigations reported in Section 4.4.

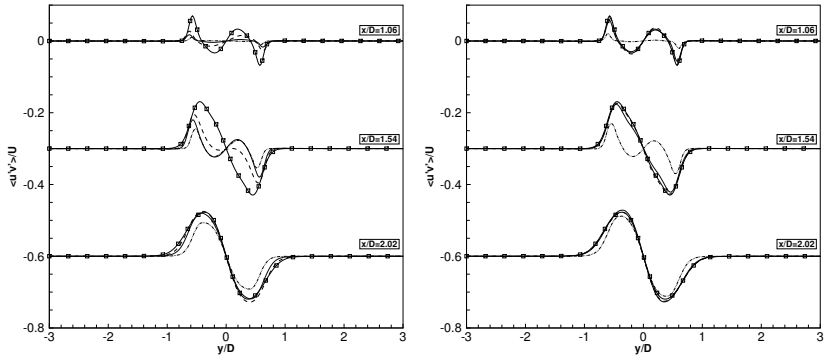


Figure B.1.: Time- and spanwise averaged velocity fluctuations $\langle u'v' \rangle$ in the cylinder wake. Line with squares: DNS results;
left: DGSEM according to Table 4.5. Dashed line: N7-A; dotted line: N5-A; dash-dotted line: N3-A.
right: PDG according to Table 4.5. Dashed line: N7-1; dotted line: N5-1; dash-dotted line: N3-1.

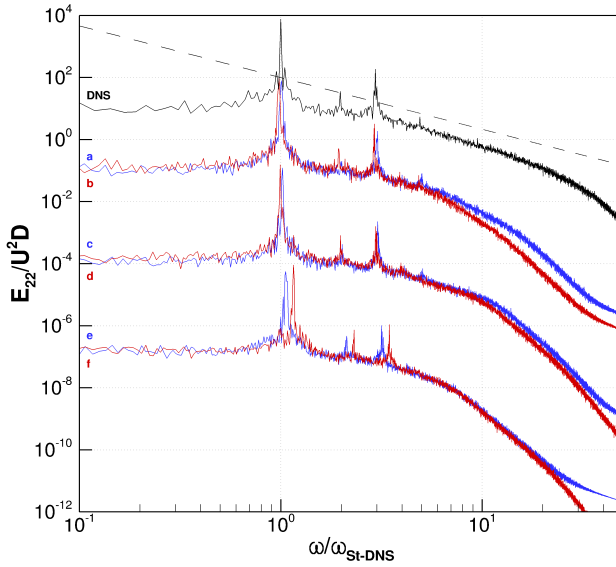


Figure B.2.: One-dimensional spectra of the crossflow velocity component in the wake at $x/D = 3.0, y/D = 0.25$. All frequencies normalized by the Strouhal frequency of the reference DNS (see Table 4.5). a) N7-1, b) N7-A, c) N5-1, d) N5-A, e) N3-1, f) N3-A; dashed line denotes Kolmogorov's $k^{-5/3}$ law.

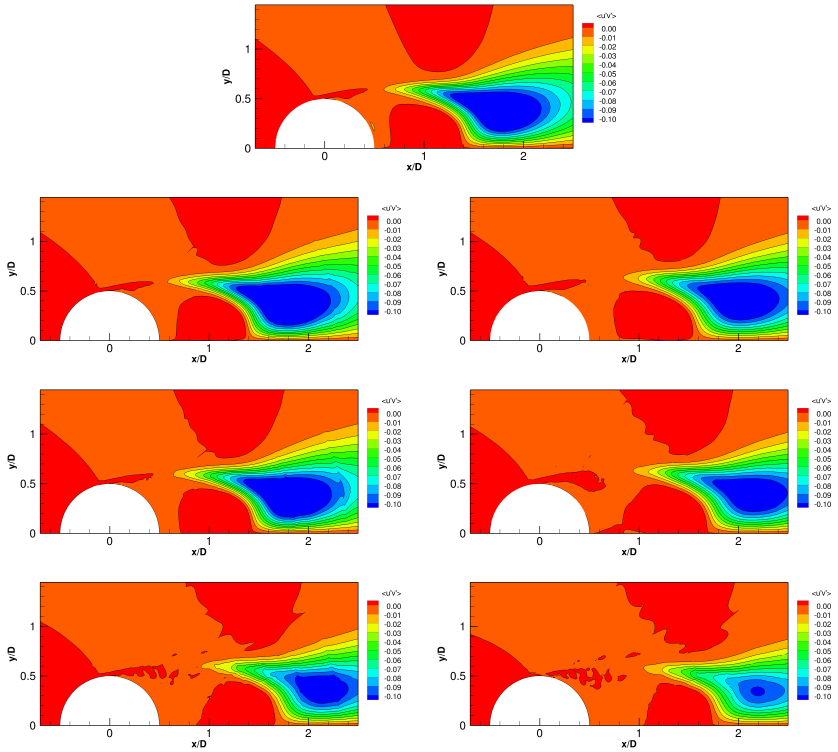


Figure B.3.: Time- and spanwise-averaged velocity fluctuations $\langle u'v' \rangle$ in the wake region, normalized by square of the free-stream velocity U_∞ . Top row: DNS result. Second to fourth row: results for N7, N5 and N3 cases, with PDG in the left and DGSEM in the right column.

B. Flow over a Cylinder at $Re_D = 3900$ - Extended Results

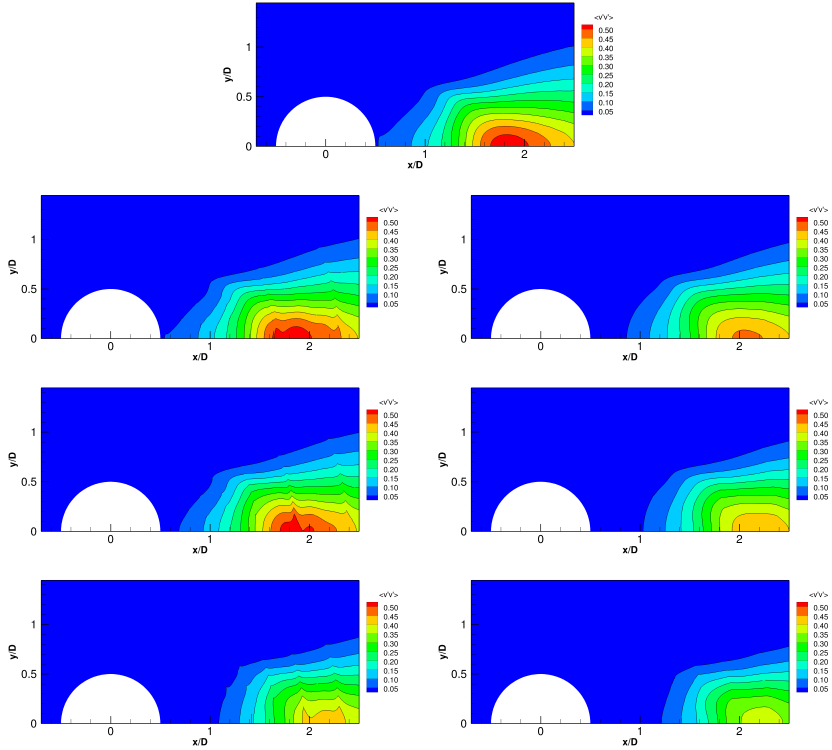


Figure B.4.: Time- and spanwise-averaged crossflow velocity fluctuations $\langle v'v' \rangle$ in the wake region, normalized by square of the free-stream velocity U_∞ . Top row: DNS result. Second to fourth row: results for N7, N5 and N3 cases, with PDG in the left and DGSEM in the right column.

Table B.1.: Simulation parameters for $Re_D = 3900$ cylinder LES computations.

C_{case}	C_s	$C_{p_{Base}}$	Str	C_D	$C_{L_{rms}}$	L_r/D	$\theta_{sepr} [^\circ]$	$\theta_{re} [^\circ]$
DNS	-	-0.979	0.204	1.082	0.246	1.160	87.2	116.3
N7-1	0.0	-0.995	0.206	1.085	0.252	1.165	81.8	117.1
N7-2	0.05	-0.938	0.206	1.050	0.190	1.329	89.8	121.4
N7-3	0.10	-0.916	0.204	1.043	0.167	1.426	87.5	126.0
N7-4	0.20	-0.867	0.198	1.013	0.118	1.626	88.9	136.7
N7-A	0.16	-0.919	0.200	1.045	0.164	1.413	87.9	124.8
N7-B	0.18	-0.893	0.200	1.030	0.143	1.506	88.7	125.6
N7-C	0.20	-0.883	0.199	1.023	0.136	1.555	89.4	128.9
N5-1	0.0	-0.975	0.208	1.072	0.232	1.217	86.0	117.2
N5-2	0.05	-0.935	0.206	1.053	0.195	1.350	87.4	121.2
N5-3	0.10	-0.895	0.205	1.026	0.145	1.499	87.1	131.1
N5-4	0.20	-0.906	0.200	1.037	0.156	1.474	88.6	125.2
N5-A	0.10	-0.878	0.203	1.016	0.127	1.560	87.6	132.7
N5-B	0.15	-0.886	0.202	1.022	0.136	1.541	88.0	131.8
N5-C	0.16	-0.878	0.200	1.018	0.130	1.570	88.1	130.8
N5-D	0.20	-0.871	0.202	1.013	0.127	1.607	88.5	133.0
N3-1	0.0	-0.847	0.216	0.927	0.106	1.569	90.5	123.4
N3-2	0.05	-0.862	0.208	0.973	0.110	1.626	87.2	124.7
N3-3	0.10	-0.875	0.202	0.999	0.122	1.598	86.7	126.6
N3-4	0.20	-0.883	0.202	1.016	0.140	1.569	90.1	128.2
N3-A	0.0	-0.767	0.236	0.800	0.059	1.655	96.8	128.0
N3-B	0.05	-0.813	0.212	0.902	0.084	1.731	90.5	125.3
N3-C	0.10	-0.854	0.200	0.981	0.105	1.683	86.7	131.6
N3-D	0.20	-0.876	0.200	1.011	0.127	1.588	90.6	132.1

$C_{p_{Base}}$: pressure coefficient at the downstream position $x = D/2, y = 0, Str$: Strouhal number of the lift coefficient $f_{Lift} D/u_\infty$, C_D : drag coefficient, $C_{L_{rms}}$: RMS value of the lift coefficient, L_r : length of separation bubble, θ_{sepr} , θ_{re} : separation and reattachment location.

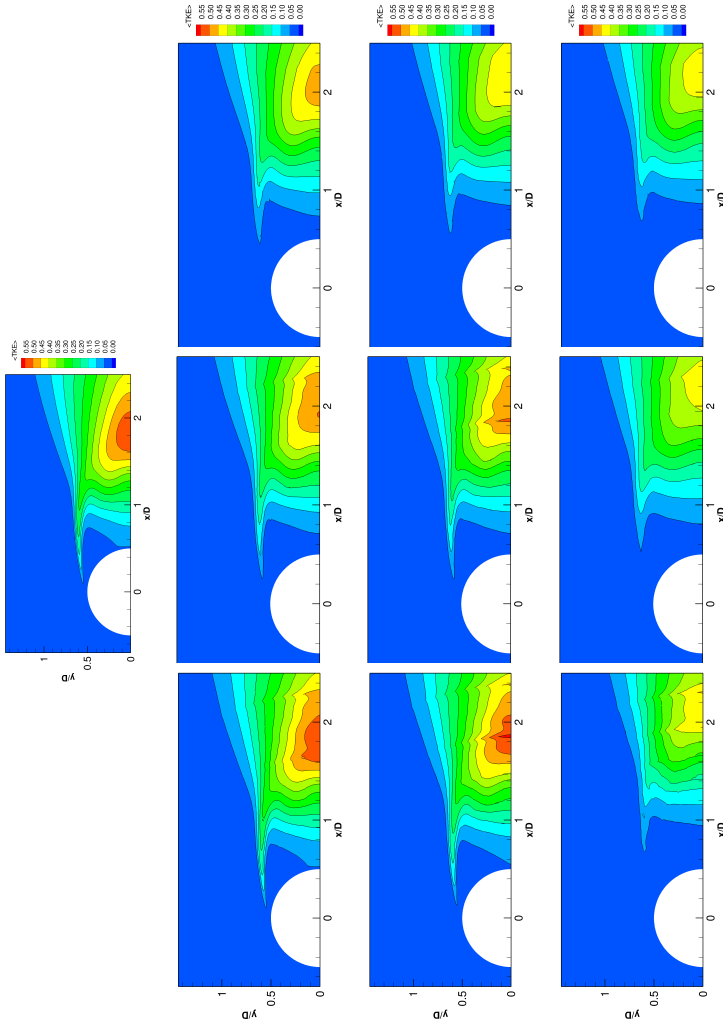


Figure B.5: Time- and spanwise-averaged turbulent kinetic energy in the wake region, normalized by free-stream kinetic energy. First row: DNS reference results, first column: PDG results, second column: PDG with Smagorinsky model, last column: DGSEM with Smagorinsky model; Second row: N7-1, N7-2, N7-A, third row: N5-1, N5-2, N5-B, fourth row: N3-1, N3-4, N3-D.

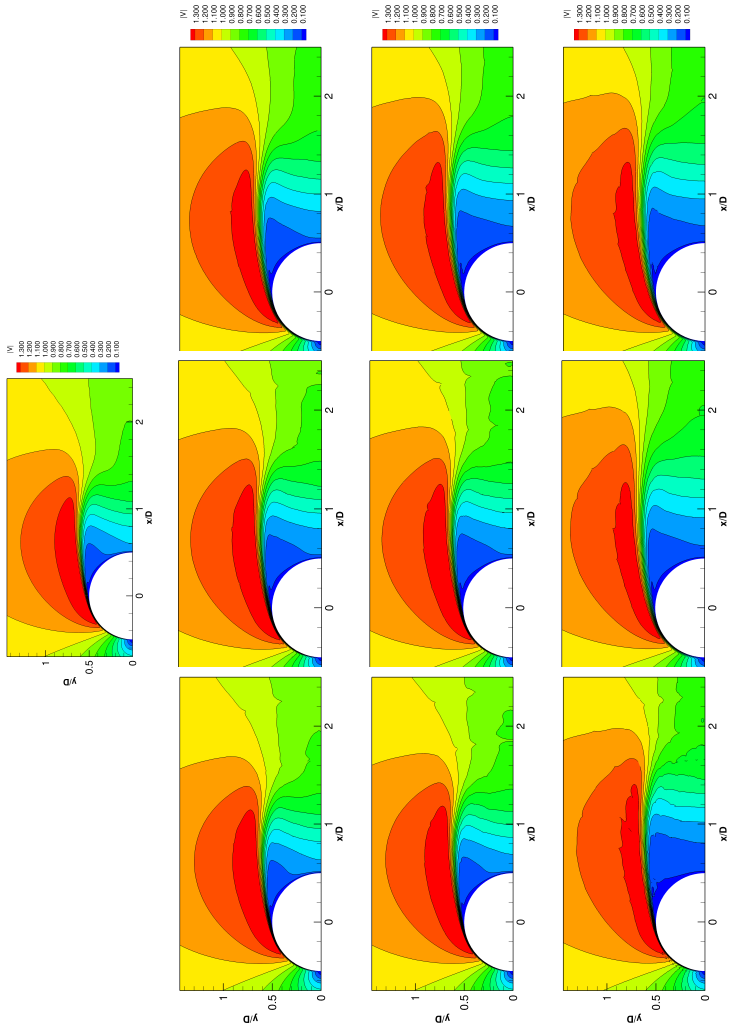
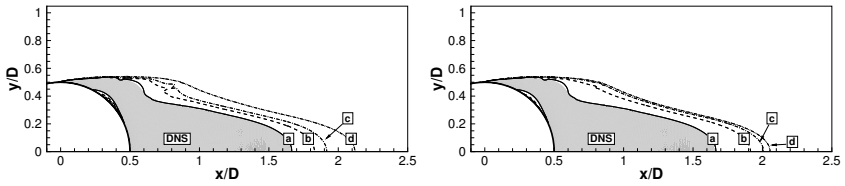


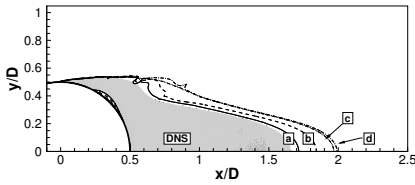
Figure B.6: Time- and spanwise-averaged velocity magnitude in the wake region, normalized by free-stream kinetic energy. First row: DNS reference results, first column: PDG results, second column: PDG with Smagorinsky model, last column: DGSEM with Smagorinsky model; Second row: N7-1, N7-2, N7-A, third row: N5-1, N5-2, N5-B, fourth row: N3-1, N3-4, N3-D.

B. Flow over a Cylinder at $Re_D = 3900$ - Extended Results

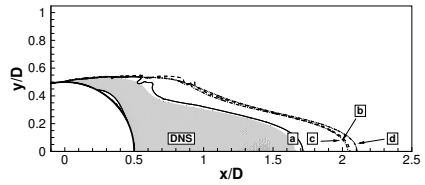


(a) PDG: a) N7-1, b) N7-2, c) N7-3, d) N7-4

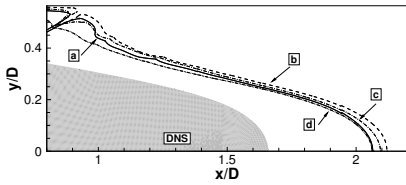
(b) DGSEM: a) N7-1, b) N7-A, c) N7-B, d) N7-C



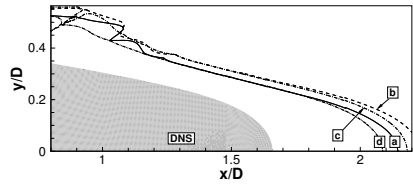
(c) PDG: a) N5-1, b) N5-2, c) N5-3, d) N5-4



(d) DGSEM: a) N5-1, b) N5-A, c) N5-B, d) N5-C



(e) PDG: a) N3-1, b) N3-2, c) N3-3, d) N3-4



(f) DGSEM: a) N3-A, b) N3-B, c) N3-C, d) N3-D

Figure B.7.: Isocontours of time- and spanwise-averaged streamwise velocity: $u = 0$. Shaded area denotes the DNS reference solution.

C. Taylor-Green Vortex - Extended Results

In this appendix, we provide the companion results for filter-stabilized DGSEM and PDG of $\mathcal{O}(8)$, i.e. $N = 7$ to the discussion in Section 4.3.1. All computations were again performed with 64^3 , i.e. on a grid with 8^3 elements. The findings discussed before also hold for the $N = 7$ computations, although the superiority of PDG over filter-stabilized DGSEM is less pronounced, due to the increased n_{PPW} requirement of a $N = 7$ discretization.

C.1. Taylor-Green Vortex at $Re=800$, $N=7$

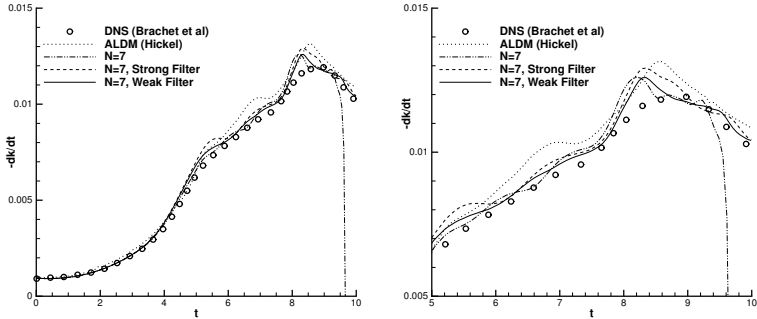


Figure C.1.: Taylor-Green Vortex at $Re = 800$. Kinetic energy dissipation rate $-\frac{dk}{dt}$ for filter-stabilized $N = 7$ (8^3 grid cells) computation. The right plot is zoomed in on the time range of maximum enstrophy production.

C. Taylor-Green Vortex - Extended Results

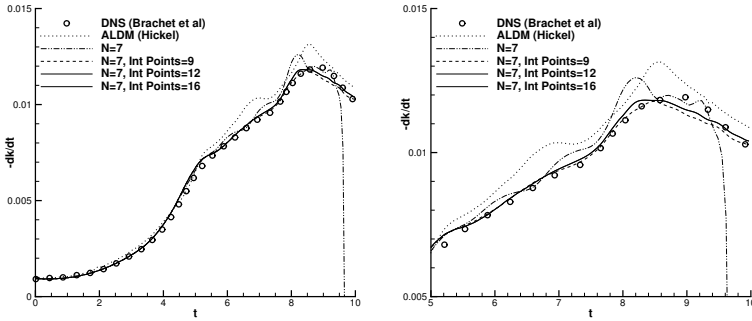


Figure C.2.: Taylor-Green Vortex at $Re = 800$. Kinetic energy dissipation rate $-\frac{dk}{dt}$ for PDG $N = 7$ (8^3 grid cells) computation. The right plot is zoomed in on the time range of maximum enstrophy production.

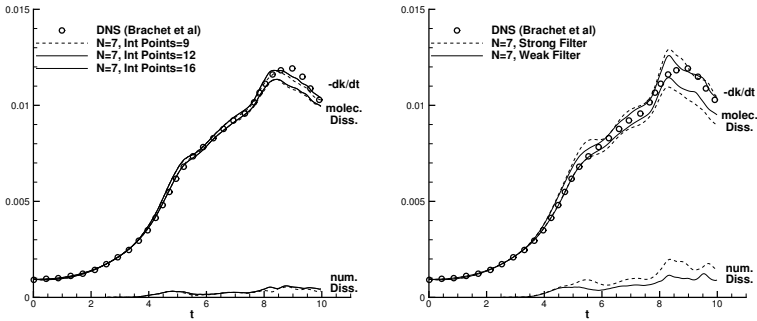


Figure C.3.: Taylor-Green Vortex at $Re = 800$. Kinetic energy dissipation rate, resolved dissipation rate and numerical dissipation rate for PDG $N = 7$ (left) and filter-stabilized DGSEM $N = 7$ computation (right).

C.2. Taylor-Green Vortex at $Re=1600$, $N=7$

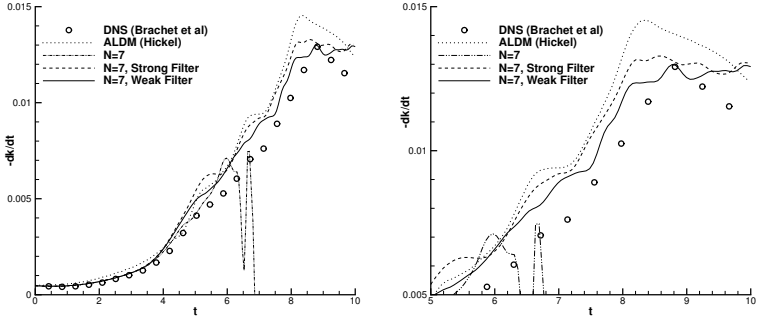


Figure C.4: Taylor-Green Vortex at $Re = 1600$. Kinetic energy dissipation rate $-\frac{dk}{dt}$ for filter-stabilized $N = 7$ (8^3 grid cells) computation. The right plot is zoomed in on the time range of maximum enstrophy production.

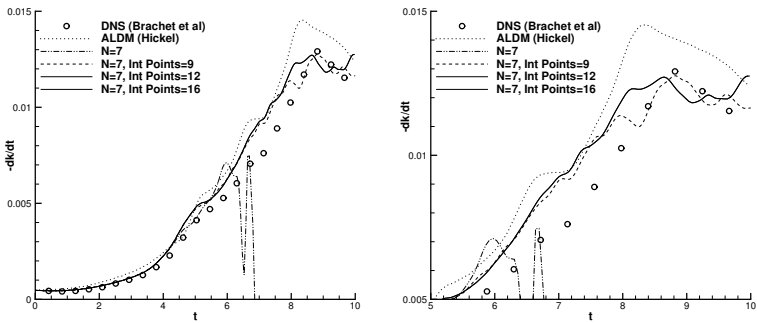


Figure C.5: Taylor-Green Vortex at $Re = 1600$. Kinetic energy dissipation rate $-\frac{dk}{dt}$ for PDG $N = 7$ (8^3 grid cells) computation. The right plot is zoomed in on the time range of maximum enstrophy production.

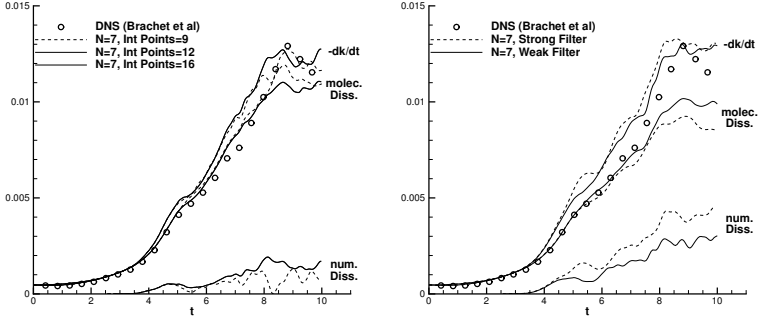


Figure C.6.: Taylor-Green Vortex at $Re = 1600$. Kinetic energy dissipation rate, resolved dissipation rate and numerical dissipation rate for PDG $N = 7$ (left) and filter-stabilized DGSEM $N = 7$ computation (right).

C.3. Results of the 1st International Workshop on High Order Methods

In the following, we provide additional results from the “1st International Workshop on High Order Methods” discussed in Section 3.4.3 and published in [200]. Comparison plots are reproduced with friendly permission of Dr. Koen Hillewaert, Cenaero. For the compressible formulation of the TGV, the total dissipation rate of kinetic energy is given by

$$\epsilon = -\frac{dE}{dt} = 2 \underbrace{\frac{\mu}{\rho} \int_{\Omega} \underline{\underline{S}}^d : \underline{\underline{S}}^d d\Omega}_{\epsilon_1 = 2\nu\mathcal{E}} + \underbrace{\frac{\mu_v}{\rho} \int_{\Omega} (\nabla \cdot \vec{v})^2 d\Omega}_{\epsilon_2 \approx 0} - \underbrace{\frac{1}{\rho} \int_{\Omega} p \nabla \cdot \vec{v} d\Omega}_{\epsilon_3 \approx 0}, \quad (\text{C.1})$$

where $\underline{\underline{S}}^d$ denotes the deviatoric part of the stress tensor and μ_v the bulk viscosity, which is assumed to be zero in this case. The results were compared by computing the follow-

ing metrics with respect to a reference solution, denoted by $(\)^{ref}$

$$\begin{aligned}\Delta\epsilon_1 &= \left\| \frac{dE}{dt} - \frac{dE^{ref}}{dt} \right\|_t, \\ \Delta\epsilon_2 &= \left\| 2\nu\mathcal{E} - 2\nu\mathcal{E}^{ref} \right\|_t, \\ \Delta\epsilon_3 &= \left\| \frac{dE}{dt} + 2\nu\mathcal{E} \right\|_t.\end{aligned}\tag{C.2}$$

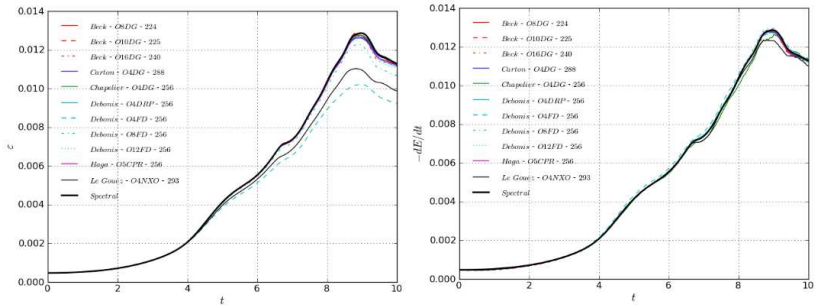


Figure C.7.: Taylor-Green Vortex at $Re = 1600$: Comparison of the resolved (*left*) and total dissipation rate (*right*) for the contributions to the high order workshop with highest order per participant. Refer to Table 3.3 for the legend.

C. Taylor-Green Vortex - Extended Results

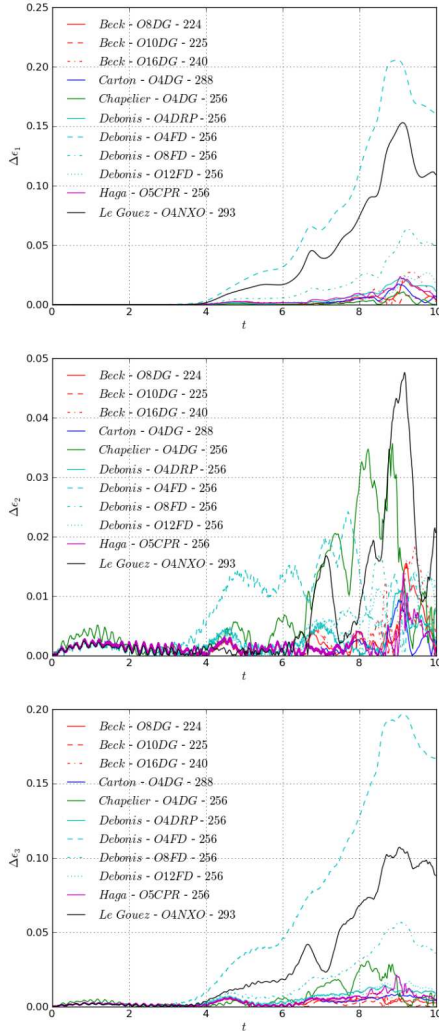


Figure C.8.: Taylor-Green Vortex at $Re = 1600$: Comparison of error measures according to Equation C.2 for the contributions to the high order workshop. For a legend refer to Table 3.3.

Figure C.9 shows the vortical structures for DGSEM with 256^3 DOF.

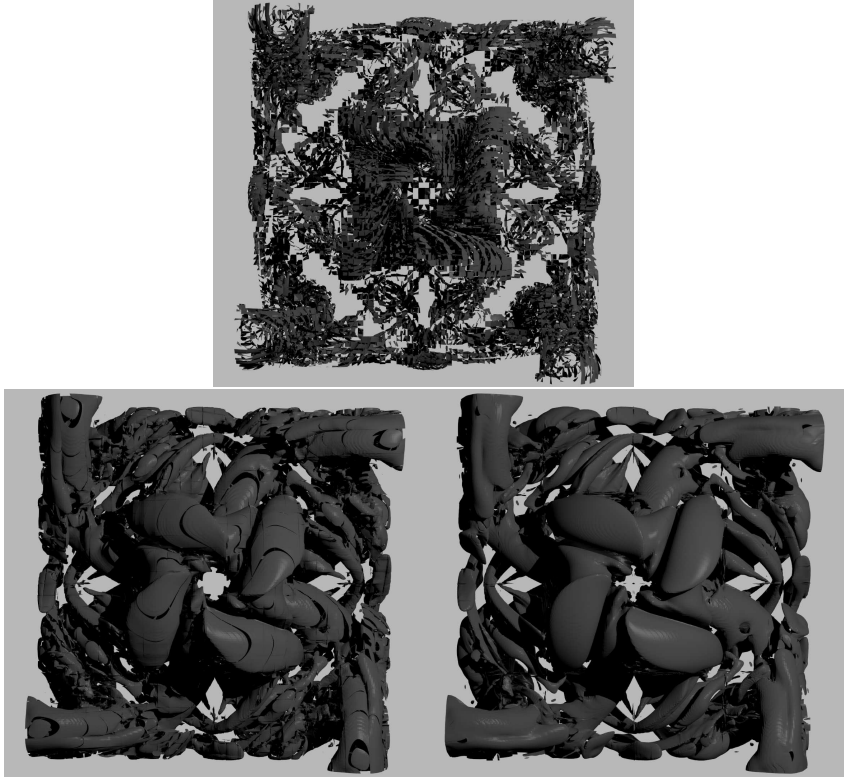


Figure C.9.: Taylor-Green Vortex at $Re = 1600$: Visualization of vortex detection criterion $\lambda_2 = -1.5$ for $N = 1$ (top), $N = 3$ (bottom left) and $N = 15$ (bottom right) computation (256^3 DOF in each case).

D. Central Finite Differences of Arbitrary Order

In [76], Fornberg introduces a shorthand notation for standard FD approximations of a function $u(x)$:

$$\begin{aligned}
 \text{D (True derivative): } & D u(x) = \frac{du(x)}{dx} \\
 \text{I (Identity operator): } & I u(x) = u(x) \\
 \text{E (Translation operator): } & E u(x) = u(x + h) \\
 \text{D}_+ \text{ (Forward difference): } & D_+ u(x) = (E - I)/h u(x) \\
 \text{D}_- \text{ (Backward difference): } & D_- u(x) = (I - E^{-1})/h u(x) \\
 \text{D}_0 \text{ (Central difference): } & D_0 u(x) = (E - E^{-1})/2h u(x)
 \end{aligned} \tag{D.1}$$

With this notation, a second order central approximation becomes

$$\begin{aligned}
 \frac{du(x)}{dx} & \approx \left(\frac{u(x+h) - u(x-h)}{2h} \right) \\
 D & \approx \frac{1}{2h} \sum_{i=-1}^1 \beta_{1,i} E^i, \quad \text{with } \beta_{1,-1} = -1, \quad \beta_{1,0} = 0, \quad \beta_{1,1} = 1, \tag{D.2} \\
 & \text{or} \\
 D & \approx \alpha_0 D_0 \quad \text{with } \alpha_0 = 1.
 \end{aligned}$$

Similarly, a fourth order approximation can be written as

$$\begin{aligned}
 D & \approx \frac{1}{2h} \sum_{i=-2}^2 \beta_{2,i} E^i, \\
 & \text{with } \beta_{2,-2} = -\beta_{2,2} = \frac{1}{6}, \quad \beta_{2,-1} = -\beta_{2,1} = -\frac{4}{3}, \quad \beta_{2,0} = 0, \quad \text{or} \tag{D.3} \\
 D & \approx D_0(\alpha_0 I - \alpha_1 h^2 D_+ D_-) \quad \text{with } \alpha_0 = 1, \quad \alpha_1 = \frac{1}{6}.
 \end{aligned}$$

D. Central Finite Differences of Arbitrary Order

For an arbitrary order of accuracy $2p$, this extends to

$$D \approx \frac{1}{2h} \sum_{i=-p}^p \beta_{p,i} E^i, \quad \text{with } \beta_{0,p} = 0, \quad \beta_{p,i \neq 0} = \frac{2(p!)^2 (-1)^{i+1}}{i(p+i)!(p-i)!}$$

or

(D.4)

$$D \approx D_0 \sum_{i=0}^{p-1} (-1)^i \alpha_i (h^2 D_+ D_-)^i \quad \text{with } \alpha_i = \frac{(i!)^2}{(2i+1)!}.$$

With relationship (D.4), an analytical derivation of the dispersion error of central FD discretizations is possible: Considering a linear transport equation for u and an initial solution of the form $u(x, t_0) = e^{I\omega x}$ with wave mode ω on a regular grid with periodic boundary conditions, the true derivative is given by

$$D u(x, t_0) = D e^{I\omega x} = I\omega e^{I\omega x}. \quad (D.5)$$

Its numerical approximation can be computed from (D.4), for example, a second order central approximation gives:

$$D_0 u(x, t_0) = \frac{e^{I\omega(x+h)} - e^{I\omega(x-h)}}{2h} = I \frac{\sin h\omega}{h} e^{I\omega x}. \quad (D.6)$$

Thus, the phase error between the true derivative and its approximation becomes

$$\frac{(D - D_0)e^{I\omega x}}{Ie^{I\omega x}} = \omega - \frac{\sin h\omega}{h} e^{I\omega x}. \quad (D.7)$$

From Equation (D.4), Fornberg showed that for a general approximation of order $2p$, this dispersion error becomes

$$\omega - \frac{\sin \omega h}{h} \sum_{i=0}^{p-1} \alpha_i 2^{2i} \left(\sin \frac{\omega h}{2} \right)^{2i}. \quad (D.8)$$

E. Derivation of the Vorticity Equation

Incompressible Navier Stokes equations in Vectorial Form:

$$\nabla \cdot \mathbf{u} = 0, \quad \text{divergence-free condition on the velocity field} \quad (\text{E.1})$$

$$\frac{\partial \mathbf{u}}{\partial t} + (\mathbf{u} \cdot \nabla) \mathbf{u} = -\frac{\nabla p}{\rho} + \nu \nabla^2 \mathbf{u} \quad \text{vectorial momentum equation.} \quad (\text{E.2})$$

Vorticity is defined as the vector aligned with the local axis of fluid rotation, with the sign determined by the local right hand system. The length of the vector corresponds to the strength of the vortex, i.e. directly to the radial velocity gradient.

$$\boldsymbol{\omega} \equiv \nabla \times \mathbf{u} \quad (\text{E.3})$$

Taking the curl of Equation (E.2) term-by-term yields:

- First term LHS:

$$\nabla \times \frac{\partial \mathbf{u}}{\partial t} = \frac{\partial (\nabla \times \mathbf{u})}{\partial t} = \frac{\partial \boldsymbol{\omega}}{\partial t}$$

- Second term RHS:

$$\nabla \times \nu \nabla^2 \mathbf{u} = \nu \nabla^2 \boldsymbol{\omega}$$

- First term RHS:

$$\nabla \times \frac{\nabla p}{\rho} = 0,$$

since the gradient of a scalar is curl-free.

- Non-linear term LHS:

$$\nabla \times (\mathbf{u} \cdot \nabla) \mathbf{u},$$

with vector relation

$$\begin{aligned} \nabla(\mathbf{u} \cdot \mathbf{u}) &= (\mathbf{u} \cdot \nabla) \mathbf{u} + (\mathbf{u} \cdot \nabla) \mathbf{u} + \mathbf{u} \times (\nabla \times \mathbf{u}) + \mathbf{u} \times (\nabla \times \mathbf{u}) \\ &= 2(\mathbf{u} \cdot \nabla) \mathbf{u} + 2\mathbf{u} \times (\nabla \times \mathbf{u}), \end{aligned} \quad (\text{E.4})$$

E. Derivation of the Vorticity Equation

and $\omega \equiv \nabla \times \mathbf{u}$ becomes

$$\nabla \times (\mathbf{u} \cdot \nabla) \mathbf{u} = \nabla \times \nabla \left(\frac{1}{2} u^2 \right) - \nabla \times (\mathbf{u} \times \omega). \quad (\text{E.5})$$

Again, the curl of the gradient of scalar field is zero, so the first term on the RHS vanishes. Expanding Equation (E.5) yields

$$\nabla \times (\mathbf{u} \cdot \nabla) \mathbf{u} = (\mathbf{u} \cdot \nabla) \omega + (\nabla \cdot \mathbf{u}) \omega - (\nabla \cdot \omega) \mathbf{u} - (\omega \cdot \nabla) \mathbf{u}. \quad (\text{E.6})$$

Applying the incompressibility condition and noting that the divergence of the curl is zero leaves

$$\nabla \times (\mathbf{u} \cdot \nabla) \mathbf{u} = (\mathbf{u} \cdot \nabla) \omega - (\omega \cdot \nabla) \mathbf{u}. \quad (\text{E.7})$$

The Vorticity Equation

Collecting the terms derived above yields the evolution equation for vorticity

$$\frac{D\omega}{Dt} = \frac{\partial \omega}{\partial t} + (\mathbf{u} \cdot \nabla) \omega = (\omega \cdot \nabla) \mathbf{u} + \nu \nabla^2 \omega \quad (\text{E.8})$$

Remarks

- Equation (E.8) supports Kelvin's theorem: In the absence of viscosity ($\nu = 0$) then if no vorticity exists in the flow field initially ($\omega_{t=0} = 0$), none will be created.
- The first term on RHS is a source for the vorticity and a mechanism of increasing the vorticity if shear exists in the mean flow. It is commonly called the *vortex-stretching* term.
- The first term on the RHS vanishes in 2D, so no production mechanism for vorticity exists.

Bibliography

- [1] *Large Eddy Simulation and Related Techniques, Theory and Application*. VKI Lecture Series. Von Karman Institute for Fluid Dynamics, 2010.
- [2] V. I. Abramenko. Fractal multi-scale nature of solar/stellar magnetic fields. In Kosovichev A. G., de Gouveia Dal Pino E., and Yan Y., editors, *IAU Symposium*, volume 294 of *IAU Symposium*, pages 289–300, July 2013.
- [3] P. Abry, R. Baraniuk, P. Flandrin, R. Riedi, and D. Veitch. Multiscale nature of network traffic. *Signal Processing Magazine, IEEE*, 19(3):28–46, May 2002.
- [4] Ch. Altmann, A. Beck, F. Hindenlang, M. Staudenmaier, G. Gassner, and C.-D. Munz. An efficient high performance parallelization of a discontinuous galerkin spectral element method. In Rainer Keller, David Kramer, and Jan-Philipp Weiss, editors, *Facing the Multicore-Challenge III*, volume 7686 of *Lecture Notes in Computer Science*, pages 37–47. Springer Berlin Heidelberg, 2013.
- [5] B. W. Anderson and J. A. Domaradzki. A subgrid-scale model for large-eddy simulation based on the physics of interscale energy transfer in turbulence. *Physics of Fluids (1994-present)*, 24(6), 2012.
- [6] A. Aprovitola and F. M. Denaro. On the application of congruent upwind discretizations for large eddy simulations. *Journal of Computational Physics*, 194(1):329 – 343, 2004.
- [7] D. Arnold. *An Interior Penalty Finite Element Method with Discontinuous Elements*. PhD thesis, The University of Chicago, 1979.
- [8] D. N. Arnold, F. Brezzi, B. Cockburn, and L. D. Marini. Discontinuous Galerkin methods for elliptic problems. In B. Cockburn, G. Karniadakis, and C. W. Shu, editors, *Discontinuous Galerkin Methods. Lecture Notes in Computational Science and Engineering*, pages 89–101. Springer, 2000.
- [9] D. N. Arnold, F. Brezzi, B. Cockburn, and L. D. Marini. Unified analysis of discontinuous Galerkin methods for elliptic problems. *SIAM J. Numer. Anal.*, 39(5):1749–1779, 2002.

- [10] J. Bardina, J. Ferziger, and W. Reynolds. Improved subgrid-scale models for large-eddy simulation. In *Fluid Dynamics and Co-located Conferences*. American Institute of Aeronautics and Astronautics, 1980.
- [11] G. E. Barter and D. L. Darmofal. Shock capturing with PDE-based artificial viscosity for DGFEM: Part 1. Formulation. *Journal of Computational Physics*, 229(5):1810 – 1827, 2010.
- [12] F. Bassi and S. Rebay. A high order accurate discontinuous finite element method for the numerical solution of the compressible Navier–Stokes equations. *Journal of Computational Physics*, 131:267–279, 1997.
- [13] F. Bassi and S. Rebay. A high-order discontinuous Galerkin finite element method solution of the 2D Euler equations. *Journal of Computational Physics*, 138:251–285, 1997.
- [14] F. Bassi and S. Rebay. Numerical evaluation of two discontinuous Galerkin methods for the compressible Navier–Stokes equations. *International Journal for Numerical Methods in Fluids*, 40:197–207, 2002.
- [15] F. Bassi, S. Rebay, G. Mariotti, S. Pedinotti, and M. Savini. A high-order accurate discontinuous finite element method for inviscid and viscous turbomachinery flows. In R. Decuyper and G. Dibelius, editors, *Proceedings of 2nd European Conference on Turbomachinery, Fluid and Thermodynamics*, pages 99–108, Technologisch Instituut, Antwerpen, Belgium, 1997.
- [16] G. K. Batchelor. *The Theory of Homogeneous Turbulence*. Cambridge University Press, United Kingdom, 1959.
- [17] Y. Bazilevs and T. J. R. Hughes. Weak imposition of Dirichlet boundary conditions in fluid mechanics. *Computers & Fluids*, 36(1):12 – 26, 2007.
- [18] A. Beck, Th. Bolemann, D. Flad, H. Frank, G. Gassner, F. Hindenlang, and C.-D. Munz. High-order discontinuous galerkin spectral element methods for transitional and turbulent flow simulations. *International Journal for Numerical Methods in Fluids*, 76(8):522–548, 2014.
- [19] A. Beck, G. Gassner, and C.-D. Munz. High order and underresolution. In R. Ansonge, H. Bijl, A. Meister, and Th. Sonar, editors, *Recent Developments in the Numerics of Nonlinear Hyperbolic Conservation*. Springer, 2013.

-
- [20] A. Beck, G. Gassner, and C.-D. Munz. On the effect of flux functions in discontinuous Galerkin simulations of underresolved turbulence. In Mejdı Azaiez, Henda El Fekih, and Jan S. Hesthaven, editors, *Spectral and High Order Methods for Partial Differential Equations - ICOSAHOM 2012*, volume 95 of *Lecture Notes in Computational Science and Engineering*, pages 145–155. Springer International Publishing, 2014.
- [21] A. Beck, G. Gassner, C. Tonhäuser, and C.-D. Munz. The influence of polynomial de-aliasing on subgrid scalemodels. *submitted to Flow, Turbulence and Combustion*, 2014.
- [22] L. C. Berselli and T. Iliescu. A higher-order subfilter-scale model for large eddy simulation. *Journal of Computational and Applied Mathematics*, 159(2):411 – 430, 2003.
- [23] H. M. Blackburn and S. Schmidt. Large eddy simulation of flow past a circular cylinder. In *Proceedings of 14th Australasian Fluid Mechanics Conference*, 2001.
- [24] H. M. Blackburn and S. Schmidt. Spectral element filtering techniques for large eddy simulation with dynamic estimation. *Journal of Computational Physics*, 186(2):610–629, 2003.
- [25] J. P. Boris, F. F. Grinstein, E. S. Oran, and R. L. Kolbe. New insights into large eddy simulation. *Fluid Dynamics Research*, 10(4–6):199 – 228, 1992.
- [26] S. T. Bose, P. Moin, and D. You. Grid-independent large-eddy simulation using explicit filtering. In *Proceedings of the 2008 Center for Turbulence Research Summer Program*, 2008.
- [27] J. P. Boyd. *Chebyshev and Fourier Spectral Methods*. Dover Publications, USA, 2001.
- [28] M. E. Brachet. Direct simulation of three-dimensional turbulence in the Taylor–Green vortex. *Fluid Dynamics Research*, 8(1-4):1 – 8, 1991.
- [29] M. E. Brachet, D. I. Meiron, S. A. Orszag, B. G. Nickel, R. H. Morf, and U. Frisch. Small-scale structure of the Taylor–Green vortex. *Journal of Fluid Mechanics*, 130:411–452, 4 1983.
- [30] J. G. Brasseur and Ch. H. Wei. Interscale dynamics and local isotropy in high Reynolds number turbulence within triadic interactions. *Physics of Fluids*, 6(2), 1994.

- [31] M. Breuer. Large eddy simulation of the subcritical flow past a circular cylinder: numerical and modeling aspects. *International Journal for Numerical Methods in Fluids*, 28(9):1281–1302, 1998.
- [32] A. N. Brooks and T. J. R. Hughes. Streamline Upwind/Petrov-Galerkin formulations for convection dominated flows with particular emphasis on the incompressible Navier-Stokes equations. *Comput. Methods Appl. Mech. Eng.*, pages 199–259, September 1990.
- [33] J. R. Bull and A. Jameson. Simulation of the compressible Taylor Green vortex using high-order flux reconstruction schemes. In *AIAA Aviation*. American Institute of Aeronautics and Astronautics, 2014.
- [34] M. Carpenter and C. Kennedy. Fourth-order 2N-storage Runge-Kutta schemes. Technical Report NASA TM 109111, 1994.
- [35] C. Carton de Wiart and K. Hillewaert. DNS and ILES of transitional flows around a SD7003 using a high order discontinuous Galerkin method. In *Seventh International Conference on Computational Fluid Dynamics (ICCFD7)*, 2012.
- [36] C. Carton de Wiart, K. Hillewaert, M. Duponcheel, and G. Winckelmans. Assessment of a discontinuous Galerkin method for the simulation of vortical flows at high Reynolds number. *International Journal for Numerical Methods in Fluids*, 2013.
- [37] C. Carton de Wiart, K. Hillewaert, M. Duponcheel, and G. Winckelmans. Assessment of a discontinuous galerkin method for the simulation of vortical flows at high reynolds number. *International Journal for Numerical Methods in Fluids*, 74(7):469–493, 2014.
- [38] E. Casoni, J. Peraire, and A. Huerta. One-dimensional shock-capturing for high-order discontinuous Galerkin methods. *International Journal for Numerical Methods in Fluids*, 71(6):737–755, 2013.
- [39] L. Catabriga, A. L. G. A. Coutinho, and T. E. Tezduyar. Compressible flow SUPG parameters computed from element matrices. *Communications in Numerical Methods in Engineering*, 21(9):465–476, 2005.
- [40] N. Chalmers, L. Krivodonova, and R. Qin. Relaxing the CFL number of the discontinuous Galerkin method. *submitted to SIAM JSC*.

-
- [41] J.-B. Chapelier, M. de la Llave Plata, F. Renac, and E. Lamballais. Evaluation of a high-order discontinuous Galerkin method for the DNS of turbulent flows. *Computers & Fluids*, 95(0):210 – 226, 2014.
- [42] D. K. Chapman. Computational aerodynamics development and outlook. *AIAA Journal*, 17(12):1293–1313, Dec 1979.
- [43] A. Chatterjee and R. S. Myong. Efficient implementation of higher-order finite volume time-domain method for electrically large scatterers. *Progress In Electromagnetics Research B*, 2009.
- [44] H. Choi and P. Moin. Grid-point requirements for large eddy simulation: Chapman’s estimates revisited. *Physics of Fluids (1994-present)*, 24(1):–, 2012.
- [45] B. Cockburn, S. Hou, and C.-W. Shu. The Runge-Kutta local projection discontinuous Galerkin finite element method for conservation laws IV: The multidimensional case. *Math. Comput.*, 54:545–581, 1990.
- [46] B. Cockburn, S. Y. Lin, and C.-W. Shu. TVB Runge-Kutta local projection discontinuous Galerkin finite element method for conservation laws III: One dimensional systems. *Journal of Computational Physics*, 84:90–113, 1989.
- [47] B. Cockburn and C.-W. Shu. TVB Runge-Kutta local projection discontinuous Galerkin finite element method for conservation laws II: General framework. *Math. Comput.*, 52:411–435, 1989.
- [48] B. Cockburn and C.-W. Shu. The Runge-Kutta local projection p^1 -discontinuous Galerkin method for scalar conservation laws. *M²AN*, 25:337–361, 1991.
- [49] B. Cockburn and C.-W. Shu. The local discontinuous Galerkin method for time-dependent convection diffusion systems. *SIAM Journal on Numerical Analysis*, 35:2440–2463, 1998.
- [50] B. Cockburn and C.-W. Shu. Runge–Kutta discontinuous galerkin methods for convection-dominated problems. *Journal of Scientific Computing*, 16(3):173–261, 2001.
- [51] S. S. Collis. Discontinuous Galerkin methods for turbulence simulation. In *Proceedings of the 2002 Center for Turbulence Research Summer Program*, pages 155–167, 2002.

- [52] S. S. Collis. The DG/VMS method for unified turbulence simulation. In *32nd AIAA Fluid Dynamics Conference and Exhibit*, 2002.
- [53] G. Comte-Bellot and S. Corrsin. The use of a contraction to improve the isotropy of grid-generated turbulence. *Journal of Fluid Mechanics*, 25:657–682, 8 1966.
- [54] J. W. Cooley and J. W. Tukey. An algorithm for the machine calculation of complex Fourier series. *Mathematicas of Computation*, 19:297–301, 1965.
- [55] G.-H. Cottet and O. V. Vasilyev. Comparison of dynamic Smagorinsky and anisotropic subgrid-scale models. In *Proceedings of the 1998 Center for Turbulence Research Summer Program*, 1998.
- [56] R. B. Dahlburg and J. M. Picone. Pseudospectral simulation of compressible magnetohydrodynamic turbulence. *Computer Methods in Applied Mechanics and Engineering*, 80(1–3):409 – 416, 1990.
- [57] P. A. Davidson. *Turbulence*. Oxford University Press, United Kingdom, 2004.
- [58] G. De Stefano and O. V. Vasilyev. “Perfect” modeling framework for dynamic SGS model testing in large eddy simulation. *Theoretical and Computational Fluid Dynamics*, 18(1):27–41, 2004.
- [59] J. W. Deardorff. A numerical study of three-dimensional turbulent channel flow at large Reynolds numbers. *Journal of Fluid Mechanics*, 1970.
- [60] J. DeBonis. Solutions of the Taylor-Green vortex problem using high-resolution explicit finite difference methods. In *Aerospace Sciences Meetings*. American Institute of Aeronautics and Astronautics, 2013.
- [61] T. S. Deisboeck, Z. Wang, P. Macklin, and V. Cristini. Multiscale cancer modeling. *Annu Rev Biomed Eng*, 13:127–155, Aug 2011.
- [62] P. J. Diamessis, J. A. Domaradzki, and J. S. Hesthaven. A spectral multidomain penalty method model for the simulation of high Reynolds number localized incompressible stratified turbulence. *Journal of Computational Physics*, 202(1):298–322, 2005.
- [63] J. A. Domaradzki. Nonlocal triad interactions and the dissipation range of isotropic turbulence. *Physics of Fluids A: Fluid Dynamics (1989-1993)*, 4(9), 1992.

-
- [64] J. A. Domaradzki and E. M. Saiki. Backscatter models for large-eddy simulations. *Theoretical and Computational Fluid Dynamics*, 9(2):75–83, 1997.
- [65] S. Dong, G. E. Karniadakis, A. Ekmekci, and D. Rockwell. A combined direct numerical simulation–particle image velocimetry study of the turbulent near wake. *Journal of Fluid Mechanics*, 569:185–207, 2006.
- [66] D. A. Donzis, J. D. Gibbon, A. Gupta, R. M. Kerr, R. Pandit, and D. Vincenzi. Vorticity moments in four numerical simulations of the 3D Navier-Stokes equations. *Journal of Fluid Mechanics*, Volume 732:316–331, October 2013.
- [67] P. G. Drazin and W. H. Reid. *Hydrodynamic Stability*. Cambridge University Press, United Kingdom, 2004.
- [68] E. R. Van Driest. On turbulent flow near a wall. *Journal of Aeronautical Sciences*, 1956.
- [69] D. Drikakis, C. Fureby, F. F. Grinstein, and D. Youngs. Simulation of transition and turbulence decay in the Taylor–Green vortex. *Journal of Turbulence*, 2007.
- [70] M. Dröge. *Cartesian Grid Methods for Turbulent Flow Simulation in Complex Geometries*. Dissertation, University of Groningen, Netherlands, 2007.
- [71] M. Drosson and K. Hillewaert. On the stability of the symmetric interior penalty method for the Spalart-Allmaras turbulence model. *J. Comput. Appl. Math.*, 246:122–135, 2013.
- [72] H. Faisst and B. Eckhardt. Sensitive dependence on initial conditions in transition to turbulence in pipe flow. *Journal of Fluid Mechanics*, 504:343–352, 4 2004.
- [73] D. Fauconnier. *Development of a Dynamic Finite Difference Method for Large-Eddy Simulation*. PhD thesis, University of Ghent, Belgium, 2008.
- [74] D. Flad, A. Beck, G. Gassner, and C.-D. Munz. Locally filtered Large Eddy Simulation. *in preparation*.
- [75] D. Flad, A. Beck, G. Gassner, and C.-D. Munz. A discontinuous Galerkin spectral element method for the direct numerical simulation of aeroacoustics. In *AIAA Aviation*. American Institute of Aeronautics and Astronautics, 2014.
- [76] B. Fornberg. The pseudospectral method; comparisons with finite differences for the elastic wave equation. *Geophysics*, 52(4):483–501, 1987.

- [77] J. Franke and W. Frank. Large eddy simulation of the flow past a circular cylinder at $Re_D = 3900$. *Journal of Wind Engineering and Industrial Aerodynamics*, 90(10):1191 – 1206, 2002.
- [78] M. Frigo and S. G. Johnson. The design and implementation of FFTW3. *Proceedings of the IEEE*, 93(2):216–231, 2005. Special issue on “Program Generation, Optimization, and Platform Adaptation”.
- [79] U. Frisch and J. Bec. Burgulence. In M. Lesieur, A. Yaglom, and F. David, editors, *New trends in turbulence Turbulence: nouveaux aspects*, volume 74 of *Les Houches - Ecole d’Ete de Physique Theorique*, pages 341–383. Springer Berlin Heidelberg, 2001.
- [80] J. Fröhlich, W. Rodi, Ph. Kessler, S. Parpais, J.P. Bertoglio, and D. Laurence. Large eddy simulation of flow around circular cylinders on structured and unstructured grids. In Ernst Heinrich Hirschel, editor, *Numerical Flow Simulation I*, volume 66 of *Notes on Numerical Fluid Mechanics (NNFM)*, pages 319–338. Springer Berlin Heidelberg, 1998.
- [81] E. Garnier, N. Adams, and P. Sagaut. *Large Eddy Simulation for Compressible Flows*. Springer Heidelberg, Germany, 2009.
- [82] E. Garnier, M. Mossi, P. Sagaut, P. Comte, and M. Deville. On the use of shock-capturing schemes for large-eddy simulation. *Journal of Computational Physics*, 153(2):273 – 311, 1999.
- [83] G. Gassner. A kinetic energy preserving nodal discontinuous galerkin spectral element method. *International Journal for Numerical Methods in Fluids*, 2014.
- [84] G. Gassner and A. Beck. On the accuracy of high-order discretizations for under-resolved turbulence simulations. *Theoretical and Computational Fluid Dynamics*, 27(3-4):221–237, 2013.
- [85] G. Gassner and D. A. Kopriva. A comparison of the dispersion and dissipation errors of Gauss and Gauss-Lobatto discontinuous Galerkin spectral element methods. *SIAM Journal of Scientific Computing*, 33(5):2560–2579, October 2011.
- [86] G. Gassner, F. Lörcher, and C.-D. Munz. A contribution to the construction of diffusion fluxes for finite volume and discontinuous Galerkin schemes. *Journal of Computational Physics*, 224(2):1049–1063, 2007.

-
- [87] G. Gassner, F. Lörcher, and C.-D. Munz. A discontinuous Galerkin scheme based on a space-time expansion. II. Viscous flow equations in multi dimensions. *Journal of Scientific Computing*, 34(3):260–286, 2008.
- [88] G. Gassner, M. Torrilhon, A. Beck, S. Knechtel, and Th. Bolemann. Comparison of Navier-Stokes-Fourier equation and Grad’s moment equation solutions for turbulence. In *NIC Series Volume 47*. Forschungszentrum Jülich GmbH, 2014.
- [89] M. Germano, U. Piomelli, P. Moin, and W. H. Cabot. A dynamic subgrid-scale eddy viscosity model. *Physics of Fluids A: Fluid Dynamics*, 3(7):1760–1765, 1991.
- [90] B. J. Geurts. *Elements of Direct and Large Eddy Simulation*. R. T. Edwards Inc., USA, 2003.
- [91] S. Ghosal, T. S. Lund, P. Moin, and K. Akselvoll. A dynamic localization model for large-eddy simulation of turbulent flows. *Journal of Fluid Mechanics*, 286.
- [92] Ph. M. Gresho and R. L. Lee. Don’t suppress the wiggles—they’re telling you something! *Computers & Fluids*, 9(2):223 – 253, 1981.
- [93] F. F. Grinstein and C. Fureby. Recent progress on MILES for high Reynolds number flows. *J. Fluids Eng.*, 124:848–861, 2002.
- [94] F. F. Grinstein and C. Fureby. On monotonically integrated large eddy simulation of turbulent flows based on FCT algorithms. In Dmitri Kuzmin, Rainald Löhner, and Stefan Turek, editors, *Flux-Corrected Transport*, Scientific Computation, pages 79–104. Springer Berlin Heidelberg, 2005.
- [95] R. Hartmann and P. Houston. Symmetric interior penalty DG methods for the compressible Navier–Stokes equations I: Method formulation. *Int. J. Num. Anal. Model.*, 3(1):1–20, 2006.
- [96] J. S. Hesthaven and T. Warburton. *Nodal Discontinuous Galerkin Methods: Algorithms, Analysis, and Applications*. Springer Verlag, New York, 2008.
- [97] S. Hickel. *Implicit Turbulence Modeling for Large-Eddy Simulation*. Dissertation, Technische Universität München, Munich, Germany, 2008.
- [98] S. Hickel and J. Larsson. An adaptive local deconvolution model for compressible turbulence. In *Proceedings of the 2008 Center for Turbulence Research Summer Program*, 2008.

- [99] F. Hindenlang. *Mesh Curving Techniques for High Order Parallel Simulations on Unstructured Meshes*. PhD thesis, University of Stuttgart, Germany, 2014.
- [100] F. Hindenlang, G. Gassner, Ch. Altmann, A. Beck, M. Staudenmaier, and C.-D. Munz. Explicit discontinuous Galerkin methods for unsteady problems. *Computers & Fluids*, 61(0):86 – 93, 2012.
- [101] F. Hindenlang, G. Gassner, T. Bolemann, and C.-D. Munz. Unstructured high order grids and their application in discontinuous Galerkin methods. In *Proceedings of ECCOMAS*, 2010.
- [102] M.-J. Huang and A. Leonard. Powerlaw decay of homogeneous turbulence at low Reynolds numbers. *Physics of Fluids (1994-present)*, 6(11), 1994.
- [103] T. J. R. Hughes, L. P. Franca, and G. M. Hulbert. A new finite element formulation for computational fluid dynamics: VIII. the Galerkin/least-squares method for advective-diffusive equations. *Computer Methods in Applied Mechanics and Engineering*, 73(2):173 – 189, 1989.
- [104] M. Y. Hussaini and T. A. Zang. Spectral methods in fluid-dynamics. *Annual Review of Fluid Mechanics*, 19:339–367, 1987.
- [105] A. G. Hutton. The emerging role of large eddy simulation in industrial practice: challenges and opportunities. *Philosophical Transactions of the Royal Society A: Mathematical, Physical and Engineering Sciences*, 367(1899):2819–2826, 2009.
- [106] T. Ishihara and Y. Kaneda. High resolution DNS of incompressible homogeneous forced turbulence - Time dependence of the statistics. In Yukio Kaneda and Toshiyuki Gotoh, editors, *Statistical Theories and Computational Approaches to Turbulence*, pages 177–188. Springer Japan, 2003.
- [107] Y. Kaneda and T. Ishihara. Small-scale statistics in high-resolution direct numerical simulation of turbulence. In Martin Oberlack, George Khujadze, Silke Günther, Tanja Weller, Michael Frewer, Joachim Peinke, and Stephan Barth, editors, *Progress in Turbulence II*, volume 109 of *Springer Proceedings in Physics*, pages 11–16. Springer Berlin Heidelberg, 2007.
- [108] Y. Kaneda, T. Ishihara, M. Yokokawa, K. Itakura, and A. Uno. Energy dissipation rate and energy spectrum in high resolution direct numerical simulations of turbulence in a periodic box. *Physics of Fluids (1994-present)*, 15(2), 2003.

-
- [109] G-S. Karamanos and G.E. Karniadakis. A spectral vanishing viscosity method for large-eddy simulations. *Journal of Computational Physics*, 163(1):22 – 50, 2000.
- [110] G. Kesserwani, R. Ghostine, J. Vazquez, A. Ghenaïm, and R. Mosé. Riemann solvers with Runge-Kutta discontinuous Galerkin schemes for the 1D shallow water equations. *Journal of Hydraulic Engineering*, 134(2):243–255, 2008.
- [111] R. M. Kirby and G. E. Karniadakis. De-aliasing on non-uniform grids: algorithms and applications. *Journal of Computational Physics*, 191:249–264, 2003.
- [112] R. M. Kirby and S. J. Sherwin. Stabilisation of spectral/hp element methods through spectral vanishing viscosity: Application to fluid mechanics modelling. *Computer Methods in Applied Mechanics and Engineering*, 195(23–24):3128 – 3144, 2006.
- [113] C.M. Klaij, J. J. W. van der Vegt, and H. van der Ven. Spacetime discontinuous Galerkin method for the compressible Navier-Stokes equations. *Journal of Computational Physics*, 217(2):589–611, 2006.
- [114] A. Klöckner, T. Warburton, and J. S. Hesthaven. Viscous shock capturing in a time-explicit discontinuous Galerkin method. *ArXiv e-prints*, February 2011.
- [115] K. Koal, J. Stiller, and H.M. Blackburn. Adapting the spectral vanishing viscosity method for large-eddy simulations in cylindrical configurations. *Journal of Computational Physics*, 231(8):3389 – 3405, 2012.
- [116] A. N. Kolmogorov. Dissipation of Energy in the Locally Isotropic Turbulence. *Royal Society of London Proceedings Series A*, 434:15–17, July 1991.
- [117] A. N. Kolmogorov. The local structure of turbulence in incompressible viscous fluid for very large Reynolds numbers. *Royal Society of London Proceedings Series A*, 434:9–13, July 1991.
- [118] D. Kopriva and G. Gassner. On the quadrature and weak form choices in collocation type discontinuous Galerkin spectral element methods. *Journal of Scientific Computing*, 44(2):136–155, 2010.
- [119] D. A. Kopriva. Metric identities and the discontinuous spectral element method on curvilinear meshes. *Journal of Scientific Computing*, 26(3):301–327, 2006.
- [120] David A. Kopriva. *Implementing Spectral Methods for Partial Differential Equations: Algorithms for Scientists and Engineers*. Springer Publishing Company Incorporated, 1st edition, 2009.

- [121] R. H. Kraichnan and D. Montgomery. Two-dimensional turbulence. *Reports on Progress in Physics*, 43(5):547, 1980.
- [122] A. G. Kravchenko and P. Moin. Numerical studies of flow over a circular cylinder at $Re_D=3900$. *Physics of Fluids*, 12:403–417, February 2000.
- [123] A. G. Lamorgese, D. A. Caughey, and S. B. Pope. Direct numerical simulation of homogeneous turbulence with hyperviscosity. *Physics of Fluids (1994-present)*, 17(1), 2005.
- [124] G. J. Le Beau and T. E. Tezduyar. Finite element computation of compressible flows with the SUPG formulation. In *Advances in a Finite Element Analysis in Fluid Dynamics*. American Society of Mechanical Engineering, 2001.
- [125] O. Lehmkuhl, I. Rodríguez, R. Borrell, and A. Oliva. Low-frequency unsteadiness in the vortex formation region of a circular cylinder. *Physics of Fluids (1994-present)*, 25(8), 2013.
- [126] P. Lesaint and P.-A. Raviart. On a finite element method for solving the neutron transport equation. In C.A. deBoor, editor, *Mathematical Aspects of Finite Elements in Partial Differential Equations.*, pages 89–145. Academic Press, New York, 1974.
- [127] M. Lesieur, O. Metais, and P. Comte. *Large Eddy Simulation of Turbulence*. Cambridge University Press, United Kingdom, 2005.
- [128] R. J. LeVeque. *Finite Volume Methods for Hyperbolic Problems*. Cambridge University Press, United Kingdom, 2002.
- [129] A. Lew, A. Ten Eyck, and R. Rangarajan. Some applications of discontinuous Galerkin methods in solid mechanics. In B. Daya Reddy, editor, *IUTAM Symposium on Theoretical, Computational and Modelling Aspects of Inelastic Media*, volume 11 of *IUTAM BookSeries*, pages 227–236. Springer Netherlands, 2008.
- [130] G. Lodato, P. Castonguay, and A. Jameson. Structural LES modeling with high-order spectral difference schemes. In *Proceedings of the 2011 Center for Turbulence Research Summer Program*, 2011.
- [131] F. Lörcher, G. Gassner, and C.-D. Munz. An explicit discontinuous Galerkin scheme with local time-stepping for general unsteady diffusion equations. *Journal of Computational Physics*, 227(11):5649–5670, 2008.

- [132] E. N. Lorenz. Deterministic nonperiodic flow. *Journal of the Atmospheric Sciences*, 20(2):130–141, Mar 1963.
- [133] T. S. Lund. The use of explicit filters in large eddy simulation. *Computers and Mathematics with Applications*, 46(4):603 – 616, 2003.
- [134] D. A. Lysenko, I. S. Ertesvåg, and K. E. Rian. Large-eddy simulation of the flow over a circular cylinder at Reynolds number 3900 using the openfoam toolbox. *Flow, Turbulence and Combustion*, 89(4):491–518, 2012.
- [135] X. Ma, G.-S. Karamanos, and G. E. Karniadakis. Dynamics and low-dimensionality of a turbulent near wake. *Journal of Fluid Mechanics*, 410:29–65, 5 2000.
- [136] J. Malm, Ph. Schlatter, P. F. Fischer, and D. S. Henningson. Stabilization of the spectral element method in convection dominated flows by recovery of skew-symmetry. *Journal of Scientific Computing*, 57(2):254–277, 2013.
- [137] L. Marstorp, G. Brethouwer, and A. V. Johansson. A stochastic subgrid model with application to turbulent flow and scalar mixing. *Physics of Fluids (1994-present)*, 19(3), 2007.
- [138] P. J. Mason and D. J. Thomson. Stochastic backscatter in large-eddy simulations of boundary layers. *Journal of Fluid Mechanics*, 242:51–78, September 1992.
- [139] J. McDonough and R. Bywater. Effects of local large-scale parameters on the small-scale chaotic solutions to Burgers’ equation. In *Fluid Dynamics and Collocated Conferences*. American Institute of Aeronautics and Astronautics, 1985.
- [140] S. Menon and S. Srinivasan. Challenges for multiscale large-eddy simulation of application systems: Gas turbine to scramjet. In *SCIDAC 2011*.
- [141] M. Meyer, S. Hickel, and N.A. Adams. Assessment of implicit large-eddy simulation with a conservative immersed interface method for turbulent cylinder flow. *International Journal of Heat and Fluid Flow*, 31(3):368 – 377, 2010.
- [142] J. Meyers, B. J. Geurts, and P. Sagaut. A computational error-assessment of central finite-volume discretizations in large-eddy simulation using a Smagorinsky model. *Journal of Computational Physics*, 227(1):156–173, 2007.
- [143] J. Meyers and P. Sagaut. On the model coefficients for the standard and the variational multi-scale Smagorinsky model. *Journal of Fluid Mechanics*, 569:387–319, 2006.

- [144] Y. Morinishi. Skew-symmetric form of convective terms and fully conservative finite difference schemes for variable density low-mach number flows. *Journal of Computational Physics*, 229(2):276 – 300, 2010.
- [145] J. D. Murray. On Burgers' model equations for turbulence. *Journal of Fluid Mechanics*, 59:263–279, 6 1973.
- [146] B. T. Nadiga and D. Livescu. Instability of the perfect subgrid model in implicit-filtering large eddy simulation of geostrophic turbulence. *Phys. Rev. E*, 75:046303, Apr 2007.
- [147] F. Nicoud and F. Ducros. Subgrid-scale stress modelling based on the square of the velocity gradient tensor. *Flow, Turbulence and Combustion*, 3:183–200, 1999.
- [148] J. A. Nitsche. Über ein Variationsprinzip zur Lösung von Dirichlet-Problemen bei Verwendung von Teilräumen, die keinen Randbedingungen unterworfen sind. *Abh. Math. Sem. Univ. Hamburg*, 36:9–15, 1971.
- [149] C. Norberg. An experimental investigation of the flow around a circular cylinder: influence of aspect ratio. *Journal of Fluid Mechanics*, 258:287–316, 1994.
- [150] A. M. Obukhov. On the distribution of energy in the spectrum of turbulent flow,. *Dokl. Akad. Nauk SSSR*, 32:22–24, 1941.
- [151] L. Ong and J. Wallace. The velocity field of the turbulent very near wake of a circular cylinder. *Experiments in Fluids*, 20(6):441–453, 1996.
- [152] S. A. Orszag. Numerical methods for the simulation of turbulence. *Physics of Fluids (1958-1988)*, 12(12), 1969.
- [153] S. A. Orszag. On the elimination of aliasing in finite-difference schemes by filtering high-wavenumber components. *Journal of the Atmospheric Sciences*, 28(6):1074–1074, Sep 1971.
- [154] S. A. Orszag. Numerical simulation of the Taylor-Green vortex. In R. Glowinski and J. L. Lions, editors, *Computing Methods in Applied Sciences and Engineering Part 2*, volume 11 of *Lecture Notes in Computer Science*, pages 50–64. Springer Berlin Heidelberg, 1974.
- [155] S. A. Orszag and G. S. Patterson. Numerical simulation of three-dimensional homogeneous isotropic turbulence. *Phys. Rev. Lett.*, 28:76–79, Jan 1972.

- [156] S. Ossia and M. Lesieur. Energy backscatter in large-eddy simulations of three-dimensional incompressible isotropic turbulence. *Journal of Turbulence*, 2000.
- [157] H. Ouvrard, B. Koobus, A. Dervieux, and M. V. Salvetti. Classical and variational multiscale LES of the flow around a circular cylinder on unstructured grids. *Computers & Fluids*, 39(7):1083 – 1094, 2010.
- [158] N. Park, J. Y. Yoo, and H. Choi. Discretization errors in large eddy simulation: on the suitability of centered and upwind-biased compact difference schemes. *Journal of Computational Physics*, 198(2):580 – 616, 2004.
- [159] Ph. Parnaudeau, J. Carlier, D. Heitz, and E. Lamballais. Experimental and numerical studies of the flow over a circular cylinder at Reynolds number 3900. *Physics of Fluids*, 20:85–101, 2008.
- [160] R. Pasquetti. Spectral vanishing viscosity method for large-eddy simulation of turbulent flows. *Journal of Scientific Computing*, 27(1-3):365–375, June 2006.
- [161] A. T. Patera. A spectral element method for fluid dynamics: Laminar flow in a channel expansion. *Journal of Computational Physics*, 54(3):468 – 488, 1984.
- [162] J. Peraire and P.-O. Persson. The compact discontinuous Galerkin (CDG) method for elliptic problems. *SIAM J. Sci. Comput.*, 30(4):1806–1824, 2008.
- [163] P.-O. Persson. A sparse and high-order accurate line-based discontinuous Galerkin method for unstructured meshes. *Journal of Computational Physics*, 233:414–429, January 2013.
- [164] R. Peyret. *Spectral Methods for Incompressible Viscous Flow*. Springer Heidelberg, 2002.
- [165] N. J. Phillips. An example of non-linear computational instability. In *The Atmosphere and the Sea in Motion*, pages 501–504. Rockefeller Institute Press, 1959.
- [166] U. Piomelli, W. H. Cabot, P. Moin, and S. Lee. Subgrid scale backscatter in turbulent and transitional flows. *Physics of Fluids A: Fluid Dynamics (1989-1993)*, 3(7), 1991.
- [167] S. B. Pope. *Turbulent Flows*. Cambridge University Press, 2000.
- [168] S. B. Pope. Ten questions concerning the large-eddy simulation of turbulent flows. *New Journal of Physics*, 6(1):35, 2004.

- [169] J. Qiu. A numerical comparison of the Lax-Wendroff discontinuous Galerkin method based on different numerical fluxes. *Journal of Scientific Computing*.
- [170] J. Qiu, B. C. Khoo, and C.-W. Shu. A numerical study for the performance of the Runge-Kutta discontinuous Galerkin method based on different numerical fluxes. *Journal of Computational Physics*, 212:540 – 565, 2006.
- [171] W. H. Reed and T. R. Hill. Triangular mesh methods for the neutron transport equation. Technical Report LA-UR-73-479, Los Alamos Scientific Laboratory, 1973.
- [172] J. Reiss and J. Sesterhenn. Conservative, skew-symmetric discretization of the compressible navier-stokes equations. In Andreas Dillmann, Gerd Heller, Hans-Peter Kreplin, Wolfgang Nitsche, and Inken Peltzer, editors, *New Results in Numerical and Experimental Fluid Mechanics VIII*, volume 121 of *Notes on Numerical Fluid Mechanics and Multidisciplinary Design*, pages 395–402. Springer Berlin Heidelberg, 2013.
- [173] O. Reynolds. On the dynamical theory of incompressible viscous fluids and the determination of the criterion. *Philosophical Transactions of the Royal Society of London. (A.)*, 186:123–164, 1895.
- [174] P. J. Roache. Code verification by the method of manufactured solutions. *Journal of Fluids Engineering*, 124(1):4–10, Nov 2001.
- [175] R. S. Rogallo. Numerical experiments in homogeneous turbulence. Technical Report NASA TM 81215, 1981.
- [176] R. S. Rogallo and P. Moin. Numerical simulation of turbulent flows. *Annual Review of Fluid Mechanics*, 16(1):99–137, 1984.
- [177] P. Sagaut. *Large Eddy Simulation for Incompressible Flows*. Springer Heidelberg, Germany, 2006.
- [178] R. Salmon. *Lectures on Geophysical Fluid Dynamics*. Oxford University Press, USA, 1998.
- [179] K. Sengupta, F. Mashayek, and G.B. Jacobs. Large-eddy simulation using a discontinuous Galerkin spectral element method. In *45th AIAA Aerospace Sciences Meeting and Exhibit*, 2007.

-
- [180] T. K. Sengupta and M. T. Nair. Upwind schemes and large eddy simulation. *International Journal for Numerical Methods in Fluids*, 31(5):879–889, 1999.
- [181] J.-M. Senoner, M. Garcia, S. Mendez, G. Staffelbach, O. Vermorel, and T. Poinso. Growth of rounding errors and repetitivity of large eddy simulations. *AIAA Journal*, 46(7):1773–1781, Jul 2008.
- [182] L. Shtilman and J. R. Chasnov. LES versus DNS: A comparative study. In D. Spinks, editor, *Studying Turbulence Using Numerical Simulation Databases*, pages 137–143, November 1992.
- [183] Ch.-W. Shu, W.-S. Don, D. Gottlieb, O. Schilling, and L. Jameson. Numerical convergence study of nearly incompressible, inviscid Taylor-Green vortex flow. *Journal of Scientific Computing*, 24(1):1–27, 2005.
- [184] I. Silberman. Planetary waves in the atmosphere. *Journal of Meteorology*, 11(1):27–34, Feb 1954.
- [185] B. Sjögreen and H.C. Yee. On skew-symmetric splitting and entropy conservation schemes for the Euler equations. In Gunilla Kreiss, Per Lötstedt, Axel Målqvist, and Maya Neytcheva, editors, *Numerical Mathematics and Advanced Applications 2009*, pages 817–827. Springer Berlin Heidelberg, 2010.
- [186] J. Smagorinsky. General circulation experiments with the primitive equations. *Mon. Wea. Rev.*, 91:99–164, 1963.
- [187] C. G. Speziale. Galilean invariance of subgrid-scale stress models in the large-eddy simulation of turbulence. *Journal of Fluid Mechanics*, 156:55–62, 7 1985.
- [188] S. Stolz and N. A. Adams. An approximate deconvolution procedure for large-eddy simulation. *Physics of Fluids (1994-present)*, 11(7), 1999.
- [189] E. Tadmor. Convergence of spectral methods for nonlinear conservation laws. *SIAM Journal on Numerical Analysis*, 26(1):30–44, Feb 1989.
- [190] G. I. Taylor and A. E. Green. Mechanism of the production of small eddies from large ones. *Proceedings of the Royal Society of London. Series A, Mathematical and Physical Sciences*, 158(895):pp. 499–521, 1937.
- [191] R. Temam. Approximation of attractors, large eddy simulations and multiscale methods. *Proceedings: Mathematical and Physical Sciences*, 434(1890):pp. 23–39, 1991.

- [192] H. Tennekes and J. L. Lumley. *A First Course in Turbulence*. MIT Press, 1972.
- [193] S. Tenneti and S. Subramaniam. Particle-resolved direct numerical simulation for gas-solid flow model development. *Annual Review of Fluid Mechanics*, 46(1):199–230, 2014.
- [194] T. E. Tezduyar and M. Senga. Stabilization and shock-capturing parameters in SUPG formulation of compressible flows. *Computer Methods in Applied Mechanics and Engineering*, 195(13-16):1621 – 1632, 2006. A Tribute to Thomas J.R. Hughes on the Occasion of his 60th Birthday.
- [195] J. Thuburn, J. Kent, and N. Wood. Cascades, backscatter and conservation in numerical models of two-dimensional turbulence. *Quarterly Journal of the Royal Meteorological Society*, 140(679):626–638, 2014.
- [196] E. F. Toro. *Riemann Solvers and Numerical Methods for Fluid Dynamics*. Springer, June 1999.
- [197] A. Tsinober. *An Informal Conceptual Introduction to Turbulence*. Springer Netherlands, 2009.
- [198] A. Uranga, P.-O. Persson, M. Drela, and J. Peraire. Implicit large eddy simulation of transition to turbulence at low Reynolds numbers using a discontinuous Galerkin method. *International Journal for Numerical Methods in Engineering*, 87(1-5):232–261, 2011.
- [199] F. van der Bos and B. J. Geurts. Computational error-analysis of a discontinuous Galerkin discretization applied to large-eddy simulation of homogeneous turbulence. *Computer Methods in Applied Mechanics and Engineering*, 199(13–16):903 – 915, 2010.
- [200] Z.J. Wang, K. Fidkowski, R. Abgrall, F. Bassi, D. Caraeni, A. Cary, H. Deconinck, R. Hartmann, K. Hillewaert, H.T. Huynh, N. Kroll, G. May, P.-O. Persson, B. van Leer, and M. Visbal. High-order CFD methods: current status and perspective. *International Journal for Numerical Methods in Fluids*, 72(8):811–845, 2013.
- [201] T. C. Warburton and G. E. Karniadakis. A discontinuous Galerkin method for the viscous MHD equations. *Journal of Computational Physics*, 152(2):608 – 641, 1999.
- [202] L. Wei and A. Pollard. Direct numerical simulation of compressible turbulent channel flows using the discontinuous Galerkin method. *Computers & Fluids*, 47(1):85 – 100, 2011.

- [203] V. Wheatley, H. Kumar, and P. Huguenot. On the role of Riemann solvers in discontinuous Galerkin methods for magnetohydrodynamics. *Journal of Computational Physics*, 229(3):660–680, 2010.
- [204] D. C. Wilcox. *Turbulence Modeling for CFD*. D C W Industries, 2006.
- [205] N. J. Zabusky and C. J. Galvin. Shallow-water waves, the Korteweg-deVries equation and solitons. *Journal of Fluid Mechanics*, 47:811–824, 6 1971.
- [206] J. Zhu, Y. T. Zhang, S. A. Newman, and M. Alber. Application of discontinuous Galerkin methods for reaction diffusion systems in developmental biology. *Journal of Scientific Computing*, 40:391–418, 2009.

List of Tables

2.1.	L_∞ -errors with respect to \tilde{u} for different resolutions N_v of the v -problem at time $t = 0.25$ with the pseudo-spectral method.	43
2.2.	L_∞ -errors with respect to \tilde{u} for different resolutions N_v of the v -problem at time $t = 0.25$ with the FD method.	44
3.1.	$n_{PPW_{min}}(N, \delta)$ for the Gauss DGSEM and the 6th order compact FD for a given dispersion error δ and the degree N of the local polynomial ansatz. Reproduced with permission from [85].	58
3.2.	Estimated operation count for one-dimensional spatial operators for different discretizations.	83
3.3.	Contributors and scheme details for the 1st International High Order Workshop, test case 3.5, see Figure 3.9.	86
3.4.	Computational cost for DNS simulations with DGSEM. All computations were run on the “Hermit” Cray XE6 at HLRS, except the TGV case, which was run on the “Jugene” BlueGene P at JSC.	91
4.1.	Maximum values of the real parts of the eigenvalues of the DGSEM operator ($N = 15$) spectrum with different number of integration points for the polynomial advection velocity.	112
4.2.	Maximum values of the real parts of the eigenvalues of the DG operator ($N = 15$) spectrum with different number of integration points for the sinusoidal advection velocity.	114
4.3.	Integral quantities and simulation parameters for $Re_D = 3900$ cylinder flow, reproduced from [18]. $C_{p_{Base}}$: pressure coefficient at the downstream position $x = D/2, y = 0$, Str : Strouhal number of the lift coefficient $f_{Lift} D/U_\infty$, C_D : drag coefficient, L_r : length of separation bubble.	134
4.4.	Computational cost for the cylinder flow computations.	138

4.5.	Simulation details for the cylinder flow with minimal C_s . $C_{p_{Base}}$: pressure coefficient at the downstream position $x = D/2, y = 0$, Str : Strouhal number of the lift coefficient $f_{Lift} D/U_\infty$, C_D : drag coefficient, C_L^{rms} : RMS value of the lift coefficient, L_r : length of separation bubble, $\theta_{sep}, \theta_{re}$: separation and reattachment location.	144
4.6.	Integral quantities and simulation parameters for $Re_D = 3900$ cylinder flow, as a function of the Euler flux function. $C_{p_{Base}}$: pressure coefficient at the downstream position $x = D/2, y = 0$, Str : Strouhal number of the lift coefficient $f_{Lift} D/u_\infty$, C_D : drag coefficient, L_r : length of separation bubble.	159
B.1.	Simulation parameters for $Re_D = 3900$ cylinder LES computations.	175

List of Figures

1.1.	Temporal evolution (from left to right) of two temperature bubbles in a stably stratified medium. Shown are isocontours of temperature difference $\Delta\theta = \theta - \theta_{background}$	2
2.1.	Decaying homogeneous isotropic turbulence. Computations with pseudo-spectral code <i>Spex</i> described in Section 3.2.1. <i>Left</i> : Temporal evolution of the spectrum of kinetic energy $E(k)$. Dashed line denotes Kolmogorov's $k^{-5/3}$ law. <i>Right</i> : Temporal evolution of total kinetic energy E . Dashed lines denote decay laws published by [53] and [102].	12
2.2.	Solution of the Lorenz System (Equation (2.5)) with $a = 3, b = 25, c = 1$. Blue lines: initial condition $\vec{x}_0 = [1, 1, 2]$; Black lines: initial condition $\vec{x}_0 = [1.00001, 1, 2]$. <i>Top</i> : Solution trajectories up to $t_{end} = 10$ (<i>left</i>) and $t_{end} = 90$ (<i>right</i>). Green and red markers show the particle position of blue and black trajectories at t_{end} . <i>Bottom</i> : Temporal evolution of x -components of particle positions.	14
2.3.	Vortex interactions in two dimensions, shown are contours of vorticity magnitude. From left to right: initial random vorticity field at $t = 0$, resulting fields at $t = 100, 500, 10000$	16
2.4.	Interaction of two mono-scale vortices: Development of vortical structures and scale cascade. Shown are $\lambda_2 = -0.001$ isocontours, colored by normalized helicity. Temporal evolution from upper left to lower right.	17
2.5.	Temporal evolution of the Taylor-Green vortex, from upper left to lower right at time $t = 0.4s, 1.4s, 2.7s, 5.9s, 8.9s$ and $15.5s$ Shown are contours of vorticity, colored by relative helicity.	25
2.6.	Integral quantities of the Taylor-Green vortex flow. <i>Left</i> : Spectrum of kinetic energy for $Re = 5000$ at $t = 9.0$, dashed line: $k^{-5/3}$ slope. <i>Right</i> : Temporal evolution of the rate of kinetic energy dissipation for $Re = 1600$	26

2.7. Spectrum of kinetic energy of isotropic homogeneous turbulence (Taylor-Green Vortex at $Re = 5000, t = 11s$). I: Anisotropic large scale energy production, II: Inertial subrange region, III: Small scale isotropic dissipation range.	30
2.8. Moving shock solution of the viscous Burgers' equation. <i>Left</i> : DNS and filtered solution at $t = 0.25$. <i>Right</i> : Corresponding energy spectra. . . .	42
2.9. Temporal evolution of the energy spectrum of the source $S(x, t)$	42
2.10. Comparison of different approximate solutions to the v -problem at time $t = 0.25$	43
2.11. Solution of the v -problem with the pseudo-spectral method. <i>Left</i> : Solution v computed with $N_v = 64$ grid points at $t = 0.25$. <i>Right</i> : Corresponding energy spectrum.	44
2.12. Coarse solution of the u -problem with $N_u = 64$. <i>Left</i> : Coarse solution u at $t = 0.25$. <i>Right</i> : Plot of the corresponding energy spectrum.	45
2.13. Solution of the v -problem with the FD $\mathcal{O}4$ method. <i>Left</i> : Solution v_{FD} computed with $N_v = 128$ grid points at $t = 0.25$ and comparison to the DNS results. <i>Right</i> : Corresponding energy spectra.	46
2.14. Smagorinsky model for laminar flow. Kinetic energy dissipation rate over time as a function of the model constant C_s	50
3.1. Global vs. local approximation of spatial derivatives. The regular grid is denoted by circles, the boundary points by squares. Blue lines denote the solution, red and yellow lines the approximate solution based on the stencil indicated by the arrows. Vertical black lines indicate a subcell.	57
3.2. Dispersion relation for the linear transport Equation (3.3) of DGSEM with Gauss nodes, central finite differences and global spectral (exact) scheme. $K^* = \frac{K}{N+1}$ is the normalized wavenumber and $\Omega^* = \frac{\Omega}{N+1}$ is the corresponding modified normalized numerical mode (eigenvalue). For FD, $K^* = K$ and $\Omega^* = \Omega$	59
3.3. <i>Left</i> : Ratio R of resolved scales (limit determined by phase error e_i) to available scales on a $N_{Grid} = 1024$ grid, $e_{i=1,2,3} \in \{0.1, 0.01, 0.001\}$, p : order of central FD discretization <i>Right</i> : Percentage of modes lost to dispersion error $1 - R$ as a function of p for increasing number of grid points.	60
3.4. Dissipation rate $-\frac{dk}{dt}$ of the kinetic energy of the Taylor-Green Vortex at $Re = 800$. Results for the DNS data taken from Brachet [29]. The required wall-clock time for each computation is indicated in $[h]$	62

-
- 3.5. Taylor-Green Vortex at $Re = 1600$. Comparison of the spectra of kinetic energy for $N = 1$, $N = 3$, de-aliased $N = 7$ and de-aliased $N = 15$ solution. All discretizations with a total of 64^3 DOF, except DNS. 63
- 3.6. L_2 error of density over grid spacing h for the pseudo-spectral code *Spex*, obtained with the method of manufactured solutions. 69
- 3.7. Spectrum of kinetic energy for the Taylor-Green vortex at $Re = 1600$ and $t = 9s$. Comparison of pseudo-spectral codes *Spex* and *Louvain* and DGSEM code *Flexi*. 70
- 3.8. Strong scaling of DGSEM on BlueGene Q “JuQueen” at JSC. 128^3 elements, $N = 7$ up to 262, 144 ranks (131, 072 cores with $2\times$ hyper-threading). Results from the Porting and Scaling Workshop, 2013. . . . 85
- 3.9. Code comparison for DNS of Taylor-Green Vortex at $Re = 1600$. *Top*: Error in computed vs. reference dissipation rate over DOF. *Bottom*: Error in computed vs. reference dissipation rate over Work Units (CPU time). Results from the 1st International Workshop on High Order Methods in CFD, 2012, with permission from Koen Hillewaert (Cenaero) and from [200]. For legend refer to Table 3.3. 88
- 3.10. Flow over a sphere at $Re = 1000$ and $Ma = 0.3$. The computation was run the Cray XE6 “Hermit” at HLRS on 4096 cores. The picture shows the laminar separation, the vortex street and the transition in the wake ($\lambda_2 = -0.01$ criterion, colored by vorticity magnitude). Computation by F. Hindenlang [100]. 93
- 3.11. Vortex Cascade at $Re = 1000$. *Left*: λ_2 isocontours, colored by helicity. *Right*: Temporal development of energy spectrum. 94
- 3.12. Taylor-Green Vortex at $Re = 5000$. Computation with 384^3 and 600^3 DOF on 125, 000 cores on BlueGene P (“Jugene”) at JSC. *Left*: Isocontours of vorticity magnitude, colored by helicity. *Right*: Spectrum of kinetic energy for 384^3 and 600^3 DOF, corresponding cut-off wavenumbers denoted by dashed lines. 94
- 3.13. Flow over a circular cylinder at $Ma = 0.1$, $Re = 3900$. Computation with 164 mio DOF on 4, 992 cores on Cray XE6 “Hermit” at HLRS. $\lambda_2 = -0.001$ criterion, colored by vorticity magnitude. *Top*: side view. *Bottom*: Top view of near wake. 95

4.1. Dispersion (<i>left</i>) and dissipation error (<i>right</i>) for DGSEM with Gauss nodes. $K^* = \frac{K}{N+1}$ is the normalized wavenumber and $\Omega^* = \frac{\Omega}{N+1}$ is the corresponding modified normalized numerical mode (eigenvalue). Bottom row: logarithmic plot with zoom on low wavenumber region. Note that the error is cut off at 10^{-10} to avoid numerical noise. Plots with permission from [85].	101
4.2. Taylor-Green Vortex at $Re = 1000$. Effect of aliasing on flow physics. <i>Left</i> : Mean temperature and kinetic energy dissipation rate over time. <i>Right</i> : Maximum vorticity over time.	107
4.3. Operator spectrum for constant advection speed and $N = 15$ with either $M + 1 = 16$ or 26 integration points, respectively. The maximum of the real parts of the eigenvalues is 0.	110
4.4. Operator spectrum for polynomial advection speed and $N = 15$ with $M + 1 = 16$ integration points (original DGSEM scheme). The maximum of the real parts of the eigenvalues is 0.016.	111
4.5. Operator spectrum for polynomial advection speed and $N = 15$ with different number of integration points $M + 1$. The right plot shows a zoomed view of the imaginary axis.	112
4.6. Operator spectrum for sinusoidal advection speed, Equation (4.14a), and $N = 15$ with different number of integration points $M + 1$. The right plot shows a zoomed view of the imaginary axis.	113
4.7. Operator spectrum for sinusoidal advection speed, Equation (4.14b), and $N = 15$ with different number of integration points $M + 1$. The right plot shows a zoomed view of the imaginary axis.	114
4.8. Plot of the kinetic energy dissipation rates of the Taylor-Green Vortex (<i>Left</i> : $Re = 800$, <i>Right</i> : $Re = 1600$), computed with with 64^3 DOF using either a low order method (2nd order, $N = 1$) or a very high order method (16th order, $N = 15$).	121
4.9. Transfer functions for the weak and strong variant of the modal filters for $N = 15$	122
4.10. Taylor-Green Vortex at $Re = 800$. Kinetic energy dissipation rate $-\frac{dk}{dt}$ for filter-stabilized $N = 15$ (4^3 grid cells) computation. The right plot is zoomed in on the time range of maximum enstrophy production. . . .	123
4.11. Taylor-Green Vortex at $Re = 800$. <i>Left</i> : Kinetic energy spectra at $t = 9$. <i>Right</i> : Kinetic energy dissipation rate $-\frac{dk}{dt}$, the resolved (molecular) dissipation rate and the numerical dissipation rate for filter-stabilized $N = 15$ (4^3 grid cells) computation.	124

4.12. Taylor-Green Vortex at $Re = 1600$. Kinetic energy dissipation rate $-\frac{dk}{dt}$ for filter-stabilized $N = 15$ (4 grid cells) computation. The right plot is zoomed in on the time range of maximum enstrophy production.	125
4.13. Taylor-Green Vortex at $Re = 1600$. <i>Left</i> : Kinetic energy spectra at $t = 9$. <i>Right</i> : Kinetic energy dissipation rate $-\frac{dk}{dt}$, the resolved (molecular) dissipation rate and the numerical dissipation rate for filter-stabilized $N = 15$ (4 grid cells) computation.	125
4.14. Taylor-Green Vortex at $Re = 800$. Kinetic energy dissipation rate $-\frac{dk}{dt}$ for PDG $N = 15$ (4 grid cells) computation. The right plot is zoomed in on the time range of maximum enstrophy production.	127
4.15. Taylor-Green Vortex at $Re = 800$. <i>Left</i> : Kinetic energy spectra at $t = 9$. <i>Right</i> : Kinetic energy dissipation rate $-\frac{dk}{dt}$, the resolved (molecular) dissipation rate and the numerical dissipation rate for PDG $N = 15$ (4 grid cells) computation.	127
4.16. Taylor-Green Vortex at $Re = 1600$. Kinetic energy dissipation rate $-\frac{dk}{dt}$ for PDG $N = 15$ (4^3 grid cells) computation. The right plot is zoomed in on the time range of maximum enstrophy production.	129
4.17. Taylor-Green Vortex at $Re = 1600$. <i>Left</i> : Kinetic energy spectra at $t = 9$. <i>Right</i> : Kinetic energy dissipation rate $-\frac{dk}{dt}$, the resolved (molecular) dissipation rate and the numerical dissipation rate for PDG $N = 15$ (4^3 grid cells) computation.	129
4.18. Taylor-Green Vortex at $Re = 800$. Comparison of kinetic energy dissipation and numerical dissipation (<i>left</i>) and energy spectra (<i>right</i>) for $N = 15$ (4^3 grid cells) computations with stabilization via polynomial de-aliasing vs. filtering.	130
4.19. Taylor-Green Vortex ($Re = 800$). Isocontours of $\lambda_2 = -1.5$ at $t = 8.5$. All computations with 64^3 DOF except DNS. From upper left to lower right: i) 16th order filtered computation, ii) 16th order computation with polynomial de-aliasing, iii) 2nd order computation, iv) DNS reference result with 384^3 DOF.	131
4.20. Comparison of LES methods: Kinetic energy dissipation rate for $Re \in \{800, 1600, 3000\}$ for PDG computations with $N = 15$ compared to DNS and LES reference data.	133
4.21. Time- and spanwise-averaged streamwise velocity component and grid. <i>Left</i> : $N = 11$ grid with $8 \times 8 \times 6$ elements (circumferential, radial and spanwise), <i>right</i> : $N = 7$ grid with $16 \times 16 \times 12$ elements.	135
4.22. Instantaneous flow field in the cylinder region. <i>Left</i> : u -velocity, <i>middle</i> : Modal resolution indicator, <i>right</i> : Difference between projection and collocation of u^2	137

4.23. Mean streamwise velocity at different downstream locations in the wake of the circular cylinder flow at $Re_D = 3900$. *Left*: $N = 11$ computation, *Right*: $N = 7$ computation. Solid lines: present DG results, dashed lines: computational LES results from [141], open squares: computational LES results from [122], filled circles: experimental results from [159]. 138

4.24. Kinetic energy dissipation rate for the Taylor-Green Vortex with increasing Reynolds number: 8^3 Elements, $N = 7$. $M + 1$ denotes the number of quadrature points for the non-linear fluxes, C_s indicates the Smagorinsky model constant and is 0.0 unless stated otherwise. 140

4.25. Grid for the DNS computation, detailed view of cylinder vicinity. 142

4.26. From left to right: Grids I, II and III for the LES computations, detailed view. Grid details: I: $16 \times 16 \times 32$ elements (circumferential, radial and spanwise direction), $N = 7$, II: $22 \times 22 \times 44$, $N = 5$, III: $32 \times 32 \times 64$, $N = 3$ 143

4.27. Time- and spanwise-averaged streamlines. Upper left plot: DNS. Rest: a) N7-1, b) N7-A, c) N5-1, d) N5-A, e) N3-1, f) N3-A 145

4.28. Time- and spanwise averaged velocity fluctuations $\langle u'u' \rangle$ in the cylinder wake. Line with squares: DNS results; *Left*: DGSEM according to Table 4.5. Dashed line: N7-A; dotted line: N5-A; dash-dotted line: N3-A; *right*: PDG according to Table 4.5. Dashed line: N7-1; dotted line: N5-1; dash-dotted line: N3-1. 146

4.29. One-dimensional spectra of the streamwise velocity component in the wake at $x/D = 3.0, y/D = 0.25$. All frequencies normalized by the Strouhal frequency of the reference DNS (see Table 4.5). a) N7-1, b) N7-A, c) N5-1, d) N5-A, e) N3-1, f) N3-A; dashed line denotes Kolmogorov's $k^{-5/3}$ law. 147

4.30. Time- and spanwise-averaged velocity fluctuations $\langle u'u' \rangle$ in the wake region, normalized by U_∞^2 . Top row: DNS reference. First column: PDG results, second column: PDG with Smagorinsky model, last column: DGSEM with Smagorinsky model; second row: N7-1, N7-2, N7-A, third row: N5-1, N5-2, N5-B, fourth row: N3-1, N3-4, N3-D. 150

4.31. Kinetic energy dissipation rate for the Taylor-Green Vortex at $Re = 1600$: Comparison of convective numerical flux function influence for different polynomial degrees N with same total no. of DOF (64^3). *Square* symbol denotes the reference DNS solution [28], *dashed* line denotes the LLF flux result, the *solid* line denotes the Roe flux result. Plot reproduced from [20]. 155

4.32. Kinetic energy dissipation rate for the Taylor-Green Vortex at $Re = 3000$: Comparison of LDG flux and BR1 flux with DNS, 4^3 elements, polynomial degree $N = 15$. <i>Right</i> : Detailed view. Plot reproduced from [20].	156
4.33. Optimization of the penalty parameters α_1 and α_2 for the kinetic energy dissipation rate. Shown is the L_2 deviation between DNS and LES results as a function of α_1 and α_2	156
4.34. Kinetic energy dissipation rate for the Taylor-Green Vortex: <i>Left</i> : $Re = 800$: Comparison of classical Roe flux and modified Roe flux with DNS. <i>Right</i> : $Re = 1600$: Comparison of modified combined flux and standard fluxes with DNS.	158
4.35. Comparison of Cylinder LES results for Roe and Rusanov-flux for computation described in Section 4.3.2. <i>Left</i> : Pressure coefficient along geometry. Filled circles denote experimental data for $Re = 5000$ of Son & Hanratty for vorticity and for $Re = 4020$ of Norberg for pressure coefficient (taken from [141]). Open squares denote DNS results [135]. <i>Right</i> : Mean crossflow velocity at different downstream locations in the wake of the circular cylinder flow at $Re_D = 3900$, $N = 11$ computation. Solid black lines: DGSEM with Rusanov flux. Solid blue lines: DGSEM with Roe flux. Dashed lines: computational LES results from [141]. Open squares: computational LES results from [122]. Filled circles: experimental results from [159].	159
5.1. Kinetic energy spectra of HIT at $Re_\lambda = 82$. DNS (solid line) computed with $Spex$ on 512^3 nodes. Dashed line denotes PDG result, solid line with markers denotes LAD result, both with 72^3 DOF ($N = 11$). Data taken from [74].	168
A.1. Coefficients α (<i>left</i>) and β (<i>right</i>) in wave space for a box spectrum $E(k) = \text{const}$ for $4 \leq k \leq 12$, $E(k) = 0$ otherwise.	170
A.2. Scatter plot of u - v and v - w correlations from Rogallo's procedure (Equations (A.1) and (A.2)).	170
B.1. Time- and spanwise averaged velocity fluctuations $\langle u'v' \rangle$ in the cylinder wake. Line with squares: DNS results; <i>left</i> : DGSEM according to Table 4.5. Dashed line: N7-A; dotted line: N5-A; dash-dotted line: N3-A. <i>right</i> : PDG according to Table 4.5. Dashed line: N7-1; dotted line: N5-1; dash-dotted line: N3-1.	171

B.2.	One-dimensional spectra of the crossflow velocity component in the wake at $x/D = 3.0, y/D = 0.25$. All frequencies normalized by the Strouhal frequency of the reference DNS (see Table 4.5). a) N7-1, b) N7-A, c) N5-1, d) N5-A, e) N3-1, f) N3-A; dashed line denotes Kolmogorov's $k^{-5/3}$ law.	172
B.3.	Time- and spanwise-averaged velocity fluctuations $\langle u'v' \rangle$ in the wake region, normalized by square of the free-stream velocity U_∞ . Top row: DNS result. Second to fourth row: results for N7, N5 and N3 cases, with PDG in the left and DGSEM in the right column.	173
B.4.	Time- and spanwise-averaged crossflow velocity fluctuations $\langle v'v' \rangle$ in the wake region, normalized by square of the free-stream velocity U_∞ . Top row: DNS result. Second to fourth row: results for N7, N5 and N3 cases, with PDG in the left and DGSEM in the right column.	174
B.5.	Time- and spanwise-averaged turbulent kinetic energy in the wake region, normalized by free-stream kinetic energy. First row: DNS reference results, first column: PDG results, second column: PDG with Smagorinsky model, last column: DGSEM with Smagorinsky model; Second row: N7-1, N7-2, N7-A, third row: N5-1, N5-2, N5-B, fourth row: N3-1, N3-4, N3-D.	176
B.6.	Time- and spanwise-averaged velocity magnitude in the wake region, normalized by free-stream kinetic energy. First row: DNS reference results, first column: PDG results, second column: PDG with Smagorinsky model, last column: DGSEM with Smagorinsky model; Second row: N7-1, N7-2, N7-A, third row: N5-1, N5-2, N5-B, fourth row: N3-1, N3-4, N3-D.	177
B.7.	Isocontours of time- and spanwise-averaged streamwise velocity: $u = 0$. Shaded area denotes the DNS reference solution.	178
C.1.	Taylor-Green Vortex at $Re = 800$. Kinetic energy dissipation rate $-\frac{dk}{dt}$ for filter-stabilized $N = 7$ (8^3 grid cells) computation. The right plot is zoomed in on the time range of maximum enstrophy production.	179
C.2.	Taylor-Green Vortex at $Re = 800$. Kinetic energy dissipation rate $-\frac{dk}{dt}$ for PDG $N = 7$ (8^3 grid cells) computation. The right plot is zoomed in on the time range of maximum enstrophy production.	180
C.3.	Taylor-Green Vortex at $Re = 800$. Kinetic energy dissipation rate, resolved dissipation rate and numerical dissipation rate for PDG $N = 7$ (<i>left</i>) and filter-stabilized DGSEM $N = 7$ computation (<i>right</i>).	180

C.4.	Taylor-Green Vortex at $Re = 1600$. Kinetic energy dissipation rate $-\frac{dk}{dt}$ for filter-stabilized $N = 7$ (8^3 grid cells) computation. The right plot is zoomed in on the time range of maximum enstrophy production.	181
C.5.	Taylor-Green Vortex at $Re = 1600$. Kinetic energy dissipation rate $-\frac{dk}{dt}$ for PDG $N = 7$ (8^3 grid cells) computation. The right plot is zoomed in on the time range of maximum enstrophy production.	181
C.6.	Taylor-Green Vortex at $Re = 1600$. Kinetic energy dissipation rate, resolved dissipation rate and numerical dissipation rate for PDG $N = 7$ (<i>left</i>) and filter-stabilized DGSEM $N = 7$ computation (<i>right</i>).	182
C.7.	Taylor-Green Vortex at $Re = 1600$: Comparison of the resolved (<i>left</i>) and total dissipation rate (<i>right</i>) for the contributions to the high order workshop with highest order per participant. Refer to Table 3.3 for the legend.	183
C.8.	Taylor-Green Vortex at $Re = 1600$: Comparison of error measures according to Equation C.2 for the contributions to the high order workshop. For a legend refer to Table 3.3.	184
C.9.	Taylor-Green Vortex at $Re = 1600$: Visualization of vortex detection criterion $\lambda_2 = -1.5$ for $N = 1$ (top), $N = 3$ (bottom left) and $N = 15$ (bottom right) computation (256^3 DOF in each case).	185

Lebenslauf

05.01.1979 Geboren in Trier
1985 - 1989 Grundschule Wincheringen
1989 - 1998 Angela-Merici Gymnasium der Ursulinen, Trier
1998 Allgemeine Hochschulreife
1998 - 2002 Studium der Luft- und Raumfahrttechnik
an der Universität Stuttgart, Vertiefungsrichtungen:
Strömungslehre, Raumfahrttechnik
2002 - 2004 Studium am Georgia Institute of Technology, USA,
Vertiefungsrichtung Aerodynamics & Fluid Mechanics
2004 Abschluß Master of Science in Aerospace Engineering
2009 - 2015 Wissenschaftliche Mitarbeiterin am
Institut für Aerodynamik und Gasdynamik

Stuttgart, den 1. Mai 2015

Andrea Beck